

**Building blocks of a silicon photonic integrated wavelength division
multiplexing transmitter for detector instrumentation**

**Bausteine für einen integrierten siliziumphotonischen
Wellenlängenmultiplexsender zur Detektorinstrumentierung**

Zur Erlangung des akademischen Grades eines
DOKTORS DER INGENIEURWISSENSCHAFTEN (Dr.-Ing.)

von der KIT-Fakultät für Elektrotechnik und Informationstechnik des
Karlsruher Instituts für Technologie (KIT)

angenommene

DISSERTATION

von

M. Sc. Yunlong Zhang

Tag der mündlichen Prüfung: 15. 12. 2020

Hauptreferent: Prof. Dr. Marc Weber

Korreferent: Prof. Dr. Christian Koos

Abstract

This thesis investigates data transmission systems for detector instrumentation and the challenges of this unique application. Limited by the high radiation level, available space, low temperature etc. the state-of-the-art detector readout bandwidth is in the range of several tens of Gb/s per fiber. Given the ever increasing data volume, improving the transmission bandwidth is an urgent problem to solve. Thus, this thesis proposes a generic concept for an integrated transmitter based on wavelength division multiplexing technology and a silicon-on-insulator platform. The aimed transmission bandwidth in the first stage is 40 Gb/s. Two key building blocks of the integrated transmitter, the Mach-Zehnder modulator and the wavelength demultiplexer are studied in detail. A series of modulators with different lengths and etching depths are designed, fabricated and characterized. For the demultiplexer design, a customized design method based on two stigmatic points is developed. A new design parameter is introduced to this method to make it more flexible and easier to use. The effect of modifying the introduced parameter is investigated by a series of comparable devices. All the characterizations validate the feasibility of the proposed concept.

Table of contents

Abstract.....	iii
Table of contents	v
1 Introduction.....	1
2 Theoretical Background.....	5
2.1 Basic properties of silicon	5
2.2 Silicon on insulator wafer and photonic chip fabrication	5
2.3 Popular material platforms for optical communication	11
2.4 Waveguide and effective refractive index	12
2.5 Fiber-chip coupling.....	14
2.6 Plasma dispersion and pn junction	17
2.7 Diffraction theory	19
3 Optical Data Readout in Detector Instrumentation.....	21
3.1 The Large Hadron Collider and the CMS experiment.....	21
3.2 The Adaptive Gain Integrating Pixel Detector at X - FEL	24
3.3 State-of-the-art optical data readout in detector instrumentation	27
3.4 A novel multi-channel optical detector read-out system	32
4 Mach-Zehnder Modulators	35
4.1 Different modulation effects.....	35
4.2 Concept of a Mach-Zehnder modulator.....	37
4.3 Different modulation schemes	39
4.4 Simulation flow of the pn phase shifters	40
4.5 pn-phase shifter design	42
4.6 Multimode Interferometers.....	62
5 Echelle Grating (De-)Multiplexer.....	69
5.1 Filter types	69
5.2 Rowland circle method and the designed devices	72
5.3 Two stigmatic point method and the additional parameter ΔN	83
6 Optical Link Demonstration	99
6.1 Fiber to chip coupling.....	99
6.2 Demonstrator setup.....	101
7 Conclusion	108
8 Acknowledgements.....	110
A List of abbreviations	111
B List of mathematical symbols	113
References	115

1 Introduction

Detector instrumentation plays an important role in fundamental research and many breakthroughs are associated with it. To name a few, the top quark found in 1995 [1] and the tau neutrino found in 2000 [2] were both discovered by the world-leading detector systems at the time. Later on, the excited neutral Xi-b baryon particle was found by the more advanced CMS (Compact Muon Solenoid) detector in 2011. The European Organization for Nuclear Research (CERN), as a famous large fundamental research center, operates a powerful accelerator, the Large Hadron Collider (LHC). Based on the measurements from the detector CMS and ATLAS (A Toroidal LHC Apparatus) [3][4], scientists announced that they found Higgs-like particles [5]. Large-scale detectors are also employed in photon science with e.g. the AGIPD (Adaptive Gain Integrating Pixel Detector) detector of the European X – FEL, which provides ultra-short highly coherent X-ray pulses to revolutionize scientific experiments. Along with the development of particle physics and photon science, scientists have to upgrade or build bigger colliders to increase the collision energy to find new physics. In this scenario, the collider needs to be upgraded further to accelerate the particles to the required energy and gain more evident proof during which the detectors will be upgraded as well.

The number of pixels of the detectors is ever increasing that the energy, time and spatial resolution of the particle detection can be refined. The massive data is read out by massively parallelized data links from the detector elements to the front-end electronics, then to the post processing electronics, and finally to the counting room. Within the entire link, the step from the front-end electronics to the counting room is progressively becoming the bottleneck. To cope with the challenge, state-of-the-art infrastructures employ optical links to realize high-bandwidth data transmission. For example, in the phase 1 upgrade of the Large Hadron Collider (LHC), directly modulated laser diodes are employed as the on-detector transmitter units featuring a transmission speed of up to 4.8 Gb/s per link. Even at such a high transmission bandwidth, there are still more than 100,000 optical links in use [6]. Nevertheless, only a small fraction of the data from the detector elements can be read out and the bulk of the data is thrown away. In terms of the LHC phase 3 upgrade, the experiment data will increase significantly again [7]. Moreover, the irradiation will increase to a level that the on-detector laser diodes can not withstand. Under these circumstances, a new high-speed solution is required to cope with all the above-mentioned challenges.

To address the high-bandwidth transmission challenge, it is beneficial to look at datacom and telecommunication technologies, since they are also using optical fiber communications and facing similar challenges. For example, as written in [8], in 2016 Youtube users were uploading 400 hours of new videos onto the Youtube servers every minute. While on the other hand, they were also watching more than four million videos per minute in 2019. Nevertheless, the uplink and downlink data rates keep increasing so that the communication companies have to continue upgrading the products to meet with the ever increasing requirements from the users. Driven by the markets, corresponding research to deal with high speed transmission was extensively carried out. In 1997, the wavelength division multiplexing (WDM) technique was developed and used in transceiver design. State-of-the-art products at that time featured 16 channels at 2.5 Gb/s at each [9]. Since then, the products upgraded every three to five years and yielded transceivers of several hundreds of gigabits per second. Nevertheless, these products are rather expensive and not designed in consideration of the harsh ambient operating environment of large

scale physical detectors, for example limited space, low temperatures, strong magnetic fields, and high irradiation levels. A direct use of the technology or the devices in detector instrumentation is infeasible.

But inspired by the network products, a WDM system can be introduced into the detector readout system as well, where the key factors limiting the transmission speed will be both the available number of transmission channels and the maximum modulation speed of each channel. On this basis, we propose a generic solution, based on WDM and Mach-Zehnder modulation technology on silicon on insulator (SOI), suitable for particle physics and photon science as well, as depicted in Figure 1.1.

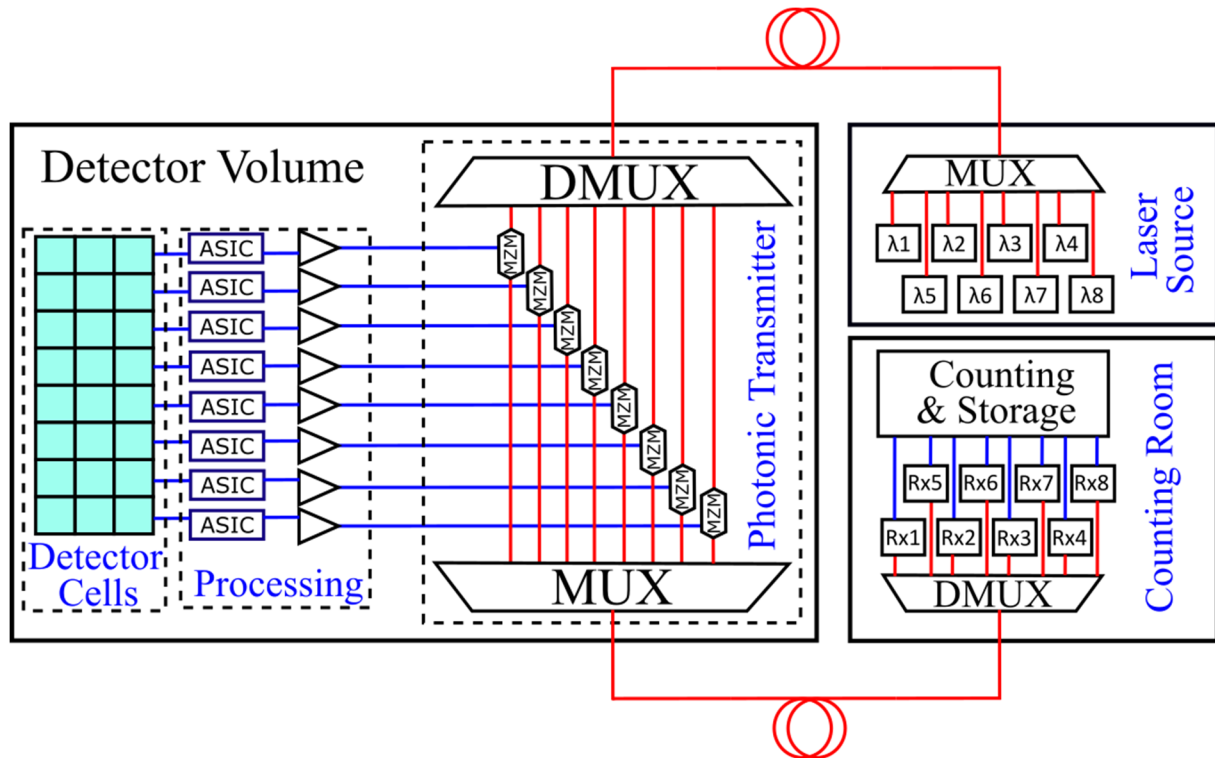


Figure 1.1: Schematic of the proposed generic high-speed transceiver design.

In the proposed solution, the transmission bandwidth per fiber can be improved in two respects. On one hand, the transmission speed of each Mach Zehnder modulator (MZM) can be improved individually and the target speed in this thesis is 10 Gb/s. On the other hand, a pair of wavelength (de-)multiplexers (DMUXs) can be used to realize an on-chip WDM system by allocating several MZM modulators, operating at different wavelengths, to share one common optical fiber. The total transmission bandwidth per fiber can be increased by adding more channels to the DMUX. In Figure 1.1, the laser sources are located outside of the detector in areas with negligible radiation. A number of stabilized wavelength carriers from the laser sources are combined by an optical multiplexer to be transmitted over a common single mode glass fiber (SMF) to the transmitter units on a photonic chip inside the detector. On this chip, the optical carriers are separated by wavelength through a wavelength demultiplexer and forwarded to a number of Mach-Zehnder modulators. Electrical signals from the sensor elements are pre-processed, mapped to available transmitter channels and amplified to the required levels to drive the electro-optic MZMs. The modulated optical signals are combined by a wavelength multiplexer and transmitted to the counting room through a common SMF. There, the signals are demultiplexed again and fed into individual receivers. The photonic chip inside the detector volume will be completely customized and tailored to the requirements, while the off-detector components are commercial off-the-shelf products to lower development costs.

Since the available modulation channels per fiber can be increased and the modulation speed of each modulator can be improved as well, the proposed concept is highly scalable. A further upgrade is easy to realize and a transmission bandwidth per fiber at the scale of Tb/s is feasible. However, from the systemic point of view, to demonstrate the data transmission, several other essential parts are required, which are the 1) multi-wavelength laser source, 2) multi-channel electrical driver for the MZM, 3) multi-channel receiver, and 4) optical and electrical packaging.

In the framework of the research topic Detector Technologies and Systems (DTS), which is part of the Helmholtz-program Matter and Technology (MT), the Institute of Data Processing and Electronics (IPE) of the Karlsruhe Institute of Technology (KIT) has all the required expertise to carry out the development. Preliminarily, the development was started aiming at a 4-channel system. An integrated 4-wavelengths laser source has been built and on this basis, a customized n -wavelengths laser source can be built in the future as well. Secondly, two versions of 4-channel electrical drivers have been developed and fabricated. The second version is miniaturized and can provide high frequency driving signals of up to 30 Gb/s per channel. Thirdly, a corresponding high-speed receiver system has been set up based on an FPGA (Field-Programmable Gate Array) and off-the-shelf components. In terms of packaging, a very stable surface-coupling method was studied to realize dual fiber-chip coupling and wire bonding will be used for the electrical packaging.

The above massive preparation work enables the development of a multi-wavelength integrated transmitter. This thesis aims at the development of key building blocks of an n - λ (n channels with different wavelengths share one common fiber) integrated transmitter, mainly the DMUX and the MZM. A preliminary 4 - λ integrated transmitter will be demonstrated together with the measurement results of a complete 1 - λ data transmission. The thesis is structured as follows:

In chapter 2, the theoretical concepts used all-over the thesis are summarized. This chapter contains a collection of the basic equations.

In chapter 3, the LHC collider is introduced in terms of the basic theory, structure, and harsh operating environment of the CMS detector. On this basis, the challenges of the readout system are analyzed and addressed. Afterwards, the state-of-the-art readout scheme used within the CMS detector will be investigated and the challenges to use it for the phase 3 upgrade will be discussed as well. At the end of this chapter, the novel proposed readout concept is introduced in detail and compared with the current scheme.

In chapter 4, the design of the key building block MZM, which is comprised of pn phase shifters, power splitters and combiners, is presented. For the pn phase shifter, we studied the modulation efficiency variation induced by different doping concentrations and different modulator lengths. The experimental DC and AC measurements of a set of MZM modulators with different lengths will be shown and discussed. A comparison of the cut-off frequency of different modulators will be summarized and analyzed. In addition, the expected radiation effects in the pn phase shifter and their mitigation will be discussed briefly as well. Finally, two different fabricated 3-dB multi-mode interferometers (MMIs) for use as splitters and combiners will be compared in terms of total insertion loss and footprint. In addition, a 86:14 MMI, which can be used for feedback control, is introduced as well.

Introduction

Chapter 5 comprises two popular design methods for Echelle grating demultiplexer design, which are the Rowland circle (RC) method and the two stigmatic points (TSP) method. An 800-GHz channel spacing device will be presented as an example for the Rowland circle design method with simulation and measurement results. For the TSP method, a new design parameter ΔN is introduced to enable more flexible and more efficient designs. The effect of modifying ΔN will be examined by extensive simulations on a set of 800-GHz channel spacing DMUXs. Finally, several devices with narrow channel spacings of 400 GHz and 200 GHz will be presented to show the potential of this method in integrated silicon photonics.

In chapter 6, the entire system setup of a complete optical link will be shown and characterized. The stability of the system is verified by a long-time low-error transmission measurement. Eye diagrams and bit error rate (BER) tests of the transmission will be presented and analyzed as well.

Chapter 7 finally summarizes the work and gives an outlook for future research and applications.

2 Theoretical Background

In this chapter, the basic properties of silicon and the theories of the components used in the integrated transmitter design are introduced.

2.1 Basic properties of silicon

Silicon forms crystals with a diamond-like structure and is an indirect semiconductor, which means that the maximum of its valence band and the minimum of its conduction band occur at different places in the k -space, as shown in Figure 2.1. W_G is the bandgap energy of the indirect semiconductor and W_G' is the band to band energy difference at $k_\mu = 0$. For silicon, the energies have the following values: $W_G = 1.13$ eV and $W_G' = 3.4$ eV. These correspond to the photons with a wavelength of 1.1 μm and 0.36 μm , respectively. Thus, Si is optically transparent at 1.3 μm and 1.55 μm , enabling its application in telecommunications.

In indirect semiconductors, an electron transition from W_C (the bottom of the conduction band) to W_V (the top of the valence band) is accompanied with a crystal momentum change of $\hbar k = \hbar \cdot \pi/a$ as shown in Figure 2.1. And, the momentum variation cannot be transferred to the emitted photons with

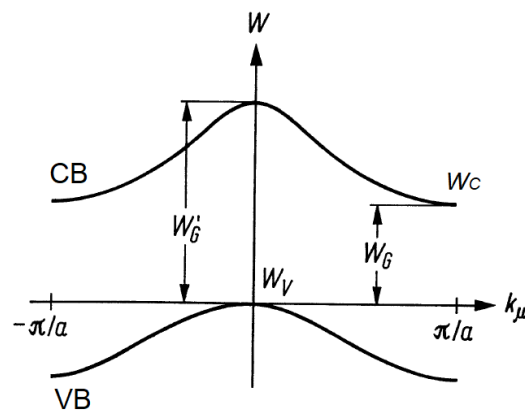


Figure 2.1: Band structure of indirect semiconductors, adapted from [14].

momentum $\hbar k = \hbar \cdot 2\pi/\lambda$ since the lattice constant 'a' is much smaller than the the wavelength λ . Therefore, in this band-band transition process of silicon, a third interaction particle with sufficient momentum is necessary. However, the three-particle interaction is less probable compared to a two-particle interaction so that the emission and absorption of photons at energies slightly larger than $hf = W_G$ take place very unlikely. Only when the energy of photons is close to W_G' or larger than W_G' , the absorption and emission is very likely to happen. Therefore, the silicon is not suitable for efficient light sources. However, a silicon crystal can be used as photodetector since its low indirect-semiconductor absorption probability can be enhanced by increasing the interaction length.

2.2 Silicon on insulator wafer and photonic chip fabrication

This section will introduce the manufacturing of pure silicon wafers and the silicon on insulator (SOI) wafers. In addition, a general fabrication procedure of silicon photonics chips based on SOI platform will be shown as well.

2.2.1 Manufacturing of SOI wafers

A silicon wafer is made in a complex procedure which can be generally summarized in four steps [10]. Firstly, one can utilize the chemical reduction $\text{SiO}_2 + \text{C} \rightarrow \text{Si} + \text{CO}_2$ to obtain the so-called “metallurgical-quality silicon” from sand. Secondly, we need to refine the silicon via the reaction $\text{Si} + 3 \text{HCl} \rightarrow \text{SiHCl}_3 + \text{H}_2$ and followed by the intermediate filtration and purification through distillation, the trichlorosilane is finally decomposed into HCl and silicon. The third step is the growth of an silicon crystal realized by the Czochralski growth (CZ growth), as shown in Figure 2.2. The silicon is melted

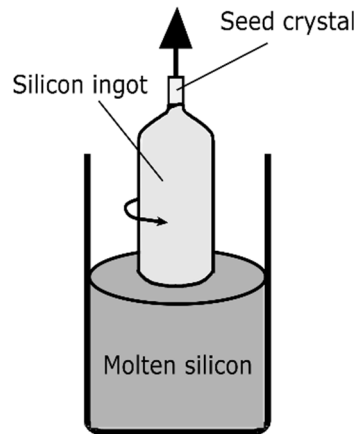


Figure 2.2: Czochralski growth. [10]

in a quartz crucible into which a small seed silicon crystal is dipped. The seed crystal is spun and slowly pulled out of the molten silicon. Silicon starts to crystallize because of the temperature difference between the molten silicon and the cooler ambient temperature, resulting in a rod-like silicon ingot. During the growth, dopants like boron or phosphorous can also be added into the molten silicon to obtain p- or n- type silicon of the desired resistivity. Finally, one can cut the ingot into wafers with different thicknesses depending on its applications and the requirements from customers. The wafers are mirror polished using a combination of mechanical and chemical polishing agents afterwards.

There are three layers of the silicon on insulator (SOI) wafers: the handle layer, the device layer and the buried oxide (BOX) layer. The handle layer is substrate at the bottom and provides mechanical support. The device layer is crystalline silicon and its thickness can range from a few hundred nanometers to several micrometers. The BOX layer acts as a lower cladding for suppressing the radiation of the light confined in the core into the substrate. There are three popular methods to fabricate SOI wafers: the Separation by IMplanted OXYgen (SIMOX) method, the Bond and Etch-back (BE) method and SmartCut process [11].

The SIMOX method is very popular for the fabrication of large volumes of SOI material. It relies on implanting massive oxygen ions below the surface of a silicon wafer. The required implanted ion dose is usually larger than 10^{18} cm^{-2} . In the low-dose ($<10^{16} \text{ cm}^{-2}$) scheme, the oxygen profile is Gaussian-like; in the high-dose scheme, the peak concentration of oxygen ions (O^+) saturates at the level for stoichiometric SiO_2 ; in the over-dose scheme, the profile is flattened, forming a buried, continuous layer. The depth and the thickness of the buried SiO_2 layer is closely related to the implantation energy. For example, with an impantation energy of 200 keV, the thicknesses of SiO_2 and crystalline silicon layer are $0.5 \mu\text{m}$ and 300 nm, respectively.

The BE method exploits the phenomenon that two hydrophilic surfaces (SiO_2) brought into intimate contact can form very strong bond. There are three steps for the BE method: oxidation of the two wafers to be bonded, formation of the chemical bond and thinning (etching) one of the wafers. In brief, two oxidated wafers are brought into contact at room temperature so that an initial bond is formed. Afterwards, the bond strength is increased by subsequent thermal processing at extremely high temperatures. For the last step, chemical mechanical polishing (CMP) is a very popular process. In the CMP process, one of the silicon surfaces is brought into contact with a rotating pad. At the same time, a chemically reactive slurry containing an abrasive component (like alumina and glycerine) weakens and removes the surface layer. With this rough removing silicon method, silicon overlayer of only $10\ \mu\text{m}$ is achievable. Some improvements can be made by the use of end-stop [12] but will not be discussed in this thesis.

The SmartCut process [13] is developed by LETI and relates to both methods. As shown in Figure 2.3, a thermally oxidised wafer is firstly implanted with hydrogen ion resulting in Gaussian-like ion



Figure 2.3: SmartCut process: implantation for a thermally oxidized wafer (left), a second wafer is bonded to the implanted wafer similar to the BE method (middle), removal of excess part through thermal processing and subsequent polishing (right).

profile which is similar to the SIMOX method. Depending on the energy of the implanted ions, the profile achieves its maximum value at different depths below the wafer surface varying from several hundreds of nanometers to several micrometers. At the position where the H^+ profile is the highest, the lattice bonds are significantly weakened since most implanted ions are stopped there. Then, the implanted wafer is brought into contact with a second handling wafer to form the room-temperature bonding, similar to the BE method. Finally, a thermal processing splits the implanted wafer along the peak of the hydrogen implantation profile. The roughness of the silicon surface is reduced by subsequent polishing, and can be further improved by epitaxial growth.

2.2.2 Silicon photonic chip fabrication and its compatibility with CMOS technology

The fabrication of silicon photonic chips is complex and sophisticated. A simplified flow is shown in Figure 2.4, including the following steps: wafer cleaning, coating with photo resist, exposure, development, etching, resist stripping, and cladding deposition [14].

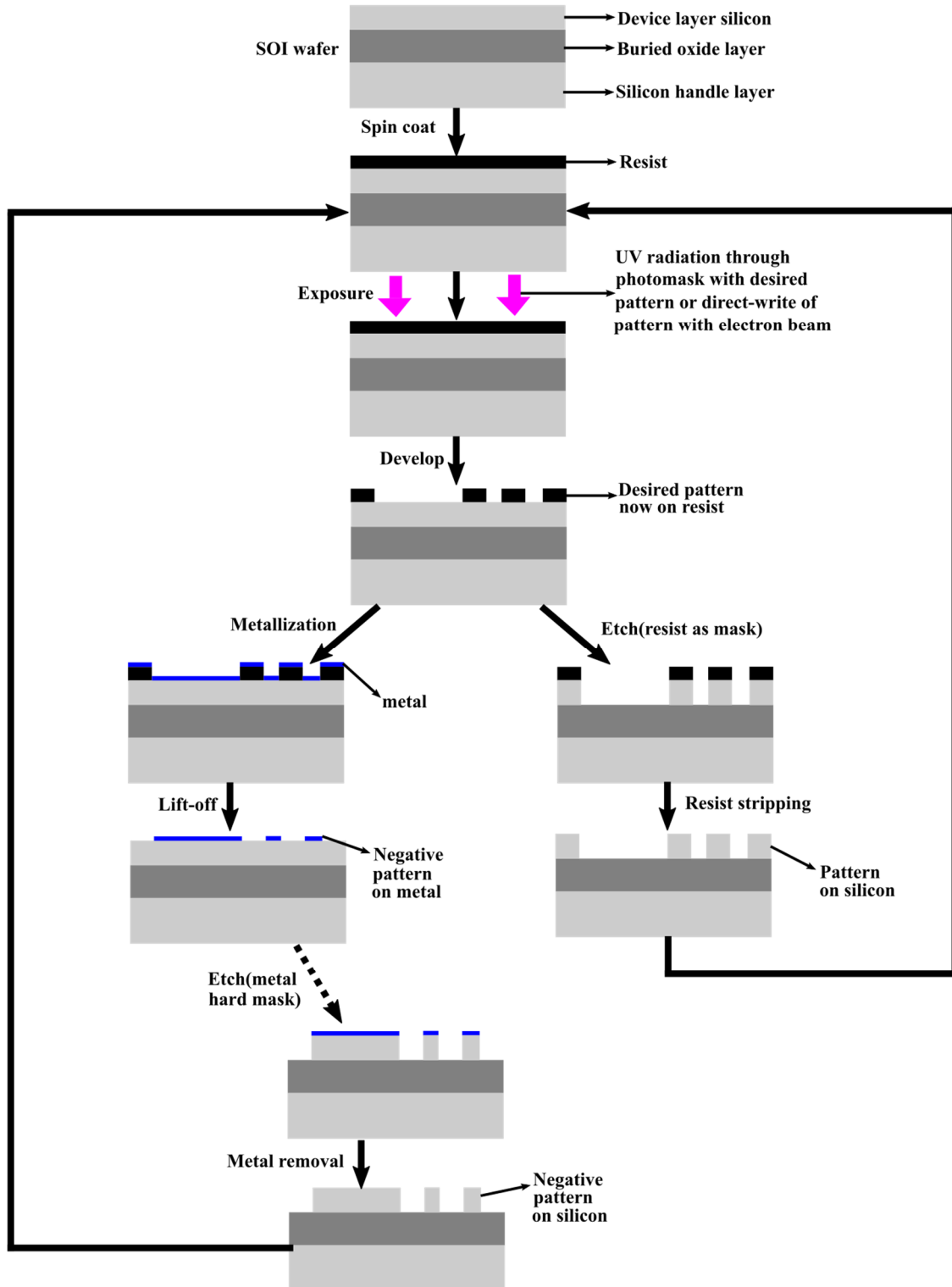


Figure 2.4: A simplified process of silicon photonic chip fabrication including both a lift-off process (left) and standard etching process (right). The lift-off process can also be part of the etching process (as shown at the bottom).

In Figure 2.4, the wafer cleaning and dehydration are not shown while actually they are the first step within the full process. The wafer can be cleaned with acetone, methanol, and a subsequent isopropanol (IPA) in the case of brand new wafer and in laboratory use. Oxygen plasma is used in dehydrating the surface of the substrate.

Before coating a wafer with photo resist, a prestep to improve the adhesion of the photoresist is necessary since the SiO_2 is hydrophilic and there is usually a thin film of moisture on the surface of the silicon wafer. The solution can be either oxygen plasma or baking the wafer in an oven at a temperature around $200\text{ }^\circ\text{C}$. For optical lithography, a bottom antireflective coating is applied before the resist to minimize the standing wave effect induced by the reflections at the interface between resist and wafer.

The next step is coating the wafer with resists, for which the choice of resists and the thickness of resist are very important. Some examples in [14] can be helpful with selecting the suitable resist. A general rule in a standard process requires the resist thicker than the height of the original topography. However, if the resist is over thick, it will lead to lower resolution, more slanted sidewalls, or mechanical collapse above a certain aspect ratio. After resist application, the wafer is spun at a controlled acceleration and speed determined by the desired thickness. Afterwards, the wafer is baked in an oven to vaporize some of the solvent to decrease the possibility of bubble formation.

The resist-coated wafer is then exposed to either electron bombardment in an e-beam system or to UV radiation in a mask aligner, stepper or scanner tool. In this step, the 2-D pattern from a GDS file (e-beam) or the mask (UV) will be transferred to the resist on the wafer.

Then the resist is developed. Depending on positive or negative tone resists is used, the exposed and unexposed regions are respectively dissolved in the resist. In consequence, the intended pattern is left on the wafer. The resist residuals can be removed away from the open regions either by an oxygen-reactive ion etching or a plasma barrel etcher.

If the chip does not need metallization, then the wafer is introduced to an etch chamber. During the etch process, the resist thickness will diminish, but some should remain on the wafer at the end of the etch process and must be removed afterwards. A following step 'resist stripping' removes the remaining resist. It can be done by either immersing the wafer into a solvent named 'stripper' or subjecting the wafer to an oxygen plasma.

Finally, an upper cladding is deposited to protect the photonic circuit. The deposited cladding materials are typically polymer or SiO_2 with a thickness of around $1\text{ }\mu\text{m}$. There are different methods [15] to achieve a flat cladding layer and once a flat surface is obtained, it can be lowered to the desired thickness by blanket etching.

Photonic chips with active components requires metallizations. And this step should be done before the etching step if it exists. In the case of CMOS-compatible electrical contacts, a metal stack of Ti/TiN/AlCu is usually used and deposited by physical vapor deposition (PVD). The bottom Ti layer acts as an adhesion layer to the substrate. The interlayer TiN is a barrier layer to prevent interdiffusion. The top AlCu layer contains small percentage of Cu in Al is used to suppress electromigration [16].

Another very important process not shown in the flow is the ion implantation. Normally, the implanted ions are boron, phosphorous and arsenic to construct pn junctions. One can adjust the dose

and the energy of the implanted ions to control the implantation depth and profile accurately. In the process, resist is usually used to cover the region to be implanted while implanting the other regions. An example is illustrated in Figure 2.5. In the first step, the middle part of the wafer is implanted with boron ions for p- doping while the regions covered by the photo resist are protected. Then the wafer is etched to obtain the desired structured. Finally, the region desired n- doping is realized by another doping process where the unwanted doped regions are protected by the photo resist.

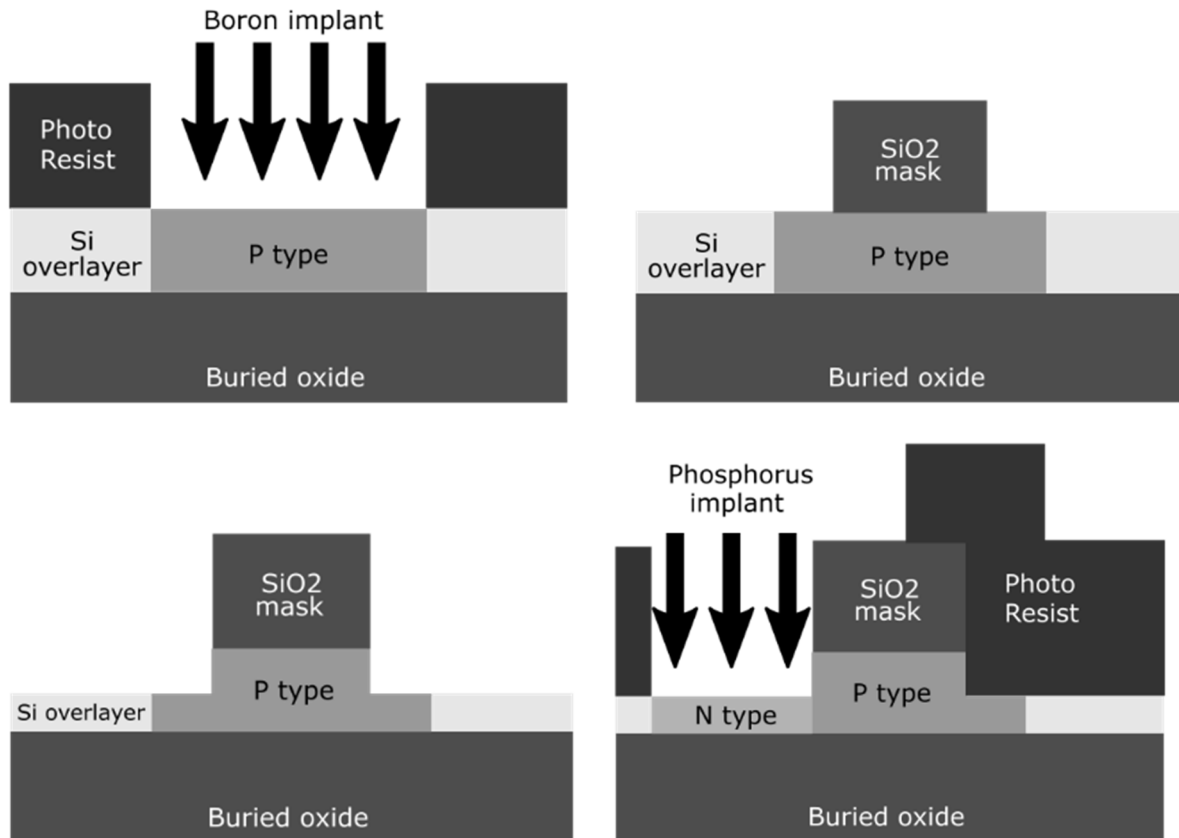


Figure 2.5: A general flow of ion implantation.

The fabrication flow of photonic chips is very similar to that of the dominant fabrication technology in the semiconductor industry, namely the CMOS (complementary metal–oxide–semiconductor) technology. A general interation of photolithography for the CMOS technology can be summarized as: SOI wafer → Photoresist coating → Exposure → Development → Etching → Resist washing → Feature realization (diffusion, deposition, implantation, etc.) → Oxide growth or deposition. This cycle may be repeated many times and followed with metallization to obtain the final chip. The comparison of two technologies yields the term CMOS compatibility which means fabrication of photonic components can be accomplished on the CMOS platform with minor changes. And the advantages of CMOS compatibility are multifold:

1) The CMOS technology is already relatively mature based on decades of experience, using the CMOS technology can lower fabrication budget compared with developing a new technology.

2) Silicon photonics would seldom need lithography better than 60 nm, it makes economic sense to use advanced platforms to fabricate the electronic integrated circuits (IC) while using the older generation fabs to fabricate phtonic circuits.

3) In some cases, the electronic and photonic devices are required to be manufactured on a common wafer. It is easier and more beneficial to realize the fabrication using only one technology.

In terms of the design in this thesis, SOI wafers are used, the compatibility with CMOS is feasible from the point of view of material system. On the other hand, there are also no additional steps introduced.

2.3 Popular material platforms for optical communication

Although the devices designed in this thesis are based on SOI wafers, there are several other popular materials for photonic research and active in the market. This section will take a short glimpse at the general characteristics of these three material systems.

2.3.1 LiNbO₃ wafers

The available size of the LiNbO₃ wafers range from 4" to 6" with a thickness of the device layer varying from 300 nm to 900 nm. The cladding materials of LiNbO₃ wafers are flexible and therefore the material refractive index contrast is flexible. Based on this material, commercially available modulators achieve 30 Gb/s, and laboratory research achieve 56Gb/s.

2.3.2 Silicon nitride wafers

The size of commercially available silicon nitride (Si₃N₄) wafer has achieved 12" since 2001, the same as the SOI wafer. The thickness of the device layer for Si₃N₄ wafer varies from 10 nm to 2 μm. Since the refractive index of Si₃N₄ is 2.05, much smaller than that of silicon, resulting in lower refractive index contrast and larger devices compared to silicon based devices.

2.3.3 III-V compound wafers

Typical III-V compounds used for photonic components are gallium arsenide (GaAs) and indium phosphide (InP). The available wafer sizes for them are 2"-6" and 2"-4", respectively. Different from the above materials, by engineering their bandgap and conductivity one can obtain interesting properties which makes them well suited for active component design. Nevertheless, limited by the wafer size, III-V compounds product are still budget unfriendly since larger wafers generally correspond to higher yield. Currently the InP has successfully stepped into the photonic market while the GaAs has't yet. The III-V compound wafers can feature a small refractive index contrast, like the InP platform has a low index contrast of $\Delta n = 0.2\sim 0.5$.

2.4 Waveguide and effective refractive index

2.4.1 Waveguide mode and light confinement

Mode is a basic concept in optics, representing how the light is propagating in the waveguide. To understand this term, we firstly make the hypothesis that the incident light is a plane wave or at least it can be regarded as a plane wave. As shown in Figure 2.6, the light is transmitted in a sandwiched

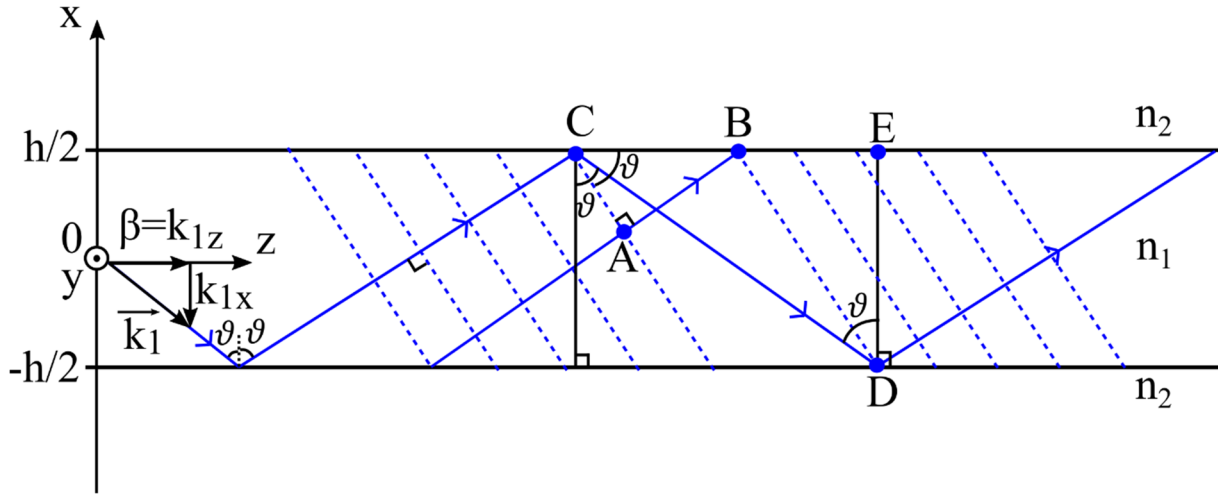


Figure 2.6: Graphical demonstration for the waveguide mode calculation.

symmetric structure where the core has a refractive index of n_1 while the outer two cladding layers have a refractive index of n_2 with the precondition of $n_1 > n_2$. Furthermore, we imagine the incident angle of the light is bigger than the critical angle so that total internal reflection takes place. The full lines are the actual light path and the phase fronts are dashed lines, perpendicular to the propagation direction. There are five marked points in the picture, A and C lie on a common phase front, and the same applies to points B and D. Therefore, the phase difference between AB and CD is an integer multiple of 2π . The ray from point A to point B does not undergo any reflection while the longer ray from C to D is reflected twice. Based on this, we have Equation 2.1 where m is positive integer and φ_p is the phase variation induced by the reflection at the material boundary.

$$-n_1 k_0 \overline{AB} = -n_1 k_0 \overline{CD} + 2\varphi_p + m2\pi, \quad m \in \mathbb{N}, \quad \text{Equation 2.1}$$

From geometrical point of view we have Equation 2.2 and Equation 2.3:

$$\overline{AB} = (h \times \tan \vartheta - h / \tan \vartheta) \sin \vartheta \quad \text{Equation 2.2}$$

$$\overline{CD} = h / \cos \vartheta \quad \text{Equation 2.3}$$

Substituting Equation 2.2 and Equation 2.3 into Equation 2.1 yielding Equation 2.4:

$$2hn_1 k_0 \cos \vartheta = 2\varphi_p + m2\pi \quad \text{Equation 2.4}$$

The solution of ϑ in relation Equation 2.4 is discretized and each solution is a waveguide mode. Only these discretized eigenvalues can propagate in the given waveguide, namely the propagation constant β of the waveguide mode. The propagation constant with other values are either attenuated along the z -direction or radiate into the claddings. Nevertheless, its generalized Equation 2.5 is more popular where $u = k_{1y} \frac{h}{2}$, $w = k_{2y} \frac{h}{2}$, $V = \frac{h}{2} k_0 A_N = \sqrt{u^2 + w^2}$ and $B = \frac{w^2}{V^2} = \frac{\beta^2 - k_2^2}{k_1^2 - k_2^2}$.

$$w_m = \sqrt{V^2 - u_m^2} = \begin{cases} u_m \tan(u_m), & m = 0, 2, 4, \dots \\ -u_m \cot(u_m), & m = 1, 3, 5, \dots \end{cases} \quad \text{Equation 2.5}$$

The graphical solutions of Equation 2.5 are given by Figure 2.7 where each intersection of the left picture represents one solution. And the dispersion relation of each mode for weak guidance (low

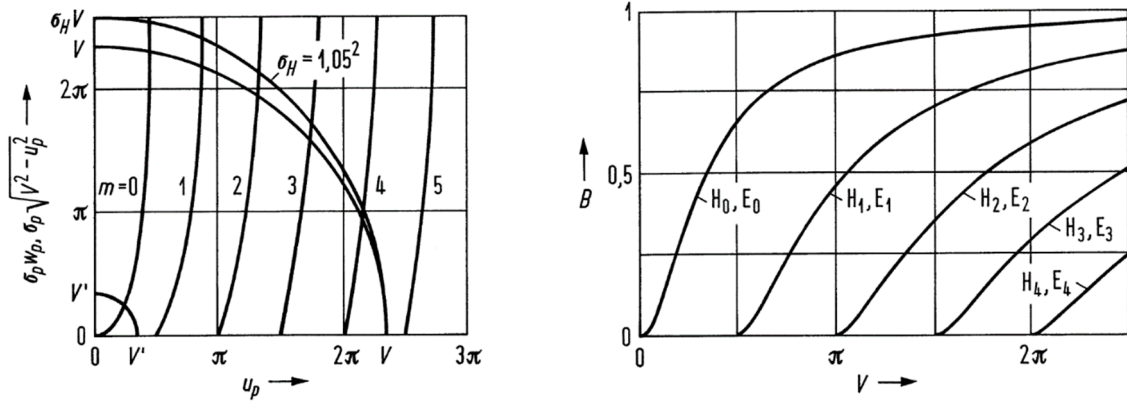


Figure 2.7: Graphical solution of the equation for TE- and TM-modes (left) and dispersion relation $B(V)$ of various modes for the case of a low index-contrast waveguide (right).

waveguide index contrast) is illustrated in the right of Figure 2.7, there is no cutoff frequency for the H_0 and E_0 mode, they can always exist in the waveguide.

2.4.2 Different waveguides and effective refractive index

There are several basic types of waveguides used in integrated photonics as shown in Figure 2.8, they are the channel waveguide, channel waveguide, rib waveguide and ridge waveguide respectively.

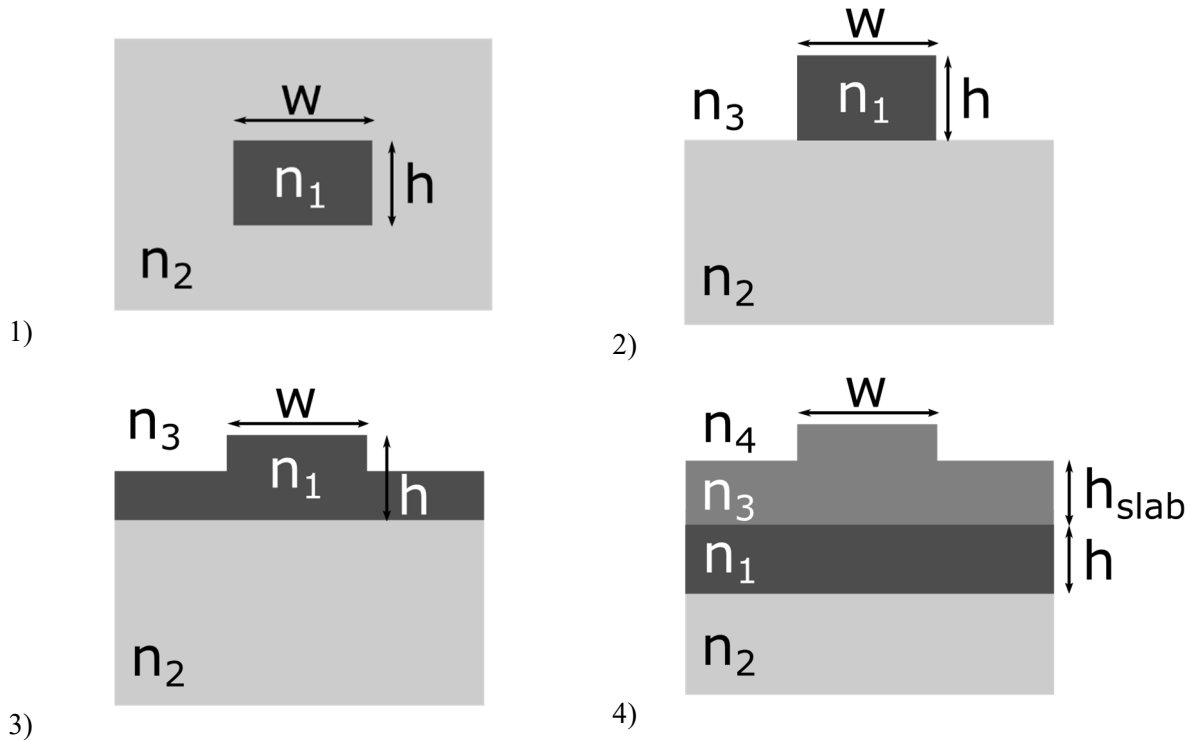


Figure 2.8: Basic types of waveguides; (1) Channel waveguide; (2) Strip waveguide; (3) Rib waveguide; (4) Ridge waveguide.

The channel waveguides consist of a rectangular core with a refractive index of n_1 , embedded in a uniform cladding material with a refractive index of n_2 ($n_1 > n_2$). The strip waveguides consist of a rectangular core structure of refractive index n_1 while this core structure is deposited on the substrate of a lower refractive index n_2 directly and covered by a medium of refractive index n_3 . The rib waveguides comprise a film layer deposited on a substrate and there is a protruding ridge for the film layer. Ridge waveguides consist of a continuous core layer of refractive index n_1 and a laterally structured top layer with a protruding ridge of lower refractive index n_3 which is in turn covered by the top cladding (refractive index n_4). These waveguides have different light confinement abilities and have to be chosen according to the requirements and the available material system.

Usually, waveguides and also some other optical structures have large dimension so that the calculation of their field distribution requires significant computing resources. Under this circumstance, we can use an ‘effective refractive index’ method to transfer the 3D structures to 2D structures where the effective refractive index n_{eff} is defined by the division of propagation constant β by the free-space wavenumber k_0 : $n_{\text{eff}} = \beta/k_0$. Thereafter, one can understand the effective refractive index in a way that a plane wave would propagate in a medium of refractive index n_{eff} with the same phase velocity as the guided mode with the phase constant β [17]. Nevertheless, the essence of the problem is still to solve the Maxwell’s equation for which we need to make two assumptions: 1) the light is propagating in the z direction and the refractive index profile can be written as $n(\mathbf{r}) = n(x, y)$; 2) The waveguide is lossless throughout the medium so that we can write $\mathbf{E}(\mathbf{r}, t) = \underline{\mathbf{E}}(x, y) \exp(j(\omega t - \beta z))$ and $\beta = n_{\text{eff}}k_0$. If the structure of the waveguide is rather simple and its refractive index contrast is weak, one can obtain n_{eff} with the effective index method [18]. However, in most cases (like high-index contrast, complex and irregular-shape waveguides) n_{eff} can not be determined analytically so that we have to rely on some commercial software packages like Lumerical [19], Rsoft [20], COMSOL Multiphysics [21] etc. to obtain the numerical result. In this thesis, COMSOL Multiphysics is commonly used.

2.5 Fiber-chip coupling

2.5.1 Fiber mode

The optical fiber confines the light mainly in the fiber core. The modes can be calculated by solving the Maxwell’s equations in the cylindrical coordinate system based on the same abovementioned two assumptions. For step-index single mode fibers, the normalized solutions [11] can be classified into the following two situations:

- 1) If $\Delta = \frac{n_1^2 - n_2^2}{2n_1^2}$ is not very small (like silica fiber, Δ is between 0.3% and 1%) where n_1 and n_2 are the refractive indices of core and cladding respectively, then:

TE modes can be solved by the equations $u^2 + \omega^2 = V^2$ and $\frac{J_1(u)}{uJ_0(u)} = -\frac{K_1(\omega)}{\omega K_0(\omega)}$

TM modes can be solved by the equations $u^2 + \omega^2 = V^2$ and $\frac{J_1(u)}{uJ_0(u)} = -\left(\frac{n_2}{n_1}\right)^2 \frac{K_1(\omega)}{\omega K_0(\omega)}$

Hybrid modes can be solved by the equations $u^2 + \omega^2 = V^2$ and $\left[\frac{J'_v(u)}{uJ_v(u)} + \frac{K'_v(\omega)}{\omega K_v(\omega)} \right] \left[\frac{J'_v(u)}{uJ_v(u)} + \left(\frac{n_2}{n_1} \right)^2 \frac{K'_v(\omega)}{\omega K_v(\omega)} \right] = v^2 \left[\frac{1}{u^2} + \frac{1}{\omega^2} \right] \left[\frac{1}{u^2} + \left(\frac{n_2}{n_1} \right)^2 \frac{1}{\omega^2} \right]$

- 2) If $\Delta = \frac{n_1^2 - n_2^2}{2n_1^2}$ is very small, typically smaller than 0.3%, the LP modes are solved based on equations $u^2 + \omega^2 = V^2$ and $\frac{uJ'_v(u)}{J_v(u)} = \frac{\omega K'_v(\omega)}{K_v(\omega)}$

For both situations: $u = a\sqrt{n_1^2 k_0^2 - \beta^2}$, $\omega = a\sqrt{\beta^2 - n_2^2 k_0^2}$, $V = ak_0\sqrt{n_1^2 - n_2^2}$, with the Bessel functions $J_v(u)$ used to describe the radial field distribution in the core and the modified Bessel function $K_v(\omega)$ is to the radial field distribution in the cladding. For the single mode fiber (SMF), only the

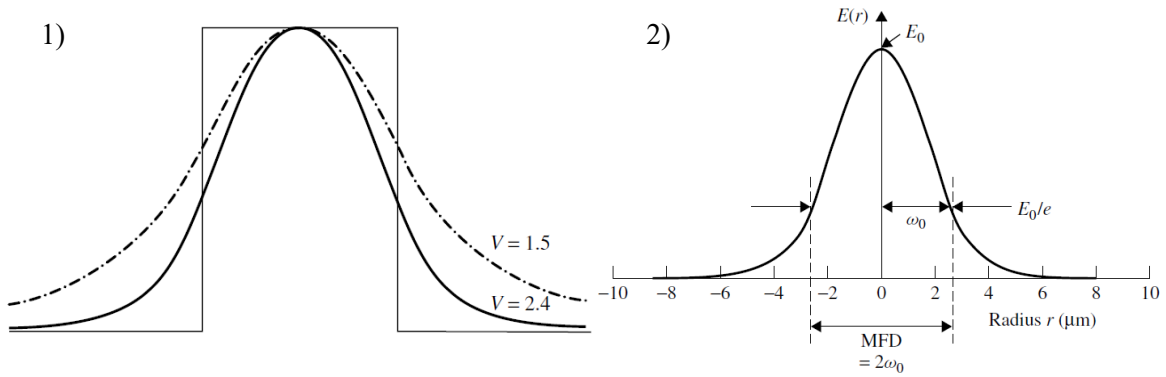


Figure 2.9: Field shape of the fundamental mode of a step-index fibre for normalized frequencies of $V = 1.5$ and $V = 2.4$ (1) and approximation to the fundamental mode, showing the mode-field diameter (MFD) and the spot size ω_0 , (2). Adapted from [22].

fundamental mode is supported, namely the hybrid HE_{11} mode. The left picture in Figure 2.9 shows that increasing the normalized frequency can improve the mode confinement while there is still much power is transmitted in the cladding. In addition, the shape of the mode profile is gaussian-like so that Gaussian function is often used to approximate the fundamental mode profile. The right picture in Figure 2.9 shows the definition of mode field diameter (MFD) and the spot size (also named mode field radius) ω_0 where the MFD is taken as the width of the function at an amplitude of $1/e$ width of the peak value.

2.5.2 Out-of-plane grating coupler

The cross section of the fiber modes is circular with a diameter of several micrometers while the cross section of the channel waveguide modes is rectangular with dimension of merely several hundreds of nanometers. Due to this significant mode profile mismatch, an intermedia device is usually required to couple light between two types of waveguides efficiently. Out-of-plane coupling is a very flexible and

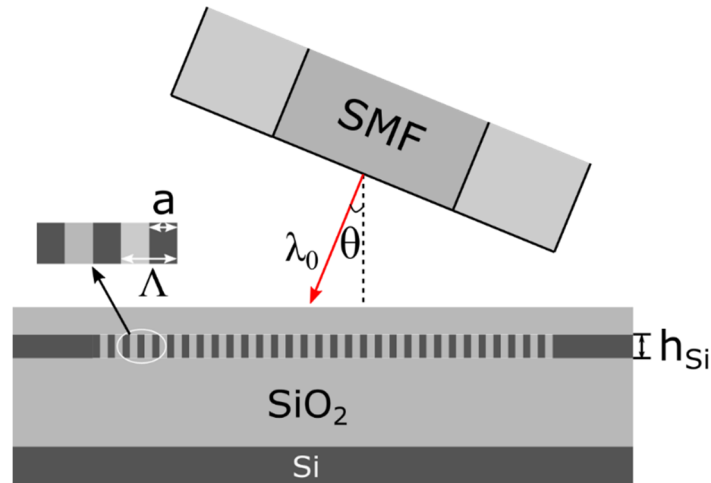


Figure 2.10: Schematic for the out-of-plane fiber.

easy-to-use method for wafer-scale characterization probing as shown in Figure 2.10. The basic formula used here is the diffraction formula Equation 2.6, where n_{eff} is the effective refractive index of the waveguide, Λ is the grating period and θ is the angle between the fiber axis and the grating normal. Usually the value of θ is around 10° , then the grating period can be roughly derived by Equation 2.6 correspondingly. Nevertheless, accurate grating design can be complex and difficult and will not be the focus of this thesis.

$$\lambda_0 = \Lambda(n_{eff} - n_{clad} \sin \theta) \quad \text{Equation 2.6}$$

2.5.3 Angle-polished fibers for in-plane fiber coupling

The above mentioned coupling method is suitable for wafer-scale design but not for a stable working system. In this case, a surface coupling method shown in Figure 2.11 with an angle-polished fiber makes more sense. As can be seen, a fiber is aligned horizontally above the gratings and is polished with an

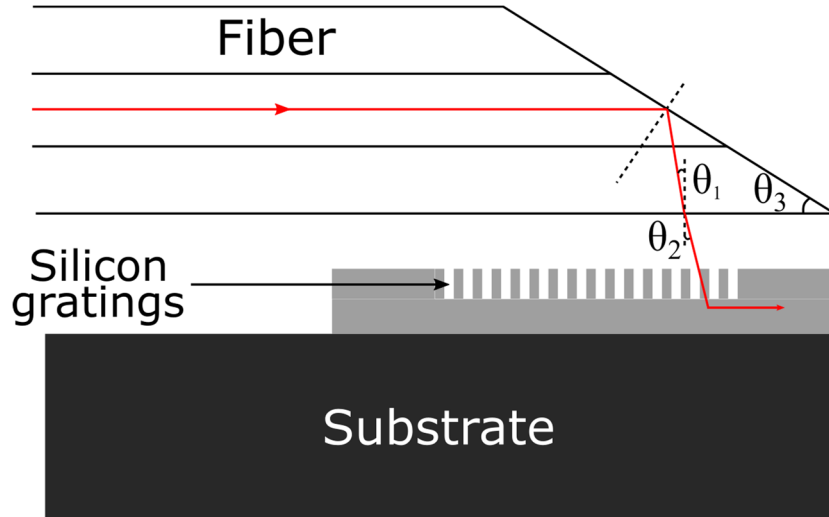


Figure 2.11: Schematic of a surface coupling method with an angle polished fiber.

angle θ_3 . When θ_1 is small enough, θ_1 and θ_2 can be approximated as identical while even though not, θ_1 can still be calculated by θ_2 according to the Snell's Law Equation 2.7. In this case, θ_2 here corresponds to the angle θ in Figure 2.11. Therefore, the key point is the accurately polished angle θ_3 which is determined by θ_1 . If $\theta_1 = 10^\circ$ then the polish angle θ_3 should be 40° .

$$n_1 \sin \theta_1 = n_2 \sin \theta_2 \quad \text{Equation 2.7}$$

2.6 Plasma dispersion and pn junction

This section will introduce the plasma dispersion effect and the formula used to calculate the width of pn junction.

2.6.1 Plasma dispersion

For silicon, the strongest effect in changing the refractive index is the plasma dispersion effect where the light is scattered by the mobile free carriers. With injecting or depleting free carriers, the absorption spectrum of the material will shift. And, the changes of the attenuation constant is predicted by the Drude-Lorenz Equation 2.8. In this relation, λ_0 is the free space wavelength, e the electronic charge, c_0 the speed of light in vacuum, ϵ_0 the permittivity of free space, ΔN_e the free electron concentration, ΔN_h the free hole concentrations, μ_e the mobility of the electrons, μ_h the mobility of the holes, and m_{ce}^* and m_{ch}^* are the effective mass of electrons and holes respectively.

$$\Delta\alpha = \frac{e^3 \lambda_0^2}{4\pi^2 c_0^3 \epsilon_0 n} \left(\frac{\Delta N_e}{\mu_e (m_{ce}^*)^2} + \frac{\Delta N_h}{\mu_h (m_{ch}^*)^2} \right) \quad \text{Equation 2.8}$$

According to the Kramers-Kronig dispersion relation, the change of attenuation constant is typically accompanied by a change of refractive index and described by Equation 2.9.

$$\Delta n = \frac{-e^2 \lambda_0^2}{8\pi^2 c_0^2 \epsilon_0 n} \left(\frac{\Delta N_e}{(m_{ce}^*)^2} + \frac{\Delta N_h}{(m_{ch}^*)^2} \right) \quad \text{Equation 2.9}$$

These effects are successively investigated and presented in [23] and [24]. In the later literature, the power-law model was fitted to the index change obtained by applying the Kramers-Kronig relation to the measured values of absorption for free carrier concentrations ranging from 10^{17} cm^{-3} to 10^{20} cm^{-3} . At 1550 nm, the change in attenuation and refractive index of doped silicon is expressed by the following equations:

$$\Delta \alpha = \Delta \alpha_e + \Delta \alpha_h = 8.88 \times 10^{-21} (\Delta N_e)^{1.167} + 5.84 \times 10^{-20} (\Delta N_h)^{1.109} \quad \text{Equation 2.10}$$

$$\Delta n = \Delta n_e + \Delta n_h = -[5.40 \times 10^{-22} (\Delta N_e)^{1.011} + 1.53 \times 10^{-18} (\Delta N_h)^{0.838}] \quad \text{Equation 2.11}$$

2.6.2 pn junction

As introduced in section 2.2.2, the SOI wafer can be either p- or n- doped by implanting different types of atoms. Once the p-type and n-type semiconductors are in contact, a pn junction is formed. At thermal equilibrium, the diffusion and the drift of electrons inside the semiconductor achieve a dynamic equilibrium and a depletion region is formed. If the doping technique is ideal that the p- and n- region are homogeneously doped, some parameters of the formed pn junction, like intrinsic potential, junction width etc., can be derived analytically by solving the Poisson Equation 2.12 where ϵ_s is the permittivity of the semiconductor, q the electric quantity of an electron, ρ the local charge density ($\text{C}\cdot\text{cm}^{-3}$), p the hole density of the intrinsic semiconductor (without dopants), n the electron density of the intrinsic semiconductor (without dopants), N_d^+ the concentration of ionized donor atoms in the semiconductor and N_a^- the concentration of ionized acceptor atoms in the semiconductor.

$$\nabla^2 \Phi(x, y, z) = -\frac{\rho(x, y, z)}{\epsilon_s} = -\frac{q}{\epsilon_s} (p - n + N_d^+ - N_a^-) \quad \text{Equation 2.12}$$

Since in one-dimensional case and using the Boltzmann relations we have Equation 2.13 and Equation 2.14, (the electrons and holes density, respectively) equation Equation 2.12 can be simplified to Equation 2.15 [10] if no external applied potential exists where $N_d^+ = N_d$, $N_a^- = N_a$.

$$n(x) = n_i \exp\left(\frac{E_F - E_{i0} + q\Phi_0(x)}{KT}\right) = n_0 \exp\left(\frac{q\Phi_0(x)}{KT}\right) \quad \text{Equation 2.13}$$

$$p(x) = n_i \exp\left(-\frac{E_F - E_{i0} + q\Phi_0(x)}{KT}\right) = p_0 \exp\left(-\frac{q\Phi_0(x)}{KT}\right) \quad \text{Equation 2.14}$$

$$\frac{d^2 \Phi(x)}{dx^2} = -\frac{q}{\epsilon_s} \left\{ p_0 \exp\left(\frac{-q\Phi(x)}{KT}\right) - n_0 \exp\left(\frac{q\Phi(x)}{KT}\right) + N_d^+ - N_a^- \right\} \quad \text{Equation 2.15}$$

Using the depletion approximation, Equation 2.15 can be solved analytically and therefore the junction potential is Equation 2.16; the maximum electric field is Equation 2.17; the width of the depletion region is Equation 2.18. If applying an external field the junction width will be expressed by Equation 2.19 where V_a is the external applied potential. Thereas, if defining V_a is positive when the potential of the p-type region is higher than that of the n-type region, the depletion region of the junction width will increase when a reverse bias ($V_a < 0$) is applied and decrease when a forward bias ($V_a > 0$) is applied.

$$\Phi_0 = \Phi_{n0} - \Phi_{p0} = \frac{qN_a}{2\varepsilon_S} l_{p0}^2 + \frac{qN_d}{2\varepsilon_S} l_{n0}^2 = \frac{KT}{q} \ln\left(\frac{N_a N_d}{n_i^2}\right) \quad \text{Equation 2.16}$$

$$\varepsilon_{max} = -\frac{qN_a}{\varepsilon_S} l_{p0} = -\frac{qN_d}{\varepsilon_S} l_{n0} \quad \text{Equation 2.17}$$

$$d = l_{p0} + l_{n0} = \sqrt{\frac{2\varepsilon_S \Phi_0 (N_a + N_d)}{q N_a N_d}} \quad \text{Equation 2.18}$$

$$d = l_{p0} + l_{n0} = \sqrt{\frac{2\varepsilon_S (\Phi_0 - V_a) (N_a + N_d)}{q N_a N_d}} \quad \text{Equation 2.19}$$

2.7 Diffraction theory

Diffraction gratings, featuring periodic structures, are commonly used for splitting and diffracting light into multiple beams in optics. The directions of these diffracted beams are dependent on the wavelength and the spacing between the gratings. The principles of diffraction gratings was firstly discovered by James Gregory in quite early time (about one year later than Newton's prism experiment) [14]. Since then, the man-made diffraction gratings were improved continuously and became easily available when Henry Augustus Rowland developed the Rowland circle method in 1883.

Figure 2.12 is a classical Rowland mounting. The grating circle has a radius of $2R$ and the Rowland circle has a radius of R . Point O and point O' are the center and axis pole of the Rowland circle, respectively. Assuming light is incident from $A(x_A, y_A)$, diffracted on $O(0, 0)$ and $P(x_P, y_P)$, then to $B(x_B, y_B)$ identically. The incident and diffracted angle with respect to the x axis are α and β , respectively. The light path can be calculated by Equation 2.20 and Equation 2.21.

$$AP = \sqrt{(x_P - x_A)^2 + (y_P - y_A)^2} \quad \text{Equation 2.20}$$

$$PB = \sqrt{(x_B - x_P)^2 + (y_B - y_P)^2} \quad \text{Equation 2.21}$$

The interference at point B is dependent on the light paths AOB and APB and their path difference Δl is calculated in Equation 2.22.

$$\Delta l = AP + PB - (AO + OB) \quad \text{Equation 2.22}$$

Points O , A and B are located in the Rowland circle and O' is the center of the Rowland circle. The coordinates of A and B can be calculated in the same way and the calculation of point B is given as an example in the following. To this end, we extract the triangle $OO'B$ and zooming into it as shown at the bottom in Figure 2.12. Since OO' is identical to $O'B$ with a length of R , $OB^2 = R^2 + R^2 - 2 \times R \times R \times \cos(180^\circ - 2\beta) = 2R \cos\beta$. On this basis, the coordinates of A and B can be calculated and given in Equation 2.23 and Equation 2.24.

$$y_B = OB \times \cos\beta = 2R \cos\beta \times \cos\beta = 2R \cos^2\beta, \quad x_B = OB \times \sin\beta = 2R \cos\beta \sin\beta \quad \text{Equation 2.23}$$

$$y_A = 2R \cos^2\alpha, \quad x_A = 2R \cos\alpha \sin\alpha \quad \text{Equation 2.24}$$

Since P is located on the grating circle with $(x_P - 2R) + y_P = 4R^2$, Equation 2.22 is calculated out in Equation 2.25.

Theoretical Background

$$\Delta l = -(\sin \alpha + \sin \beta)y_P + \frac{1}{64} \frac{1}{R^3} \left(\frac{\sin^2 \alpha}{\cos \beta} + \frac{\sin^2 \beta}{\cos \alpha} \right) y_P^4 + \text{higher order} \quad \text{Equation 2.25}$$

For paraxial approximation with $y_P \ll R$, the higher orders can be ignored and Equation 2.25 can be simplified as Equation 2.26.

$$\Delta l = -(\sin \alpha + \sin \beta)y_P \quad \text{Equation 2.26}$$

For constructive interference, there is Equation 2.27, known as the grating equation. In the grating

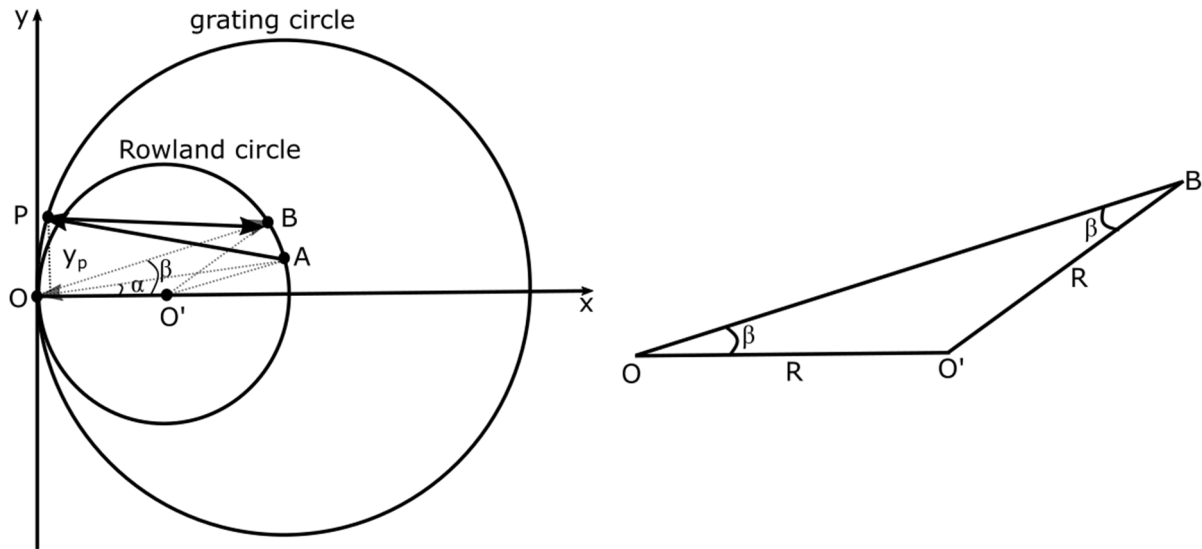


Figure 2.12: Schematic for the Rowland mounting (the small triangle $OO'B$ is also zoomed out).

equation, m is the diffraction order, λ is the vacuum wavelength of light, and n is the effective refractive index of the grating. $d = y_P/i$ (i as the grating order) is the distance in the y direction between adjacent constructive interference points. The grating equation is the design basics for the Echelle gratings in chapter 5.

$$(\sin \alpha + \sin \beta)d = m \frac{\lambda}{n} \quad \text{Equation 2.27}$$

3 Optical Data Readout in Detector Instrumentation

This chapter will introduce the structure and the corresponding experiments of two large-scale detectors, the CMS detector and AGIPD detector. In terms of the massive data from the large-scale detectors and the harsh environment, a generic optical high-bandwidth readout concept is proposed.

3.1 The Large Hadron Collider and the CMS experiment

The Large Hadron Collider (LHC) at the European Organization for Nuclear Research (CERN) is a proton-proton collider with a circumference over 26 km located at the French-Swiss border at a depth ranging from 50 m to 175 m underground. The LHC is composed of two synchrotron rings and the two independent proton beams inside will circulate in opposite directions and be accelerated to a very high energy for collision. The proton beams injected into the LHC ring are created by using an electric field to strip the atoms in a hydrogen gas of their electrons. Then, they are accelerated in bunches in a linear accelerator (LINAC2) to an energy of 50 MeV. Afterwards they are injected into the Proton Synchrotron Booster (PSB), and boosted to an energy of 1.4 GeV before being accelerated in the Proton Synchrotron (PS) to 26 GeV. Finally, the beams are pushed up to the injection energy of 450 GeV in the Super Proton Synchrotron (SPS) before the protons are finally injected into the two beam pipes of the LHC.

The two independent proton beams inside LHC rings are focused using quadrupole magnets and collided at four intersection points where four main detectors ATLAS (A Toroidal LHC Apparatus), LHCb (Large Hadron Collider beauty) [25], ALICE (A Large Ion Collider Experiment) [26] and CMS (Compact Muon Solenoid) are installed. The collider is designed to finally accelerate protons up to a collision energy of 14 TeV and a luminosity of $10^{34} \text{ cm}^{-2}\text{s}^{-1}$ [27]. For the commissioning in 2010, the commission energy was enhanced to 7 TeV while the luminosity was still two orders of magnitude less than the nominal value [28]. Till 2015, the collision energy was continuously improved to 14 TeV, thereafter the LHC was at its nominal luminosity, $10^{34} \text{ cm}^{-2}\text{s}^{-1}$.

Those four major experiments mentioned above are large, complex and comprised of massive sub-detectors with several tens of millions channels in total. Of the four major detectors, ALICE is designed to detect heavy ions and investigate the properties of the quark-gluon plasma at extreme values of energy density and temperature in nucleus-nucleus collisions [29]. The LHCb experiment is specialized in detailed investigation of the relations and differences between matter and antimatter [30]. These two experiments are exposed to a luminosities lower than the nominal value. In comparison, ATLAS and CMS are general-purpose detectors and are designed to withstand the nominal luminosity, performing physics studies from the analysis of proton-proton collisions delivered by the LHC. To be detected is the high-resolution energy, momentum, and positions of the charged particles.

Although the four mentioned detectors have different detection tasks and design criteria, the basic comprised components of them are the same: 1) a magnet for measuring particle momentum; 2) a tracking station which is used for trajectory identification of the charged particles; 3) calorimeters for measuring particles' energies; 4) muon tracking stations, located in the outermost regions; 5) on-line data discrimination system or so-called trigger system to reduce the event rate. Since they have quite similar components, this thesis will merely focus one detector as an example, the CMS detector.

A 3-D schematic of the CMS detector is shown in Figure 3.1. The CMS detector is composed of a cylindrical barrel closed by two end-caps with a total length of 21.6 m and a total weight of around

12500 tons. The central superconducting solenoid of the CMS detector is 13 m long, providing a 4 T magnetic field, and the magnetic field is kept by a massive steel return yoke. On one hand, the strong magnetic field can bend the trajectories of the charged particles for accurate measurement of their momenta, on the other hand, it can also reduce the pile-up of the soft hadrons in the muon system. The solenoid is built large enough (6 m inner diameter) to accommodate other structures inside, namely the inner silicon trackers and calorimeters. The silicon trackers are still divided into an inner and an outer tracker subsystem where the former one located closest to the interaction region and comprised 66 million silicon pixel-detectors on three cylindrical layers. With this, 3D vertex reconstruction is provided. In contrast, the outer layer is comprised of ten layers and the number of the silicon microstrips is about 10 million.

The crystal electromagnetic calorimeter (ECAL), surrounding the inner detectors, is mainly designed for measuring the energy and position of electrons and photons [31]. There are 137.000 individual electronic channels in ECAL detector. The ECAL is divided into barrel and endcap detectors. It consists

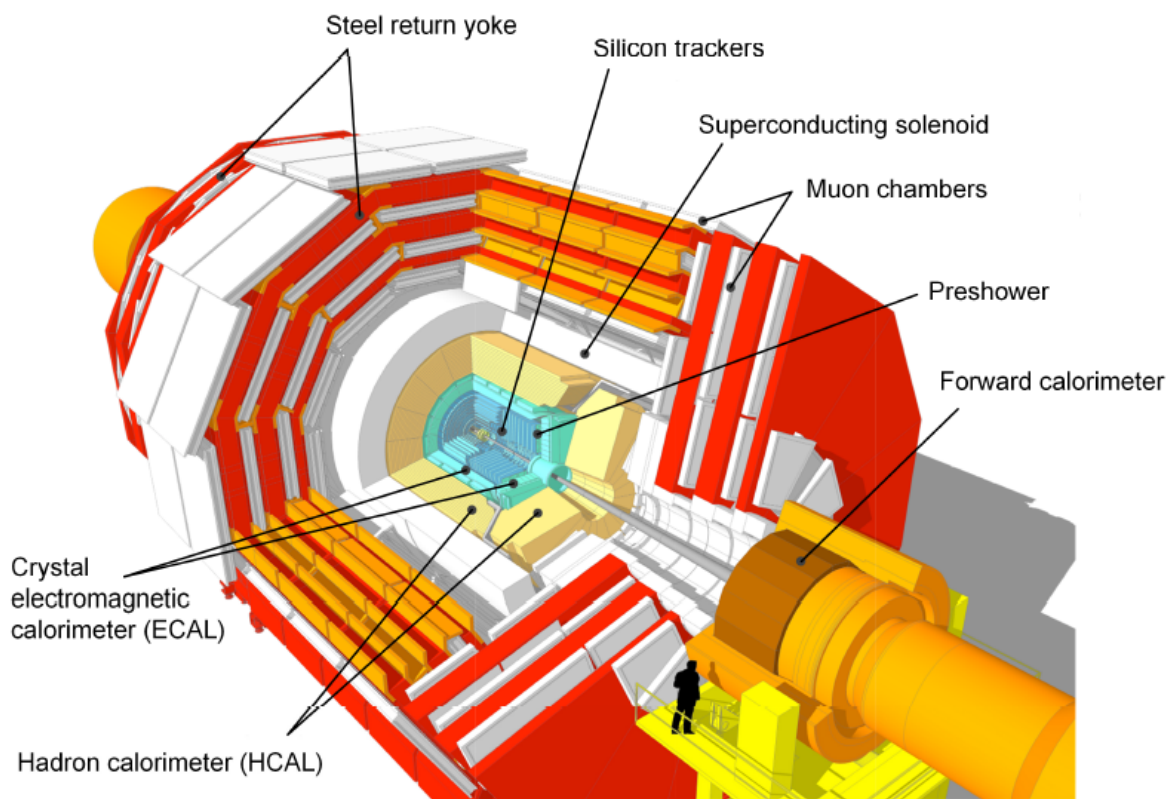


Figure 3.1: The 3-D view of the CMS detector. [31]

of over 70.000 scintillation crystals from lead tungstate (PbWO_4) for which over 60.000 crystals are located in the barrel and the left are in the endcap. In front of the endcaps is the preshower with which the required length for electromagnetic shower can be reduced and the accuracy of electron and photon position is also improved.

Outside the ECAL is the hadron calorimeter (HCAL), aims at measuring hadron jets and the missing transverse energy due to neutrinos or exotic particles as they require a hermetic detector coverage [32]. The electronic channel number of HCAL is in the range of 10.000. HCAL is a sampling calorimeter, comprised of alternating layers which are absorbing plates and plastic scintillator tiles, respectively. The materials have to be thick enough to absorb the major energy of the shower. In addition, high hermeticity

is required for the detection task so that the central barrel and end-cap HCAL are complemented by forward calorimeters which are located outside the muon chamber.

The muon system, located at the most external part of the CMS detector, is interleaved with the iron wheels and works as the return yoke of the magnet. It aims at identifying muons and providing accurate measurement of their transverse momenta together with other inner trackers. The muon system can further be divided into three independent subsystems: 1) in the barrel, Drift Tube (DT) chambers are installed; 2) in the two end-caps, Cathode Strip Chambers (CSC) are installed; 3) Resistive Plate Chambers (RPC) for redundancy in both barrel and end-caps region.[33].

It is unclear for the structure of CMS detector only with its 3D schematic. On this basis, a 2D cross-sectional view of the CMS detector is presented in Figure 3.2. As can be seen, the trajectories of electrons, muons and other charged particles are bent by the strong magnetic field. These charged particles are

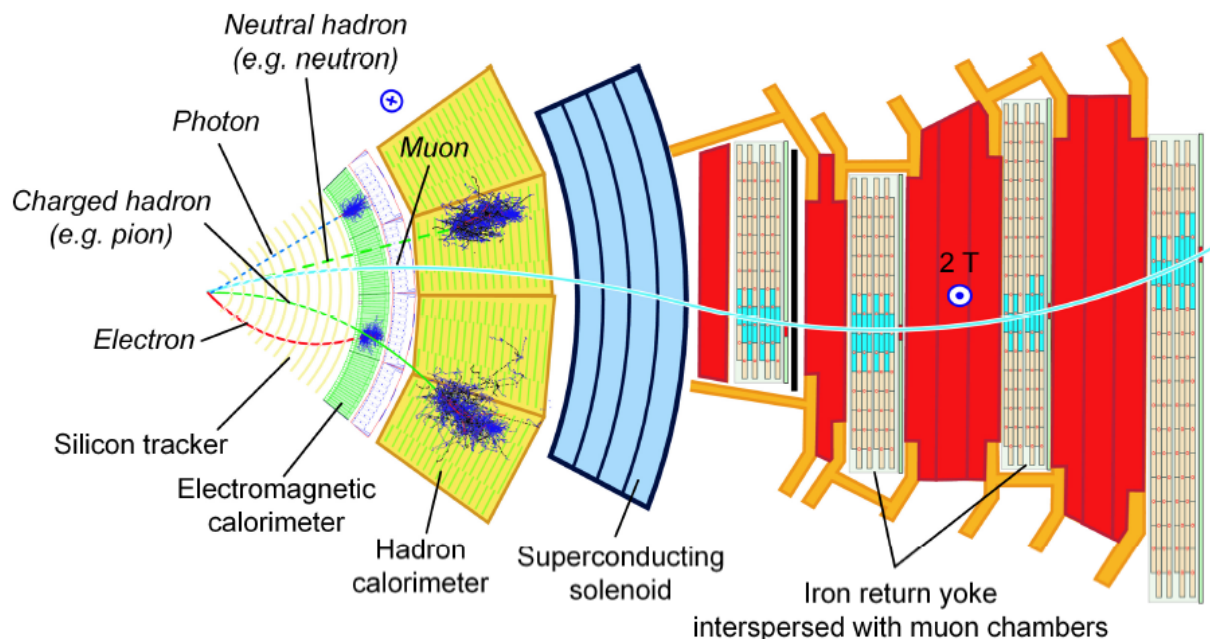


Figure 3.2: Cross-sectional view of the CMS detector [31]. The trajectories of different particles as they move out the detector through different layers are shown as well.

detected by the inner-most section, namely the silicon tracker detector. This detection can provide excellent precision measurements of their momentum and energy. The electromagnetic calorimeter is the second inner-most subdetector and is used for collecting electrons and photons; once a particle hit, an electric signal which is proportional to its energy will be created. Those hadrons which can travel through the electromagnetic calorimeter will be absorbed in the outer layer, the hadron calorimeter. In comparison, muons have the most powerful penetrativity and are identified by the muon system.

With the above detector structure and under the nominal luminosity, there will be up to 10^9 inelastic events per second. Typically an event will require one MB storage room resulting a data rate of 320 Tbit/s, which makes it impossible to record and analyze all the events [34]. In this case, detectors have to possess an effective data discrimination system to throwing the non-interesting collisions away online, namely the trigger system.

Actually, this trigger system is a combination of hardware and software algorithms to make a fast decision on whether an event is interesting or not. The trigger system of CMS detector contains two levels

which are called Level 1 (L1) [35] and High-level Trigger (HLT) [36]. The first level L1 merely uses part of the data from the muon system and the calorimeters to make the decision; the full data is stored temporarily, waiting the decision result to proceed further. The decision process has to be completed within a latency of $3.2 \mu\text{s}$ according to the deposited energy in the calorimeters, the hit patterns in the muon chamber etc [37]. After the selection of L1, the event rate will be significantly lowered to 75 kHz.

The HLT system can access the data of all the CMS subdetectors with full granularity and resolution. However, it still uses partial information firstly for the preliminary decision and afterwards the full data for the final decision. An average decision time of the HLT is about 100 ms and after which the event rate will be further reduced to a few hundred Hz.

With the help of the advanced trigger system, the challenge for real-time data readout and processing ability is alleviated. However it still cannot and will not meet the requirements of the upgrades of LHC: 1) after the long shutdown from February 2013 to March 2015, luminosity was improved to the nominal value; 2) in the Phase-1 upgrade, started at the end of 2018, the luminosity was further improved to $5 \times 10^{34} \text{ cm}^{-2}\text{s}^{-1}$; 3) for the next Phase-2 upgrade, the peak luminosity will achieve $5 \times 10^{34} \text{ cm}^{-2}\text{s}^{-1}$ in 2025 as summarized in the High-Luminosity LHC Project. The remarkably increased luminosity poses not only new challenges to the detectors [38] but also to its trigger and data readout system [39], [40] where the event rate will increase significantly resulting in much data volume.

3.2 The Adaptive Gain Integrating Pixel Detector at X - FEL

The challenge of limited transmission bandwidth exists in photon science as well and one example is from the detector AGIPD (Adaptive Gain Integrating Pixel Detector) used in the European X-Ray Free-Electron Laser Facility (XFEL). XFEL is an international project to build a large-scale linac in Hamburg, Germany, aiming at providing extremely brilliant and ultra-short pulses of spatially coherent x-rays with wavelength down to 0.1 nm [41]. The essential components of the facility are the injector, linear accelerator (linac), beam distribution system, undulators, photon beamlines and the experimental stations. Different from the CMS at CERN, the accelerator of XFEL is linear therefore all the above-mentioned components are disposed almost linearly in a line as long as 3.4 km as shown in Figure 3.3.

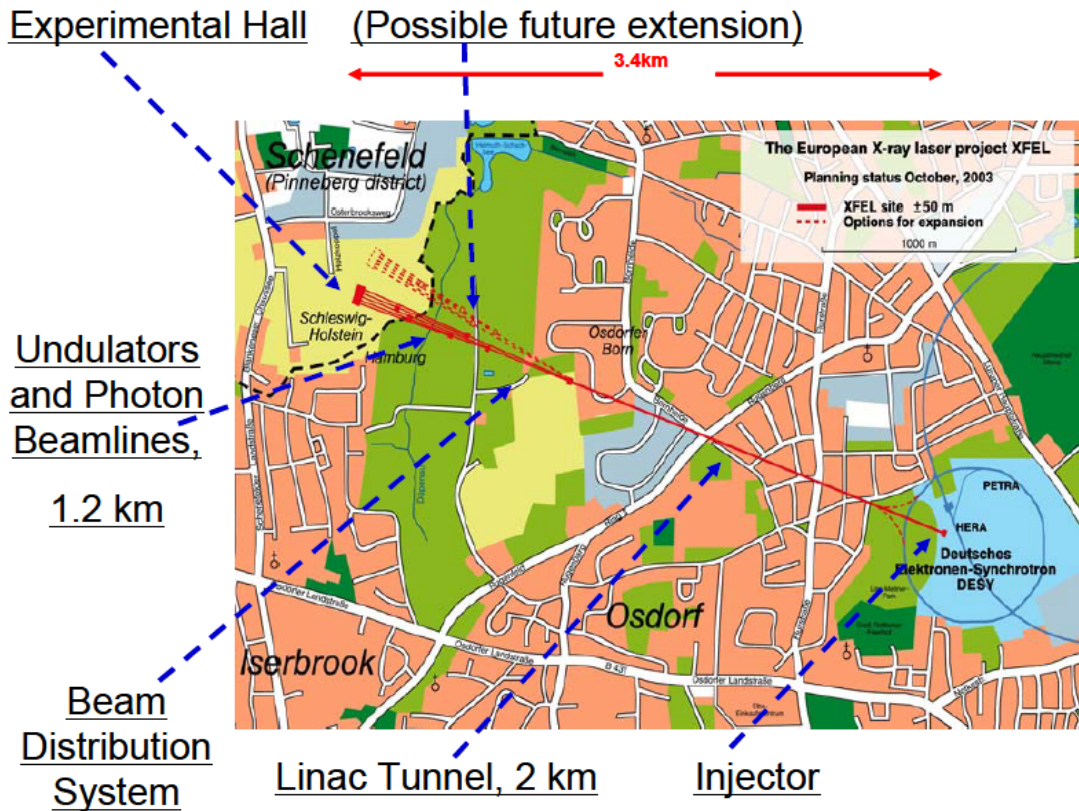


Figure 3.3: Schematic layout of the main components of the European XFEL Facility, adapted from [41].

In the first functional component ‘Injector’, electrons are firstly extracted from a solid cathode by a laser beam, these extracted electrons are then accelerated to an energy of 120 MeV by an electron radio frequency (RF) gun and injected to the linac directly. The linac tunnel is 2.1 km long and comprised of superconducting accelerating modules, magnets and diagnostic equipment after which the electrons will be further accelerated up to 20 GeV while 17.5 GeV is the foreseen energy for standard model. At the end of the linac, a beam distribution system channels the accelerated electron bunch to two alternative beamlines. A schematic of the two beamlines is illustrated in Figure 3.4. The electrons at beamline 1

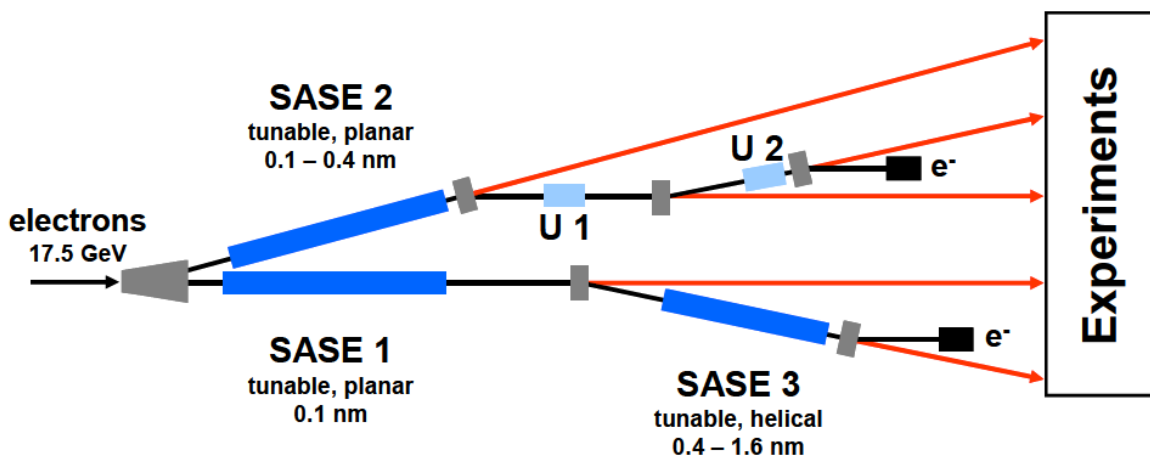


Figure 3.4: Schematic layout of the arrangement of undulators at the European XFEL. The initial configuration of the facility does not include the undulators U1 and U2, nor the helical version of SASE3, which is going to be initially built in the planar version, adapted from [42].

follow a trajectory from SASE 1 (self-amplified spontaneous emission) to SASE 3 and produce hard x-ray photons with a fixed wavelength of 0.1 nm and softer x-ray photons with wavelength of 0.4-1.6 nm, respectively. After the stage of SASE3, photons and electrons are separated by deviating the electrons to a beam dump. The electrons to beamline 2 follow a trajectory to SASE 2, undulators (which are actually special arrays of magnets) U1 and finally undulators U2. In this link, hard x-ray photons with a tunable wavelength from 0.1 nm to 0.4 nm can be generated through station SASE 2. Through stations U1 and U2, very hard x-ray photons can be further generated with a wavelength down to 0.014 nm and 0.06 nm, respectively. At the end of U2, the electrons are guided to a beam dump as well. Finally, at the experimental hall, the scientific experiments are conducted accordingly. Since the entire facility is to generate X-rays, all the experiments conducted at XFEL are X-ray based. There are six classes of experiments in total, which are 1) Femtosecond X-ray Experiments (FXE), 2) Single Particles, Clusters, and Biomolecules & Serial Femtosecond Crystallography (SPB/SFX), 3) Spectroscopy and Coherent Scattering (SCS), 4) Small Quantum Systems (SQS), 5) High energy density matter (HED), 6) Materials imaging and Dynamics (MID). In this thesis, a brief review of the detector AGIPD used in the SPB and MID experiment will be made.

AGIPD is a classical hybrid pixel array detector and is composed of 16 modules as the basic building blocks. Each comprised module is actually an independent detector system whose main four parts are detector head, vacuum board, analogue part and digital part. The detector head is a 512×128 pixel sensor bump bonded to 8×2 ASICs. The vacuum board provides a flexible connection between the detector head and the analog part. The analog part has 64 analog-to-digital converter (ADC) channels on a two-board system, digitizing the analog signal into 14-bit-resolution digital signal and finally sending to the digital part. The digital part is made up of an FPGA daughter board on carrier board, the digital signals are processed by them and formed to data packets to send out [43] by four 10 Gb/s Ethernet links. On this basis, a general signal process squence looks like the following: the incident photons generate small electrical signals, which are amplified by the ASICs to the required level for further processing by the ADCs, these analog signals are converted to digital signals by ADCs and being forwarded to the digital part to be packed according to the transmission protocols and finally being sent out in the required format. In the future, the data volume of the detector will also increase significantly, current transmission bandwidth will not meet the requirements.

3.3 State-of-the-art optical data readout in detector instrumentation

The basic readout structure of the CMS detector in the early stage is shown in Figure 3.5. As can be seen, the entire structure can be divided into the experimental cavern and the counting room, which are 65 meters away from each other. The transmission is bi-directional with downlinks for timing trigger

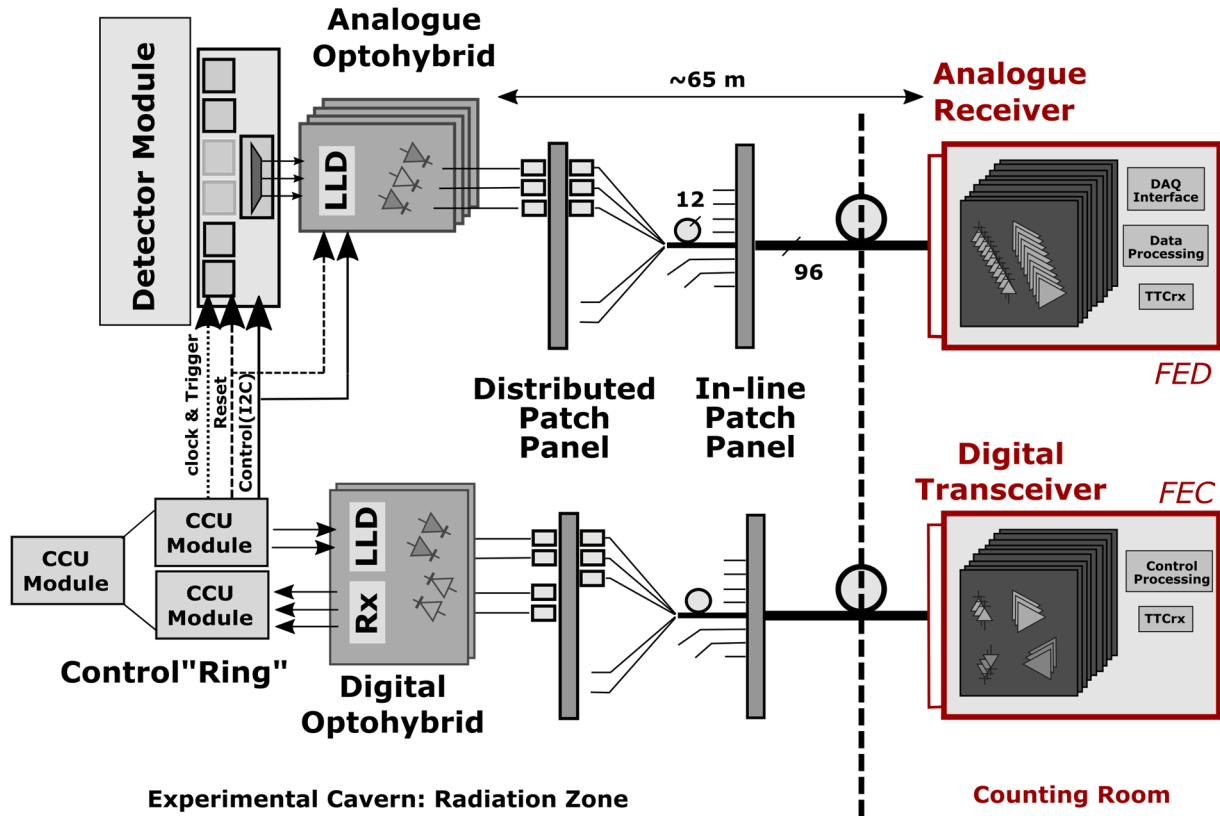


Figure 3.5: Overview of the transmission system of the CMS detector [44].

and control signals should be uploaded to the electronics units inside the detector volume and the detected data should be capable of being transmitted into the counting room as well. The transmission between two halves adopts optical link because of the galvanic isolation between on-detector and off-detector electronics [45], avoiding electromagnetic interference and being low-loss, low-power and low-mass. The architecture of the tracker control system is token-ring-like where the front end controller is the master control node located in the counting room and multiple communication and control units (CCU) (kind of slave nodes) are placed on the silicon trackers.

For reading data out, the process starts from amplifying the detected signal by the front-end ASIC to a suitable level and storing it in an analog pipe-line waiting for the trigger signal. After receiving the trigger signal, such data is time-multiplexed and forwarded to the next stage, namely the analog optohybrid module. There, the amplified electrical signal from the detector will be an input for the custom designed laser driver ASIC, called LLD [46]. The LLD can directly modulate the drive current of the laser diode, i.e. a light amplitude modulation. The optical signal with a wavelength of 1310 nm is transmitted by single-mode fibers (SMF). Each SMF is connected to a fan-in by a special connector merging 12 fiber signals to a 12-fiber ribbon in the distributed patch panel. Further 8 sets of 12-channel fiber ribbons are packed forming an 8×12 multi-ribbon cable in the in-line patch panel. Each cable is connected to an analog optical receiver module in the counting room where the received data will be finally processed and stored.

For transmitting signals to the units inside the detector, the digital control and clock signals are firstly transformed into optical signals by the digital transceivers and then optically transmitted to the digital optohybrid module. There, optical signals are converted back into electrical signals by the on-detector receiver, passing sequentially around the ring of CCU modules electrically. Digital signals can also be transmitted back to the counting room in the reverse way.

Among the above mentioned data transmission concept, most parts of the right half, located in the counting room, can be realized by commercial products. In comparison, the left half (namely the experimental cavern) is entirely exposed in the radiation environment and most parts are hardly available commercially. And, a lot of radiation experiments had been carried out in the past [47][48][49] to validate the components' radiation hardness. Due to the upgrade of colliders, the optical links have also been improved a lot and will be further improved for the next phase of upgrade.

There are two radiation levels for the components used in the radiated regions: the total dose of the calorimeter systems is 10 kGy (5×10^{14} neutrons/cm²) and the dose for the inner detector is up to 500 kGy (5×10^{14} neutrons/cm² and 1×10^{15} hadrons/cm²). They are referred to as calorimeter-grade and tracker-grade, respectively. In addition, the components inside detector have to withstand a temperature range of -30 °C to 60 °C and a magnetic field of 4 T. For the phase-I upgrade of the LHC detector, the Versatile Link (VL) [50] and the Gigabit Transceiver (GBT) project [51] were established for both ATLAS and CMS detectors aiming at building a bi-directional general-purpose and radiation tolerant optical link which integrates all the following kinds of data: the detector readout data, the slow control,

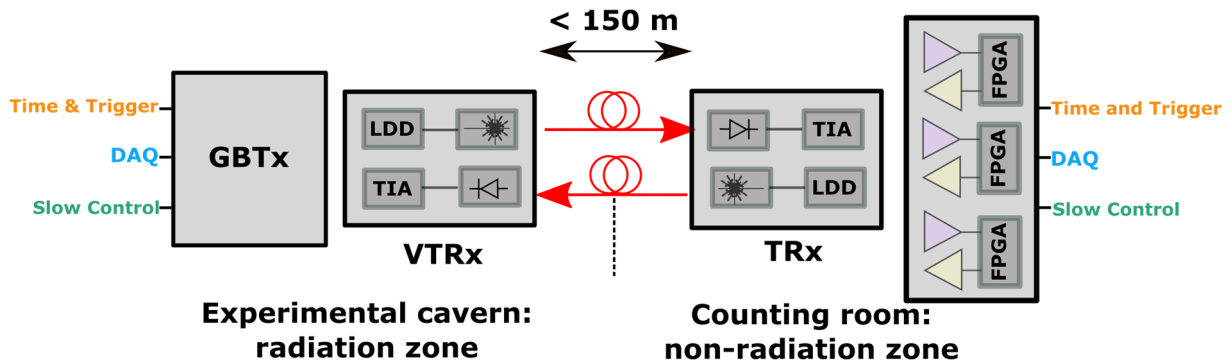


Figure 3.6: Schematic of the VL architecture for detected data, timing, trigger and control signal transmission.

timing and trigger signals, the operating environment monitoring signals. A schematic of the VL architecture is presented in Figure 3.6. The GBT focuses mainly on the customized transceiver module which is located inside the detector experiencing a harsh ambient environment. The serializer-deserializer (GBTx) ASIC can realize data format transformation between general-format data to the required serialized-format data acting as the interface between the GBT protocol and the front end electronics. On the other hand, a versatile transceiver (VTRx) provides the interface between electronic signals and optical signals and is composed of a custom laser diode driver ASIC (sketched as LDD in Figure 3.6) and a transimpedance amplifier ASIC (sketched as TIA in Figure 3.6). The laser diodes used, operates at a wavelength of either 850 nm (multimode) or 1310 nm (single mode) for compatibility reasons to the existing infrastructure. The feasibility of using the custom designed transceiver in radiation region was validated by the demonstration in [50] which is based on an SFP+ module. The transceivers at the counting room, away from the radiation area, are off-the-shelf products and the

corresponding research on their radiation hardness is presented in [52]. Based on the above design, the final transceivers could feature a data transmission speed of 4.8 Gb/s and pluggable property.

For the phase-II upgrade, another common optical link is required due to the successful VL project applied in phase-I upgrade. Whereas, the targeted transmission bandwidth is improved to ~ 10 Gbit/s per link. The components used in the transceiver design have to be capable of resisting the tracker-grade-level radiation under the circumstance of improved luminosity. However, if still using a similar scheme like the VL project, not only LDD but also the laser diodes have to be developed further a lot. Commercially available vertical-cavity surface-emitting laser diodes (VCSEL) can be favorable alternatives for the laser diodes in terms of the transmission speed while they are limited by other issues and this will be discussed next.

VCSEL is a kind of semiconductor laser diode emerged in the 1990s. While different from the conventional edge-emitting semiconductor lasers, its emitted laser beam is perpendicular to the pn junction plane with the characteristics of low divergence and a circular profile. A simplified structure of VCSEL is illustrated in Figure 3.7. Its top and bottom layers are both metal contacts. Beneath the top

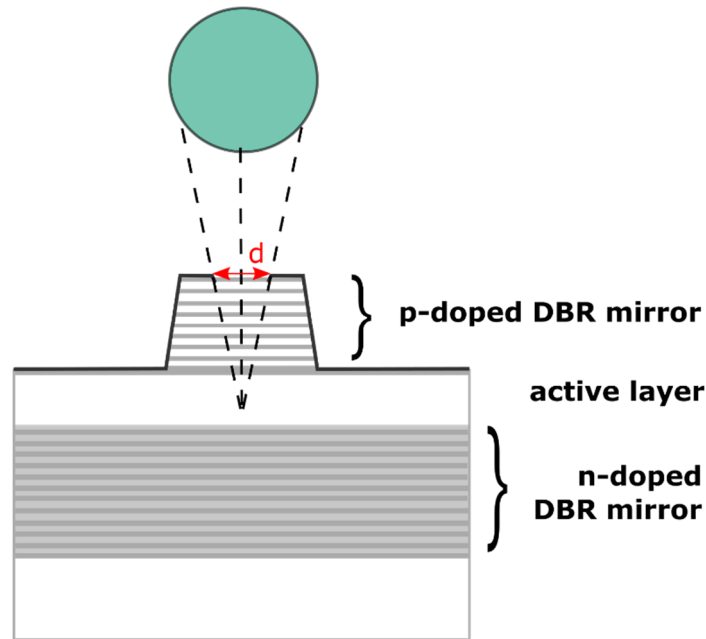


Figure 3.7: A cross-sectional view of a VCSEL.

metal layer is the upper distributed Bragg reflectors (DBR) which are usually p-type doped. And, there is a corresponding layer is n-type doped at lower layer. Between two DBR layers is an active layer which is actually a quantum well with a thickness usually smaller than $1 \mu\text{m}$. Below the n-doped DBR layer there is still a thick n-type substrate layer. The aperture of VCSEL is generally circular with a very small diameter d (in the range of several micrometers) and the diameter will affect the linewidth of the laser beam.

For vertical resonators, the length of the gain medium is defined by the thickness of the pn junction. Therefore the gain medium length is very small due to the thin pn junction. So as to achieve laser operation, Bragg reflectors working as resonator mirrors are used to compensate the low gain in a VCSEL. For example, the lower resonator mirror can be made up of several tens of alternating layers of $\text{Al}_x\text{Ga}_{1-x}\text{As}$ and AlAs . Each layer has a thickness of $\lambda_{\text{emitting}}/4$, resulting in an optical power reflection

rate around 99.99%. In contrast, the top mirror has fewer $\lambda_{\text{emitting}}/4$ layers with a smaller reflection rate around 99.9%. One unique characteristic of the mirror is that any light, reflected back towards the laser from other part of the optical system with a different wavelength, cannot enter the resonator again. This makes VCSEL effectively isolated against such kind of reflection. Both the thin gain medium and the high resonator efficiency contribute to a very small threshold current (only several mA). Because of this low operating current, VCSEL are suitable to use in many scenarios.

The emitted laser signal is single mode or multimode depending on the resonator design. The mode will tune within the gain profile when the laser temperature varies, allowing VCSEL to be temperature-tuned over a range of several nanometers without mode hopping. The lasing wavelength is determined by the Fabry-Perot resonance defined dominantly by the distributed Bragg reflector (DBR) design. Popular VCSELs in the market are in the wavelength range from 760 nm to 960 nm and the typical output power is 0.3 - 0.5 mW for single mode VCSELs. 5 mW output power multimode VCSEL is also available [53]. Driven by the optical interconnects and telecom, VCSELs with wavelengths at 1310 and 1550 nm with a high pump power arose as well.

The attractive features for VCSELs in optical interconnects are the following: low driving power, high-speed current modulation for multi-Gbit/s data generation and also a simple mounting technology like light-emitting diodes (LED). For a given VCSEL product, once the injected current is larger than the threshold current, the output power of the laser is almost linearly proportional to the current and can be expressed by the laser rate Equation 3.1 [54] where η is the differential quantum efficiency (affected by temperature) describes the fraction of injected electrons used to produce coherent emission, $\hbar\omega$ is the reduced Planck's constant with $\hbar = h/2\pi$, ω is the angular frequency, I is the injected current and I_{th} is the threshold current of VCSEL.

$$P(I, T) = \eta(T) \frac{\hbar\omega}{q} (I - I_{th}(T)) \quad \text{Equation 3.1}$$

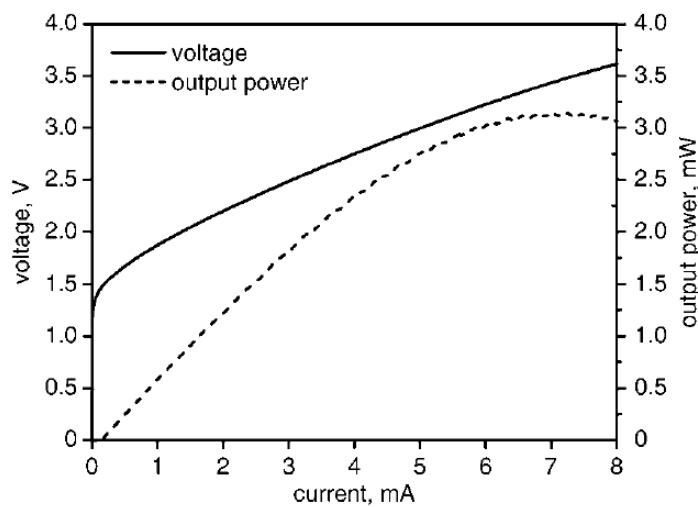


Figure 3.8: L-I-V curves for a 3 μm diameter device at room temperature adapted from [55].

If regarding the item $\eta \frac{\hbar\omega}{q}$ and I_{th} as constants, the output power is merely a function of injected current. For example, Figure 3.8 from [55] can express the relation between applied voltage, the output

power and injected current under such circumstance, namely a typical L-I-V curve of the example VCSEL. The used device for this measurement is a 993-nm VCSEL with an aperture diameter of 3 μm and a differential quantum efficiency of 54%. According to the measurement, the threshold current of this example device under room temperature is as low as 0.144 mA and the corresponding threshold voltage is 1.47 V. The roll-over current is 7 mA resulting in a maximum output power of 3.1 mW. In the region between threshold current and roll-over current, the L-I curve is nearly linear.

In terms of optical interconnect, large signal modulation of VCSELs is of more interest where the biasing current is usually several mA. For VCSELs with lasing wavelength between 760 nm and 960 nm, the 3-dB modulation frequency can achieve a few tens of GHz in research with careful designing the structure of VCSEL and selecting a suitable biasing current. As an example, in [55], the authors successfully demonstrated a 35 Gbit/s error-free transmission with a tapered-oxide-aperture 980 nm VCSEL. The threshold current of their used device is merely 0.144 mA while a biasing current of 4.4 mA was used and the AC signal had a peak to peak voltage signal of 0.84V. Along with the arising of VCSELs suitable for telecom and Datacom application, progresses were also made at the wavebands of 1310 nm and 1550 nm. In [57], a demonstration of 3.2 Gb/s using 1310 nm VCSEL was presented. With continuous developments, the transmission speed in research at wavelengths suitable for telecom was already beyond 20 Gb/s [58][59].

However, the ambient temperature can make significant effects on both VCSEL's DC and AC performance. With varying the ambient temperature, the gain peak of the quantum well emission and the resonance of the DBR mirrors will change at different rates. In the meanwhile the threshold current varies with temperature and the threshold current is found to have a parabolic relation with the temperature that the threshold current will achieve a maximum value I_0 at a specific temperature. Nevertheless, the typical variation of I_{th} is less than 1 mA compared with its value at 25 °C [56].

On the other hand, the intrinsic bandwidth of VCSEL is determined by its resistance and capacitance while the resistance of VCSEL is also a function of temperature. A rough relation Equation 3.2 can be found in [56] where $R(T_A)$ is the corresponding resistance at the desired temperature T_A . ΔR and ΔT are determined by values around T_A and $R(T_A)$. Depending on the characteristics of different VCSELs, the bandwidth will be affected by temperature to different extents.

$$R(T) \approx R(T_A) \times [1 - (T - T_A) \times \Delta R / \Delta T] \quad \text{Equation 3.2}$$

The large signal modulation effect of VCSEL is also affected by the operating temperature. For a given VCSEL and transmission speed, say 20Gb/s, the bit error rate can increase dramatically between 25°C to 85°C as shown in [60]. Nevertheless, the challenge of employing VCSELs in the next phase upgrade at CERN and even for future readout systems design is not dominantly from their temperature dependence but from their radiation hardness.

In radiation environment, the performance of laser diodes differ a lot. As shown in [61], the used 850 nm GaAs multimode VCSEL's threshold current increases with neutron irradiation and the slope efficiency ($\Delta P / \Delta I$ around the biasing current in the L-I-V curve) decreases as well. This indicates that the modulation depth will be smaller under the same biasing and input signal. In consequence, a higher biasing current will be more beneficial while the internal optical loss will increase and the quantum efficiency of the laser will decrease at a higher biasing current due to more energy generated from self-heating at a higher current [62]. On the other hand, [61] and [63] show that the estimated failure point

for VCSELs is around $1 \times 10^{16} \text{ cm}^{-2}$ for 20 MeV neutron fluence. However, for Phase-II upgrade, the radiation level of most parts of the detector will be higher than this failure point. Therefore, looking for a more competitive alternative is not only beneficial for the next phase upgrade but inevitable for the future development.

3.4 A novel multi-channel optical detector read-out system

Above, the concept of modulating laser diodes was introduced as one important proposed scheme for the next detector upgrade at CERN. However, let alone the radiation hardness of III-V compounds, whether the modulation speed at the wavelengths fitting into the CERN infrastructure (1310 nm and 1550 nm) can be improved continuously is still unknown. In this case, it makes sense to look into multiplexing techniques instead of only focusing on improving the modulation speed of an individual unit. In general, there are four multiplexing techniques which are space division multiplexing (SDM), time division multiplexing (TDM), frequency division multiplexing (FDM) and wavelength division multiplexing (WDM). While, in terms of the confined room inside the detector, SDM will not fit especially when the detector structure requires to be changed in the future. Due to the requirements of dealing with the detected events instantaneously, TDM isn't a possible solution either. FDM and WDM are similar while the former is maturely used in radio and television broadcasting, the latter is popular in fiber-optic communication in comparison. For both, signals of different transmission channels are coded onto carriers with different frequencies and transmitted through the same medium.

A WDM system can multiplex multiple optical carrier signals with different wavelengths onto a single fiber, enabling bidirection high-speed communication with a limited number of fibers. WDM has been successfully applied to optical transmission systems for a few decades and enlarged the transmission capacity a lot. If there is a solution for the detector upgrade which can successfully make use of the WDM technique, it would be a very promising solution. On one hand, the transmission bandwidth can be increased without paving massive fibers fitting into the current infrastructure at CERN. On the other hand, the researchers can upgrade the transceiver design in two aspects: increasing the number of used wavelengths and the transmission speed at each individual transmission wavelength.

In the WDM transceiver market, there is no product providing a full system that can be used in detector instrumentation fitting into the harsh requirements of the footprint, operating temperature and the strong radiation. In recent years, the fabrication technology has made significant progress, making silicon on insulator (SOI) platform very popular. In consequence, silicon photonics also becomes one technology under development for future high energy (HEP) physics application. Since the SOI platform can provide a high refractive index difference between silicon (≈ 3.5) and SiO_2 (≈ 1.4), the silicon photonic components fabricated on SOI feature a very compact footprint. In the past few years, several foundaries (for instance IBM and ST Microelectronics) added silicon photonics to their manufacturing lines, developing customized high-speed, compact and low-cost transceivers becomes feasible.

On the basis of the developing technology from all aspects, there had been many researches reporting on WDM transmission link in recent years. Generally, we can categorize them by material system and modulation mechanism. One very popular concept for the SOI platform is to make use of ring resonator to realize WDM system on chip. This method can provide very compact footprint since the radius of the ring to realize filtering the wavelengths is usually several micrometers. By cascading several micro rings

with different wavelength selectivity, a multiple-channel transmitter is formed. In the example from [64], the authors utilized a 130 nm SOI CMOS platform to fabricate an $8\text{-}\lambda$ integrated transmitter based on micro-ring resonators. Since each ring modulator features a transmission speed of 10 Gb/s, the aggregated transmission speed of the entire transmitter is as high as 80 Gb/s. The energy consumption is also within an acceptable level with 6 mW/channel, achieving an energy efficiency of 100 fJ/bit at 10 Gb/s operation. However, the drawback of this concept is the narrow bandwidth of microring and its sensitivity to ambient temperature. Only a small variation of the ambient temperature can induce significant deviation of the operating wavelength.

Another concept based on SOI is the combination of MZMs and wavelength filter units. On-chip wavelength filters can be realized in several different ways like Echelle gratings, arrayed waveguide gratings etc.. This will be discussed in the later chapter. The designs of MZM are almost the same while slight difference can exist in the pn phase shifter design. One example is from [65], the authors successfully demonstrated a 50 Gb/s transmission system based on carrier depletion based MZMs and an on-chip wavelength filter. There are four usable transmission channels in total and all the wavelengths are fitting into the ITU-T G.694.2 grid. Each channel of the system has a transmission speed of 12.5 Gb/s. The laser sources providing four carrier wavelengths are bonded to the silicon structure. With the same platform, another transceiver design based on Echelle gratings (de-)multiplexers and electro-absorption modulators was presented in [49]. An error-free transmission of each individual channel at a speed of 10 Gb/s was achieved.

There is also another method to realize the system integration on chip based on III-V compounds. A $4\text{-}\lambda$ transmitter with integrated electro-absorption modulators and lasers was presented in [49]. In this paper, the signals' multiplexing was realized by multimode interferometers (MMI). Since each channel has a modulation speed of 28 Gbit/s, the aggregated transmission speed can achieve 112 Gb/s.

Based on the above investigations of different concepts of integrated transceiver design, we propose a generic high-speed data transmission system as shown in Figure 3.9. This generic transceiver is

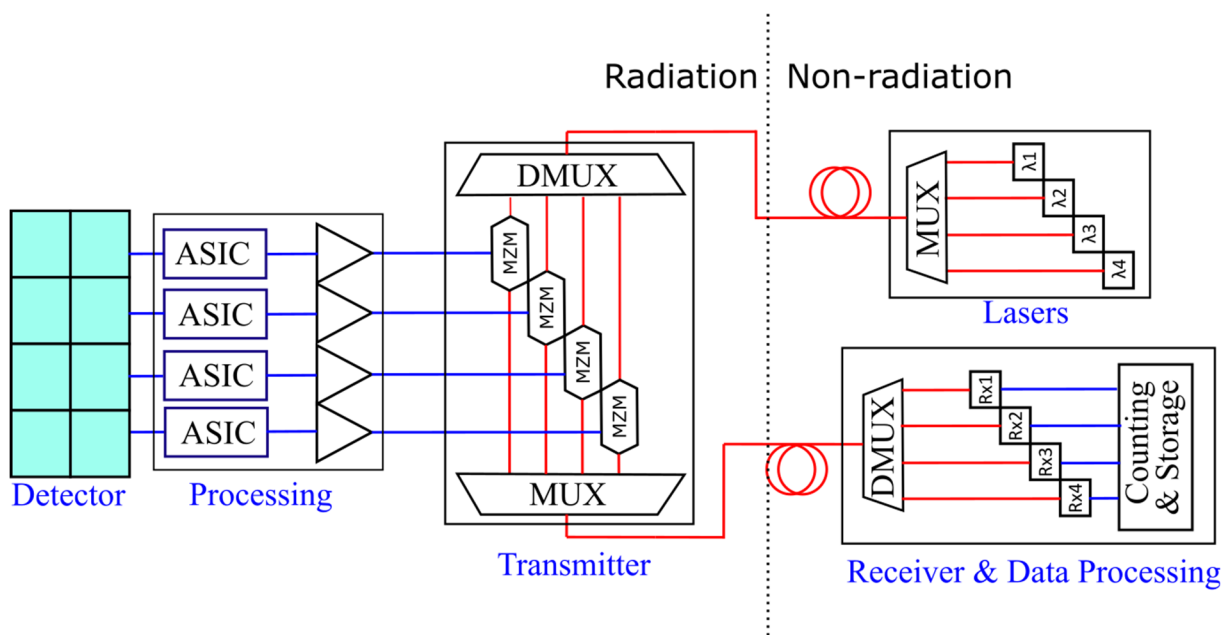


Figure 3.9: The proposed data transmission system based on WDM technology for detector instrumentation.

designed based on the MZMs and Echelle grating (de-)multiplexers which realize the electro-optic

modulation and wavelength division multiplexing, respectively. In this thesis, a preliminary 4- λ transmitter is designed and fabricated to verify the feasibility. As already mentioned in the introduction, the detected signal from the detector elements will be amplified and preprocessed by the front-end ASICs. Modulator drivers amplify their output signals to meet the requirements of the MZMs. Each channel is connected to an individual MZM on a photonic chip. The photonic chip integrates an Echelle grating demultiplexer, several MZMs and an Echelle grating multiplexer. The input signal of each MZM is divided equally by a 3-dB MMI and linked to two phase shifters. If the two phase shifters are biased differently, light will have different propagating constants and depending on their phase relation at the shifter end, constructive or destructive interference will take place, resulting in an on-off shift keying modulation. As the laser sources are located outside the detector volume and the optical carriers are transmitted by a SMF to the photonic chip, radiation will not be an issue for the lasers. The transmission bandwidth per fiber is determined by the modulation speed of the modulator, the useable channels of the EG-DMUX and the bandwidth of the ASICs and the drivers.

It is noticeable that an integrated transmitter is the key part of the whole transmission system. The

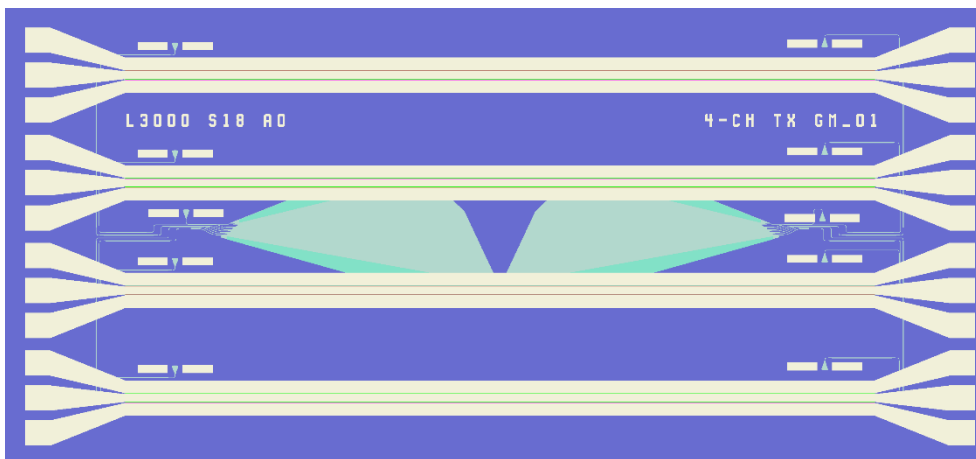


Figure 3.10: Microscope picture of a 4- λ integrated WDM transmitter.

microscope picture of an integrated 4- λ transmitter unit is illustrated in Figure 3.10. As can be seen, each transmitter unit is composed of four MZMs (white coplanar horizontal stripes with tapers at their ends), one Echelle grating demultiplexer (green, center left), one mirrored Echelle grating multiplexer (green, center right) and several grating couplers. In consequence, each transmitter unit has a footprint of $3.8 \times 1.67 \text{ mm}^2$ and identical design parameters except that two of them employ 1×7 (de-)multiplexers and the other two employ 1×9 (de-)multiplexers. In reality, merely 4 channels of the (de-)multiplexers are in use for the transmission. The MZMs use two 2×2 3-dB MMIs as optical splitters and combiners, namely each MZM has 2 inputs and 2 outputs. One MZM input is connected to the demultiplexer and one MZM output is connected to the multiplexer. The residual ports are connected to grating couplers for characterizing the modulators individually. Several test structures were placed between the MZMs of the transmitter units to make full use of the on-chip resource while they are omitted here.

4 Mach-Zehnder Modulators

4.1 Different modulation effects

One dominant requirement for the material in communications is the ability to perform optical modulation. And, in terms of the modulation mechanisms, there are generally two kinds of effects we can make use of which are the electro-optic effect and the thermal-optic effect. For the former one, the most widely studied types are: 1) Pockels effect, 2) Kerr effect, 3) Franz-Keldysh effect, 4) free-carrier plasma dispersion effect.

The Pockels effect is a linear electro-optic effect where the change on the real refractive index Δn is proportional to the applied electrical field E [66]. In consequence, the refractive index change is proportional to the applied voltage under the circumstance that the applied field is uniform. On the other hand, this effect is polarization dependent that the change of refractive index is also determined by the direction of the applied electric field with respect to the crystal axes. Unfortunately, since the group IV crystalline alloys have diamond cubic lattice and the elements have inversion symmetry, the Pockels effect disappears completely in silicon crystalline. However, this effect is important for some materials used in the communication field like lithium niobate (LiNbO_3). In general, the applied electric field is aligned to the direction of one principal axis of the crystal so that the electro-optic effect becomes strongest for the material. Still take LiNbO_3 as an example, its so-called coefficient ‘ r_{33} ’ is equal to 30.8×10^{-12} m/V and the effect on the refractive index resulting from the applied electric field is given by Equation 4.1 where Δn is the induced real refractive index, E is the applied electric field, n_{33} is the refractive index in the direction of the applied electric field. While actually when the silicon is deliberately strained, the Pockels effect will occur [67].

$$\Delta n = -r_{33}n_{33} \frac{E}{2} \quad \text{Equation 4.1}$$

The Kerr effect, which changes the refractive index n quadratically with the applied electric field, presents in all the group IV material. The change may be expressed as shown in Equation 4.2 where n_0 is the original refractive index without the perturbation, s_{33} is the Kerr coefficient and E is the applied electric field. This effect was quantified by Soref and Bennett theoretically at a wavelength of $1.3 \mu\text{m}$ for which the change of refractive index is predicted to reach 10^{-4} at an applied field of 10^6 V/cm [23]. This value is already larger than the break down field of a lightly doped silicon which means this effect is still a relatively weak effect in silicon. This was verified in [23] that Kerr effect is weaker than the plasma-dispersion effect (which will be introduced later). Also, the literature shows the effect has a fairly flat wavelength dependence compared to the Franz-Keldysh effect, which will be introduced next.

$$\Delta n = s_{33}n_0 \frac{E^2}{2} \quad \text{Equation 4.2}$$

The Franz-Keldysh effect [68] may rise to both the electrorefraction and the electroabsorption while the latter one is more primary. This effect is due to the change of energy bands when applying an electric field. In consequence, the absorption properties of the material change as well, especially at the wavelength close to the bandgap. Therefore the refractive index of the material also changes. The effect was also quantified by Soref and Bennett theoretically [23]. A plot of Δn with respect to the applied electric field was plotted around the wavelength of $1.07 \mu\text{m}$ where the Franz-Keldysh effect is strongest.

And an applied electric field of 2×10^5 V/cm can result in a change of Δn with a value of 10^{-4} . Nevertheless, this effect becomes significantly weaker at the telecommunication wavelengths 1.31 μm and 1.55 μm . In [23], a Δn of 1.7×10^{-6} was measured near 1550 nm with an applied electric field of 10^5 V/cm, which is already in the same order of the breakdown field magnitude of a diode having an intrinsic doping concentration.

Another important and widely investigated effect is the free carrier plasma dispersion effect. The complex refractive index of a material can be expressed by Equation 4.3 in which n is the real part and k the extinction coefficient. The absorption can be calculated by $\alpha = 4\pi k/\lambda_0$. Since the complex relation has to be analytic, the real part and the imaginary part are linked by the Kramers-Kronig relation [69]. Since in practice it's easier to measure the absorption spectrum, the effective index change is usually evaluated by this relation. The attenuation constant is expressed by relation 2.8 which is determined by the free space wavelength, electronic charge, light speed in the vacuum, the free space permittivity of the material, concentrations of free carriers and their effective masses. Correspondingly, the refractive index change is expressed by relation 2.9. In [24], the authors even gave the relations of silicon at the wavelength of 1550 nm as shown in 2.10 and 2.11.

$$\bar{n} = n + ik \quad \text{Equation 4.3}$$

Since the free-carrier plasma dispersion effect is strongest in silicon compared to other effects mentioned above [23], the modulators in the integrated transmitter will be designed based on this effect. While before that, it is worthwhile to study the effect induced by the two kinds of carriers. Based on the relations 2.10 and 2.11, we calculate the induced variation on the attenuation constant and the refractive index with respect to different carrier concentrations (from 10^{17} to 10^{20}) at the telecommunication wavelength 1.55 μm . As shown in Figure 4.1, with the same change on the refractive index, a smaller

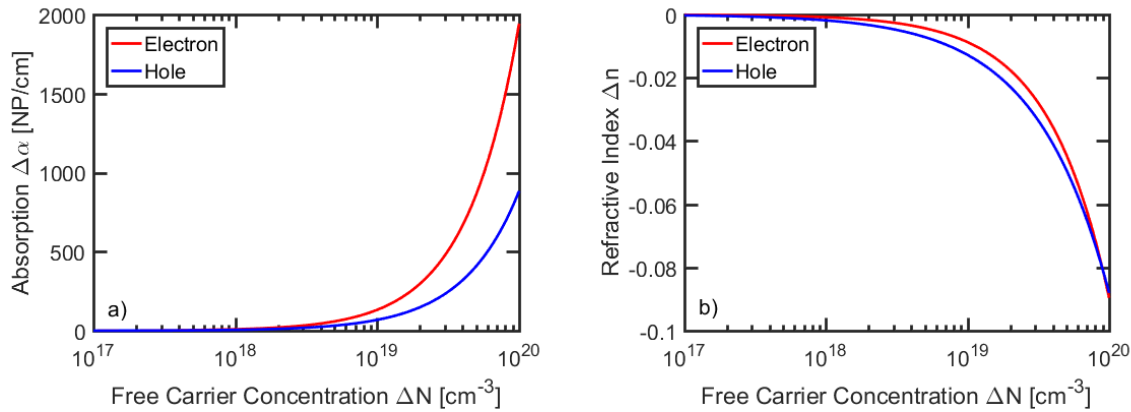


Figure 4.1 Change of attenuation constant a) and refractive index b) of silicon at wavelength 1.55 μm with respect to different carrier concentrations.

hole concentration is required while the difference between two kinds of carriers is quite small from 10^{17} to 10^{18} . In the meanwhile, the attenuation constant of the holes is also smaller than that of electrons at the same carrier concentration, which is especially evident for concentration larger than 10^{19} . According to the comparison, holes are more efficient than electrons in the free-carrier plasma dispersion effect also with less attenuation with the same concentration than electrons. On this basis, a pn junction with higher p- doping can be more efficient which is helpful to the pn junction design in the later chapter.

The thermal-optic effect is physically related to the contraction or expansion of the materials' atom lattice when the ambient temperature changes. With changing the temperature, the interband transition energy will be modified where the absorption spectrum of the material varies accordingly. Therefore the thermoabsorption accompanying with thermorefraction will take place when the photon energies are close to the fundamental bandgap. The important parameter related to the thermal-optic effect is the thermo-optic coefficient. For silicon this index is $dn/dT = 1.86 \times 10^{-4}/K$ [14] which means a temperature variation of one Kelvin results in a refractive index change of 1.86×10^{-4} . It is worthwhile to mention that the refractive index is positively related to the applied thermal energy while injecting free carriers will decrease refractive index, therefore in a design one should take both effects into account reasonably to avoid them cancelling out mutually.

There had been quite some publications of modulators based on the thermo-optic effect [70][71][72] in the past years. In [72], the authors built single-mode channel waveguides operating at 1550 nm. The waveguides were heated by directly passing current through them which results in a switching power of 6 mW and a rise time of 0.6 μs . The research shows a switch time of 10 ns will require about 23 mW power. A thermal modulator will be a necessary part both for the MZM and the ring resonator modulator for the operating point control which will be discussed in the following section.

4.2 Concept of a Mach-Zehnder modulator

A Mach-zehnder interferometer (MZI) is widely used in optical circuits and is the basis of modulators, switches and filters. Although there are different input \times output interferometers, we will introduce the basic concept with the simplest 1×1 MZI as shown in Figure 4.2. But of course there could be several

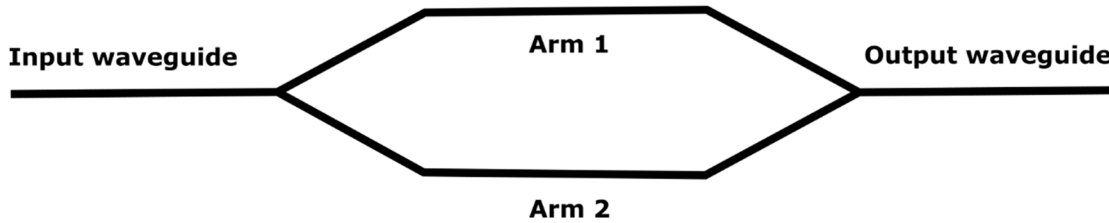


Figure 4.2: A schematic of 1×1 MZI.

input and output ports for an MZI using different couplers which will be introduced in a later section in this chapter. Firstly, we assume the input signal is TE polarized and the input signal will be in-phase and evenly split by the splitter into the two arms. At the output end, two signals will be combined with using the same splitter in the reverse way. Considering the mode propagating in each arm, we can write their electric field according to Equation 4.4 and Equation 4.5 where two arms have the same electric field but different propagation constants [11]. Then the transferred intensity at the output end can be expressed by Equation 4.6.

$$E_1 = E_0 \sin(\omega t - \beta_1 z) \quad \text{Equation 4.4}$$

$$E_2 = E_0 \sin(\omega t - \beta_2 z) \quad \text{Equation 4.5}$$

$$S_{Tr} = ((E_1 + E_2) \times (H_1 + H_2)) = S_0(E_1 + E_2)^2 \quad \text{Equation 4.6}$$

We assume arm 1 and arm 2 have two different lengths z_1 and z_2 , then we expand Equation 4.6 yielding Equation 4.7. By using the trigonometric identities, Equation 4.7 can be rewritten into Equation 4.8. As the optical frequency is overhigh, only the time average of these waves can be observed. On this

basis, we replace all the terms in Equation 4.8 with their average equivalent and the result is shown in Equation 4.9. The relation Equation 4.9 is the so-called interferometer transfer function. It can be seen that the output optical intensity is dependent on the phase term $\cos(\beta_2 z_2 - \beta_1 z_1)$ and the maximum is obtained when $\beta_2 z_2 = \beta_1 z_1$. The intensity is depicted in Figure 4.3. As shown, the output intensity can be changed to be a minimum or a maximum by varying the relative phase of the two arms and the modulation quadrature point should be selected with respect to the normalized output intensity of the MZI as well. To be more specific, if there is π -phase shift in one arm with respect to the other arm, destructive interference will take place and all the light will be extinct at the output end. If the phase difference between two arms is multiple 2π , then the constructive interference will take place. On the other hand, we see that the phase term can be changed either by the propagation constant in each arm or by the propagation length which provide two aspects of inducing phase difference.

$$S_{TR} = S_0[E_0^2 \sin^2(\omega t - \beta_1 z_1) + E_0^2 \sin^2(\omega t - \beta_2 z_2) + 2E_0^2 \sin(\omega t - \beta_1 z_1) \sin(\omega t - \beta_2 z_2)] \quad \text{Equation 4.7}$$

$$S_{TR} = S_0 \left\{ E_0^2 \left(\frac{1}{2} [1 - \cos(2\omega t - 2\beta_1 z_1)] \right) + E_0^2 \left(\frac{1}{2} [1 - \cos(2\omega t - 2\beta_2 z_2)] \right) + E_0^2 [\cos(\beta_2 z_2 - \beta_1 z_1) - \cos(2\omega t - \beta_2 z_2 - \beta_1 z_1)] \right\} \quad \text{Equation 4.8}$$

$$S_{TR} = S_0 \left\{ \frac{E_0^2}{2} + \frac{E_0^2}{2} + E_0^2 [\cos(\beta_2 z_2 - \beta_1 z_1)] \right\} \quad \text{Equation 4.9}$$

$$= S_0 \{ E_0^2 [1 + \cos(\beta_2 z_2 - \beta_1 z_1)] \}$$

On one hand, we can consider applying the free-carrier plasma dispersion effect into a MZI design

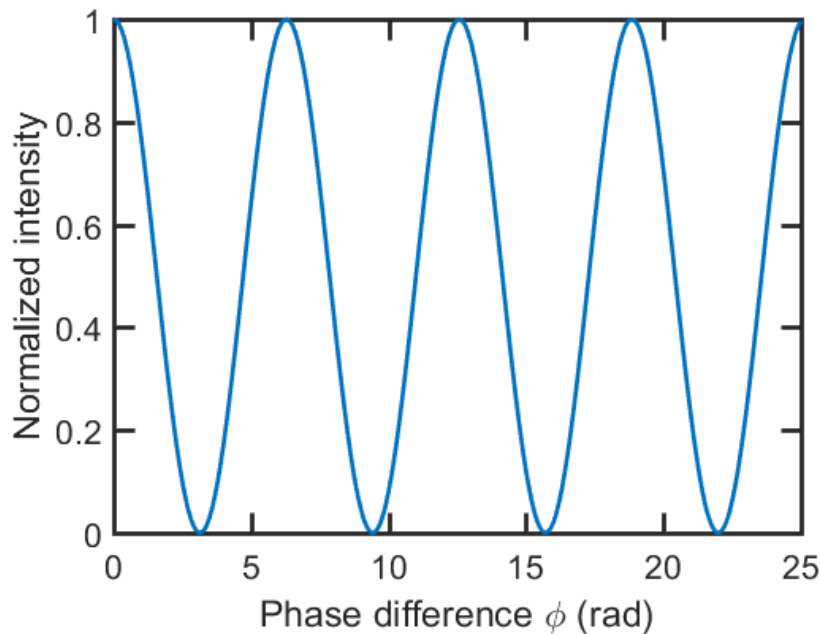


Figure 4.3: Normalized transfer function of a Mach-Zehnder interferometer.

to realize electro-optic modulation, namely the Mach-Zehnder modulator (MZM). In this case, the phase difference between two identical arms can be written as Equation 4.10. For a 2 mm long phase shifter, the required effective refractive index difference for a π -phase shift at $1.55 \mu\text{m}$ is around 3.9×10^{-4} . Considering a 2 mm MZM with two identically long phase shifters, a small change on the effective

refractive index can induce a large transmission difference. Using the transfer function of MZI we know that an effective refractive index of 0.00002 will result in a transmission variation of around 0.03 dB, 0.0002 will result in a transmission variation of around 3.2 dB. On the other hand, if assuming the two arms are identically doped, namely they have an identical effective refractive index at a specific wavelength, an arm length difference will induce phase variation as well. For example, if the effective refractive index is 2.5, then a difference of 100 nm between two arms at 1.55 μm will induce a transmission variation of 3.3 dB. Since the smallest feature size of the nowadays fundaries is generally 60 nm, a relatively strong phase difference between two arms can not be eliminated. This sensitivity will strongly affect the performance of a MZM.

$$\Delta\varphi = \Delta\beta z = \left(\frac{2\pi}{\lambda_0} \Delta n_{eff}\right) z \quad \text{Equation 4.10}$$

4.3 Different modulation schemes

The simplest modulation that can be employed to the above-mentioned 1×1 MZI is the 2-level amplitude shift keying and a typical format is the on-off shift keying (OOK). For the commonly used photodetector, if the detected optical intensity of the reconstructed signal is higher than a defined value, a digital '1' is received, otherwise, a digital '0'. Another widely used modulation scheme in optical communication is phase shift keying (PSK) within which the coherent binary PSK (BPSK) is a typical one. The two levels of BPSK have different phases and generally they are 0 and π but with the same frequency and the same signal amplitude. The BPSK signals can be graphically represented by a signal constellation in a two-dimensional coordinate system like shown in Figure 4.4. In general, the modulator

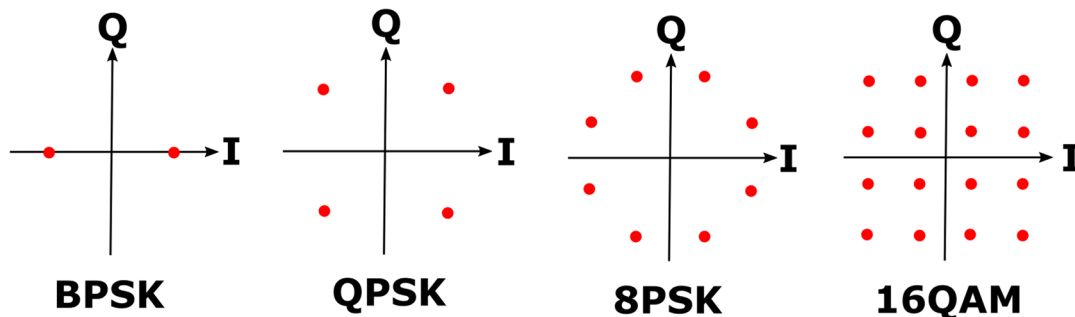


Figure 4.4: Constellation diagrams of different formats in the complex plane: BPSK, QPSK, 8PSK and 16QAM.

has a signal source like an oscillator (corresponds to laser carrier in optical communication) and a bipolar data source (corresponds to a phase shifter in optical communication). By multiplexing the two signals, the modulated signal is generated. For the demodulator, a coherent receiver will be introduced, which also allows extracting data encoded by manipulating the frequency and polarization apart from the phase. In this way, the symbol spacing is enhanced compared with the OOK scheme. The next higher level scheme is the quadrature phase shift keying (QPSK). As can be seen, there are four constellation points on the I-Q plane where all the symbols have the same signal amplitude but with a phase difference of $\pi/2$. Thus, two bits per symbol are realized. With halving the phase difference between two adjacent symbols further ($\pi/4$), an eight level PSK is obtained, namely the 8PSK as shown below. If modulating both the amplitude and the phase of the signal, more bits can be encoded onto one symbol which is referred to as multilevel quadrature amplitude modulation (m-QAM). The constellation diagram of 16-

QAM is shown as an example. As can be observed, there are three different signal amplitudes and 12 phase levels resulting in four bits per symbol.

By using more advanced modulating scheme, the transmission speed can be enhanced dramatically. The above mentioned formats are widely used in the communication field while each has a slightly different dominant market. For example, the BPSK is dominantly adopted in commercial systems applied in submarine links. In comparison, the QPSK is mainly used in commercial systems for long-haul terrestrial systems. The more advanced 16QAM is mainly for metropolitan and regional networks [74]. By employing these advanced modulation formats, the transmission speed was continuously increased [75][76][77] in the past years. Nevertheless, in this thesis, the OOK modulation format is adopted for the purpose of prototype verification. In the future, a more advanced modulation format will be introduced to improve the transmission bandwidth.

4.4 Simulation flow of the pn phase shifters

The rib waveguide is widely used in the modulator design which is introduced in the second chapter. In practice, the doping technique is nonideal so that the doping profile within a rib waveguide is not homogeneous ideally. Most often the doping profile is Gaussian-like along the x- and y- direction of the cross section of a doped rib waveguide. On the other hand, the profile of the depletion region is not inerratic regular either and it varies with the applied voltage. To know the phenomenon well, a numerical simulation software is required. In this thesis, three kinds of software are involved in the pn phase shifter flow which are the Technology Computer Aided Design (TCAD) tool Synopsis Sentaurus, COMSOL Multiphysics and MATLAB. Sentaurus TCAD is a professional software for semiconductor physics simulation and is good for solving the poisson's equation. COMSOL is good for multiphysics simulation and is also for the waveoptics simulations.

Since the 3-D simulations call for quite a lot of resources, 2-D simulations are uniformly conducted in this thesis. A full simulation flow for the pn phase shifter is shown in Figure 4.5. For the first step,

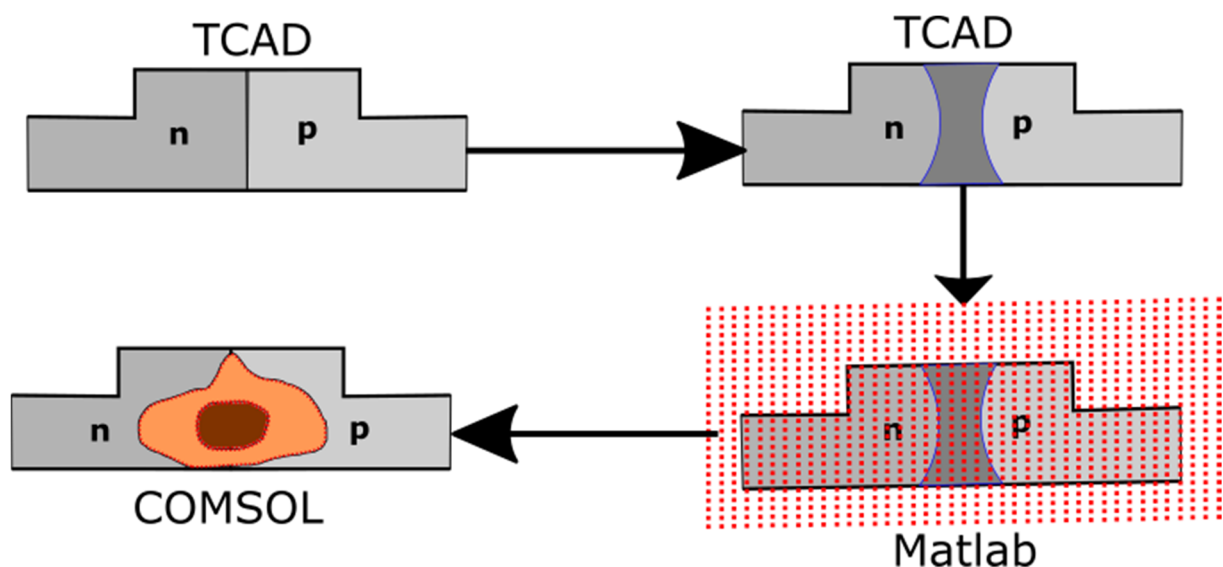


Figure 4.5: Simulation flow of a pn phase shifter.

the geometry of a designed rib waveguide is defined in TCAD, which is completed in the Sentaurus structure editor (SDE) interface. Apart from the dimensions of the cross section of a phase shifter, the

doping profiles are also defined in this step. Also, an electric contact is added to a proper position for the next step. Finally a meshed geometry is generated as required.

The next step for the simulation is the electrostatic calculation in the interface SDEVICE. In the 'File' module, on one hand the necessary files to be imported is stated, including the geometry and mesh files generated in the SDE interface etc.; on the other hand, the output data can also be written to a specified file. Further, in the 'Electrode' module, the parameter for the electrical contact was defined. An electrode model connects the electrodes which have been defined in the device file for virtual simulation electrodes, at which high voltage can be applied and the current can be measured. The user can sweep the applied voltages onto these defined electrods. The 'Physics' module is very important, all the required physical phenomena can be included in this module. It is worthwhile to mention that one can also define a general physics module for the entire device geometry and an additional physics module for a specific part. For example, in the simulation of the radiation effect of a pn junction, one can define a general physics model for the entire geometry, for example defining the ambient temperature. One can also define a physics model for an individual material, for example silicon, whereas, one can define a special physics model for the radiation effect merely takes place at the interface between silicon and silicon dioxide as well. For the simulation of the pn junction, the physics in silicon has to activate the 'Fermi', 'Mobility' and 'Recombination' module as those will take place in silicon. For the radiation effect, the 'Traps' model has to be activated where a typical trap is specified by six parameters: the donor or acceptor trap, the energy level, where the energy leveled is calculated from, the concentration of the traps in the bulk, electron cross section and the hole cross section. Then in a 'Solve' module, the users define what kinds of problems will be solved in the simulation. Normally, a solution for the initial state has to be found by solving the poisson's equation for all the grid points. Based on this, one can further acquire the desired parameters for example the distribution of carrier concentrations under different applied voltages. Whereas, a precedent requirement is defining the mathematical method used in solving the problem, namely controls how the equations on the grid are solved. There are several available solvers from TCAD like Pardiso etc.. In this part, one can configure the computing mode and

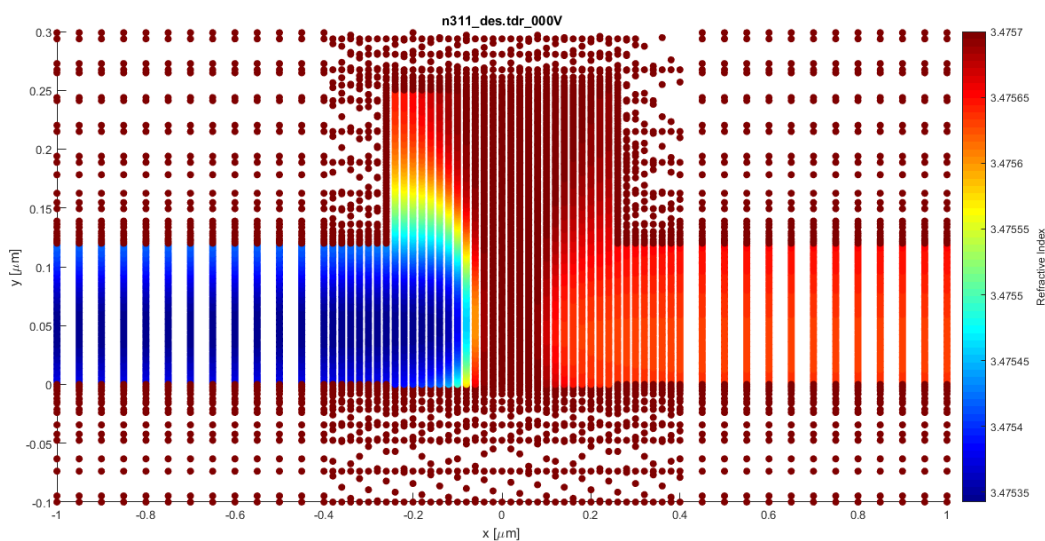


Figure 4.6: An example of the calculated refractive index profile using the MATLAB program where the data is imported from the simulations in TCAD sentaurus.

the accuracy of the solution by assigning the task to multiple CPUs and defining the number of digits, respectively. Finally, the solution will be exported into a file defined in the ‘File’ module.

The most important export files from the TCAD simulation are the carrier concentrations at different positions. Whereas, the exported files are individual results for electrons and holes, also with a data format that can not be recognized by COMSOL. In this case, an additional MATLAB program is required. In general, this program takes the exported data from the previous TCAD simulation, plots the refractive index profile using the plasma dispersion effect and exports the result as a readable file to COMSOL. An example plot of the MATLAB program is presented in Figure 4.6. With applying a higher bias voltage, the depletion region expands accordingly. As the output of this step, a calculated refractive index profile of the designed geometry is generated and will be used as an input file for the COMSOL Multiphysics.

The last step of the simulation is realized in COMSOL Multiphysics, the calculated refractive index is imported and added to the material property. In the WaveOptics model, we build a geometry corresponding to the one used in TCAD simulation and allocate the materials to corresponding parts. Then the numerical calculation will be performed in the frequency domain using the finite-element method. In this step, the propagation constants for the confined propagation modes under different applied reverse voltages and operating wavelengths can be obtained. The modulation efficiency can therefore be evaluated.

4.5 pn-phase shifter design

4.5.1 Waveguide design

In the second chapter, several types of waveguides were introduced while the two major waveguides considered in this thesis are the channel waveguides and the rib waveguides. In the used 250 nm SOI platform in the thesis, the core is 250-nm-thick silicon, the top and bottom claddings are usually silicon dioxide resulting in a refractive index difference over two. For this reason, the light is well confined in the channel waveguides since they are surrounded by SiO₂ at every side, resulting in a high optical confinement and low cross-talk with the waveguides in its vicinity. However, the channel waveguides may suffer from higher scattering loss due to the side-wall roughness from the manufacturing [78]. In comparison, the rib waveguide is formed by placing a channel waveguide onto a slab. Such kinds of rib waveguides will have lower light confinement that a larger separation of around 2 μm to adjacent waveguides is required. However, the optical mode is less intense at the side-walls and thus less affected

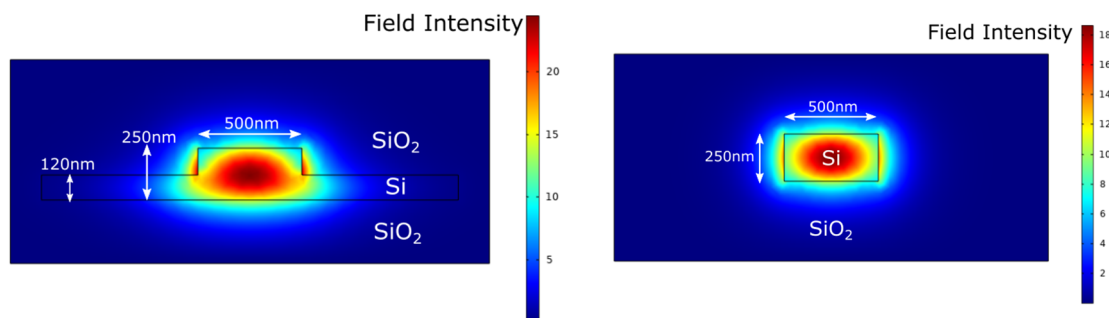


Figure 4.7: Optical modes at 1550 nm in the rib waveguide and channel waveguide for TE polarization.

by the roughness of the sidewalls. The simulated fundamental mode profiles (TE polarization) of a channel waveguide and a rib waveguide are illustrated in Figure 4.7.

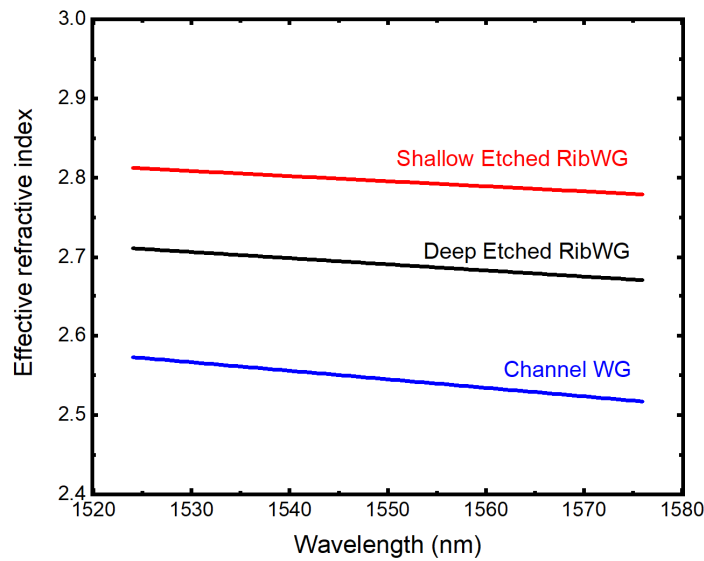


Figure 4.8: Simulated effective index of the deep etched and shallow etched rib waveguide and the channel waveguide.

On the other hand, different types of waveguides also have significantly different effective refractive indices. Using a $500 \text{ nm} \times 250 \text{ nm}$ channel waveguide, and two different rib waveguides used in this thesis (the geometries of waveguides can be find in the later section) as simulation models, their simulated effective refractive indices are shown in Figure 4.8. As can be observed, the rib waveguides have a larger effective refractive index than channel waveguides. With a shallow etching depth, the effective refractive index can be improved further. On the other hand, the channel waveguide is most dispersive (the effective refractive indices are quite different at different wavelengths) and the shallow etched rib waveguide is the least dispersive in comparison. In this case, the group index is usually introduced to describe the dispersion effect as described in Equation 4.11 [79].

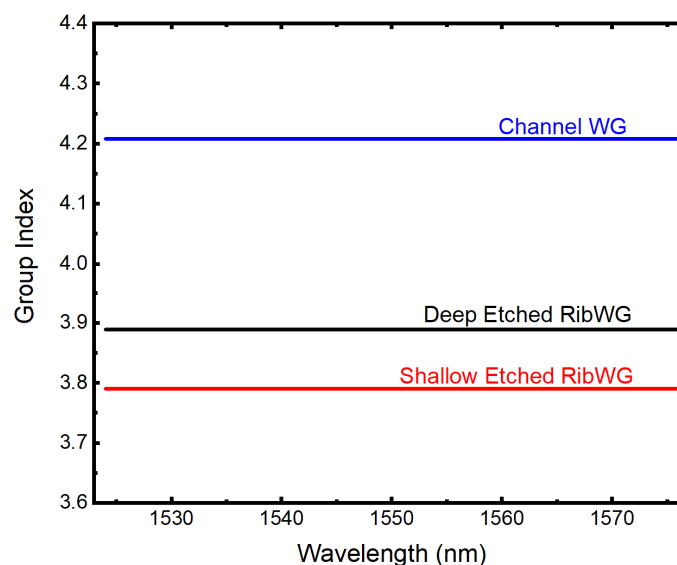


Figure 4.9: Simulated group index of the silicon rib waveguides and the channel waveguides.

Based on Equation 4.11 and the simulated effective refractive index of the three waveguides, the group index of the abovementioned three waveguides can be calculated as well, the results are shown in Figure 4.9. The rib waveguides have a smaller group index in reverse and they show a slightly decreasing tendency along with increasing the wavelength. The shallow etched rib waveguide has an even smaller group index compared to the deep etched rib waveguide.

$$n_g = n_{eff} - \lambda_0 \frac{dn_{eff}}{d\lambda_0} \quad \text{Equation 4.11}$$

Due to the dispersion effect of these waveguides, it is possible to introduce one more degree of freedom into the MZI design. Normally, the MZI is named symmetric if its two arms are physically identical. However, they can also be designed asymmetrically with setting different lengths to two arms. Such an imbalance can introduce additional phase shift in one arm with respect to the other one. In consequence, the transfer function becomes periodic with respect to the operating wavelength and results in the free spectral range (FSR, in meter) that can be expressed as Equation 4.12 [80] where ΔL is the path difference between two arms, n_g is the group refractive index and λ is the wavelength to calculate n_g . According to the required FSR, the length difference between the two arms can be designed accordingly. Therefore, asymmetric MZIs are helpful to the designer to get an appropriate operating point with the help of the measured transmission spectrum.

$$\text{FSR} = \frac{\lambda^2}{n_g \Delta L} \quad \text{Equation 4.12}$$

4.5.2 Different profiles of pn junctions

Even though uniformly using the identical rib waveguide geometry, the resulted pn junctions can be very different depending on the doping requirements. There are several different types of modulators with different types of pn junctions featuring different ways of changing the free carrier concentrations. Three most popular types are carrier accumulation, carrier injection and carrier depletion. A basic structure of a carrier injection modulator is based on a pin diode. As shown in Figure 4.10, the central

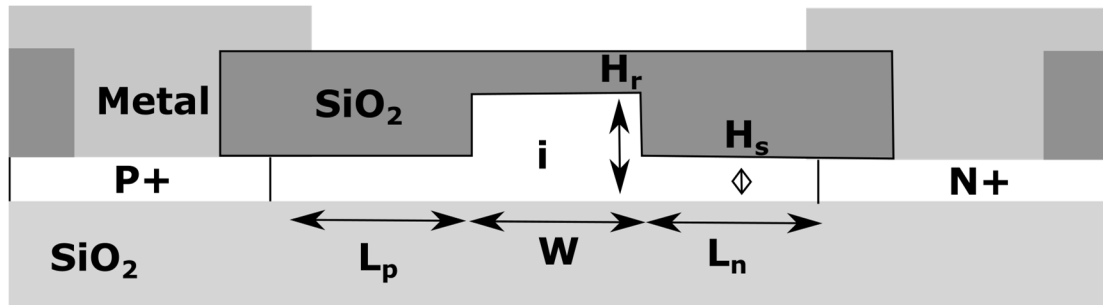


Figure 4.10: Cross section of a carrier-injection pin diode.

part of the diode is intrinsic silicon. Two slab regions besides the ridge are p- and n- doped, respectively. Once the diode is forward biased, holes and electrons can be injected into the waveguide region resulting in a reduction of the refractive index so that the phase of the propagating light inside is changed. Although the modulators based on carrier injection effect improved a lot in the past, their modulation

bandwidth is ultimately limited by the carrier lifetime in this scheme so that most of the early-stage modulators featured MHz-order modulation bandwidth [81][82][83][84]. One effective method proposed to overcome the drawback was employing a pre-emphasis driving signal. By using such a technique, modulators with a bandwidth of Gbit/s were reported [85][86]. Nevertheless, this solution will introduce quite a lot of complexities in driver electronics design, the electronics should be upgraded significantly at each improvement of the modulation bandwidth.

The carrier accumulation method can avoid the limitation of the minority carrier lifetime to achieve a higher modulation bandwidth. As depicted in Figure 4.11, the p- and n- regions are isolated by a thin

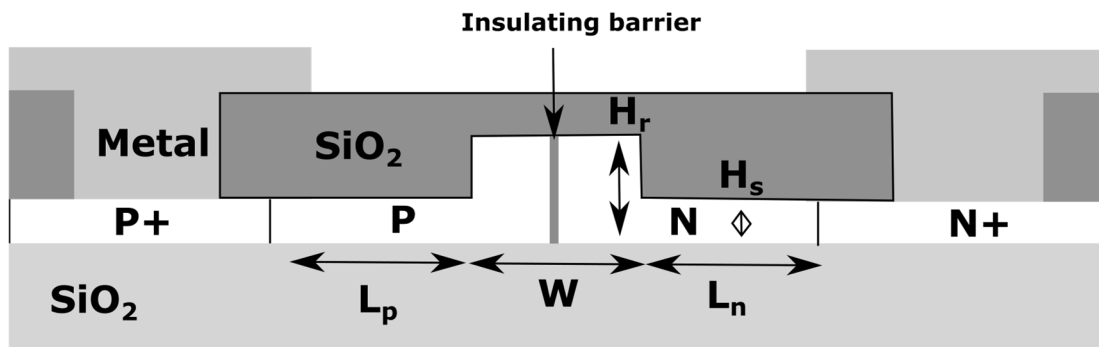


Figure 4.11: Cross section of a carrier-accumulation pn diode.

insulating layer which is located in the middle. When the diode is biased, free carriers will accumulate on either side of the insulating layer. Accumulated carriers reduce the refractive index of silicon as well and finally realize phase modulation. In comparison to the carrier injection structure, the carrier density changes locally in carrier accumulation structure. Therefore its efficiency is higher and the required dimension is smaller. It is worthwhile to mention that increasing the thickness of the insulation layer can help to improve the bandwidth while on the other hand it also lowers the phase modulation efficiency. Several example modulators with a bandwidth above 1 Gb/s were reported [87][88], while the fabrication of this type of modulator is much more complex than carrier injection type modulators due to the insulating layer in the middle. How to construct a thin insulating layer while forming the entire waveguide structure with the merits of low loss and good electrical properties is a real challenge.

Carrier depletion is also a technique that is not limited by the minority carrier lifetime and can therefore potentially achieve a high bandwidth. As depicted in Figure 4.12, two p- and n-doped regions

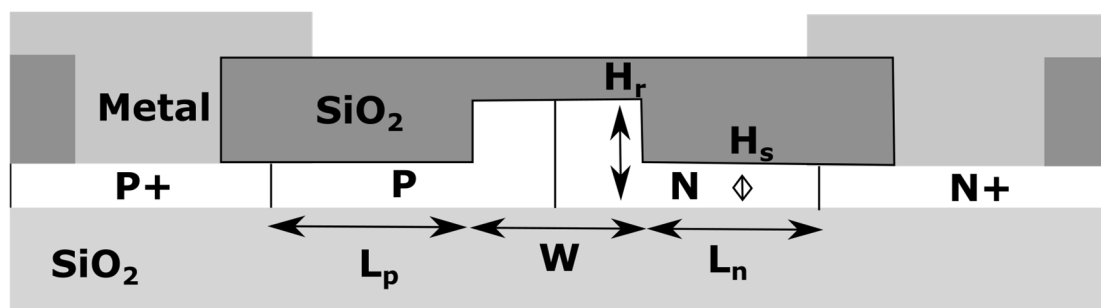


Figure 4.12: Cross section of a carrier-depletion pn diode.

are brought into contact to form a depletion region. The propagating light is dominantly confined around the formed pn junction. In general, this technique is based on reverse biased pn junctions. With applying a reverse bias, the depletion region widens, reducing the carrier density within the waveguide and

therefore increasing the effective refractive index which realizes the phase modulation. Similar to the carrier accumulation concept, this method also enables small devices since it features localized free carrier density variation. The phase efficiency of this concept is highly dependent on the doping concentration of the p- and n- region and also the junction profiles and location with respect to the waveguide, which will be introduced next. More importantly, the modulation bandwidth is strongly influenced by the transmission line design instead of the pn phase shifter design. Based on the analysis above, the carrier depletion type is adopted in this thesis.

Although commonly based on carrier depletion, the diodes can still be designed differently according to the doping arrangements. In general, they are classified into lateral, vertical and interdigitated three types according to the direction of pn junction as shown in Figure 4.13. The lateral pn junction has two

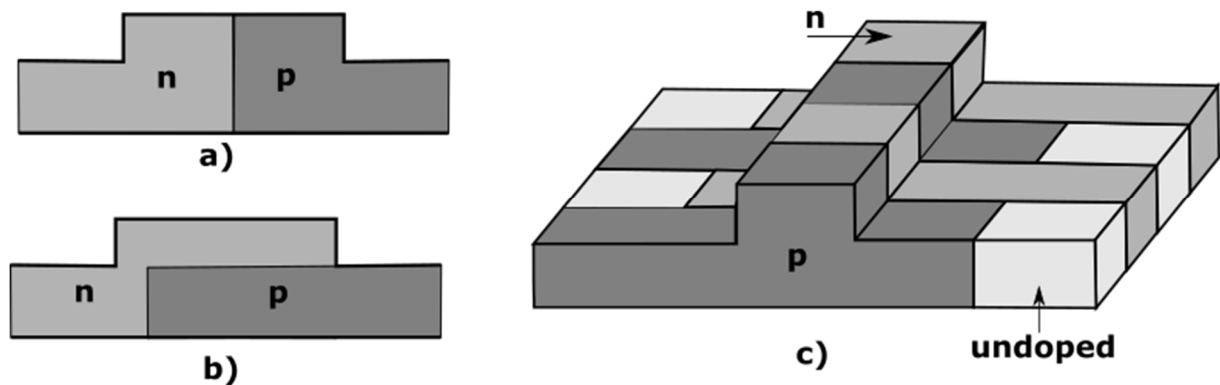


Figure 4.13: Different geometries of pn junctions: lateral, vertical and interdigitated.

doped regions in the left half and the right half with a formed depletion region in the middle. For lateral pn junctions, several aspects can affect its efficiency: the junction line position, the doping concentration and the slab thickness (will be discussed in the later section). The lateral pn junction is a popular and easy-to-realize doping scheme in most foundries. In comparison, the vertical pn junctions feature a much longer junction line since a common rib waveguide has a ridge width of 500 nm. In this case, it has a greater overlap between the modulation region and the optical mode therefore resulting in a higher modulation efficiency. However, this kind of pn junction requires unique fabrication techniques, which are not available in many foundries. From enlarging the overlap between the optical mode and the modulation region point of view, an interdigitated pn junction would be the most beneficial to improve the modulation efficiency. As seen in Figure 4.13c), p- and n- doped regions are aligned interdigitally to form multiple pn junctions. Therefore the modulation efficiency is determined by the density of the junctions along the length of the modulator. Because the junctions completely overlap with the optical mode, it is shown that the $V_{\pi}L$ can be 40% lower than that of a lateral-pn-junction modulator [89]. However, on one hand the required doping technique for interdigitated junctions is quite complex. On the other hand, the interdigitated junctions have a much higher capacitance compared to the other two types since the capacitance is highly determined by the overlap length. Also, this makes the driver design more difficult. To sum up, the lateral pn junctions are easy to fabricate with a reasonable bandwidth. For this reason, this thesis will adopt lateral pn junction designs for the intergrated transmitter.

4.5.3 Design of lateral pn junction based phase shifters

Figure 4.14 is used to describe the geometry of the phase shifter design. As can be seen, the p and n doped regions are dependent on the position of the doping reference line. If the reference line is set at

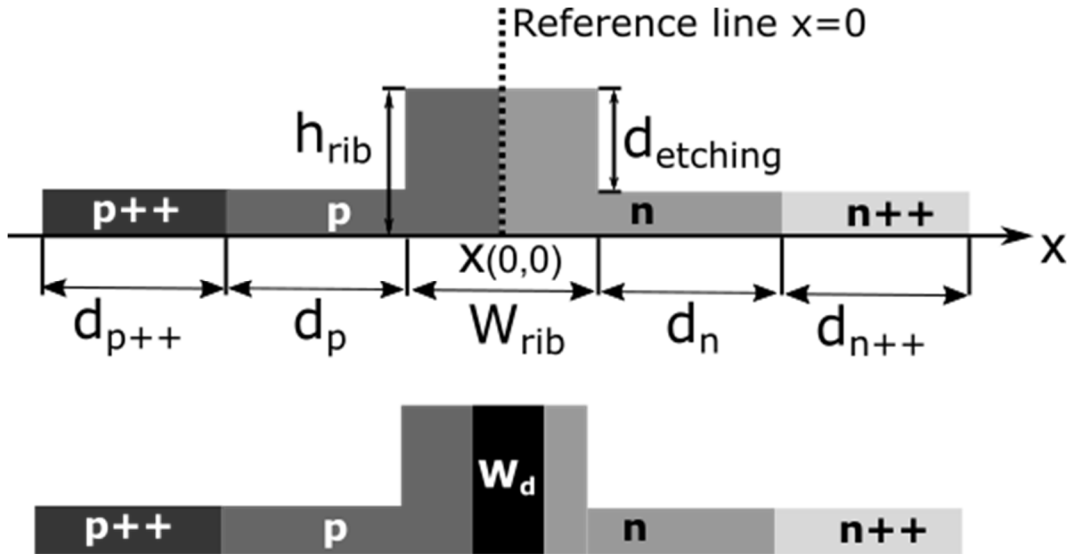


Figure 4.14: Cross section of a pn phase shifter and the generated depletion region.

$x=0$, the rib region will be doped symmetrically with respect to the middle line. Since the entire design is on the 250 nm SOI platform, h_{rib} is 250 nm, W_{rib} is 500 nm. The length of the p- doped slab regions and the n- doped slab regions are set to $d_p = 1.75 \mu\text{m}$ and $d_n = 1.75 \mu\text{m}$, respectively. To enhance the conductivity for the electrical contact, highly doped p⁺⁺ and n⁺⁺ regions are also included and their lengths are $d_{p^{++}} = 7 \mu\text{m}$ and $d_{n^{++}} = 7 \mu\text{m}$, respectively. The etching depth is marked as $d_{etching}$. After doping, there will be a depletion region generated between the p- and n- doped regions with a width of W_d . With applying a larger bias voltage, the width W_d will increase. The resistance of the pn junction is composed of four parts the p, p⁺⁺, n and n⁺⁺ doped regions, and their conductivity can be calculated analytically with the assumption of homogeneous doping concentration. However, for a Gaussian-like doping profile, the calculation is complex and can only be solved numerically. The electrical conductivity is a function of temperature, dopant concentration and the carrier's mobility. On the other hand, the carrier's mobility is also a function of temperature and the dopant concentration. At room temperature, all the doped atoms are assumed to be ionized. Since the number of intrinsic carriers is small compared to the dopant concentration, it can be assumed that the electrical conductivity is dominantly contributed from the dopant concentration, namely the conductivity can be estimated by using relations Equation 4.13 and Equation 4.14 [90], where n and p are the corresponding dopants' concentration, μ_e and μ_p are the electron mobility and hole mobility, respectively, and q is the electron charge, 1.602×10^{-19} C. General used data for μ_e and μ_p are $1350 \text{ cm}^2/\text{V}\cdot\text{s}$ and $480 \text{ cm}^2/\text{V}\cdot\text{s}$, respectively [91]. An estimated resistance for each individual region can be obtained by Equation 4.15 [91]. Normally the resistance is merely tens of Ohms, the accurate value can be supplied by the foundry or be measured by unique means. If assuming the pn depletion region as a parallel-plate capacitor, the capacitance can be calculated by Equation 4.16 [91], where $\epsilon_0 = 8.854 \times 10^{-12} \text{ C}/(\text{V}\cdot\text{m})$ is the vacuum permittivity and ϵ_s is the relative permittivity of the material (for silicon $\epsilon_s = 11.8$), A is the urface area of the parallel plates and d is the distance between two plates. Normally, the capacitance is quite small, in the order of multiple pF/m. Therefore, the intrinsic electrical bandwidth is usually tens of GHz or even hunderds of GHz, not the dominant limitation for the transmission bandwidth. In comparison, the transmission bandwidth can usually be determined by the transmission line design and the driver circuits.

$$\sigma \cong n|e|\mu_e \quad \text{Equation 4.13}$$

$$\sigma \cong p|e|\mu_p \quad \text{Equation 4.14}$$

$$R = \rho \frac{l}{A} = \frac{l}{\sigma A} \quad \text{Equation 4.15}$$

$$c = \frac{\epsilon_0 \epsilon_s A}{d} \quad \text{Equation 4.16}$$

The modulation efficiency of the given modulator geometry is easy to be carried out. For the MZM designs here, the etching depth is set to be 130 nm, namely the parameter $d_{\text{etching}} = 130 \text{ nm}$. To compare the effects induced by the doping reference line offset, the offset is set to -0.15, -0.1, -0.05, 0, 0.05, 0.1 and 0.15 in μm . Then the phase shifters are simulated via the aforementioned simulation flow. The simulation results are shown in Figure 4.15. The modulation efficiency is proportional to the phase difference between two arms, a bigger effective refractive index difference corresponds to a larger phase shift, namely a higher modulation efficiency. As can be seen, when the junction line offset is set to

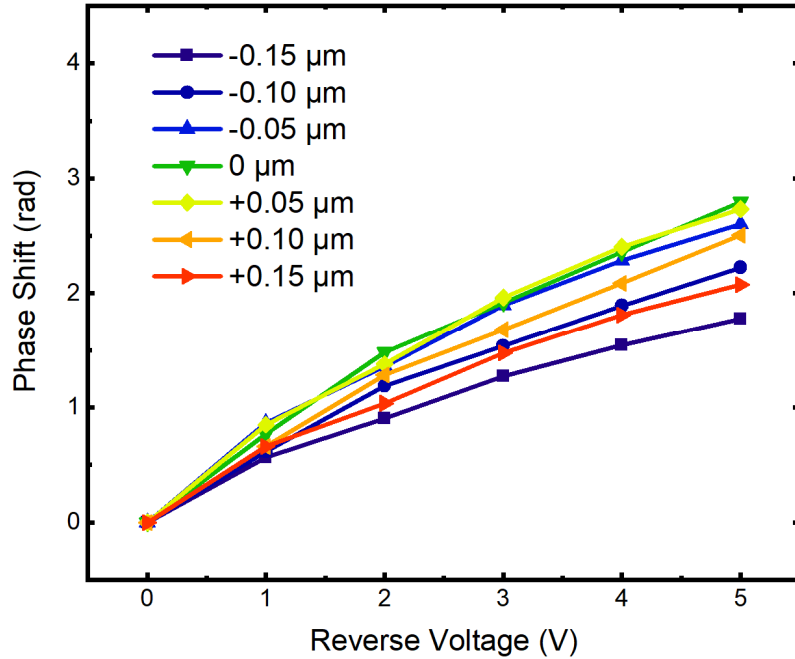


Figure 4.15: Simulated phase shifts of the 3-mm phase shifters with different junction line offsets.

$x = 0 \mu\text{m}$ or $x = +0.05 \mu\text{m}$, the modulation efficiency is higher than the other configurations. The modulation efficiency difference between $x = 0 \mu\text{m}$ and $x = +0.05 \mu\text{m}$ is very small and in the region of the foundaries' accuracy so that the doping reference line in this thesis is uniformly set to $x = 0 \mu\text{m}$.

In some cases, even though the doping reference line is set to $x = 0 \mu\text{m}$, there can be a deviation existing on both sides due to the doping technique. In consequence, a pin phase shifter is generated by accident instead of the PN phase shifter. To investigate the influence, another set of simulations were made by setting the widths of the i region to be 0 nm, 10 nm, 20 nm, 30 nm, 40 nm, 50 nm and 60 nm respectively. The simulation results are presented in Figure 4.16. With having an i region in the pn phase shifter, the modulation efficiency is decreased accordingly. The wider the i region is, the lower the modulation efficiencies become. Nevertheless, the efficiency does not deteriorate too much.

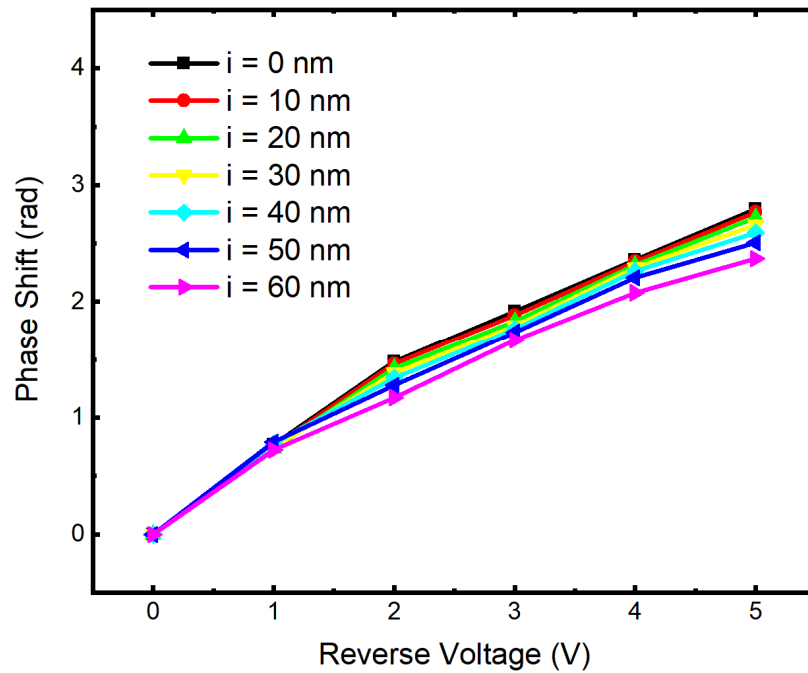


Figure 4.16: Simulated phase shifts of the 3-mm phase shifters with different widths of the i regions.

The thickness of the slab (determined by the etching depth) is another important factor affecting the modulation efficiency. As shown in Figure 4.17, a set of simulations were carried out with varying the

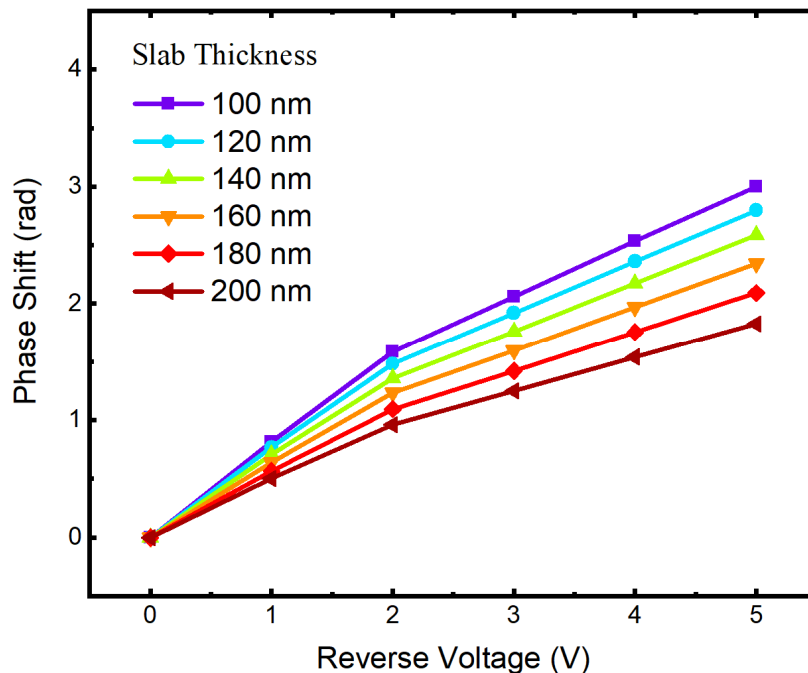


Figure 4.17: Simulated phase shifts of the 3-mm phase shifters with different slab thicknesses.

slab thickness from 100 nm to 200 nm. With increasing the slab thickness, the modulation efficiency decreases significantly. To achieve high modulation efficiency, a deep etching is preferable and an etching depth of 120 nm is adopted for the deep etched type modulators in this thesis. Whereas, shallower etched modulators have advantages for radiation hardness, which will be introduced in a later

section. Nevertheless, it is worth mentioning that when the slab thickness is increased to 200 nm or even thicker, higher order modes can be excited.

Apart from the parameters illustrated above, the key parameter affecting the modulation efficiency is the doping concentration. To make the comparison easier, a reference doping concentration of the p- and n- regions is set and the value for them are 7×10^{17} and 5×10^{17} , respectively. This combination is referred to as 1.0 doping in the simulation. In the meanwhile, 0.5 doping means both the p- and n- doping are halved. Similarly, the doping concentrations of the other several sets can be known. As shown in

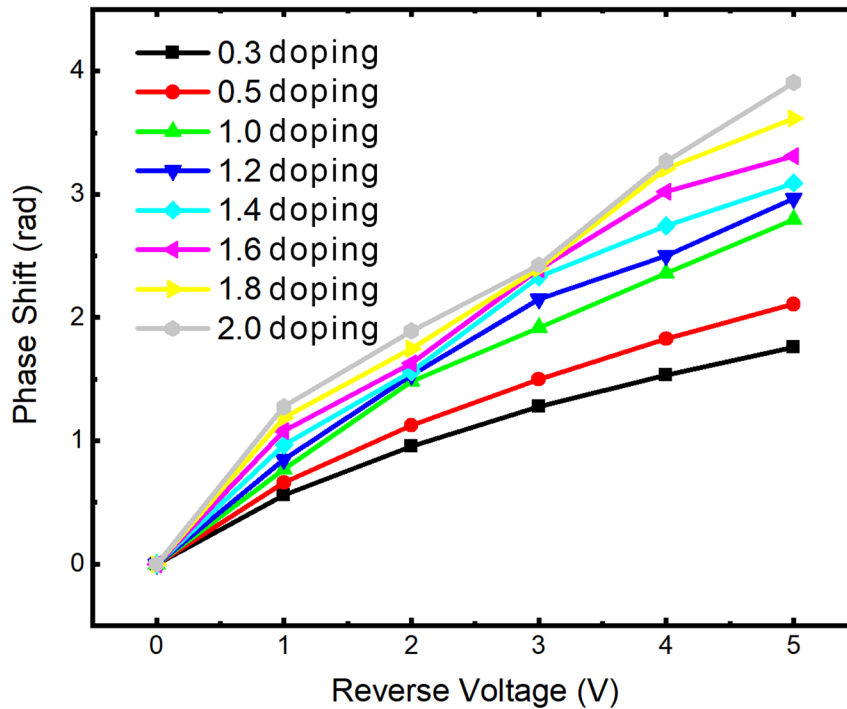


Figure 4.18: Simulated phase shifts of the 3-mm phase shifters with different doping concentrations.

Figure 4.18, increasing the doping concentration can dramatically increase the modulation efficiency. Fitting the simulation results with a polynomial of the 4th order, the derived $V_{\pi}L$ for the 1.0 doping is 1.22V·cm. However the attenuation increases as well and one has to make a tradeoff. In this thesis, the reference doping (namely the 1.0doping) is uniformly adopted.

4.5.4 A radiation-hardened modulator design

It is known that the performance of CMOS-based electrical components will degrade under the influence of irradiation and several widely studied effects are: the single event induced latchup effect [92], the single event upset effect [93] and the single event burnout effect [94]. Similarly, the radiation also induces damages to optical components especially the active ones, according to the research from CERN [95][96][97]. A radiation hardened design inspired by the abovementioned researches is also included in this thesis although the radiation effects are not the focus of this thesis.

In general, the radiation sources can be divided into charged particles and uncharged particles. The radiation investigations on the modulators can also be divided into these two types. In [96], the authors designed MZMs using a 300 nm CMOS platform. The designed phase shifter features a rib height of 220 nm, a slab height of 100 nm, a rib width of 400 nm and an arm length of 2.183 mm. The MZM are

exposed to both neutron (non-ionizing) and X-ray (ionizing) radiation where the fluence of the neutron source is 1.2×10^{15} n/cm², the ionizing dose of the X-ray source is 1.3 MGy. For both tests, the leakage currents increase a lot during the test. However, a fraction of the radiation-induced damage anneals for both tests indicating that the increase of the leakage current is dose-rate dependent. On the other hand, the non-ionizing radiation doesn't degrade the modulators' performance remarkably. In comparison, the ionizing particles make a stronger effect that the phase shift decreases when the total ionizing dose is merely several hundreds of kGy. If the total ionizing dose exceeds about MGy, the modulators stop working. In [95], the authors further increased the fluence to 2.3×10^{15} n cm⁻² to make the tests for these MZMs while the total ionizing dose still remains at 1.3 MGy. A similar test result was obtained as well. MZMs are promising options for the next phase upgrade of LHC while the ionizing radiation can significantly lower the modulators' performance.

Based on the first stage investigations in [95] and [96], the researchers at CERN conducted in-depth investigations [97]. They designed two customized modulators with different slab thicknesses. To be more specific, the waveguide rib width and height are 450 nm and 220 nm respectively, the slab etching depths of two kinds of modulators are 160 nm and 70 nm, respectively. The MZMs have an arm length of 1.9 mm with a path length difference of 30 μ m between them. In addition, a high doping concentration of around 10^{18} cm⁻³ is expected for the rib region since such a design will be more radiation resistant although the optical loss will be higher [98]. The irradiation tests were also conducted in a constant dose of 1.3 MGy with a peak X-ray energy of 10 keV. Two types of modulators behaved differently: the phase shift of the deep-etched device was reduced to 50% of its preirradiation value at a total ionizing dose of merely 70 kGy with -1 V bias voltage. In reverse, the phase shift of the shallow-etched modulator increases at first and starts to degrade above 500 kGy, and it falls back to the preirradiation value at the end of irradiation at 1 MGy with -3 V bias voltage. Apart from the radiation test, low-temperature operation was compared with the room-temperature test indicating that the low-temperature environment can improve the modulators' radiation resistance. According to this study, the customized shallow-etched modulator is a promising solution for the irradiated detector instrumentation.

Since this thesis aims at designing a generic optical transceiver which is also suitable for a radiating environment, a radiation hardened modulator design is also included in the fabricated photonic chip. The etching depth is the same $d_{\text{etching}} = 70$ nm while the silicon layer is thicker, 250 nm. As shown in Figure 4.17, the price for a radiation hardened modulator is a slightly lower modulation efficiency. Since the radiation hardness has been proved by CERN group, this thesis focuses on the DC and RF characteristics of the radiation hardened modulators.

4.5.5 The electrode design and its 3-dB frequency

In the electrical design, a distributed element analysis (or transmission line effect) is required for a long device instead of a lumped element analysis. A common rule of thumb is when the length of the device is longer than $0.1 \times \lambda_m$ where λ_m is the wavelength in the guiding material, it has to be treated as transmission line. The parameter λ_m can be calculated by Equation 4.17 where c_0 is the speed of light in the vacuum, ϵ_{re} is the relative permittivity of the guiding material. For a microwave with a frequency of 30 GHz, and if the device is longer than 1 mm, the distributed element analysis or transmission line effect have to be carried out.

$$\lambda_m = \frac{c_0}{f\sqrt{\epsilon_{re}}} \quad \text{Equation 4.17}$$

If considering the medium is composed of two different layers and the microwave travels half in the substrate and half in the air, then we can roughly use their arithmetical average to estimate the actual permittivity, namely $(\epsilon_{\text{air}} + \epsilon_{\text{Si}})/2$. However, this is just a very rough estimation, an accurate result should be calculated by a field solver.

In general, the carrier depletion based modulators are designed to be relatively long to achieve low driving voltage. In consequence, the transmission line effect has to be considered. There are two popular types of electrode designs for the MZM which are the coplanar waveguide (CPW) and coplanar strips (CPS) as shown in Figure 4.19. The key design parameters of CPW transmission lines are the width of

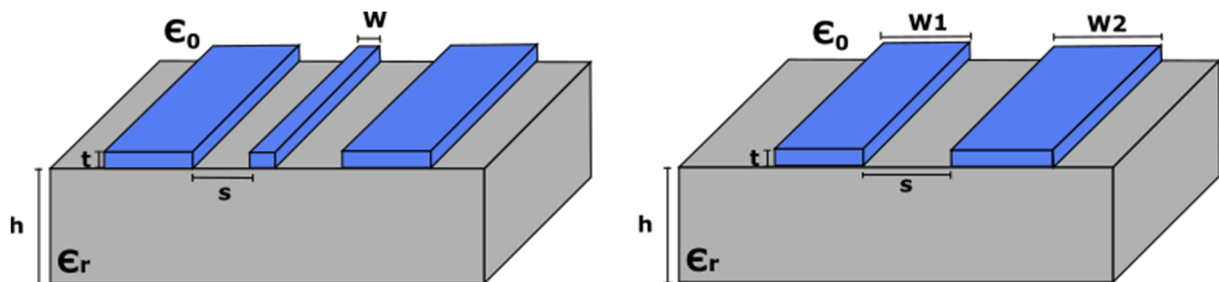


Figure 4.19: Structure of the coplanar waveguide transmission line and the coplanar strips transmission line.

the signal trace W and the width of the gaps between the signal trace and ground traces. Ideally, the ground trace should be infinitely wide while in practice it can be designed to be several times wider than the signal trace. In comparison, the key design parameters of CPS are the widths of the signal trace and the ground trace and the gap width between them.

The signal trace of the CPW transmission line is shielded by the two ground traces, therefore external interference is largely avoided and also the RF signal is prevented to affect components nearby. Normally, CPS has a higher cutoff frequency, while it's easier to be affected by the surrounding RF signal. Therefore one should retain enough space around the transmission line. Due to their characteristics, CPS are usually used as a differential (balanced) transmission line while CPW as unbalanced transmission line. In a CPW, the potential reference of the signal trace is the ground adjacent to it. In a balanced GSSG (ground-signal-signal-ground) transmission line, the potential reference is with respect to the two signals.

The MZM can be driven in three different schemes which are single drive, dual drive and single-drive push-pull (also called series push-pull) respectively. The dual drive modulator has two inputs for RF signal sources, each RF signal is fed into one arm which are biased individually. With reasonable RF signals and bias voltages, two arms can change the phase into reverse directions, which can approximately halve the driving voltage. The single drive modulator is simpler than the dual drive configuration, that only one arm of the modulator is driven by a RF signal, which results in halved efficiency therefore an approximately doubled driving voltage. In comparison, the single drive push-pull scheme is composed of two diodes, only one drive source is needed while two arms are biased to achieve identical effects of dual-drive modulators. With this driving configuration, the driving voltage is also halved and is also beneficial to remove the modulator chirp effect [99][100]. In this thesis, a CPW

transmission line is adopted to achieve a good shielding effect. Two diodes have a common electrode for RF input, the push-pull effect is achieved by biasing two diodes symmetrically. The SPP (series push-pull) configuration has the merits of small footprint, lower microwave loss and the possibility of operating at high bias voltages with negligible static power consumption. The key design parameters of

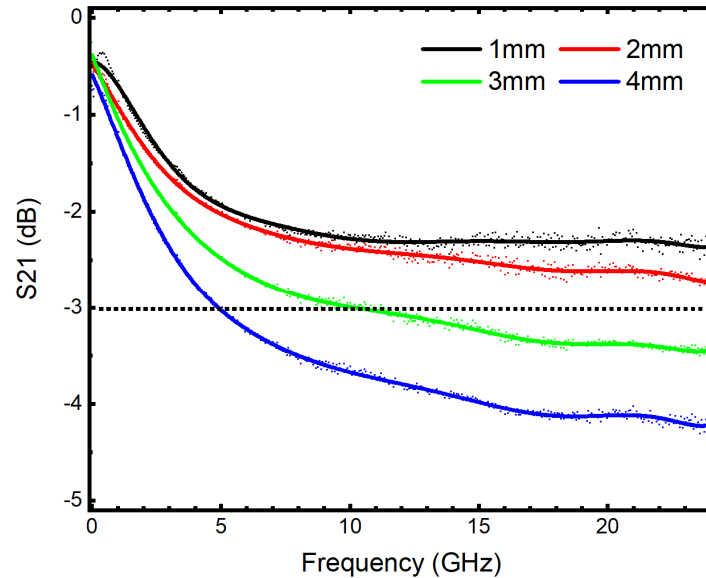


Figure 4.20: Scattering parameter measurement of the electrodes with different lengths.

the CPW are $w = 30 \mu\text{m}$ and $s = 5 \mu\text{m}$, respectively. The thickness of the electrode, $t = 0.5 \mu\text{m}$. The entire chip has a thickness around $750 \mu\text{m}$.

The characterizations of transmission lines were carried out for the convenience of discussion, shown in Figure 4.20. The scattering parameter measurements were carried out for the electrodes without the modulator loaded. The measurement were made by using a vector network analyzer (VNA) and the measurement setup will be explained in the next section. As can be seen, the cutoff frequency of the electrodes increases with decreasing lengths of the electrodes. With fitting the measured results with the ninth order polynomials, the 3-dB cutoff frequencies can be derived and they are 4.9 GHz and 10.2 GHz for the 4 mm and the 3 mm electrodes. Both the capacitance and the impedance mismatch between the transmission line and the termination resistor are factors limiting the transmission bandwidth [101]. In comparison, the 3-dB cutoff frequencies of the 1 mm and 2 mm electrodes are larger than 24 GHz, beyond the measurement range of our VNA. The goal of this thesis is to realize 10 Gb/s transmission per modulator, the length of the electrodes can be selected from 1 mm to 3 mm.

4.5.6 Setup for the steady-state and dynamic response measurements of MZMs

The characterization of the designed devices include DC (also called the steady-state modulation efficiency) and AC characterizations, where the AC characterization covers both the small signal characterization and the complete data transmission. The DC characterization is simpler with respect to the AC characterization and the measurement setup is depicted in Figure 4.21. The tunable laser source (LS) Agilent 81689A is fed to a manual polarization controller (Pctl). After achieving the required TE polarization, the optical signal is further forwarded to the device under test (DUT) (in this case is the

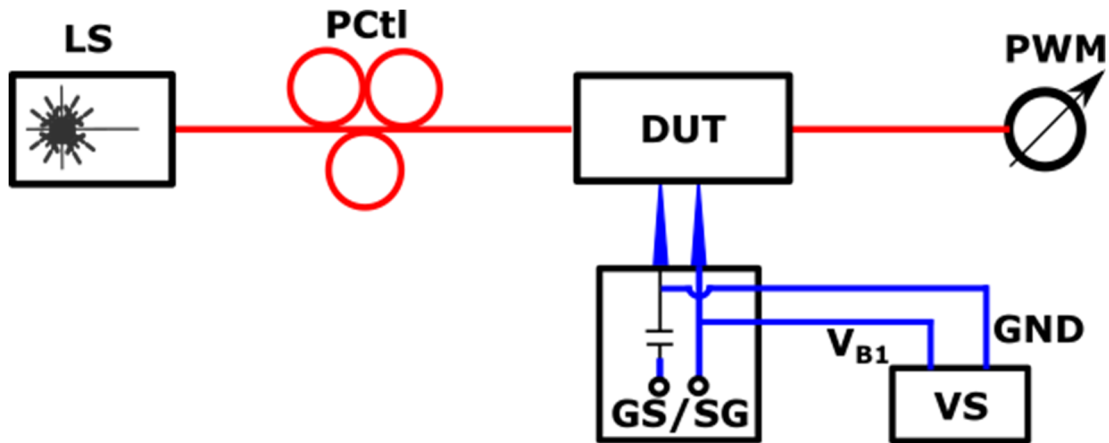


Figure 4.21: Measurement setup for the DC characterization of MZMs.

selected MZM). The required bias voltage for the modulator is provided by a voltage source (VS) ‘Keithley 2400 source measurement unit’ and connected by Picoprobe GS or SG microwave probes. Finally, the intensity of the optical signal is detected by an optical power meter (PWM) which contains an optical head and interface (Agilent 81623B and 81618A).

As aforementioned, the modulators can be designed asymmetrically long namely the two arms of the MZM have different lengths, therefore the two arms have a designed phase difference. By varying the wavelength of the optical carrier, the phase difference between the two arms will vary and result in a spectrum shifts according to the transfer function Equation 4.9. A typical spectrum can be seen in Figure 4.22. The spectrum shifts $\Delta\lambda$ from the red curve to the blue curve with a bias voltage from V_1 to V_2 . The

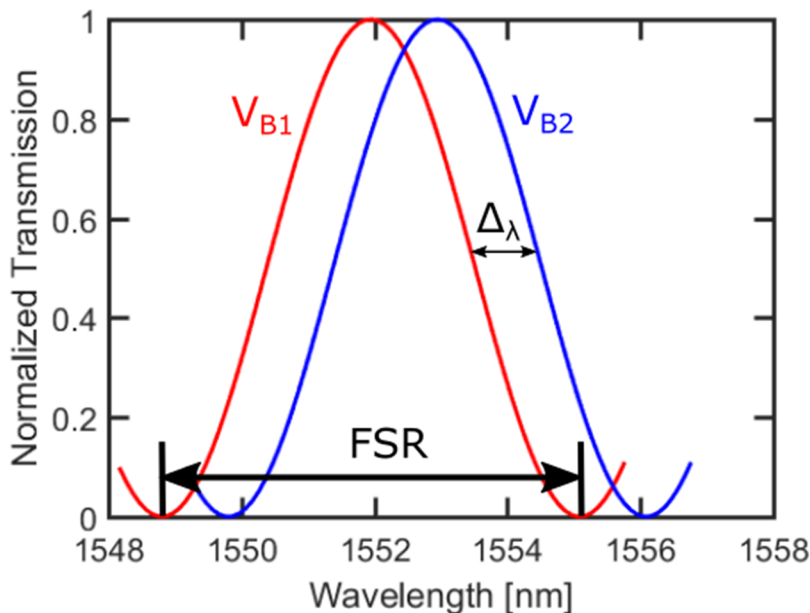


Figure 4.22: An example transmission spectrum of the DC characterization.

free spectrum range (FSR) is the wavelength interval between two adjacent maxima or minima of a transmission spectrum. The phase shift by applying a bias voltage V_2 is calculated by Equation 4.18. Usually, the figure of merit for the steady-state characterization is the voltage length product $V_\pi L$ [89] which means the required bias voltage for a modulator achieving a phase shift of π . This value can be derived from Equation 4.19 where V_{bias} is the applied bias voltage to the modulator, $\Delta\phi$ the phase shift and L the length of the modulator.

$$\Delta\phi = 2\pi \cdot \frac{\Delta\lambda}{FSR} \tag{Equation 4.18}$$

$$V_{\pi}L = V_{bias} \cdot \frac{\pi}{\Delta\phi}L \tag{Equation 4.19}$$

The setup for measuring the scattering parameters is important for the characterization of the modulators and depicted in Figure 4.23 schematically. As can be seen, a bias tee (‘SHF BT45 D’) is

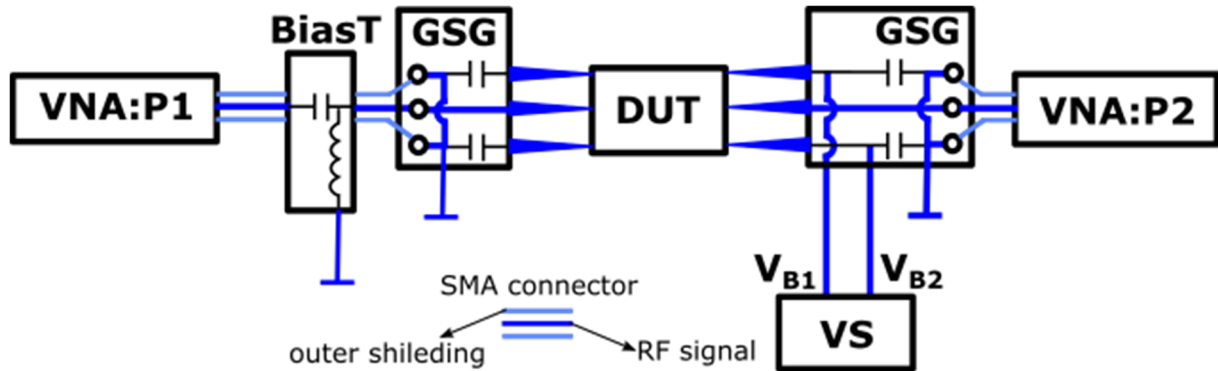


Figure 4.23: Schematic of the scattering parameter measurement and calibration setup.

used at the input side of the modulator. On one hand the RF signal can go through the capacitor from port 1 of the VNA ‘Rhode&Schwarz ZVA24’ to the modulator while any DC signal is blocked, on the other hand the DC bias voltages go through the inductor to the modulator while any AC signal is blocked. On the other side, another customized GSG microprobe is used and the signal from the ‘S’ trace is connected to port 2 of the VNA for calculating the scattering parameter of the entire link.

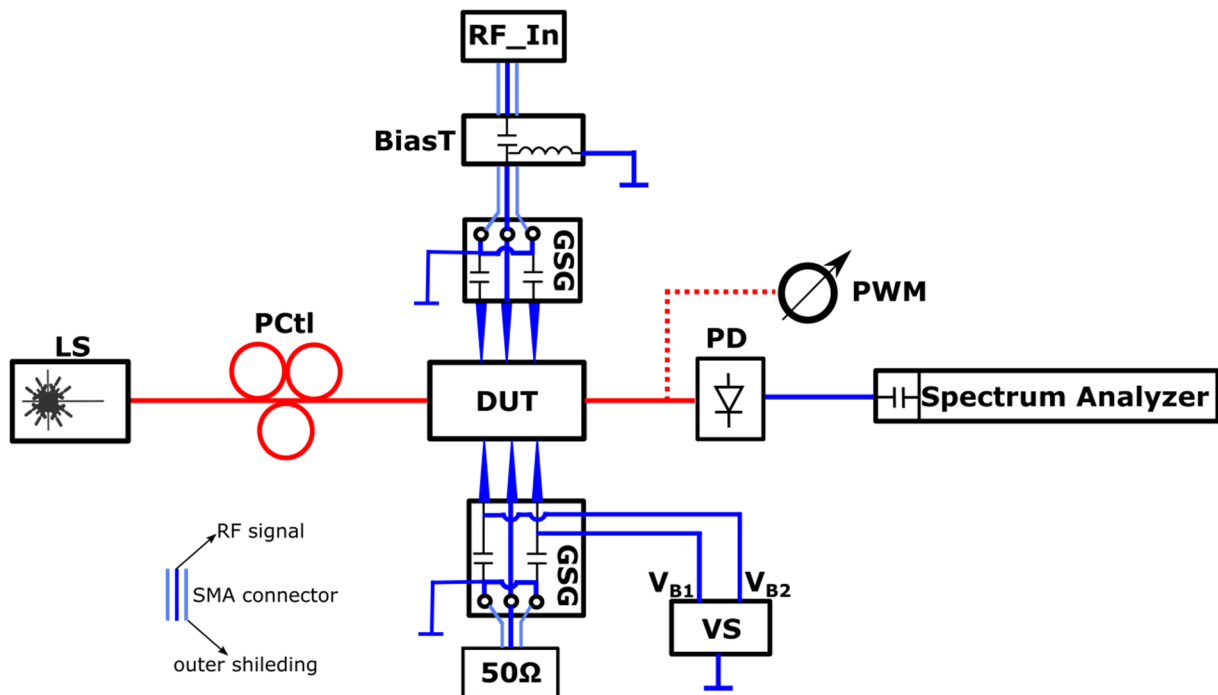


Figure 4.24: Measurement setup for small signal characterization.

Before the measurement, the system requires to be calibrated. The GS/SG and GSG calibrations for modulators are carried out based on the calibration kit ‘GGB CS-8 SG Probes’ and ‘GGB CS-5 GSG Probes’, the used model is the ‘through open short matched’ model. If only one port is used, the ‘open short matched’ model should be used instead.

The measurement setup for the small signal characterization of the MZMs is shown in Figure 4.24. On one side of the modulator, the required RF signal (from signal generator Rohde & Schwarz SMB100A) and the bias voltages (from Keithley 2400) are provided via a bias tee (‘SHF BT45 D’). A special Picoprobe GSG RF probe is used that the RF signal is fed to the common ‘S’ electrode of two phase shifters while the DC biases are fed to two ‘G’ electrodes corresponding to the individual electrode of each phase shifter. Due to the common signal node, the two phase shifters have to be biased with voltages with different polarity. On the other side of the modulator, a 50-Ohm terminator is connected. The optical carrier is generated by the abovementioned tunable laser source, after the modulation the optical signal is detected by the wideband photodetector ‘Newport 1014’. Finally the detector is connected to an electrical spectrum analyzer ‘Rohde & Schwarz FSW43’ for analyzing the RF response of the modulator.

The data transmission, another important aspect of the RF characterization, is realized by the setup shown in Figure 4.25. In this scenario, the PRBS signal is generated by a FPGA (Altera Stratix V GX)

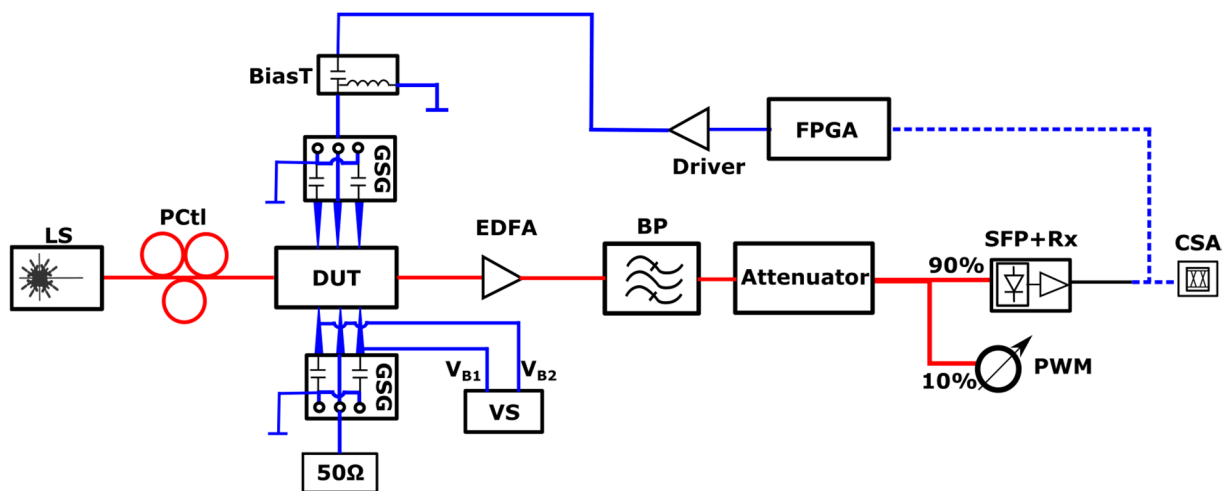


Figure 4.25: Measurement setup for RF data transmission.

on a ‘Transceiver Signal Integrity Development Board’. The pseudo-random bit sequence (PRBS) is amplified by customized driver with two Hittite HMC870 amplifiers in series. The driving signal and the bias voltages are fed to one end of the modulators by the aforementioned GSG probe, the other end of the modulator is terminated by a 50-Ω terminator. The optical carrier is generated by the aforementioned laser source and the polarization is maintained by the polarization controller. To avoid being limited by the thermal noise at the receiver side, the modulated signal out from the modulator is amplified by an IPG Photonics EAD Series erbium-doped fiber amplifier (EDFA). The spontaneous emission noise from the EDFA is filtered by a successive optical bandpass filter. With using a variable optical attenuator, the average optical power can be set to a defined value. For instance, in this scheme, the power is divided by a 90:10 splitter. The 10% branch is connected to the aforementioned power meter and the 90% branch is transmitted to the receiver side of a commercial SFP+ module (Fiberstore SFP-10GER-55), which is composed of a photodiode, a transimpedance amplifier and a limiting

amplifier. For bit error rate (BER) measurements, the electrical output signal is fed back to FPGA to compare the transmitted bit stream with the received bit stream. The limiting amplifier in the last stage can provide stable logical signal levels beneficial for the BER evaluation while on the other hand it also obstructs an analysis of the signal extinction ratio. In addition, to obtain an eye diagram (eye pattern) instead of the BER measurement, the output electrical signal can be fed into an oscilloscope (Tektronix CSA8200) which uses a Tektronix 80E04 sampling module with an analogue bandwidth of 20 GHz for the data acquisition.

4.5.7 DC and AC measurement results of modulators

With the abovementioned measurement setup, the DC and AC characterizations were carried out for the MZMs with different lengths and also the 3-mm radiation hardened modulator. Figure 4.26 shows the

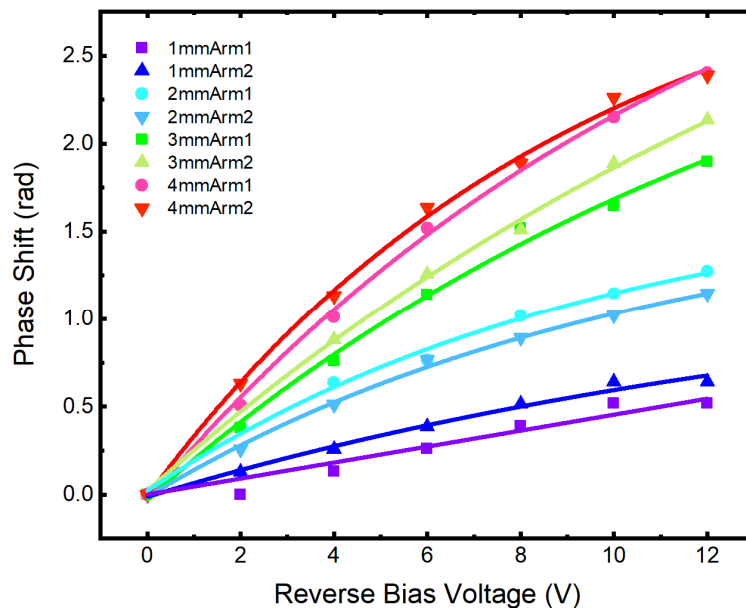


Figure 4.26: Modulation efficiency versus applied bias voltage based on the measurement results for asymmetric MZMs with different lengths (the 3rd batch chips).

measured modulation efficiency over the applied reverse bias voltage to one arm of the asymmetric MZMs with different lengths (from 1 mm to 4 mm). Since one MZM is composed of two phase shifters (be referred as arm1 and arm2 of one MZM), both shifters were measured to make comparison. It's clearly shown that under identical bias voltages, the longer the phase shifter is, the larger phase shift is achieved. For those two short MZMs (1 mm and 2 mm), their phase shift with respect to the reverse bias voltage is almost linear; whereas the curves of those two longer MZMs (3 mm and 4 mm) present smaller slopes, especially at high voltages, meaning the modulation efficiency will approach the saturation point at high reverse bias voltages. On the other hand, although two phase shifters in one MZM are designed to be doped identically, their performance differs significantly. Since the modulation efficiency of the phase shifter is determined by the doping concentration and the length of the modulator, the performance deviation between two arms result from either the nonideal doping technique or the fabrication technique. Due to this reason, an additional phase shifter is usually required in practice for operating point control. Comparing the measured modulation efficiency with the simulation result in Figure 4.18, the measured actual doping concentration of the MZM is close to 0.1 times the reference doping. The estimated actual doping concentration is one order of magnitude lower than the desired

value. The resulting modulation efficiencies calculated at the reverse bias voltage of 4 V for all modulators are shown in Table 4.1.

Table 4.1: Modulation efficiencies of the modulators with different lengths

Phase shifter	$V_{\pi}L(V \cdot cm)$	Phase shifter	$V_{\pi}L(V \cdot cm)$
1 mm MZM arm1	4.9	3 mm MZM arm2(Deep)	5.2
1 mm MZM arm2	6.9	3 mm MZM arm1(Shallow)	4.1
2 mm MZM arm1	4.9	3 mm MZM arm2(Shallow)	4.3
2 mm MZM arm2	4.4	4 mm MZM arm1	4.6
3 mm MZM arm1(Deep)	3.9	4 mm MZM arm2	4.8

Figure 4.27 shows the modulation efficiency of 3-mm MZMs with different etching depths. The deep

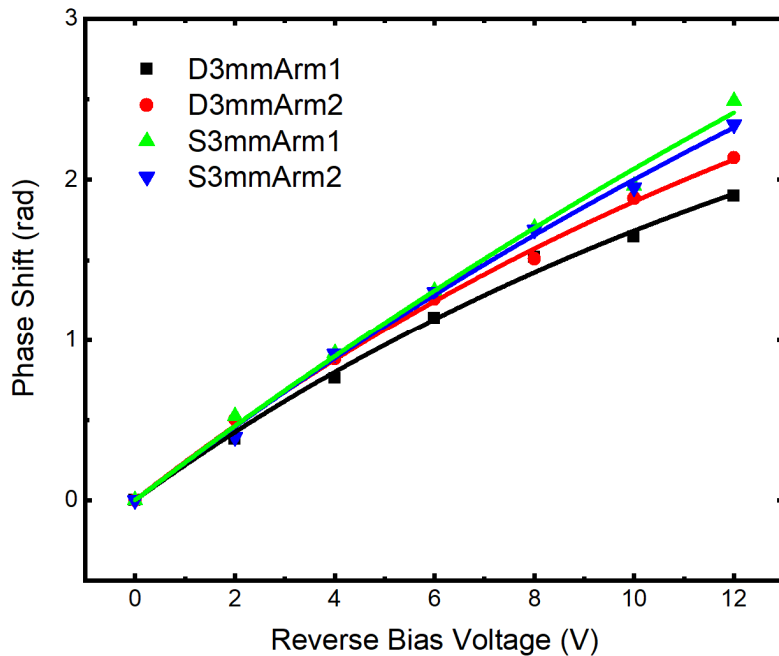


Figure 4.27: Fitted modulation efficiency versus applied bias voltage based on the measurement results for the 3mm MZMs with different etch depth (the 3rd batch chips).

etched MZM has an etching depth of 130 nm while the shallow etched MZM has an etching depth of 70 nm. According to the modulation efficiencies of the two kinds of MZMs in Figure 4.27, the shallow etched MZM has a slightly higher modulation efficiency. In addition, the two arms are proved to be doped asymmetrically since the two arms present different modulation efficiency at the identical bias voltage, especially for the deep etched MZM.

According to the DC characterization results of different kinds of modulators, the doping technique of the used foundry is not mature enough to obtain the desired doping concentrations. Therefore, the modulation efficiency of the fabricated modulators are much lower than the desired value. Even for single modulators, its two arms are not doped identically, resulting in the performance deviation between them. For unknown reason, the shallow etched modulator has more accurate doping concentrations, resulting in a higher modulation efficiency than that of the deep etched modulators; in addition, the two

arms of the shallow etched modulators are doped more homogeneously. The modulator can be improved significantly with favorable doping technique.

High frequency response of the designed modulators is very important, and the scattering parameter measurements for the electrodes without modulator loaded were carried out first of all. The measured results are shown in Figure 4.20. The 3-dB cutoff frequency decreases with increasing the length of structure. For a 3-mm structure, the cutoff frequency achieves 10.1 GHz and for the 4-mm transmission line the value is 4.9 GHz. The cutoff frequencies of the 1-mm and 2-mm MZMs are higher than the measurement range of the instrument, 24 GHz. According to this measurement result, the transmission lines can meet the required 10 Gb/s transmission speed except for the 4-mm one.

Further measurements of the scattering parameter on the electrodes with modulator loaded were made as well and the results are shown in Figure 4.28. As can be seen, the cutoff frequency is lowered

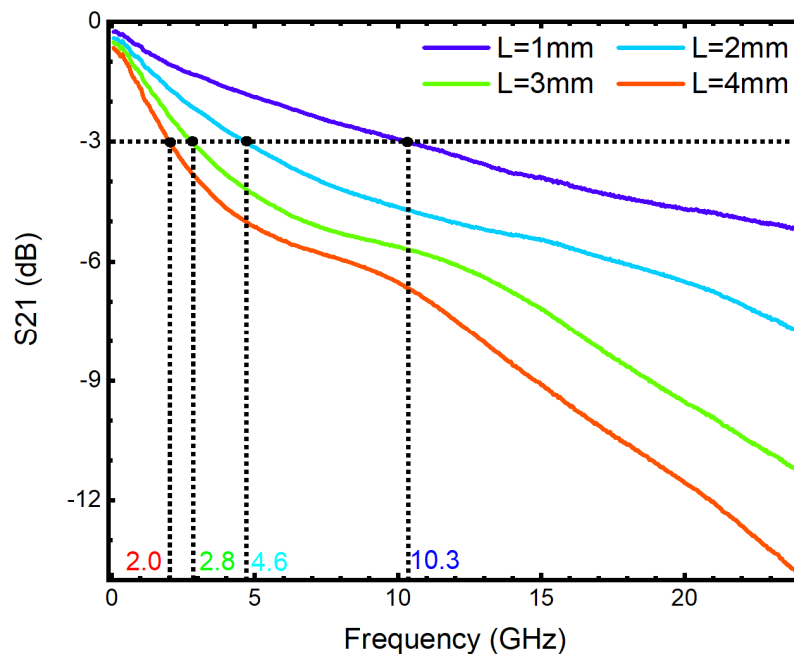


Figure 4.28: Scattering parameter measurement of the deep etched MZM with different lengths.

significantly for all the modulators with the modulator loaded. Nevertheless, with decreasing the length of the modulator, the cutoff frequency increases. The cutoff frequencies are 10.3 GHz (1 mm MZM), 4.6 GHz (2 mm MZM), 2.8 GHz (3 mm MZM), and 2.0 GHz (4 mm MZM), respectively. Based on the comparison with the scattering parameter measurement results of the electrodes without the modulator loaded, the modulator introduce quite significant attenuation. The key limiting factor of the high frequency application may result from the modulator design instead of the electrodes design.

The low cutoff frequency of the modulators presented above does not mean that the modulators cannot be applied for 10 Gb/s transmission since the modulators will be reverse biased in practical applications which will also affect the high frequency response as well. Therefore, the small signal characterization was carried out for the asymmetric MZMs with different lengths. The reverse bias voltage for both phase shifters were set to 1 V symmetrically and the power of the RF signal was set to 0 dBm corresponding to 0.6 V_{pp}. Figure 4.29 shows the measured frequency response of the MZMs with different lengths.

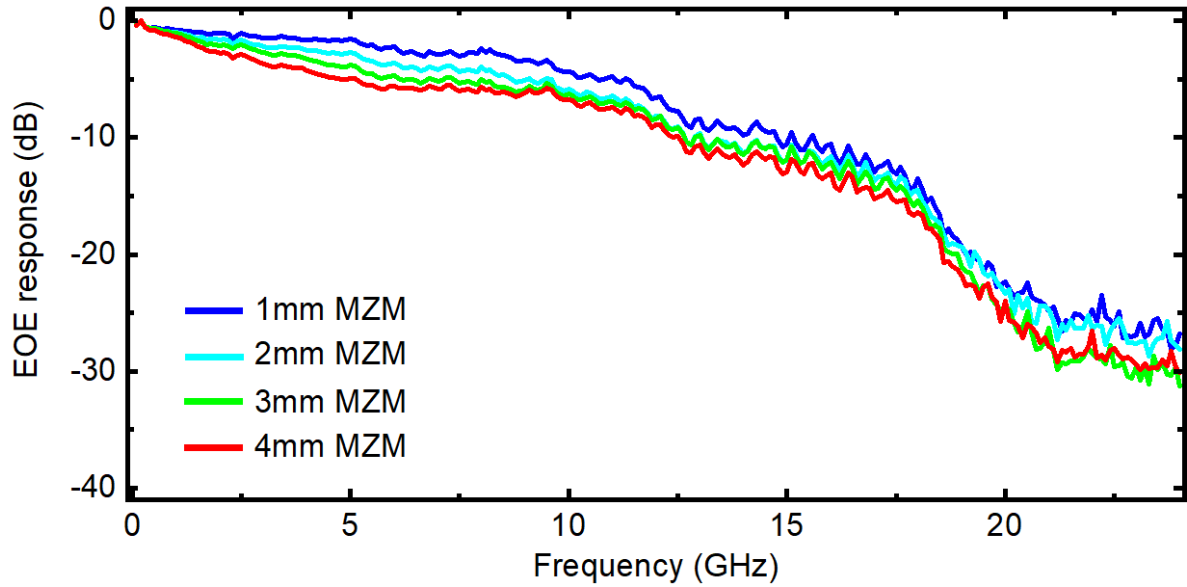


Figure 4.29: Small signal characteristics of the asymmetric MZMs with different lengths at a symmetric reverse bias voltage of 1V.

It is easy to find that the longer MZMs have worse frequency response in comparison. The 3-dB frequency of each MZM can be derived with fitting the curves with the ninth order polynomial. They are 8.1 GHz, 4.9 GHz, 3.6 GHz and 2.4 GHz for the 2-mm, 3-mm and 4-mm MZMs, respectively. The cutoff frequencies of 2-mm, 3-mm and 4-mm modulators are improved slightly, while the cutoff frequency of the 1-mm modulator decreases 2.2 GHz for unknown reasons.

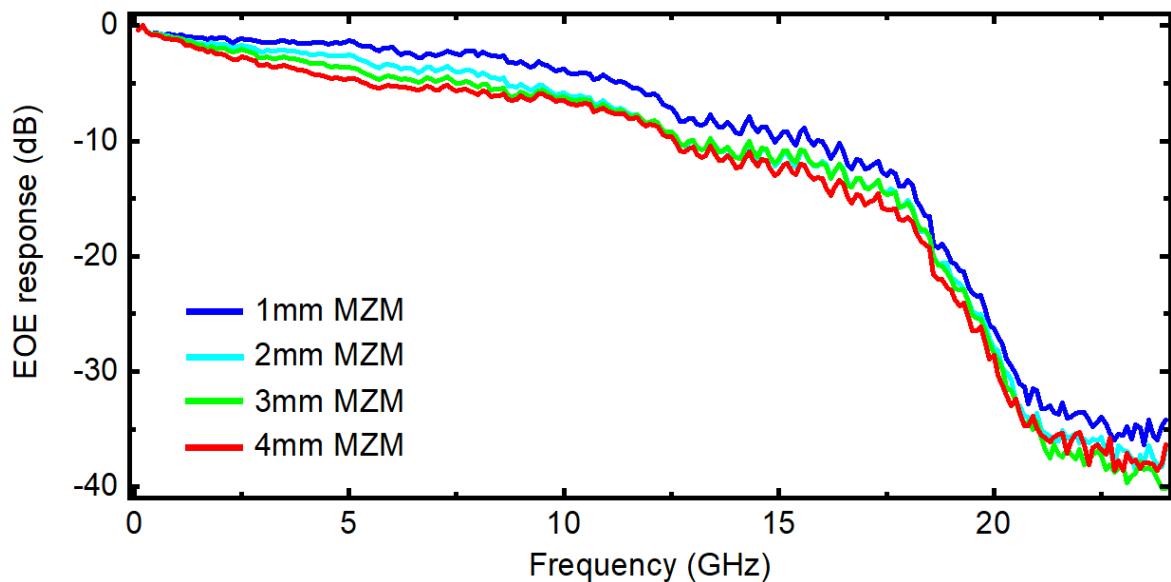


Figure 4.30: Large signal characteristics of the asymmetric MZMs with different lengths.

In practical applications, the bias voltage of the modulators can be higher than 1V. To study the performance of the modulators under larger bias voltage and RF signals, another measurement was made. The bias voltages are set to ± 2 V and the power of the RF signal to 13 dBm, corresponding to 2.8 V_{pp}. The measured results are shown in Figure 4.30, which shows a similar tendency with the previous small signal characteristics. Again, fitting the curve, the derived 3-dB cutoff frequencies are 8.8 GHz, 5.3 GHz,

3.7 GHz and 2.7 GHz, respectively. At a reverse bias voltage of 2V, the cutoff frequencies of the modulators are improved slightly. Although a higher bias voltage is beneficial to high speed transmission, it can also increase the power and loss in reverse. Therefore, a tradeoff has to be made.

All the above discussions are for the modulators with an etching depth of 130 nm, while it is also worthwhile to compare their performance with that of the radiation-hardened modulator.

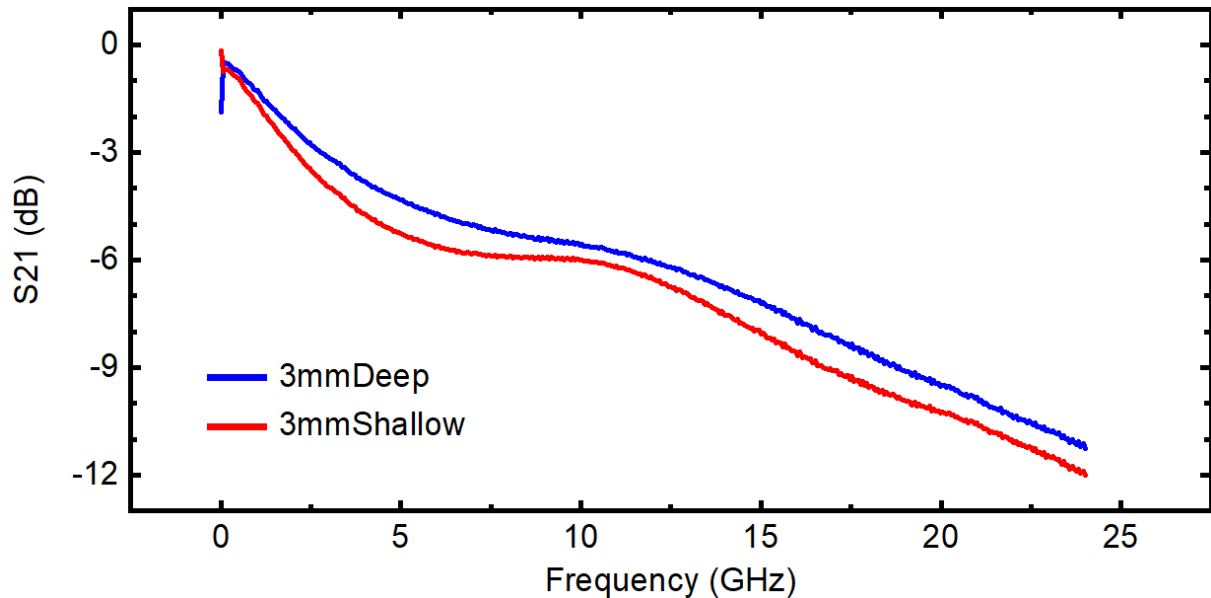


Figure 4.31: The scattering parameter of the 3-mm MZMs with different etching depths.

Figure 4.31 shows measurements of the S21 scattering parameter of the 3-mm MZMs with different etch depths. As can be seen, the two types of modulators have similar performances while the shallow etched modulator decreases the cutoff frequency slightly in comparison. The derived 3-dB frequency of the deep and shallow etched MZMs are 2.8 GHz and 2.1 GHz, respectively.

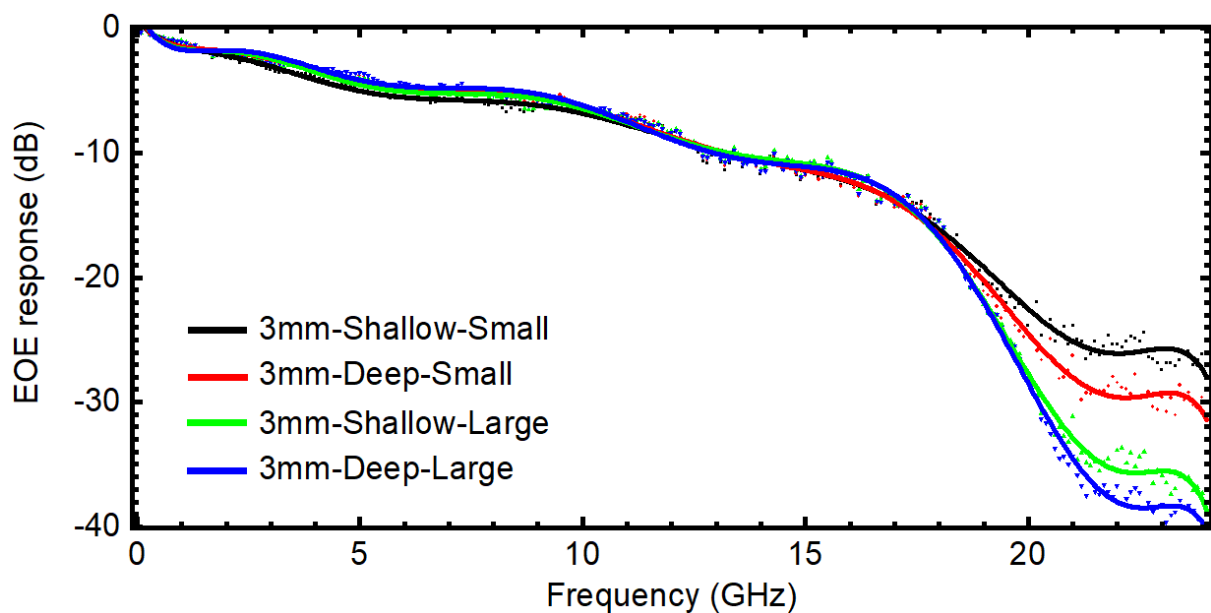


Figure 4.32: Small and large signal characterization for the 3-mm MZM with different etching depths.

The small signal characterizations at 1 V and 2 V reverse bias voltage were also made on the radiation hardened MZMs. As shown in Figure 4.32, the 3-dB frequencies at 1 V reverse bias voltage of the 3-mm shallow and deep etched MZMs are 2.9 GHz and 3.6 GHz, respectively. Similarly, at 2 V reverse bias voltage, they increase to 3.6 GHz and 3.8 GHz, respectively. According to the comparison, it can be found although the shallow etched modulators have a higher modulation efficiency, their cutoff frequency deteriorates on the other hand. The performance of the radiation hardened modulators still requires more measurements to evaluate globally.

4.6 Multimode Interferometers

The history of the discovery and development of multimode interferometers (MMIs) can date back to 1890 when the Talbot effect was firstly observed [102]: imaging a monochromatic optical plane wave incident on periodic diffraction gratings, the grating image will repeat itself at a fixed distance L . The distance L is namely the Talbot length. Afterwards, the Talbot effect was verified by Rayleigh [103] and was even proved based on the Fresnel images [104]. On this basis, the secondary imaging at $L \cdot p/q$ was also predicted [105]. It is noticeable that the Talbot effect can also be extended to two-dimensional images by relating the output image to the input source via a convolution [106]. The basic idea of the MMI is to produce a confined Talbot effect using total internal reflection in optical fiber to replicate the periodic gratings [107][108]. This phenomenon was firstly tested in 1975 by Ulrich et al. [109]. Since then, MMIs have been studied a lot and are widely used in integrated photonics nowadays.

In this thesis, the MMI design is closely related to the MZM design, because the MMIs are used as power splitter and combiner at both ends of the modulator. To realize the function of power splitting and combining, a 3-dB directional coupler and a Y-splitter can also be adopted. Within the three options, the Y splitter is very compact, while it used to be limited by the fabrication technique, featuring high insertion loss. However, with the development of the fabrication technique, fabricating a low insertion-loss, high-bandwidth and compact directional coupler is feasible as presented in [110]. The directional coupler generally requires a larger footprint than Y-splitters and MMIs, while directional coupler formed with channel waveguides can also be designed to be compact. However, this device is quite sensitive to the fabrication technique, their performance may degrade substantially with minute variations in fabrication. More tolerant devices can be realized using rib-waveguides [111] and long adiabatic directional couplers [112]. MMI couplers are significantly larger than Y-splitters, but they have the advantages of low loss, simple fabrication, high tolerance to fabrication errors and lower polarization dependence [113].

The analysis of MMIs can make use of the eigenmodes decomposition [114]. As shown in Figure 4.33, imagining there are n guided modes in the multimode region of MMI, the strongly guided

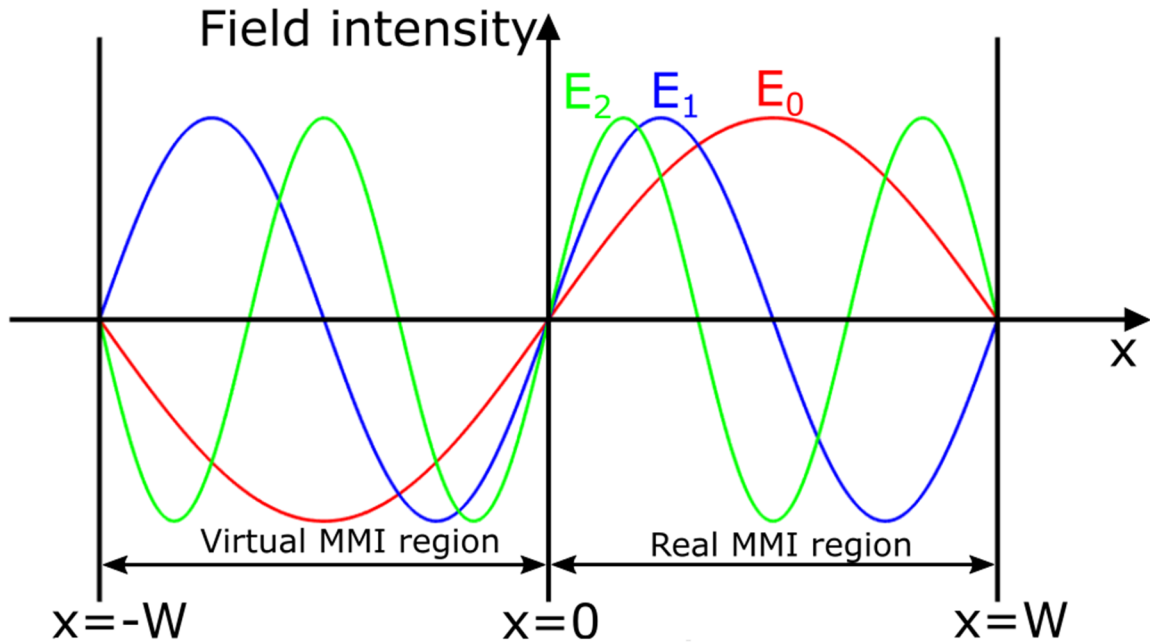


Figure 4.33: Input distribution $f(x)$ and decomposition into guided modes $E_i(x)$ of the structure.

eigenmodes are nearly completely confined in the waveguide so that their lateral mode profiles contain integer number of half-periods within the waveguide. In consequence, their transversal propagation constants are calculated by Equation 4.20 in which W is the width of the multimode region, i is a positive integer including zero. The longitudinal propagation constant can be calculated by Equation 4.21, in which n is the refractive index and k_0 the free space wave number. If using the paraxial approximation, the longitudinal propagation constant can be further approximated by Equation 4.22. Based on Equation 4.22, the difference of two propagation constants can be calculated by Equation 4.23, where L_c is the beat length (also called coupling length). The detailed derivations can be found in literature [114]. On the basis of these formulae, the design of arbitrary $M \times N$ MMI can be carried out.

$$k_{xi} = \frac{(i+1)\pi}{W} \quad \text{Equation 4.20}$$

$$\beta_i^2 = n^2 k_0^2 - k_{xi}^2 \quad \text{Equation 4.21}$$

$$\beta_i \approx nk_0 - \frac{k_{xi}^2}{2nk_0} \quad \text{Equation 4.22}$$

$$\beta_0 - \beta_m = \frac{m(m+2)}{3L_c}, L_c = \frac{\pi}{\beta_0 - \beta_1} = \frac{4nW^2}{3\lambda} \quad \text{Equation 4.23}$$

4.6.1 Two types of 3-dB power splitters or combiners

The 3-dB MMI is a typical component in integrated photonics design. There are several methods for constructing it. The easiest method is to utilize the 1×2 MMI design as shown in Figure 4.34. The input

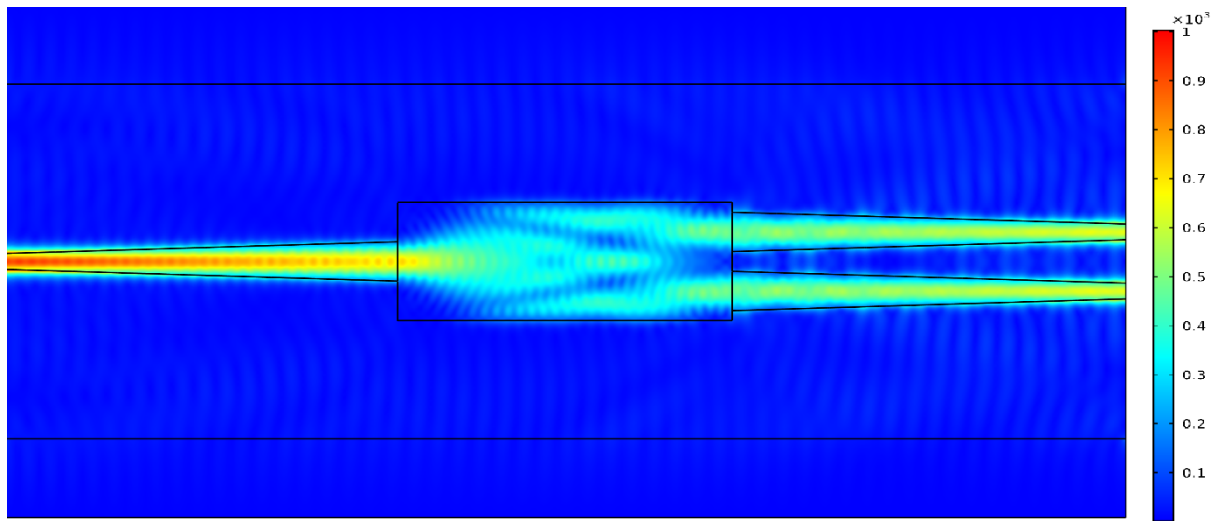


Figure 4.34: COMSOL simulation interface of the 1×2 MMI.

port is located at $W/2$ where W is the width of the MMI. The length of the MMI is $(3L_c)/8$. However, this is merely an approximated length derived based on two lowest order modes. An accurate result should be calculated numerically. In our design, the simulation is made in the commercial software COMSOL Multiphysics. The simulation is based on the 250-nm SOI platform with a 250-nm core silicon layer, $2 \mu\text{m}$ SiO_2 substrate layer, and $1 \mu\text{m}$ SiO_2 upper cladding layer. The single mode waveguide has a width of 500 nm and in the MMI design, the input port is adiabatically tapered from 500 nm to $1 \mu\text{m}$ over a length of $10 \mu\text{m}$. To make it comparable with the following two designs, the width of MMI is set to $3 \mu\text{m}$, and the length of the MMIs is swept from $6 \mu\text{m}$ to $10 \mu\text{m}$ with a step of $0.5 \mu\text{m}$. The simulated result is shown in Table 4.2. As can be seen, when $L_{\text{MMI}} = 8.5 \mu\text{m}$, the splitting ratio is closest to 50:50 and the insertion loss is also the smallest, 0.09 dB.

Table 4.2: Simulation results of the 1×2 MMI.

L_{MMI}	S21(dB)	S31(dB)	Total Insertion Loss (dB)
6	-5.85437	-5.85438	2.84408
6.5	-4.65528	-4.65535	1.64501
7	-3.89935	-3.89931	0.88903
7.5	-3.43585	-3.43591	0.42558
8	-3.10292	-3.10285	0.09258
8.5	-3.10083	-3.10079	0.09051
9	-3.49444	-3.49435	0.48409
9.5	-3.70295	-3.70295	0.69265
10	-4.63765	-4.63773	1.62739

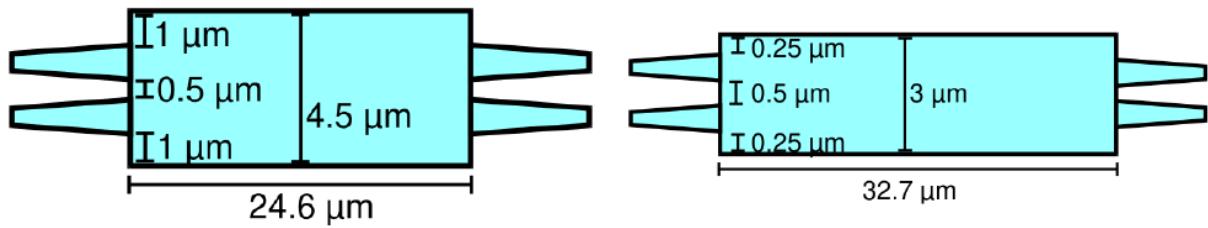


Figure 4.35: Geometries of two 2×2 3-dB MMIs with different port positions.

The above design is the simplest scheme with merely one input port. If adding another port and adjusting the position of the input port, a 3-dB MMI can also be realized. The first option is to set the input port at $W/3$ position. Then the two-fold imaging position will be located at $(3L_c)/6$. On the other hand, if the input port is adjusted to be at $W/4$, the imaging position will be located at $(3L_c)/2$. It is easy to find that when locating the input port at $W/3$ leads to the shortest MMIs. However, in practice, the input and output ports of the MMIs have a certain width and usually adiabatically tapered. That means the end of the I/O port is wider than the single mode waveguide. If two waveguides are closer, the coupling between them will be stronger. Therefore, the distance between two waveguides should be as large as possible. Considering the limited on-chip footprint, the distance is beneficial to be larger than $0.5 \mu\text{m}$. Based on this point, the width of the proposed two kinds of 3-dB MMI are $4.5 \mu\text{m}$ and $3 \mu\text{m}$, respectively. Their structures are shown in Figure 4.35. The sweep length for the $4.5 \mu\text{m}$ MMI is from $20 \mu\text{m}$ to $30 \mu\text{m}$, the sweep length for the $3 \mu\text{m}$ MMI is from $25 \mu\text{m}$ to $35 \mu\text{m}$. Their simulation results are illustrated in Figure 4.36 and Figure 4.37.

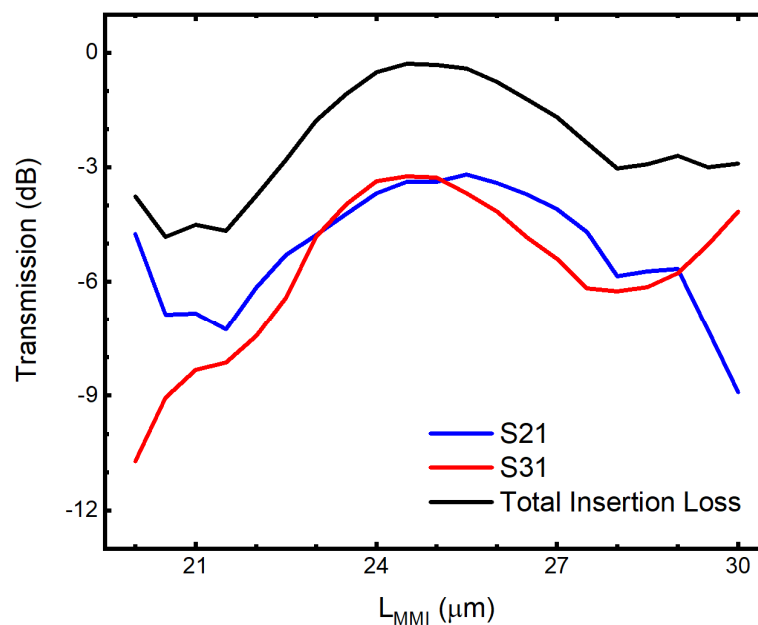


Figure 4.36: Simulated results of 3-dB MMI with a width of $4.5 \mu\text{m}$.

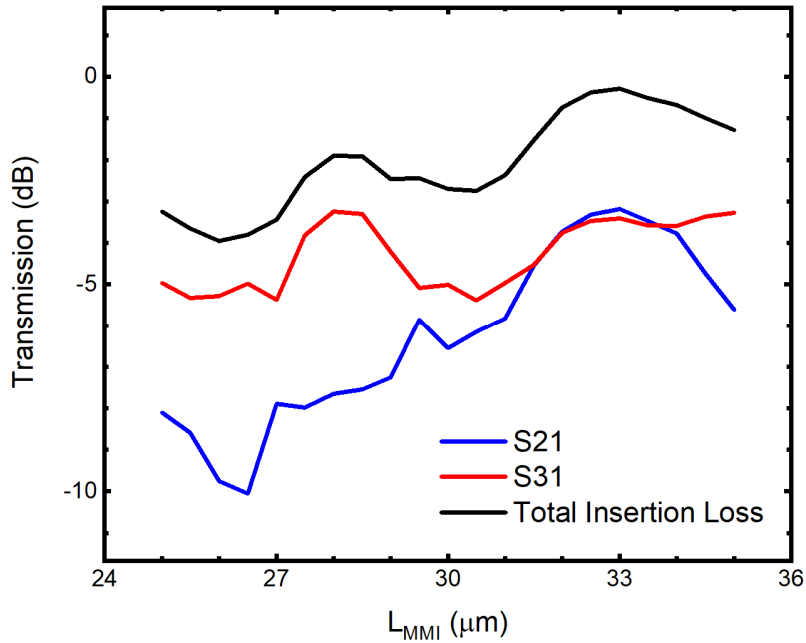


Figure 4.37: Simulated results of 3-dB MMI with a width of 3 μm .

As can be seen, the length to achieve the lowest insertion loss for two kinds of MMI are 24.5 μm and 33 μm respectively. For a finer simulation, the lengths are set to 24.6 μm and 32.7 μm , respectively. Two types of MMIs have a similar on-chip footprint, but the one shown in the left has a wider space between the coupling ports and the edge of the multimode region which is beneficial for fabrication. Due to the limited on-chip resource, only the left device was fabricated, the simulated and measured results are illustrated in Figure 4.38.

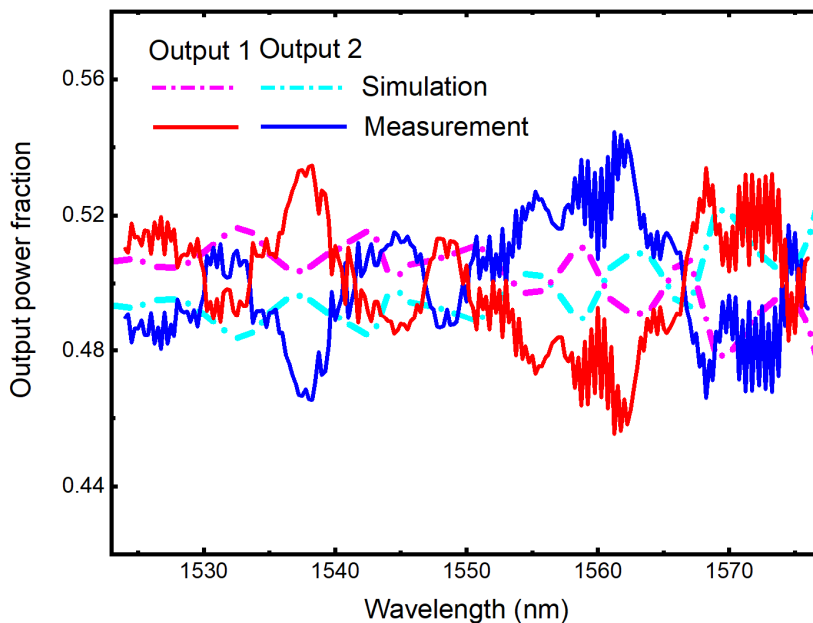


Figure 4.38: Simulated and measured result of the fabricated 3-dB MMIs.

As can be seen, there is an excellent agreement between the simulated (dash-dotted lines) and experimental (full lines) results. Across the C band, the input power from one input distributed into the two arms is split evenly, the power fraction of both arms remains close to 0.5. Even in the worst case, the power fraction is still 0.45. The measured average and maximum insertion loss are 0.43 dB and 0.84 dB, respectively. According to this result, the designed MMIs are very suitable to be used as power splitters or combiners in a MZM.

4.6.2 An 86:14 MMI for feedback control

It has been mentioned that the modulator requires a proper working point to work properly. However, the performance of a modulator is easily affected by the fabrication technique or the ambient temperature. Therefore, an additional component for working point control is necessary for which MMIs are very suitable. Since the output ports of MMIs have specific phase relations that can be calculated theoretically or estimated by numerical simulation. The 2×2 MMIs with an uneven splitting ratio can be used to branch off a small portion of the signal to track the phase relation of two arms. The requirements of the device are a small occupied area and the branch-off power should also be in the order of 10%. For the 2×2 MMI, if placing the input port at $W/4$, the $3L/4$ position is a double imaging place. However, the power splitting ratio is around 86:14, only a small portion power is guided to one arm and the two arms have a phase difference around 90° . Similar to the above design, the design of this device is also based on the numerical simulations using COMSOL Multiphysics. The Width of the MMI is fixed to $3.2 \mu\text{m}$ and the length of MMI is swept from $15 \mu\text{m}$ to $25 \mu\text{m}$. The simulation results are shown in Figure 4.39, when $L_{\text{MMI}} = 18.5 \mu\text{m}$, the total insertion loss is lowest, the phase difference between two output ports are also close to 90° .

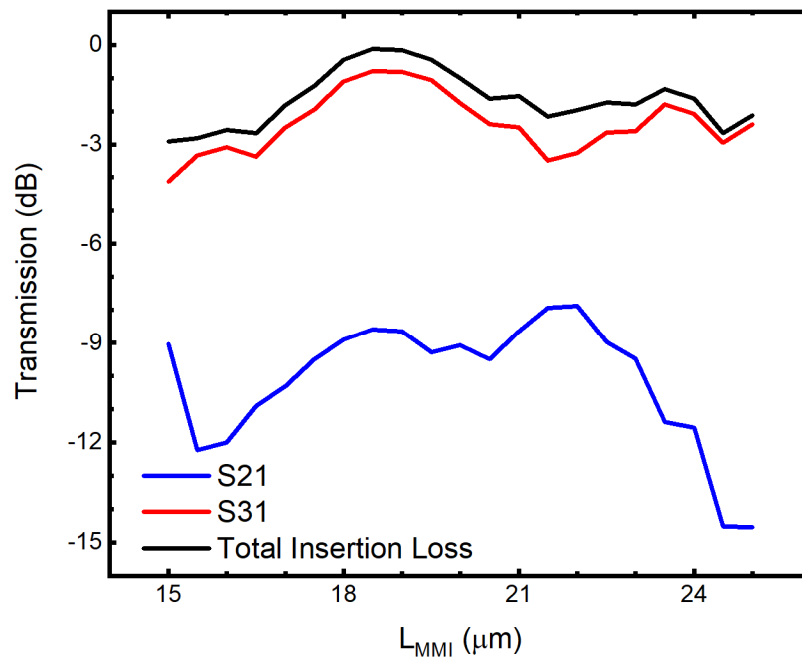


Figure 4.39: Simulation results of the 86:14 MMI.

The simulated and measured results of the two arms of the designed 2×2 86:14 MMI are illustrated in Figure 4.40 and Figure 4.41. As can be seen, the output power of the arm with the smaller share fluctuates between 12% and 17% across the C band. The output power of the arm with the larger share

fluctuates between 84% and 88%. The power splitting ratio remains quite stable and the total insertion loss of the device is as low as 0.078 dB in average. If regarding the power in the minor-power arm as insertion loss as well, namely about 86% input power is guided to this port, only 4% less power than in a common 90:10 power splitter. A 90:10 power splitter based on MMIs can only be realized by either adding additional structures (normally a phase shifter) [36] or by combining multiple MMIs, which makes the design large and complex and the fabrication expensive. In comparison, the design in this section is easier to implement, more suitable for integration with slightly less guided power, and finally the exact portion of the branched off signal is not really relevant, as long as it is known and reproducible.

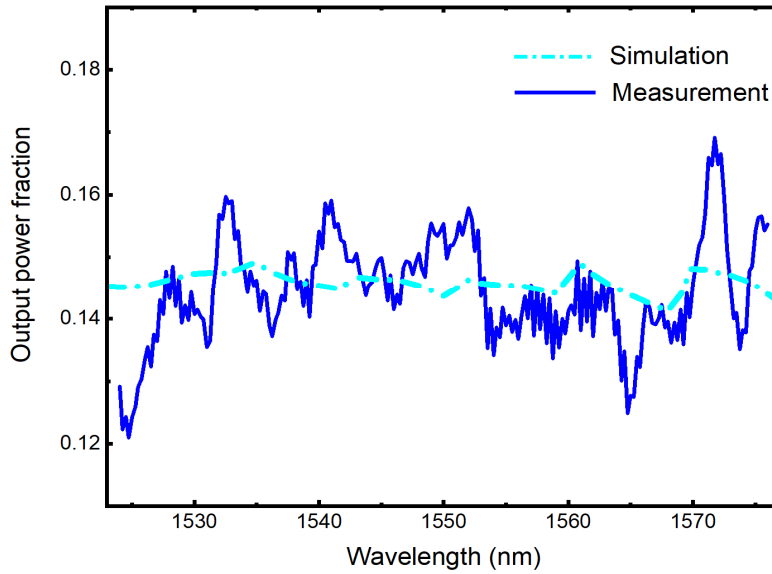


Figure 4.40: Simulated and measured results of arm1 from the designed 86:14 MMI.

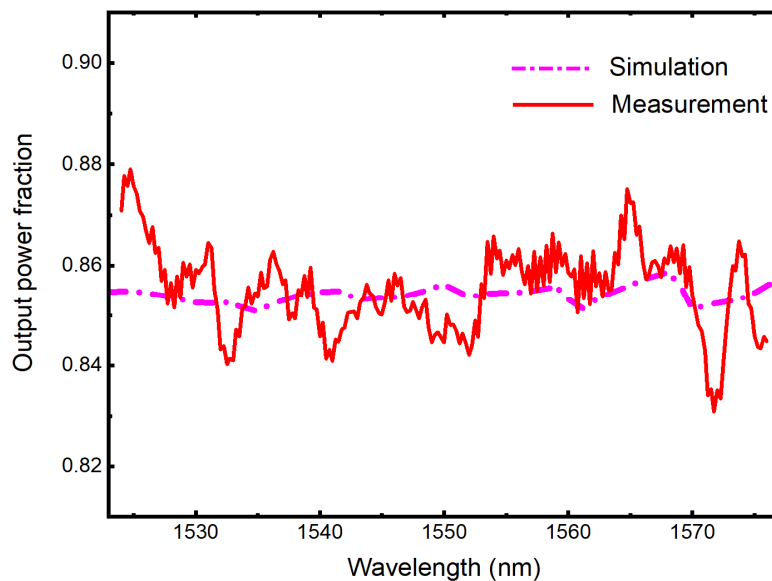


Figure 4.41: Simulated and measured results of arm2 from the designed 86:14 MMI.

5 Echelle Grating (De-)Multiplexer

5.1 Filter types

Besides the modulator, the wavelength (de-)multiplexer is another key component for an integrated WDM transmitter. In general, several key parameters can be used to evaluate the performance of a wavelength filter, they are channel number, channel spacing, insertion loss, crosstalk, on-chip footprint and 1-dB bandwidth of a channel. Channel spacing means the wavelength difference (or frequency difference) between the operating wavelengths of two adjacent channels. The insertion loss characterizes how much optical power is lost via the filtering function of the device. The crosstalk is a unit to characterize how much interference is induced to a specific working channel by the remaining channels. The 1-dB bandwidth is common to be used in narrow-bandwidth filters. If the wavelength filter can provide many useable channels and each channel is operating in a pretty narrow channel spacing, the entire transmission bandwidth of an integrated transmitter can be enlarged dramatically. If the 1-dB bandwidth of an operating channel is very narrow, the performance of a device is easily affected by the ambient environment. Therefore, from the user's point of view, the wavelength filter should have a very compact on-chip footprint, many usable channels, narrow channel spacing, low insertion loss, low crosstalk and large 1-dB bandwidth.

In the past decades, several kinds of wavelength filters have been proposed, based on different mechanisms. They are microring resonators (MRR), lattice-form filters (LFF), arrayed waveguide gratings (AWG) and planar concave gratings also called Echelle gratings (EG). According to the practical application, one can select the filter type accordingly.

A top-view schematic of a microring resonator is illustrated in Figure 5.1. As can be seen, a MRR is

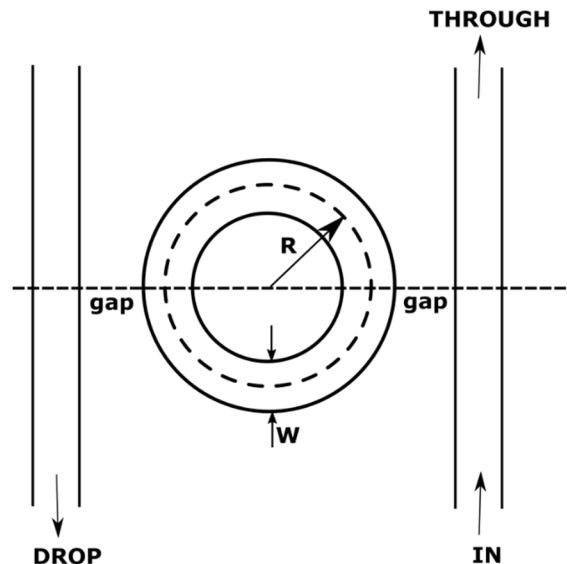


Figure 5.1: Top view of a single symmetric waveguide-coupled microring resonator.

composed of a circular waveguide and two straight waveguides [115][116][117]. The key design parameters for a MRR are the radius R of the ring, the width W of the ring and the gap between the ring and the bus waveguides. The light enters the input bus at the 'IN' port, then part of the light will couple into the microring due to the evanescent field which extends outside of the waveguide mode in an

exponentially decreasing profile. After traveling half the ring, the light in the ring will again couple into the output bus and part of the light will be guided into the ‘DROP’ port. The remaining light continue travelling and will interfere with the successive light from the ‘IN’ port: if the light in the microring travels integer times of the wavelength (the phase difference is 2π), the constructive interference happens, the remaining light will be guided to the ‘THROUGH’ port; if there is still a half wavelength apart from the integer wavelengths (their phase difference is π), destructive interference happens, the remaining light disappears. It is beneficial to decrease the gap between the ring and the waveguides and increase the coupling length to make the coupling easier. On the other hand, additional functional part can be added into the design to tune the refractive index of the ring to adjust the phase difference achieve better coupling effect [118]. With cascading multiple MRRs, the device can realize multiple wavelengths filtering function, an example is reported in [119]. The MRR can be compact, efficient and the channel spacing can be quite narrow; however it’s quite sensitive to the fabrication and the operating temperature that additional components are necessary for instance the thermal modulators.

Another type of wavelength filter is LFF, also called Mach-Zehnder demultiplexer, a general structure of LFF is shown in Figure 5.2. The LFF is composed of a straight waveguide and a snakelike delay line [120]. The snakelike delay line is composed of n-stage couplers, each coupler consists of one

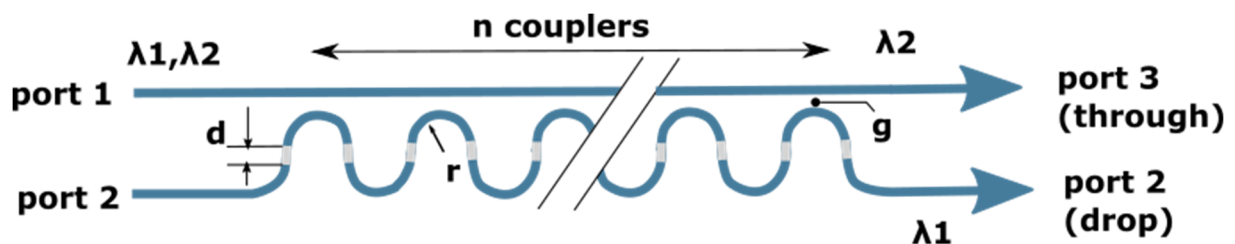


Figure 5.2: Schematic of a lattice form filter.

180° arc with radius r and short straight sections of length d used for delay adjustment. The straight waveguide encounters the delay line periodically where the gap between them is quite narrow. The combined light with wavelengths λ_1 and λ_2 enters the straight waveguide from ‘port 1’. After the filtering of the LFF, they will go to the ‘through’ and ‘drop’ ports, respectively. The key design parameters are the number of stages n of couplers, the radius r of the arc, the length d and the distance between the straight waveguide and the delay line. The LFF design can achieve very low loss, crosstalk, very flat response and also compact footprint. However, the performance of an LFF is heavily dependent on the exact optical phase length of a number of delay line waveguides and on the exact cross coupling length of a number of directional couplers. Therefore, a good control of waveguide and directional coupler dimensions is necessary [121][122][123]. The performance of this filter type used to be limited by fabrication technique. Nevertheless, a good design was reported in [124] with some optimization.

The AWGs [125][126][127] are planar devices based on an array of waveguides, possessing both imaging and dispersive properties. A schematic of AWG is shown in Figure 5.3. As can be seen, the

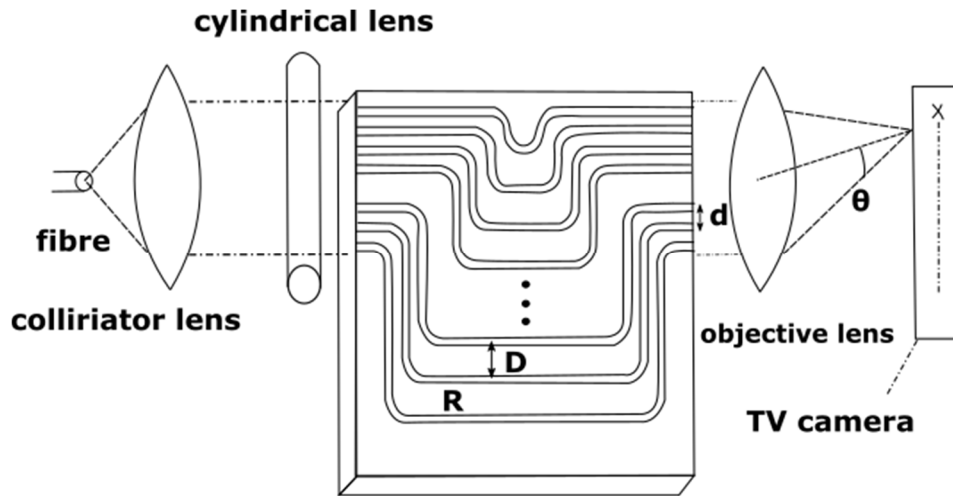


Figure 5.3: The schematic of an AWG.

gratings are composed of a set of single-mode channel waveguides. These waveguides have different lengths with bent parts of the same curvature radius. Any two adjacent waveguides have the same phase difference ΔL and it is given by $\Delta L = D - d$. Then using the diffraction relation $n_c \Delta L + n_s d \sin \theta = m \lambda$ (n_c is the refractive index of the channel waveguide, n_s is the refractive index of the converging space, θ is the diffraction angle and m is the diffraction order) [125], the light with different wavelength will be guided to different output ports. With some design and fabrication optimizations, the performance of the AWGs can be improved a lot [126] with quite narrow channel spacing. Nowadays, AWG is still a good option for dense wavelength division multiplexing (DWDM) application while for coarse wavelength division multiplexing (CWDM), the EGs (which will be introduced below) have the advantages of compact footprint, easy for fabrication and low insertion loss.

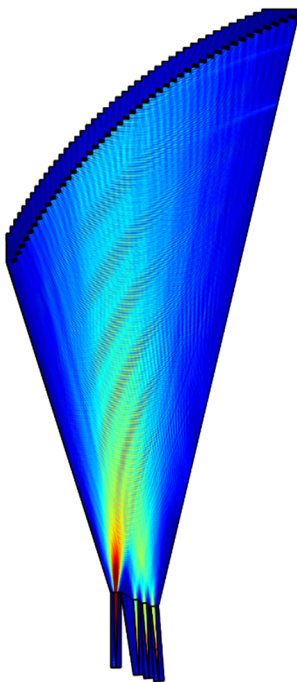


Figure 5.4: Structure of an EG.

The EG is a kind of diffraction gratings, the density of the grooves is relatively low. By optimizing the groove shape, EGs can be used in high incidence angles and therefore in high grating orders which allows for increased dispersion of spectral features. The structure of a general EG used as wavelength filter is illustrated in Figure 5.4. On top of the device there are many reflectors forming an arc-like structure. The reflectors can be designed to be different kinds like distributed Bragg reflectors (DBR), corner mirrors, plain deep etches, metallized facet using silver, and oblique total internal reflection facets [128]. Within them, the DBR is widely used due to the advantages of easy fabrication and high reflectivity. Below the gratings is a slab region, where the light can propagate freely. At the bottom, the input waveguide and the output waveguides are usually aligned closely. The structure of the EG is relatively simple compared to the abovementioned wavelength filters. The most challenging task is fabricating the grating facets accurately. With the development of the fabricating technique, fabricating such kind of structures are no longer a problem for most foundries. The EGs have

advantages on fabrication tolerance over the other above methods. Especially, in CWDM application, this method can achieve similar performance as other methods with a very compact on-chip footprint. Since the integrated transmitter in this thesis aims at four channels and each channel is operating in the C band fitting into CWDM application, the EG is a suitable method to realize wavelength filtering. In the following sections, two design methods will be introduced in detail.

5.2 Rowland circle method and the designed devices

The Rowland circle method is the earliest one to construct EGs. The basic theory of the Rowland circle was introduced in the second chapter. The dominant formula used to construct the device is based on formula Equation 5.1 while it is rewritten here:

$$(\sin \alpha + \sin \beta)d = m \frac{\lambda}{n} \quad \text{Equation 5.1}$$

A basic Rowland mounting is shown in Figure 5.5. The design usually starts with selecting a

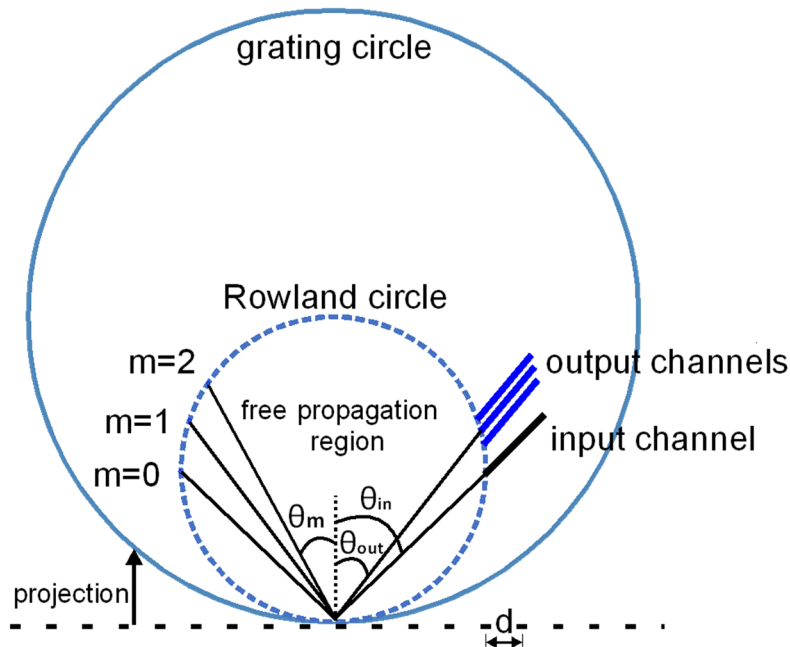


Figure 5.5: Schematic of a Rowland mounting.

coordinate system, here the Cartesian coordinate system is used. At first, the Rowland circle with using coordinate $[0, y]$ as the center and $R_R = y$ as the radius is drawn. Then the grating circle with using coordinate $[0, 2y]$ as the center and $R_G = 2y$ as the radius is drawn. As a result the two circles will be tangent at the origin $O [0, 0]$ of the coordinate system. If considering the input port as a point on the circle and knowing its coordinate, say $I [x, y]$, then the input angle is just the angle between vector \vec{IO} and the y axis which is easy to calculate. In reverse, if giving the input angle, the coordinate of the input point is easily obtained as well. In practice, we predefine the input and output angles that the coordinates of the input point and output points are calculated afterwards.

The dominant part of the entire calculation is the calculation of the grating points. To this end, the definition of the grating order should be defined first of all. In Figure 5.5, considering the y axis as the normal, the 0th order is defined as the the diffraction angle $\theta_{m=0}$ equal to the reflection angle. In this mounting, θ_{in} corresponds to α and θ_{out} to β in Equation 5.1. Substituting $m = 1$ into Equation 5.1, the

diffraction angle $\theta_{m=1}$ can be obtain accordingly. The resulted diffraction angle point on the Rowland circle can be derived as well. As shown, with increasing the diffraction order, the diffraction angle point moves towards the input point. In the design of this thesis, the input angle α , output angle β , diffraction order m , refractive index n and the operating wavelength λ are input parameters that the grating distance d can be easily obtained according to Equation 5.1. With setting a range for the grating points, say $[-x_1, \dots x_1]$, the resulting grating points can be calculated (dotted line). By projecting these points onto the grating circle, the coordinates of the final grating points are obtained.

The reflectors construction is based on the calculated grating points. As Figure 5.6 shows, we merely

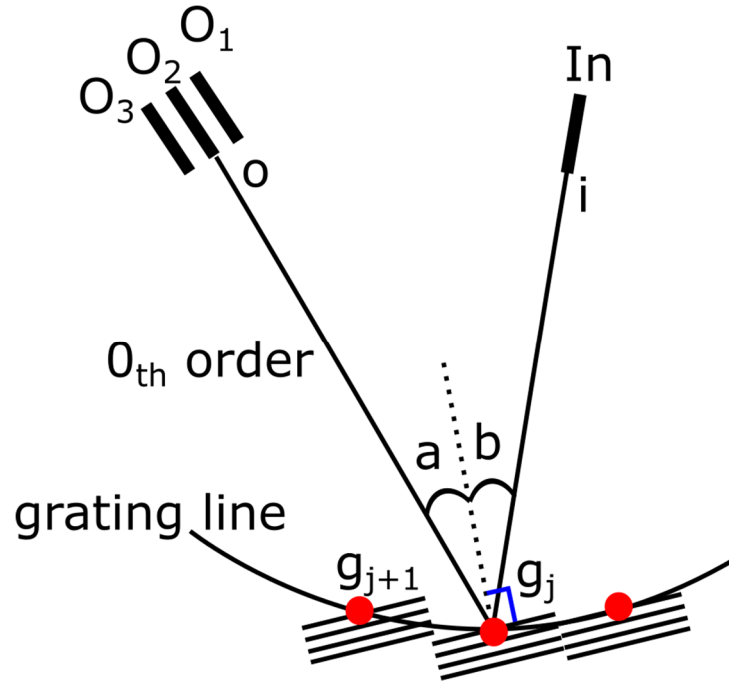


Figure 5.6: The tilting of the Bragg reflectors.

connect the input point i , one grating point g_j and the output point o , the resulting angle is $\angle ig_jo$. Then the reflector is tilt properly to reflect light from i to o , namely angle a is identical to b in the above figure. The length of the reflector can be determined by projecting the two adjacent grating points onto the already tilted reflector trace. Similarly, the remaining reflectors are calculated successively.

It is worth mentioning the reflectors used in this work are Bragg reflectors with four periodic units. The geometry of the reproduction unit in a Bragg reflector is shown in Figure 5.7. The width of one



Figure 5.7: Schematic of a reproduction unit in a Bragg reflector.

SiO₂ block is L, the distance Λ is the pitch size Λ . The general design theory is the Bragg's law in Equation 5.2 [14] where m is the order. For the first order and vertical incident, it is simplified to $\lambda = 2\Lambda$. In the material, the effective wavelength is used meaning $\lambda_{\text{eff}} = \lambda/n_{\text{eff}} = 2\Lambda$. For the SOI platform, $n_{\text{eff}} \approx (n_{\text{Si}} + n_{\text{SiO}_2})/2 \approx (3.48+1.44)/2 \approx 2.46$. In consequence, the calculated pitch size $\Lambda \approx 315$ nm for incident wavelength at 1550 nm. In our design, the value of parameters Λ and L used in the design are 322 nm and 161 nm, respectively. According to the research in [129], the reflection can achieve 98.6% and little loss is induced by the Bragg reflector design.

$$m\lambda = 2d \sin \theta \tag{Equation 5.2}$$

Another important issue in the design is the calculation of the angle of the output ports if more than one output port is used. Considering there are 5 output ports in total, their operating wavelengths are designed to be $\lambda_1, \lambda_2, \lambda_3, \lambda_4$ and λ_5 respectively. The operating wavelength difference between any two adjacent output ports is equal to $\Delta\lambda$. The calculation sequence is the same as above. However, the predefined output angle here is the angle for the 3rd output channel whose operating wavelength is λ_3 . Then the coordinate of the 3rd output port can be calculated according to the given parameters following the steps above. The coordinates of the remaining output ports requires a little more efforts. As shown in Figure 5.8, the central output port has a predefined output angle of θ_{out} . The incident light with

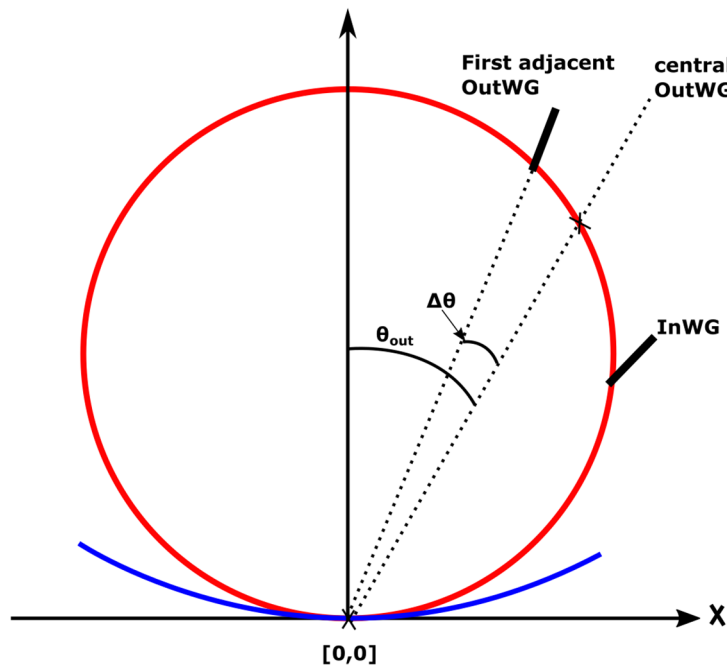


Figure 5.8: Calculation of the angle of the output ports.

wavelength λ_3 will be filtered to output port 3 (the central output port) by design. The light with wavelength λ_2 ideally will be guided to output port 2 whose output angle has an angle difference $\Delta\theta$ with respect to θ_{out} . Once the parameter $\Delta\theta$ is known, the coordinate of output port 2 can be easily calculated out with the same method above. Normally, the output angle of output port 2 can be reversely calculated out still using Equation 5.1. Then the linear relation between the output angle and the wavelength difference can be derived to be Equation 5.3. If knowing the channel spacing, the dispersion angle can be easily obtained by Equation 5.4. The channel spacing $\Delta\lambda$ is calculated by Equation 5.5 where λ_{max} and λ_{min} are the maximum and minimum operating wavelengths for the output ports. To maintain compatibility to commercially available telecommunication equipment, the (de-)multiplexer

channels should fit into the grid ITU-T G.694.1 [130]. The output angle of the output port 2 is obtained and the coordinate of this port can be obtained as well.

$$\frac{d\theta}{d\lambda} = \frac{(\sin \theta_{in} + \sin \theta_{out})}{\lambda \cos \theta_{out}} \cdot \left(1 - \frac{\lambda}{n_{eff}} \frac{dn_{eff}}{d\lambda}\right) \quad \text{Equation 5.3}$$

$$\Delta\theta = \frac{d\theta}{d\lambda} \cdot \Delta\lambda \quad \text{Equation 5.4}$$

$$\Delta\lambda = \frac{\lambda_{max} - \lambda_{min}}{N - 1} \quad \text{Equation 5.5}$$

Another important part for the design are the access waveguides connecting single mode waveguides and the slab region. To achieve adiabatic transmission, the single mode waveguide is tapered from 500 nm to 2 μm over a length of 30 μm before the light enters the slab region [131][132]. As shown in Figure 5.9, the parameter are: $wg_width = 500 \text{ nm}$, $taper_width = 2 \mu\text{m}$ and $taper_length = 30 \mu\text{m}$.

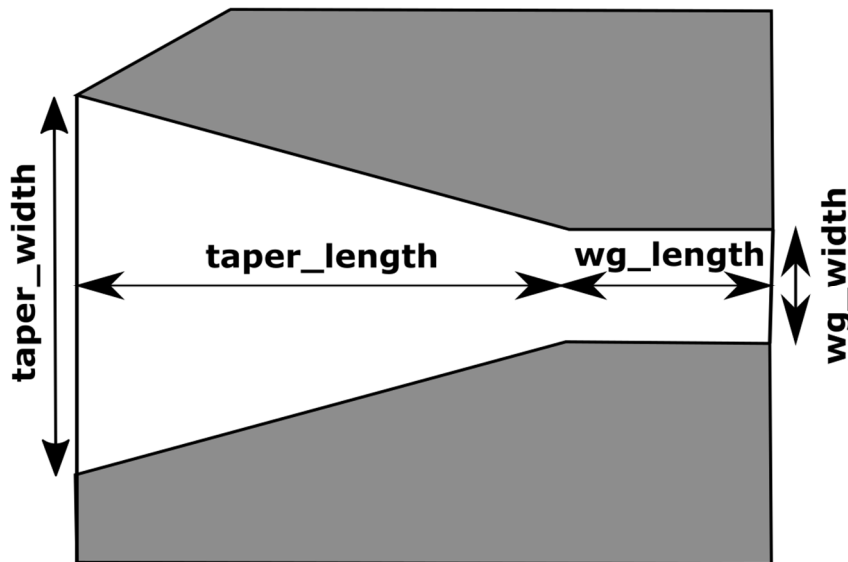


Figure 5.9: Schematic of an adiabatic taper.

5.2.1 Echelle gratings development kit

In this thesis, a customized design kit [133] is developed based on MATLAB and COMSOL Multiphysics. The MATLAB program integrates both the Rowland circle method introduced in former section and the two stigmatic point method that will be investigated in the later section. The general working process is presented in Figure 5.10.

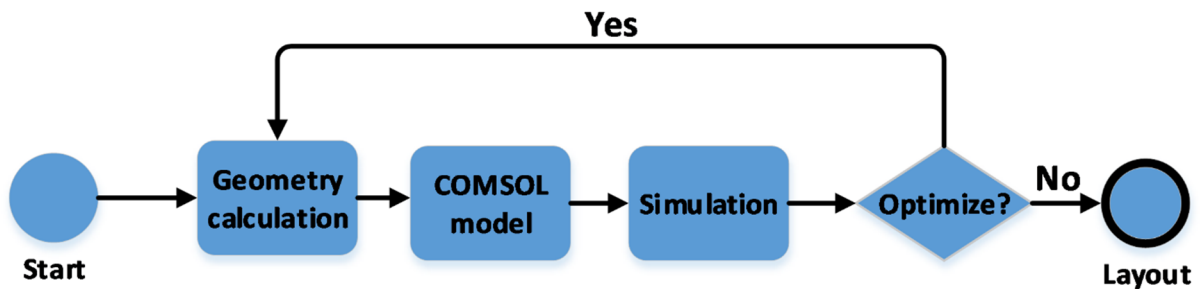


Figure 5.10: General process for designing Echelle gratings with the development kit.

The design of the EGs starts from defining the required parameters for constructing an Echelle grating DMUX for instance: the radius of the Rowland circle; the angles of the I/O ports; the number of the output ports, the maximum and minimum wavelengths for the output ports, the material system, the diffraction order etc.. Since there is a special interface between MATLAB and COMSOL Multiphysics, the programmed model in MATLAB can be transferred into a usable simulation model for COMSOL. The generated model is simulated with the ‘WaveOptics’ module in the frequency domain. By making a frequency sweep across the C band, the transmission spectrum can be obtained. Depending on the geometry size of the EGs, the simulation can be divided into several submodels since the numerical calculation takes a lot of CPU and RAM sources. According to our experience, an EG with a dimension of $100 \times 100 \mu\text{m}^2$ can use over 100 hundred GB memory.

After the complete simulation, one can make a brief analysis. If the transmission spectrum is not satisfactory, one can adjust the design parameters accordingly. Normally, adjustments on the Rowland circle radius, angles of the I/O ports and the diffraction order have a significant influence so that these parameters should be adjusted first of all. If the simulation results finally meet the requirements, a GDSII layout can be generated, which is usable for most foundries. An example GDSII layout is shown in the Figure 5.11, dominated by the free space region with the waveguide ports on the right side and the curved gratings on the left side.

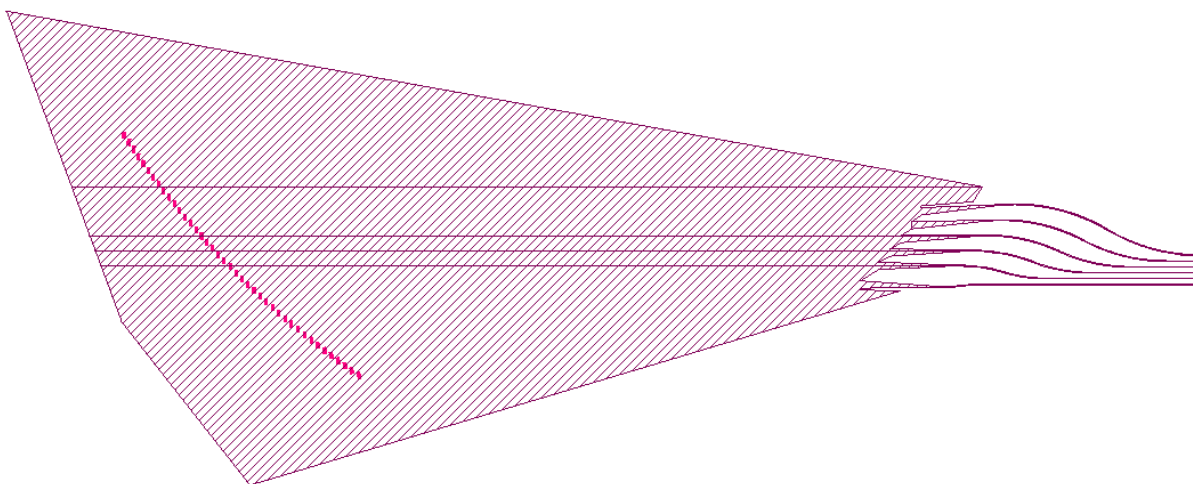


Figure 5.11: An example GDSII layout file generated by the development kit.

5.2.2 Two 1×5 1600-GHz EGs with and without absorbers

In the EGs design, the access waveguide is tapered to avoid excessive beam spread in the slab region. However, the adiabatic taper can not ensure that the light divergence angle in the slab region is smaller or comparable to the grating span. In this case, a stray light attenuation region (also called the absorber) is used for the EG design in this thesis. An example GDSII layout of an EG with highlighted absorber regions (black borders) is illustrated in Figure 5.12.

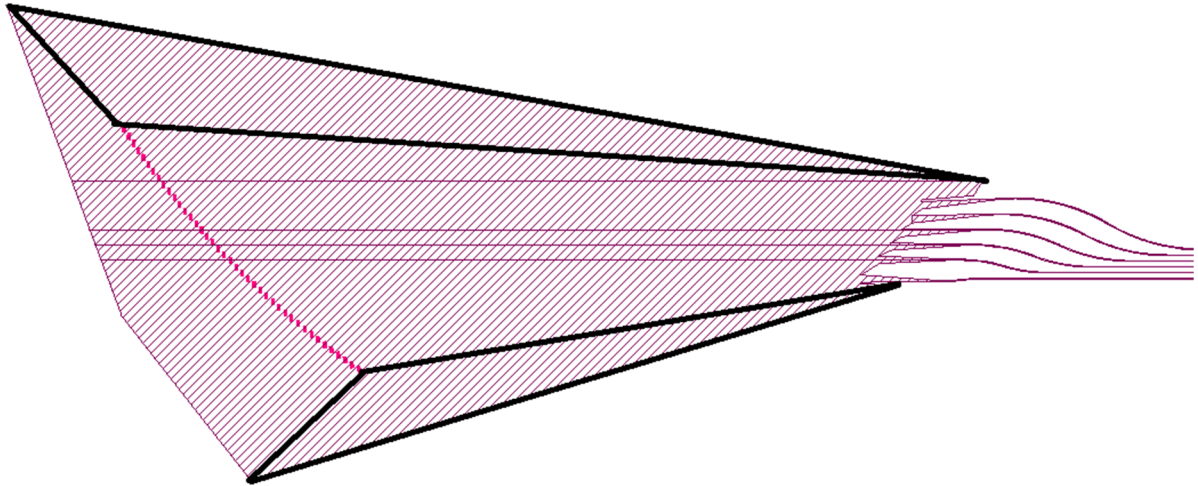


Figure 5.12: Schematic of an example GDSII layout of EGs with absorbers highlighted.

To verify the design method integrated in the development kit, the function of the added absorbers and also the simulation accuracy, a simple TE-polarized 1×5 1600-GHz example device was designed and fabricated at IMS CHIPS on a 250 nm SOI platform where the core silicon layer is 250 nm thick, the buried oxide layer is 2 μm and the top SiO_2 cladding is about 1 μm thick (without special notice, the devices presented in this thesis are all fabricated at IMS CHIPS on a 250 nm SOI platform). There are five output ports in total in this device with a designed channel spacing of 1600 GHz and the operating wavelength of the central port is 1552.5 nm. The radius of the Rowland circle is set to be 180 μm . The diffraction order of this device is nine. The angles of the input port and the central output port are 46° and 42° , respectively. The final GDS layout of the fabricated device and the corresponding transmission spectrum of the simulation and measurement results are illustrated in Figure 5.13 and Figure 5.14, respectively. For the measurement, the same tunable laser source as the one in Chapter 4 is used which can provide a wavelength range from 1524 nm to 1576 nm. The output power of the laser is set to 6 dBm. Before the laser signal enters the chip, a polarization controller is used to maintain TE polarization. The final output signal is fed to the detector head as mentioned in Chapter 4. In Figure 5.14, the full-line transmission spectrum is from the measurement result while the dot-line spectrum is from the simulation results.

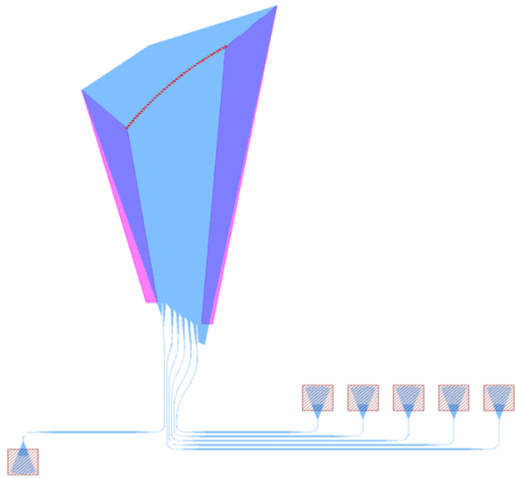


Figure 5.13: Layout of the designed 1×5 device based on RC design method.

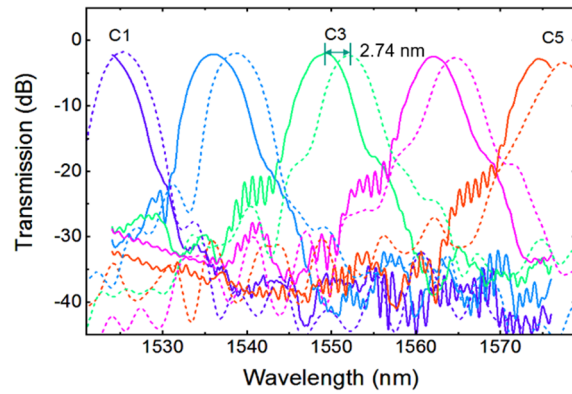


Figure 5.14: Simulated (dotted line) and measured transmission spectrum (full line) of the 1×5 device.

The on-chip footprint of this 1×5 device is about $100 \times 300 \mu\text{m}^2$, if the grating couplers are not taken into account. According to the obtained transmission spectrum, the transmission peaks of each channel are approaching a similar level resulting in an average simulated insertion loss of 2.0 dB and average crosstalk of -29.3 dB. On the other hand the measurement results are excellent as well, where the mean insertion loss and crosstalk of these channels are 2.3 dB and -30.6 dB, respectively. It can be seen that the simulation results and the measurement results fit quite well in terms of the insertion loss and crosstalk which verifies the accuracy of the used simulation model. However, there exists a significant wavelength shift as shown in Figure 5.14. The measured spectrum encounters a global red shift of 2.74 nm with respect to the simulated spectrum. In terms of the wavelength shift, there are several proposed possible reasons: the value of the used effective refractive index, the thickness variation of the core layer, the phase error induced by the approximation of RC method (a small radius of the Rowland circle), the error induced by the algorithm itself, and the diffraction order induced reflector variation. These factors will be examined subsequently in the later sections.

Another device without the absorbers but otherwise identical is fabricated as well to examine the effect induced by the absorbers. The measured transmission spectra of the two devices are illustrated in Figure 5.15 where the full line is from the EG with absorbers while the dotted line is from the EG without

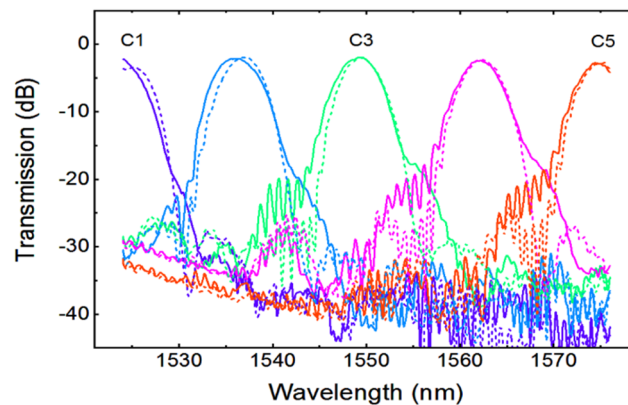


Figure 5.15: Transmission spectra of the 1×5 EGs with (full line) and without absorbers (dotted lines).

absorbers. From the comparison, no evident improvement is obtained with respect to the insertion loss and the crosstalk. The average insertion loss and crosstalk of the device without absorbers are -2.7 dB and -27.1 dB, respectively. Both data are slightly worse than the EG with absorbers. Even though the measurements are made at the same batch, the manually-made measurements cannot ensure each set of measurements are under absolutely identical test conditions. Therefore, the slightly worse performance on the insertion loss and the crosstalk do not necessarily tell the real difference between EGs with and without absorbers. Within the measurement accuracy the EGs have an identical performance.

5.2.3 800-GHz EGs

The designed EGs in the above section present a good performance, and verify the feasibility of the design method for a large channel spacing device with only a few channels. But in practice, an EG is usually required to have more channels and narrower channel spacing. Therefore, a further study on the devices is carried out in this section.

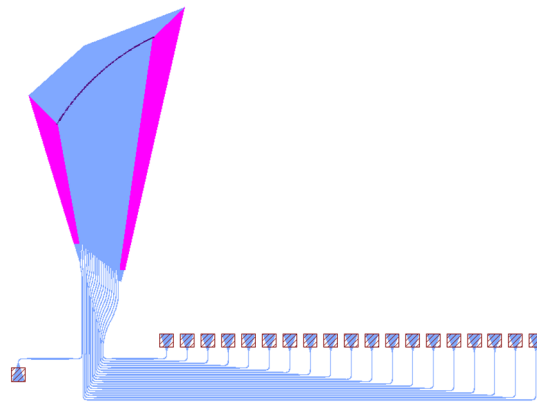


Figure 5.16: Layout of the 1×19 800 GHz EG.

The first device is designed to have a channel spacing of 800 GHz. To make it comparable with the device shown in the former section, its design parameters are kept similar as much as possible. To be more specific, the angles of the input and output angles are 48° and 42° respectively, the radius of the Rowland circle is $250 \mu\text{m}$, the diffraction order remains to be nine. Whereas, the number of channels is 19, many more than the former device. These channels are designed to be usable from 1470 nm to 1630 nm with a central wavelength of 1550 nm. Nevertheless, there are only several channels located in the C band which can be characterized by the available equipment. The final GDSII of this device is shown in Figure 5.16. The resulted on-chip footprint of this device is $250 \times 520 \mu\text{m}^2$, if the grating couplers are not considered.

The fabrication and measurement is the same as for the device presented in the former section. Limited by the wavelength range of the laser source, there are only several channels measurable for this EG. The simulated and measured transmission spectra of the device are shown in Figure 5.17. As can be observed, there is still 1.7-nm global red shift for the measured spectrum compared with the simulated

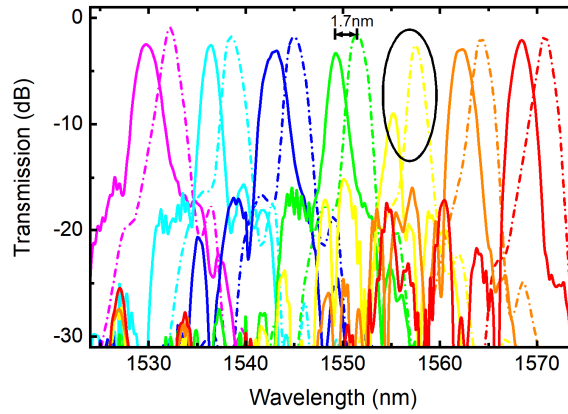


Figure 5.17: The simulated (dash dotted line) and measured (full line) transmission spectra of the designed 1×19 EGs.

result. Compared with the 1600-GHz EGs, the wavelength shift is smaller but on the other hand the channel spacing of this device is also smaller. In this design, there is an evident broken channel that is highlighted with a black circle in the graph. The measured insertion loss of this broken channel is as high as 9 dB, much higher than the value of the other channels. Except for this broken channel, the other channels work well and fit well to their simulation results. To be specific, the average measured insertion loss and crosstalk of the remaining six channels are 2.76 dB and -26.02 dB while the value from the simulation are 2.38 dB and -30.47 dB, respectively. The actual performance of this device deviates more than that of the 1×5 1600 GHz EG, showing that constructing an excellent narrow channel spacing EGs requires more efforts. Both the broken channel and the performance deterioration of the device presented in this section can be related to the fabrication accuracy and also can be related to the design itself.

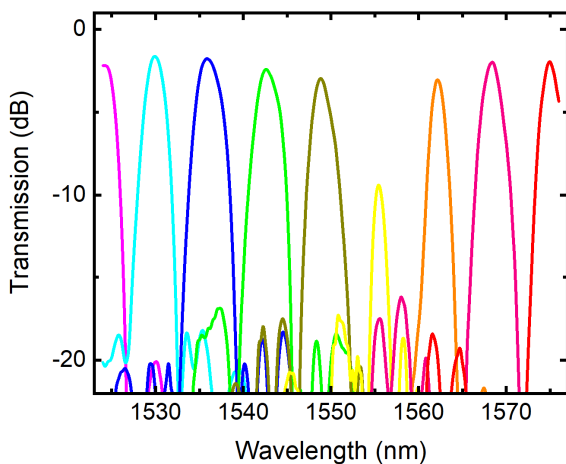


Figure 5.18: Measured transmission spectrum of the 1×11 device with $m=9$.

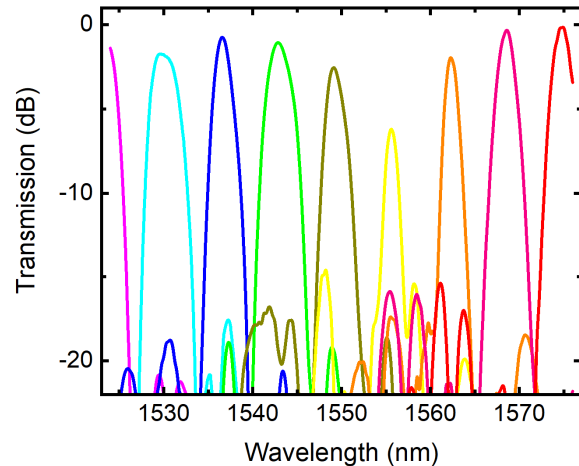


Figure 5.19: Measured transmission spectrum of the 1×11 device with $m=2$.

To check the influence of the key parameter diffraction order on the 800-GHz devices, another two similar devices were designed and fabricated to make the comparison. For both device, the angles of the

input and output ports are 46° and 41.5° , respectively (both values are close to those of the above 1×19 device). The radius of the Rowland circle is set to $320 \mu\text{m}$. There are 11 output ports whose minimum and maximum wavelengths are $1.49 \mu\text{m}$ and $1.61 \mu\text{m}$. The access waveguides of two devices are adiabatically tapered from 400 nm to $3 \mu\text{m}$ over a length of $30 \mu\text{m}$. The difference of two devices come from the diffraction order, they are two and nine, respectively. Due to their large footprint, the measurement results are illustrated in Figure 5.18 and Figure 5.19 respectively. The two devices have nearly the same peak wavelength for each channel. Taking the green spectrum as an example, the peak appears at 1542.5 nm in Figure 5.18 and 1543 nm in Figure 5.19. Both devices have a ‘broken’ channel (the yellow line in the graph). In general, the device which has a smaller diffraction order shows lower insertion loss than the other device. Similarly, if the broken channel is not taken into account, the measured average insertion loss are 2.2 dB ($m = 9$) and 1.2 dB ($m = 2$). Although the device with $m = 2$ shows around 1 dB lower insertion loss, the transmission peak of its channels differs a lot which is unexpected. On the other hand, their crosstalks are -20.5 dB ($m=2$) and -18.78 dB ($m=9$). In this design, decreasing the diffraction order decreases the insertion loss and the crosstalk. It shows a tendency that for the 800 GHz design, the device with a smaller diffraction order is beneficial to decrease the insertion loss which still requires more fabricated devices to verify. Additionally, comparing this result with the result of the abovementioned 1×19 device, a general result is: a smaller insertion loss but a bigger crosstalk is obtained with changing the I/O angles slightly and increasing the Rowland circle radius and the width of the access waveguides.

The performance variation induced by the diffraction order does not have an influence on the global wavelength shift. Another factor can be the wafer quality and the fabrication quality. To examine the effect induced by them, two identical devices are designed and located at different places on one common wafer. The design parameters are set as: the angle of the input port is 48° , angle of the output port is 42° , Rowland circle radius is $250 \mu\text{m}$, diffraction order is nine, the maximum operating wavelength is 1630 nm , the minimum operating wavelength is 1470 nm and the output channel number

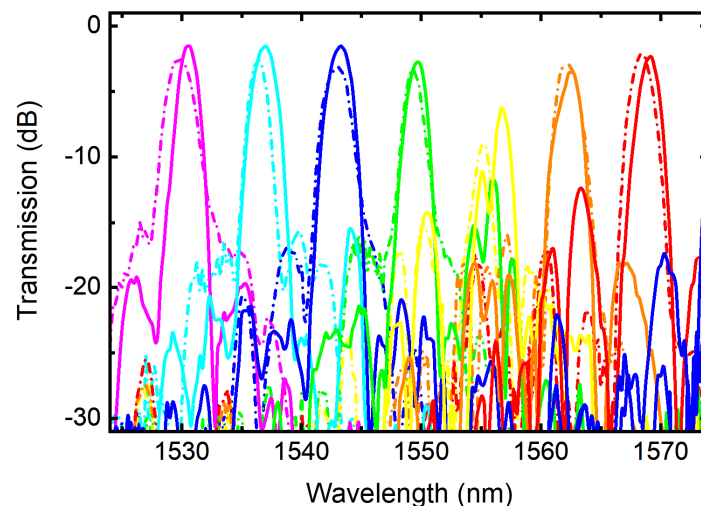


Figure 5.20: Transmission spectra of two formally identical devices at different locations on a common wafer. Device 1 is dotted line, device 2 is full line.

is 19 with a channel spacing of 800 GHz . The measured transmission spectra of the two devices are illustrated in Figure 5.20 where device 1 is represented by dotted line and device 2 by full line. In this comparison the insertion loss and the crosstalk are not the focus and omitted here. As can be seen, most

peaks overlap roughly. However, the peak wavelengths and the widths of the peaks still vary considerably. For instance, the magenta peaks appear at 1529.75 nm (dotted line) and 1530.5 nm (full line). The wavelength difference is 0.75 nm. This comparison shows that even on a common wafer, its quality is not homogeneous enough so that two formally identical devices have considerable peak wavelength difference for individual channels. Furthermore, the fabrication technique is not homogeneous either, since the spectrum shape varies significantly for each channel, even though ignoring the peak shift. To obtain stable performing devices, an improved wafer quality and fabrication quality seems to be required.

5.2.4 The 1×9 EG DMUX in the integrated transmitter

Considering the global wavelength shift between the simulated and the measured transmission spectra of devices shown before, it is beneficial to have more channels fitting into the wavelength range of the tunable laser source. Based on this consideration, the EG used in the 4-channel integrated transmitter is designed to have nine output channels with a channel spacing of 400 GHz. For this device design, the angle of input port is 53° , the angle of the output port is 51° , the radius of the Rowland circle is $600\ \mu\text{m}$, the diffraction order is nine, the maximum peak wavelength is 1533.5 nm, the minimum peak wavelength is 1559 nm, the central peak wavelength is around 1546 nm. Due to the large footprint, a simulation is not available for this device. The measured transmission spectrum of this device is shown in Figure 5.21. The average insertion loss is about 4 dB and the average crosstalk is -14.8 dB. In this

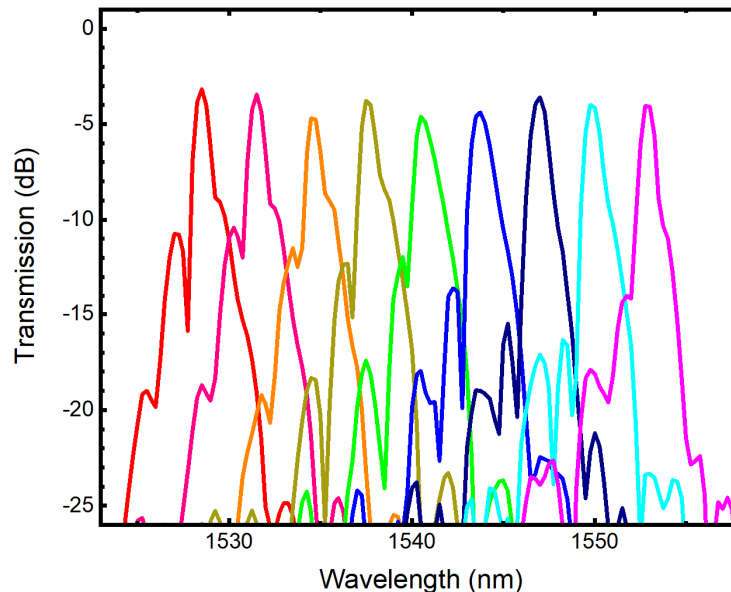


Figure 5.21: Measured transmission spectrum of the 1×9 EGs for the integrated transmitter.

design, the central peak appears at 1540.5 nm, shifting 5.6 nm from the original design. As can be observed, even though increasing the radius of the Rowland circle dramatically, the global wavelength shift still exists, the wavelength shift is therefore not dominantly determined by the phase error induced by the Rowland circle method. Comparing the general insertion loss of the 800 GHz devices shown in the former section, the insertion loss and crosstalk of a 400 GHz device is much higher (in this designed device already achieved 4 dB in average). To construct a narrower channel-spacing device with the currently used Rowland circle method and with good performance is difficult. Therefore another method is investigated, shown in the following paragraph.

5.3 Two stigmatic point method and the additional parameter ΔN

The RC method is widely used in EG design and it is also the traditional method used in our project. Whereas, the fabricated devices presented in the previous section show ‘broken’ channels for some devices, and there is considerable global wavelength shift in the device. Additionally, the degree of wavelength shift varies a lot for different cases. In the meanwhile, the performance of the designed devices deteriorates significantly from 1600 GHz to 800 GHz and 400 GHz devices, indicating that constructing a more advanced device with more channels and narrower channel spacing based on the currently used RC program will be difficult.

In this case, a more accurate design method is considered in designing the EGs, namely the Two Stigmatic Point (TSP) method [134][135][136][137]. This method was proposed quite early, while limited by the design compatibility, it is hard to be used in the SOI platform. In 2008, fabricated EGs using the TSP method on an SOI platform were reported in [138][139]. Whereas, the TSP-based devices presented by the authors feature a relatively high insertion loss of 4 dB ~ 9 dB. Afterwards, the research on using TSP method to construct EGs became more popular [128]. Inspired by this, a study on the TSP method is carried out in this thesis as well to help find the problems in our design. It is also expected to improve the performance of the designed device. Some research results from the thesis are also published in [140][141].

5.3.1 Basic design method

Different from the construction of an EG based on the RC method, the position of each grating points in the TSP method is calculated directly instead of the point projection in the RC method. Before starting the formal construction of an EG using the TSP method, it is worthwhile to mention that the basic property used in this method is from the key property of the ellipse that will be introduced in the following.

A general ellipse is shown in Figure 5.22, the two foci of the ellipse are F_1 and F_2 . The midpoint of

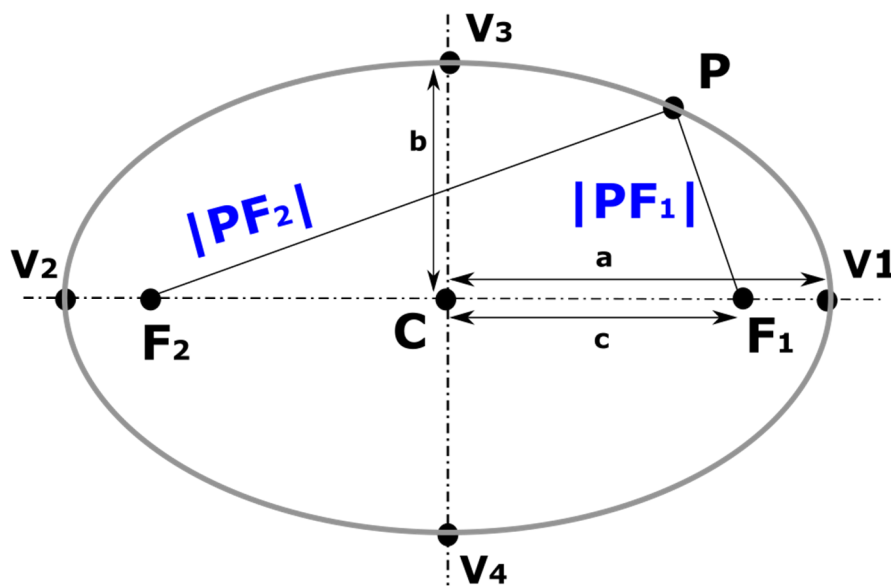


Figure 5.22: Schematic of an ellipse for introducing its basic property.

the line segment F_1F_2 is depicted as point C. If constructing a coordinate system with setting point C as

the origin, the x axis goes through points F_1 and F_2 and the y axis is perpendicular to the line segment F_1F_2 . There will be four vertices generated, V_1, V_2, V_3 and V_4 . The length of CF_1 is c , the length of V_3C is b and the major axis length of CV_1 is a . Then, any random point P on the ellipse has the property $|PF_1| + |PF_2| = 2a$. In the meantime, a, b and c have the relation that $a^2 = b^2 + c^2$ and the ellipse equation is expressed by Equation 5.6. The ellipse equation is the basis of constructing the EGs based on the TSP method in the following.

$$\frac{x^2}{a^2} + \frac{y^2}{b^2} = 1 \quad \text{Equation 5.6}$$

In the calculation of the EG geometry, the input port and the output ports are regarded as several individual points. Considering an EG has one input port and two output ports, which are marked as O, F_1 and F_2 in Figure 5.23, they are all located on the x axis with predefined coordinates. The effective

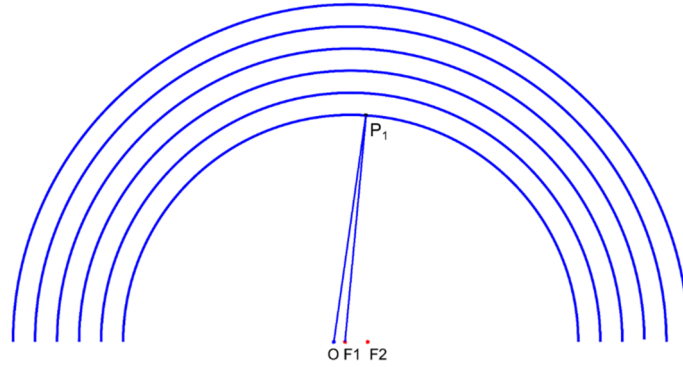


Figure 5.23: Constructing the first set of ellipses of the EGs.

operating wavelength for two output ports are λ_{eff1} and λ_{eff2} , respectively in the material. Now we select points O and F_1 as the two foci of ellipses and define their major axis length according to Equation 5.7. The parameter m is the diffraction order, and a positive integer. The parameter i is a positive integer, and a defined range. If increasing the value of i gradually, a series of ellipses can be constructed as shown in Figure 5.23.

$$2a_1 = \lambda_{eff1} \times m \times i \quad \text{Equation 5.7}$$

In the next step, the input point O and another output point F_2 are regarded as the two foci of a set of ellipses. Similarly, defining the major axis length of this ellipse has the form of Equation 5.8, so that with varying the parameter i , a_2 will change. As a consequence, another set of ellipses can be constructed as well, as shown in Figure 5.24.

$$2a_2 = \lambda_{eff2} \times m \times i \quad \text{Equation 5.8}$$

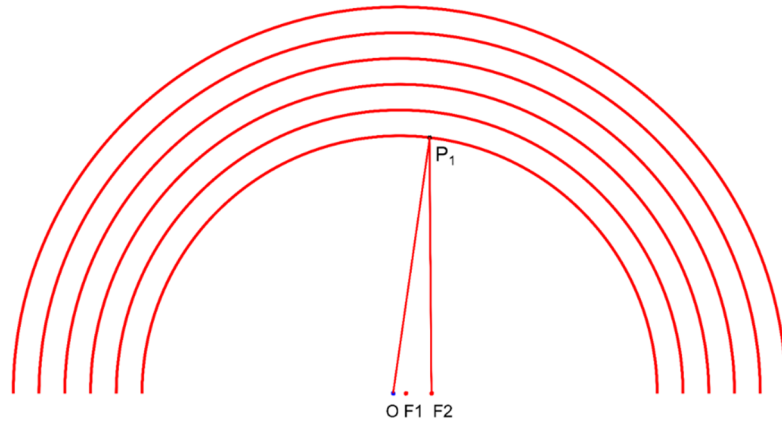


Figure 5.24: Constructing the second set of ellipses of the EGs.

The two sets of ellipses intersect and generate a set of intersections as shown in Figure 5.25. According to the property of the ellipse introduced in this section, Equation 5.9 stands for the first set

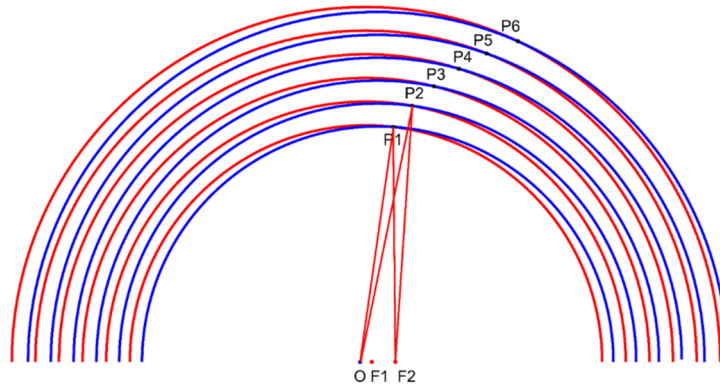


Figure 5.25: Intersections generated by the two sets of ellipses.

of ellipses indicating the optical path is integer times of the effective wavelength.

$$|\overrightarrow{OP_n}| + |\overrightarrow{P_n F_1}| = \lambda_{eff1} \times m \times i \quad \text{Equation 5.9}$$

A similar relation stands for the second set of ellipses as shown in Equation 5.10. The corresponding optical path is also a whole-number integer times the effective wavelength. It can be observed that if the light with effective wavelength λ_{eff1} is reflected at points $P_1, P_2 \dots P_n$, the reflected light can interfere constructively at point F_1 . Also, if the light with effective wavelength λ_{eff2} is reflected at points P_1, P_2, P_n , the reflected light can interfere constructively at point F_2 . It is easy to find that these resulted intersections $P_1, P_2 \dots P_n$ are suitable to place reflectors, namely the desired grating points.

$$|\overrightarrow{OP_n}| + |\overrightarrow{P_n F_2}| = \lambda_{eff2} \times m \times i \quad \text{Equation 5.10}$$

However, in practice, we usually prefer the designed EGs having more than two workable output ports. In this case, the location of the other output channels are also required to be calculated. Take a 1×3 EGs as an example. Imagine the effective wavelength for the third output port is λ_{eff3} . λ_{eff1} and λ_{eff2} are still the maximum and minimum operating wavelength and selected to be used to construct the

ellipses. The construction starts with repeating the steps above. The additional step in this case is the calculation of the coordinate of the third channel. For the third output port, similar relations stand as for output port 1 and 2. Therefore we have a general relation 5.10 for the third output port. Then the method to calculate the coordinate of the third output port F_3 can be realized by drawing a series of circles. The centers of the circles are the grating points $P_1, P_2 \dots P_n$ and the corresponding radii are given by Equation 5.11. A schematic of the construction of the third output port is shown in Figure 5.26. Ideally, these circles would intersect at only one point as drawn in the picture. However, in practice it is impossible. Therefore, the coordinate of the third output port is usually the geometrical average.

$$|\overrightarrow{P_n F_3}| = \lambda_{eff3} \times m \times i - |\overrightarrow{O P_n}| \quad \text{Equation 5.11}$$

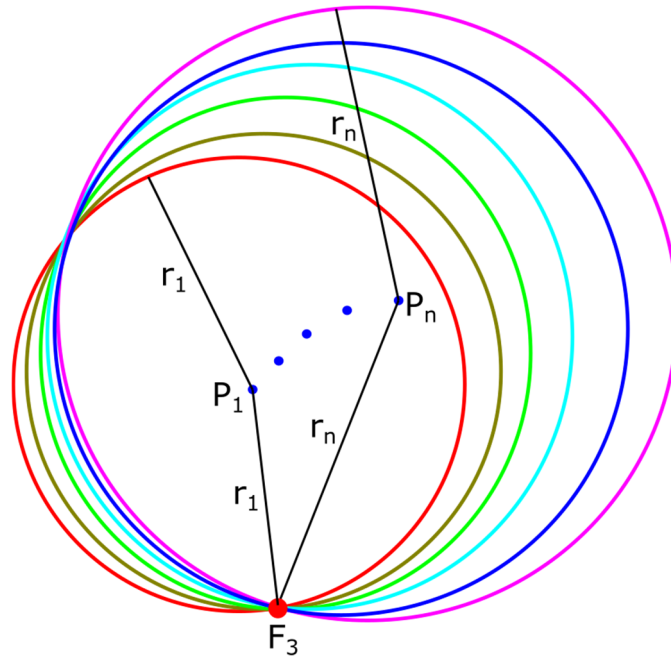


Figure 5.26: Schematic of the construction the third output port.

Based on the investigation of a 1×3 EG, a $1 \times n$ EG can be obtained as well. The maximum and the minimum wavelength are still used to calculate the grating points, the coordinates of the remaining output ports are calculated using the same method shown above.

Concerning the tilting of the reflectors, in this thesis the input point O and a central output point F_{central} are taken as the reference points. For any grating point P_n , the line segments $P_n O$ and $P_n F_{\text{central}}$ are used to construct the angular bisector ‘bisec1’ of $\angle O P_n F_{\text{central}}$. Then the reflector should be tilted to be perpendicular to the angular bisector ‘bisec1’. The length of the reflector is determined by the distance between the current grating point to the next grating point and the grating point is the midpoint of the reflector. A possible method to optimize the tilting and length of the reflectors can be found in [128], but only minor improvements were expected and could not be realized in this thesis.

5.3.2 Investigation on the introduced parameter ΔN

For the calculations in the former section, the parameter i used for constructing the grating points is uniformly considered identical for all ports. However, this parameter is not required to be identical in the construction. We can even introduce a variation into this parameter to obtain some special designs.

To study the effect of modifying the parameter i , it is worth to understand how the grating points are distributed. To this end, we can construct a series of grating points based on the common foci. The required parameters to construct the grating points are quite simple: the input point O is set as the origin $(0,0)$ of the used coordinate system, the coordinate of two foci are set to be located on the x axis $F_1(x_1,0)$ and $F_2(x_2,0)$, the effective wavelength corresponding to two foci are λ_{eff1} and λ_{eff2} , the range of the major axis length for calculating the grating points, the channel number N and the diffraction order m . On this basis, we firstly define the coordinate of the input point $O(0,0)$, output point $F_1(3\ \mu\text{m},0)$ and output point $F_2(9\ \mu\text{m},0)$. The range for calculating the major axis radius is defined from $45\ \mu\text{m}$ to $250\ \mu\text{m}$. The wavelength to be filtered to output port 1 and output port 2 are $1565.5\ \text{nm}$ and $1539.75\ \text{nm}$, respectively.

Using equation 5.6, we can get a set values for i_1 for the output port 1 and a series of ellipse functions can be obtained. Making the values of i_2 for output port 2 identical to those of i_1 , we can construct the ellipse functions for the output port 2 in the same way. Then, the two sets of functions generate the desired grating points. But if we introduce a difference between the values for i_2 and i_1 , say $i_2 = i_1 + 2$, then the resulting grating points will be different. Assuming for the first grating point, the optical path of $|\overline{OP_1}|$ and $|\overline{P_1F_1}|$ is $\lambda_{\text{eff1}} \times m \times N_1$ and the optical path of $|\overline{OP_1}|$ and $|\overline{P_1F_2}|$ is $\lambda_{\text{eff2}} \times m \times N_2$. By setting $i_2 = i_1 + 2$, the optical path of $|\overline{OP_1}|$ and $|\overline{P_1F_2}|$ will increase to $\lambda_{\text{eff2}} \times m \times (N_2 + 2)$ which also fits to all the grating points of each pair of two adjacent output ports.

Let us define $\Delta N = i_2 - i_1$ and let ΔN increases from 0 to 16. The calculated grating points are shown in Figure 5.27. While increasing ΔN from 0 to 2, the trajectory of the grating points shifts from the innermost black one to the next red one. Further increasing ΔN , the trajectory expands to the outer ones

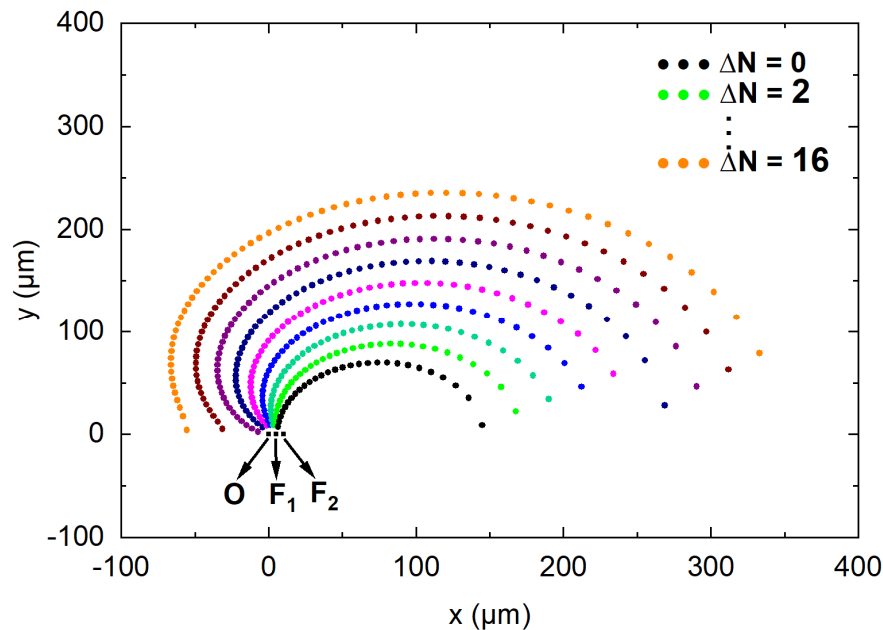


Figure 5.27: The trajectories of the constructed grating points with different ΔN .

gradually. In reverse, with decreasing ΔN , the trajectory of the grating points gradually shifts from an outer one to an inner one as well. Therefore, a change of ΔN directly determines in which trajectory the grating points will be located and can also affect the device footprint which will be further verified by the example devices later. Additionally, the grating points for each trajectory, are not evenly distributed. The distances between two neighboring grating points increase evidently with the x- coordinate where the reference line is composed of the grating points possessing the maximum y- coordinate in its corresponding trajectory.

However, the trajectories of the grating points in Figure 5.27 are the full span of the available grating points for the given parameters. In practice, we expect the footprint of the EGs to be as small as possible with a reasonable performance. Therefore, we just select a part of the grating points on a full grating span. For a given range of the major axis length, a different value of ΔN can also make a significant difference. To examine this, we still use the above mentioned model, but we shrink the range of the major axis value to $50\ \mu\text{m} - 75\ \mu\text{m}$. With this change, we can calculate the parameter i_1 for the output port 1, and we set ΔN to -8, -6, -4, -2, 0, 2, 4, 6, and 8. Then the nine generated sets of selected grating

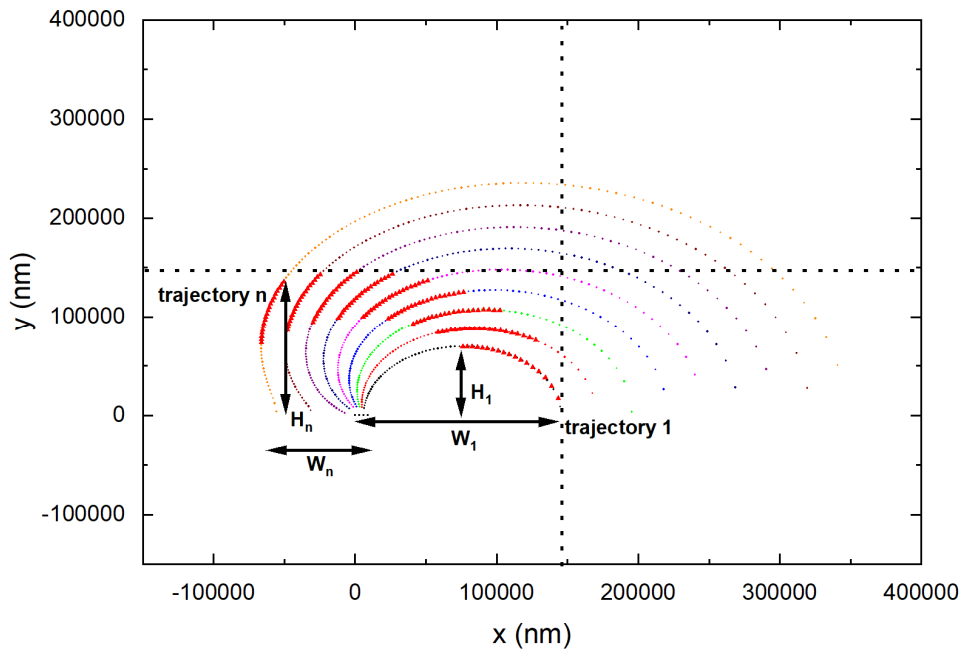


Figure 5.28: Grating points with given major axis scales and different ΔN , located on each trajectory.

points are shown in Figure 5.28. The black lines are auxiliary lines used to mark the maximum value of the y axis and the x axis resulting from these grating points. For each set of the generated grating points, W_n and H_n ($n = 1, 2, \dots, 8, 9$) are used to represent the maximum horizontal (x-) and vertical (y-) span resulting from the grating points and the I/O points. In Figure 5.29, we draw the curves for W_n and H_n as a function of ΔN . If we increase ΔN , the parameters W_n and H_n show reverse trends. W_n firstly decreases to a minimum at $\Delta N = 2$ then increases. In comparison, H_n firstly increases to a maximum at $\Delta N = 4$ then decrease. Considering that the horizontal and vertical span of an EG DMUX can represent its on-chip footprint approximately, then the product of W_n and H_n for different ΔN is shown in Figure 5.29. In this limited range of ΔN , there are two extremes, appearing at $\Delta N = -6$ and $\Delta N = 2$, respectively. Once the minimum point is found, the most compact design is usually obtained. Comparing the results of Figure 5.29 and Figure 5.30, it can be seen that W_n shows a strong impact on the on-chip footprint

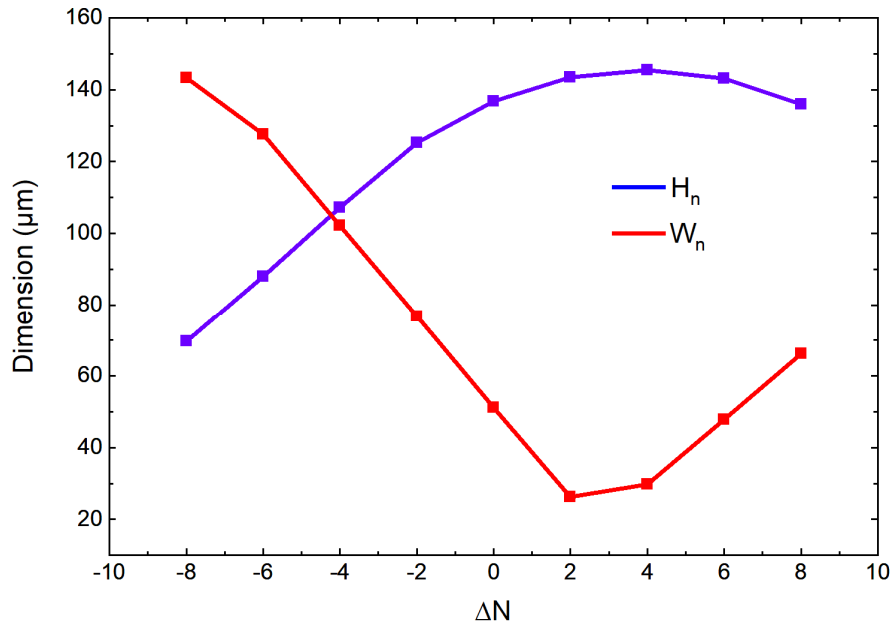


Figure 5.29: Maximum vertical and horizontal spans H_n and W_n of the calculated grating points in Figure 5.28 at different ΔN .

in this scheme. One can usually start with finding a small W_n to decrease the footprint of the device. With referring to the grating points' trajectories, if the generated grating points are located in the more densely populated region, a small W_n is easier to be obtained. Consequently, the angle of the input port will be affected as well when we adjust the parameter W_n by modifying ΔN .

The input angle is determined by calculating the angle determined by the grating points at the border and the input point. We make the input port direction to be the bisector of this angle so that the input

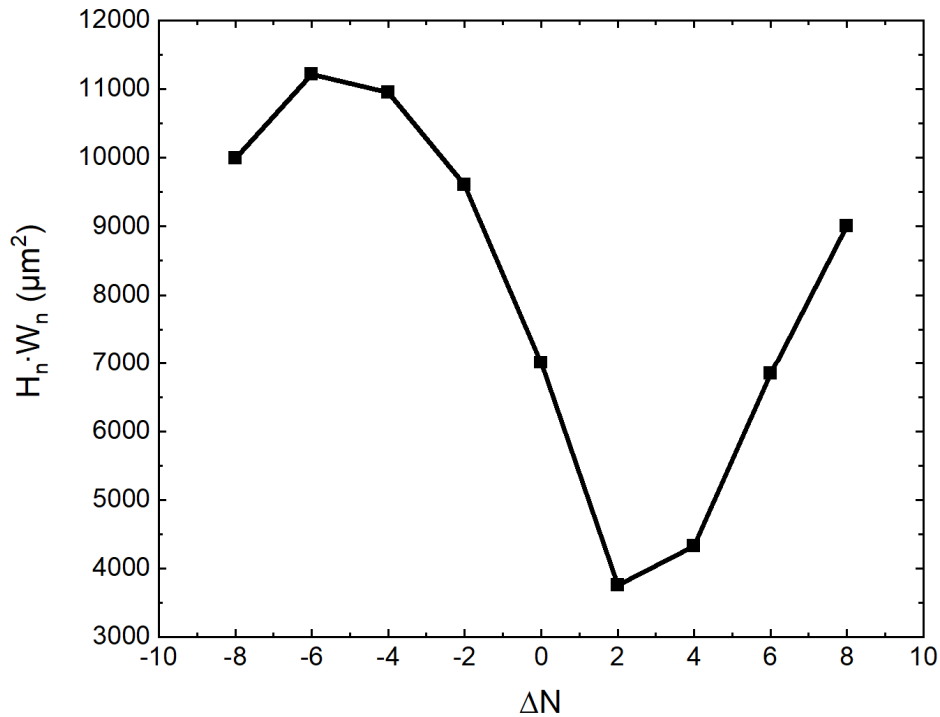


Figure 5.30: The product of H_n and W_n with respect to ΔN .

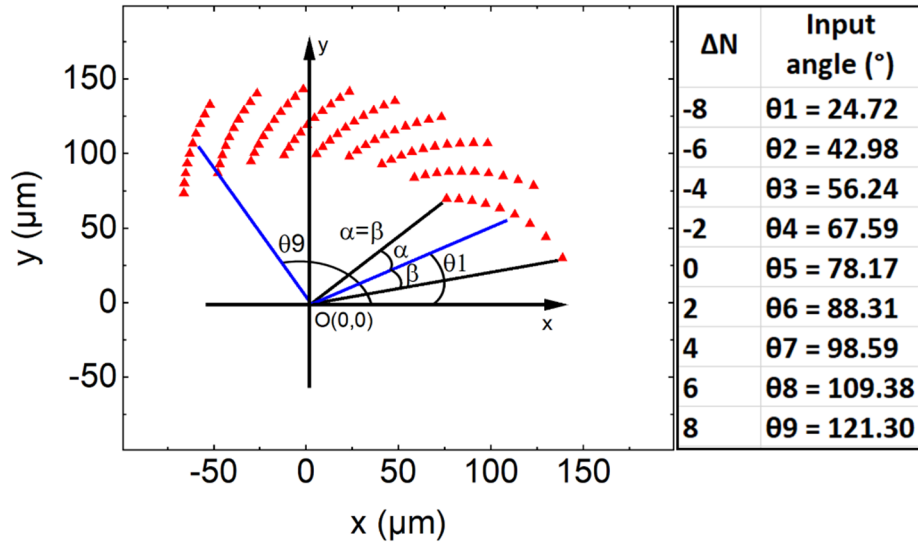


Figure 5.31: Input angles of the devices with different ΔN .

port's angle is obtained. As shown in Figure 5.31, 2α is the grating span and θ_1 is the input angle for the first set of the generated grating points. In the same way, the output port's angle can be calculated as well. Therefore, the input angle of each device varies when ΔN is changing. Then the input angle of each model is calculated and the result is listed in the inset table in Figure 5.31. According to the result, when increasing the parameter ΔN , the input angle increases as well. The minimum input angle in these models is 24.72° when $\Delta N = -8$. When $\Delta N = 2$ and $\Delta N = 4$, where W_n achieves the two smallest values, the input angles both are close to 90° , 88.31° and 98.59° respectively.

In the next, we construct several comparable devices to investigate the influence of modifying ΔN . It is worth mentioning that all the devices in this thesis are designed for TE polarization and a 250 nm silicon on insulator (SOI) platform. Commonly, we set the number of output ports to seven and the channel spacing to 800 GHz, the maximum and minimum wavelengths are 1533.45 nm and 1572 nm. The diffraction order is nine, the coordinate is in μm for point O (0, 0) and two reference output points F1 (9, 0) and F2 (39.8, 0). The major axis length used to construct the ellipses is from 398 μm to 716 μm .

ΔN is set to different values as shown in Table 5.1. Among the listed devices, EG08 (ΔN is three) has the minimum on-chip footprint, the minimum W_n and the minimum grating span. It can be seen, the smallest on-chip footprint and smallest grating span occur synchronously. With respect to EG08, either increasing or decreasing ΔN , the grating span and $W_n \cdot H_n$ show a general ascending tendency towards both sides.

Table 5.1: Performance of the comparable 800 GHz devices.

Device	ΔN	$W_n \cdot H_n$ ($\mu\text{m} \cdot \mu\text{m}$)	Input angle ($^{\circ}$)	Grating span ($^{\circ}$)	Peak transmission (dB)	Crosstalk (dB)	1-dB bandwidth (nm)
EG01	-4	$546 \times 689 = 376194$	34.04	57.22	-1.01	-34.23	1.11
EG02	-3	$464 \times 699 = 324336$	44.92	48.01	-1.28	-34.96	0.92
EG03	-2	$407 \times 703 = 286121$	53.93	42.18	-1.38	-33.55	0.74
EG04	-1	$375 \times 708 = 265500$	61.60	38.84	-1.52	-34.38	0.70
EG05	0	$361 \times 713 = 257393$	68.38	37.23	-1.55	-36.06	0.64
EG06	1	$348 \times 713 = 248124$	74.79	36.10	-1.67	-32.96	0.64
EG07	2	$343 \times 714 = 244902$	81.01	35.55	-1.73	-31.17	0.59

EG08	3	342 × 713=243846	87.17	35.49	-1.70	-35.09	0.61
EG09	4	345 × 715=246675	93.35	35.89	-1.77	-36.53	0.64
EG10	5	356 × 718=255608	99.66	36.79	-1.74	-35.99	0.64
EG11	6	367 × 718=263506	106.23	38.28	-1.64	-35.50	0.66
EG12	7	388 × 717=278196	113.22	40.61	-1.62	-31.02	0.72
EG13	8	421 × 713=300173	121.10	44.02	-1.35	-34.89	0.79
EG14	9	478 × 700=334600	130.62	50.41	-1.14	-38.52	0.83

Among these devices, we select device EG08 as a reference device. On one hand, the input angle of the devices increases when we increase ΔN and it becomes closest to 90° at device EG08. On the other hand, all devices show a low insertion loss (≤ 1.77 dB) and low crosstalk (≤ -31.02 dB). Although the crosstalk remains relatively stable, the peak transmission and the 1-dB bandwidth of these devices show an ascending tendency into both directions with respect to the reference device. With this comparison, the transmission and 1-dB bandwidth can be enhanced while modifying the input angles of the devices by changing ΔN . Together with the increased grating span, the on-chip footprint increases, as well. Among these devices, EG01 and EG14 have the most extreme input angles (34.04° and 130.62°) and the most extreme grating spans. Both have excellent performance.

To investigate the performance variation of the above devices in detail, the phase error \bar{E} of each output port is calculated by Equation 5.12, where O is the input point, F is the output point, P_l is the l^{th}

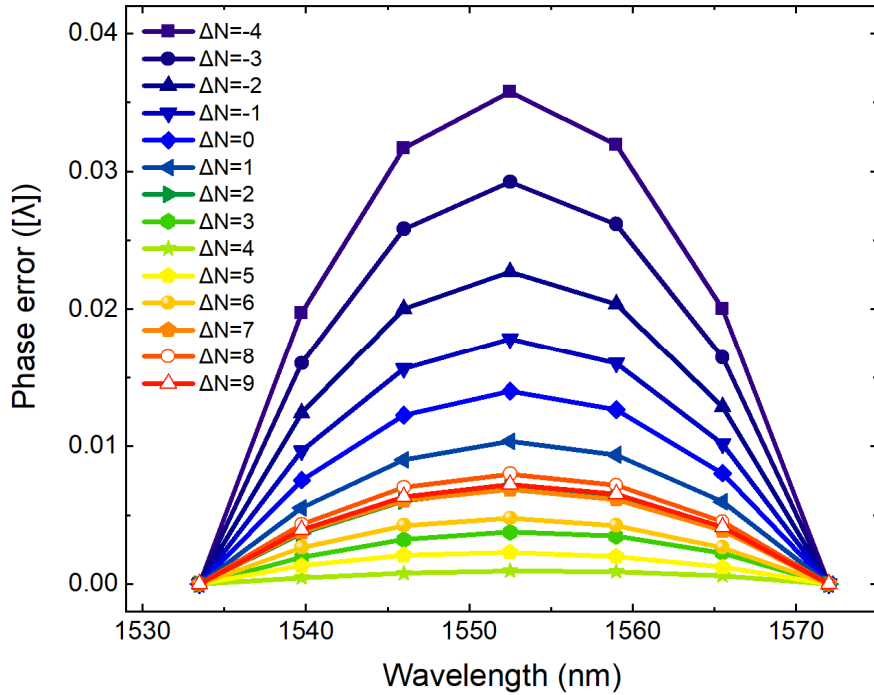


Figure 5.32: Phase error of the 800 GHz devices with different ΔN .

grating point and L_l is the optical path for the l^{th} grating point. The calculated phase errors of each output port with different ΔN are presented in Figure 5.32 for which the phase error is represented by the wavelength in the slab waveguide $[\lambda]$.

$$\bar{E} = \frac{1}{n} \times \left| \sum_1^n (|\overrightarrow{OP_l}| + |\overrightarrow{P_lF}|) - L_l \right| \quad \text{Equation 5.12}$$

As shown, two stigmatic ports have no phase error and the overall phase error shows a general decrement with ΔN . The minimum phase error for the non-stigmatic ports is in the order of 10^{-4} [λ], achieved at $\Delta N = 4$ where the input angle is 99.24° . Afterwards, the phase error increases with ΔN . Nevertheless, the phase error is basically smaller than 0.01 [λ] when $\Delta N > 0$. According to the result in Figure 5.32, it is preferable to modify ΔN to a positive value in the given design parameters to achieve a low optical phase error.

On the other hand, the simulation result in a table is not so evident. So, a comparison of the measured and simulated transmission spectra is necessary. The fabricated device EG08 has simulated and measured transmission spectra shown in Figure 5.33. The measured average insertion loss is 2.5 dB with

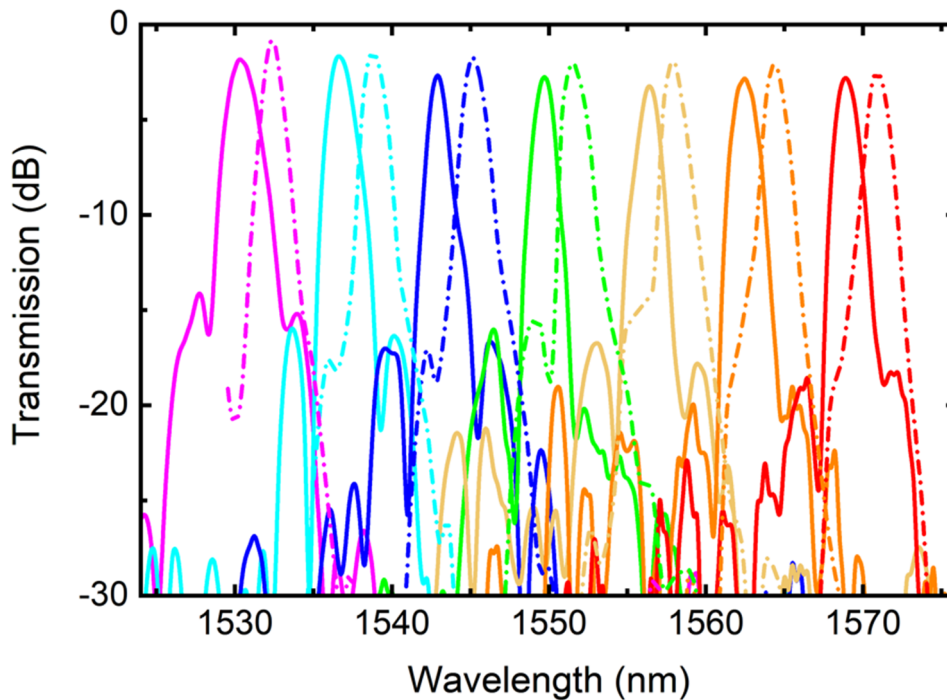


Figure 5.33: Simulated (dotted line) and measured (full line) transmission spectrum of the designed 1×7 800-GHz device with TSP method, EG08.

a maximum of 3.2 dB and a minimum of 1.6 dB. This is 0.3 dB higher than the simulated result. the measured average crosstalk is -22.81 dB with a maximum of -20.26 dB and a minimum of -37.69 dB, about 8 dB higher than the simulated result. Although there are minor mismatch, the values already match very well compared to the device designed based on the RC method. Also the performance of the device is improved significantly in terms of insertion loss and crosstalk. However, it is obvious that there still exists a wavelength shift. The simulation exhibits a red shift of 2 nm compared to the measurement. Since the TSP method is expected to eliminate the phase errors introduced in the RC method dramatically, the wavelength shift is dominantly introduced by the used effective refractive index. Following this line, we make a calibration of the effective refractive index using a random device EG04 based on the measurement. We change the effective refractive index gradually and simulate the transmission spectrum with the new refractive index, then compare it with the measurement result until they match well. Finally, we find the actual effective refractive index should be globally 0.007 (an absolute number) smaller than the used value in the initial design. After this correction, the simulation and measurements match almost perfectly, as shown in Figure 5.34. The match of simulation and

measurement on this device is not a accidental event, the effect of the correction on the effective refractive index will be verified by a more advanced device in the later section.

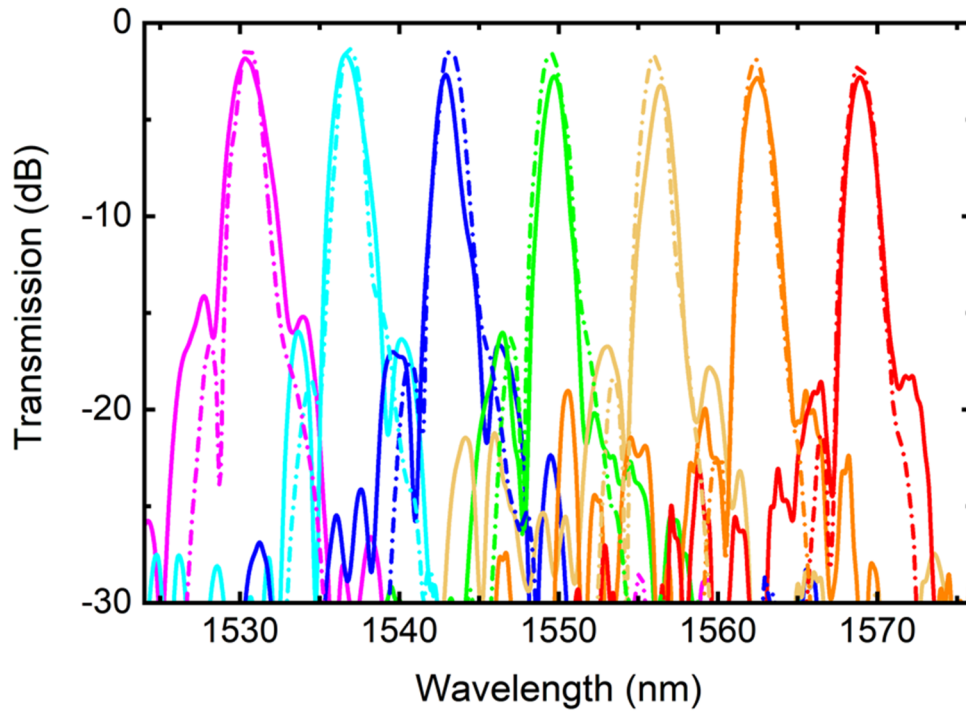


Figure 5.34: Simulated (dot line) and measured (full line) transmission spectrum of the designed 1×7 800-GHz device with TSP method after correction of the effective refractive index, EG08..

5.3.3 400 GHz channel spacing devices

On the basis of the above discussion, a more advanced device was designed. Nevertheless, it is beneficial to make systematic simulations before fabricating a device. Similar to the investigations on 800 GHz devices, the numerical simulations were made for 400 GHz devices with different ΔN .

The design parameters of the 400 GHz devices are the same to those used for the 800 GHz devices except that the output point F1 was shifted to $(9 \mu\text{m}, 0 \mu\text{m})$, the output point F2 to $(39.8 \mu\text{m}, 0 \mu\text{m})$ and the major axis length is increased to the range of $300 \mu\text{m} - 700 \mu\text{m}$. The systematic simulation results of the devices are shown in Table 5.2. Taking EG18 as the reference device with an input angle of 87.04° , the device performance shows similar variations as for the 800 GHz devices. However, it is evident that the grating span decreases significantly with the given design parameters, resulting in a global performance deterioration.

Table 5.2: Performance of the designed 400 GHz devices.

Device	ΔN	$W_n \cdot H_n (\mu\text{m} \cdot \mu\text{m})$	Input angle ($^\circ$)	Grating span ($^\circ$)	Peak transmission (dB)	Crosstalk (dB)	1-dB bandwidth (nm)
EG15	-4	$236 \times 715 = 168740$	48.03	26.78	-3.41	-24.41	0.47
EG16	-2	$197 \times 719 = 141643$	62.37	22.48	-4.97	-20.62	0.46
EG17	0	$182 \times 719 = 130858$	75.00	20.89	-5.43	-18.88	0.45
EG18	2	$180 \times 719 = 129420$	87.04	20.62	-5.57	-17.77	0.41
EG19	4	$187 \times 723 = 135201$	99.24	21.53	-4.94	-17.93	0.40
EG20	6	$206 \times 726 = 149556$	112.38	23.83	-4.13	-19.96	0.39

EG21	8	$251 \times 724 = 181724$	127.77	29.24	-3.03	-25.44	0.43
EG22	9	$301 \times 717 = 215817$	137.74	35.33	-1.85	-25.97	0.49

Subsequently, the phase errors of the 400 GHz devices were calculated as well based on Equation 5.12. The results for each device are shown in Figure 5.35. As before, the phase errors show a general decrease with increasing ΔN . In addition, the phase error is globally lower than $0.01 [\lambda]$ when ΔN is 6, 8 and 9 and the maximum grating span is obtained when $\Delta N=9$. In consequence, the device EG22 shows better performance in every aspects than the other devices.

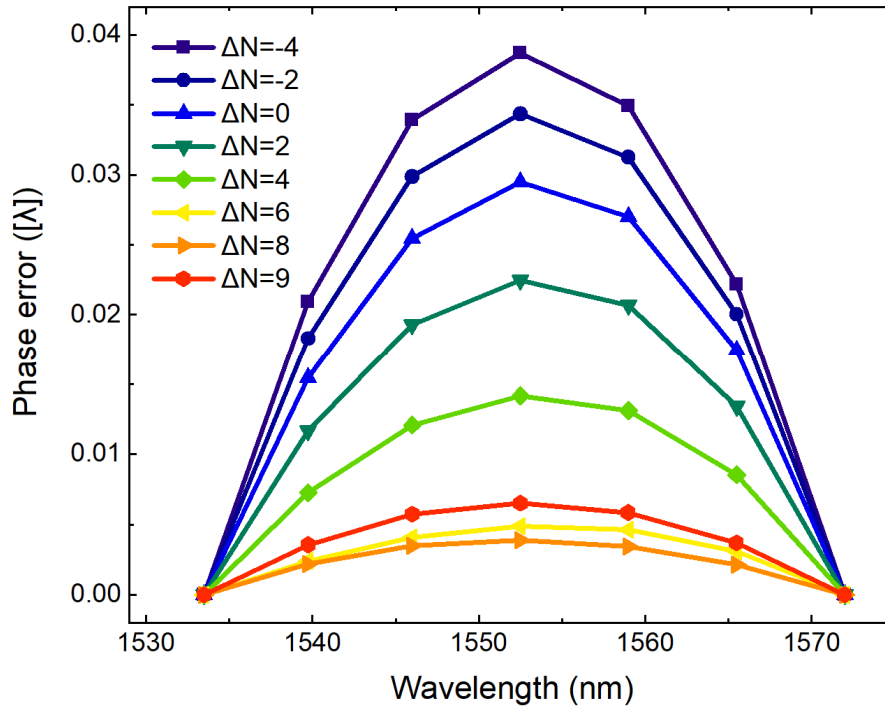


Figure 5.35: The phase error of the 400 GHz devices with different ΔN .

According to the above simulations and calculated phase errors, the device EG22 was selected for fabrication. Figure 5.36 a) is a microscope picture of the fabricated device. The two triangular regions are the so-called stray light attenuation regions, realized by heavily n-type doped with a concentration of $5 \times 10^{19} \text{ cm}^{-3}$. Figure 5.36 b) and c) are the scanning electron microscope (SEM) pictures zooming into the I/O ports and the Bragg reflectors, taken after removing the upper cladding.

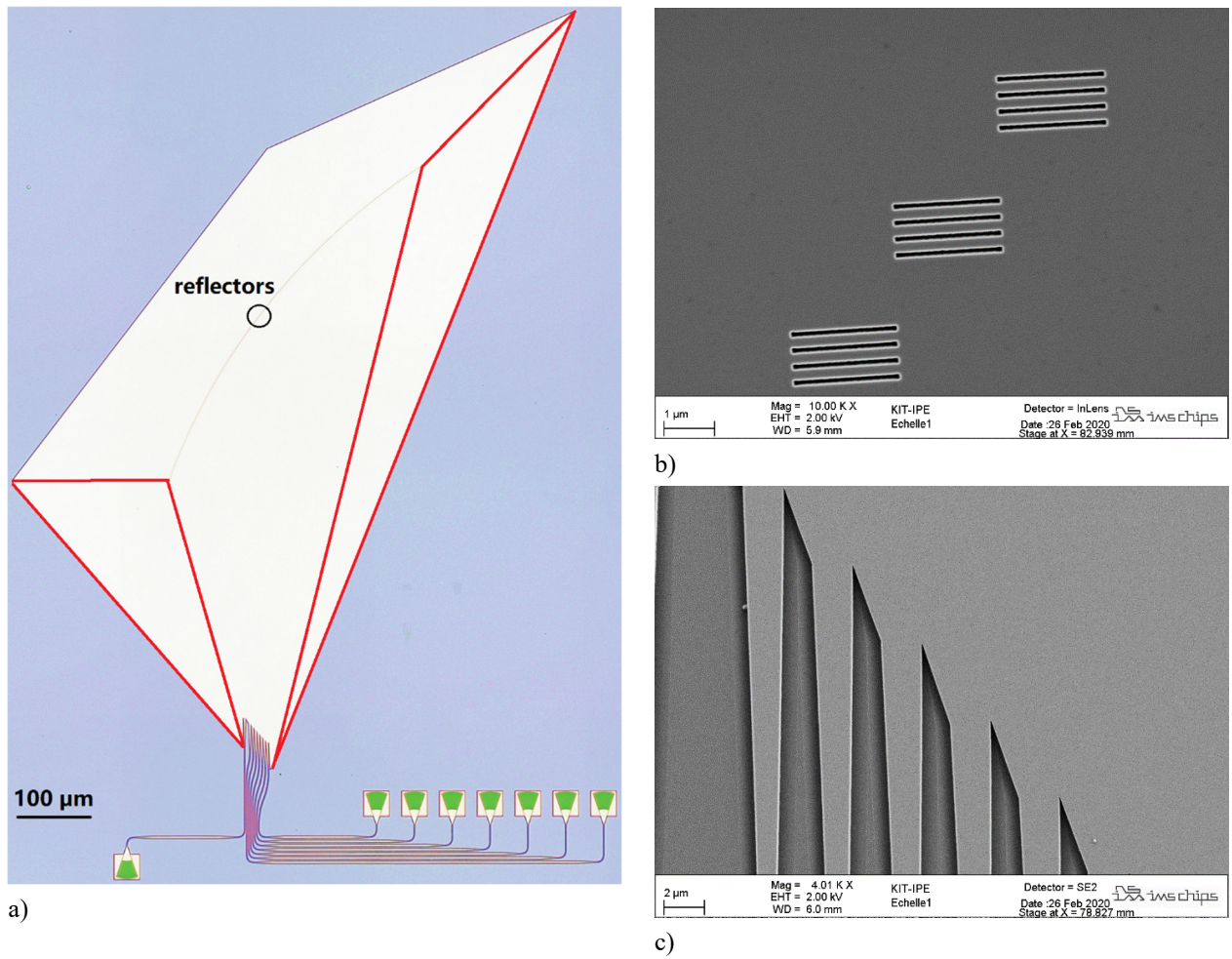


Figure 5.36: Microscope picture a) of the fabricated 1×7 400-GHz device, and SEM pictures of b) Bragg reflectors and c) optical port region of the same device. The red borders in a) show the highly doped stray light absorbers.

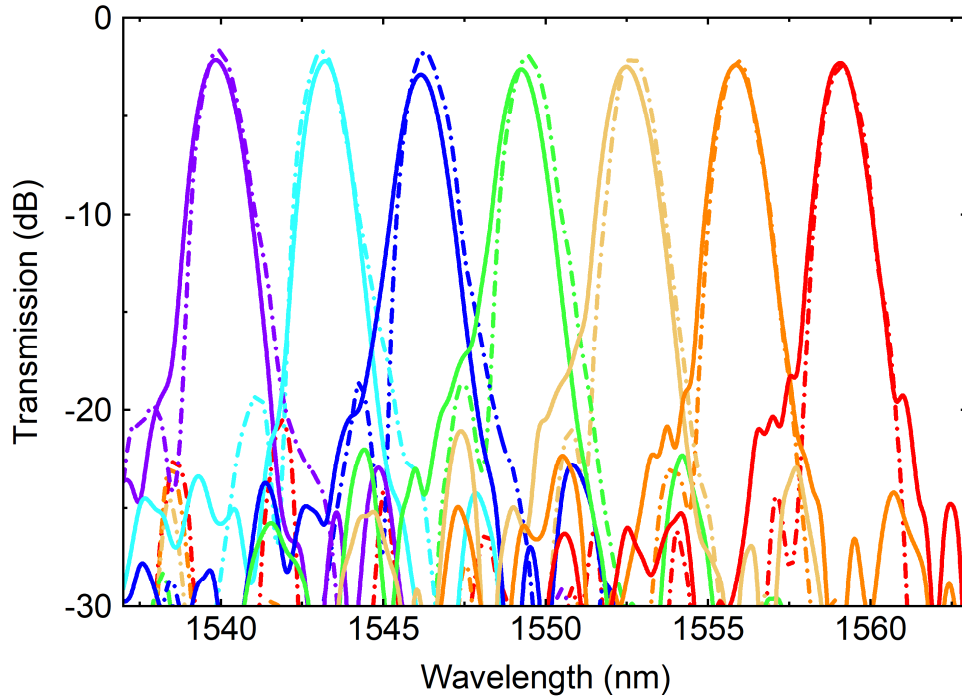


Figure 5.37: The simulated (dotted line) and measured (full line) transmission spectrum of the 1×7 400-GHz EGs.

Figure 5.37 shows the comparison of the transmission spectra of the simulated (dot-dash-dot lines) and measured (full lines) results. The simulation result in this figure was also achieved with the calibrated effective refractive index as shown above. As can be seen, the measurements and the simulations show an excellent agreement. The measured peak transmission is -2.30 dB compared to the simulated peak transmission of -1.85 dB; the measured channel-to-channel crosstalk is -24.80 dB in contrast to the simulated -25.97 dB. In addition, the 1-dB bandwidth of the measured spectrum is derived to be 0.46 nm, slightly narrower than the simulated 0.62 nm. The high performance presented by this fabricated 1×7 400 GHz device and the excellent agreement between the simulation and measurement results indicate that the design recipe is suitable to make excellent narrow-bandwidth EGs.

5.3.4 200 GHz channel spacing devices

Up to now, the TSP method developed in this thesis has shown strong advantages over the RC method in designing the EGs. However, for a scalable transmitter, which aims at an ultimate transmission bandwidth at the scale of Tb/s, a more powerful EGs is necessary. For this purpose, the channel number should be increased further in a limited usable wavelength range, which means the channel spacing must be decreased further. Therefore, another device is designed and fabricated as well to examine the possibility of using the TSP method to realize the goal.

The design parameters of this device are set as: the input point O to $(0 \mu\text{m}, 0 \mu\text{m})$, the output port 1 to $(9 \mu\text{m}, 0 \mu\text{m})$, the output port 2 to $(100 \mu\text{m}, 0 \mu\text{m})$, the maximum and minimum operating wavelengths to 1530.33 nm and 1568.77 nm with a central wavelength close to 1550 nm, the major axis length range to $400 \mu\text{m} - 1400 \mu\text{m}$.

The resulting on-chip footprint of this device is $850 \times 1300 \mu\text{m}^2$ which is too large to simulate with the available resources. Therefore, no simulation results are available for this device. The measured

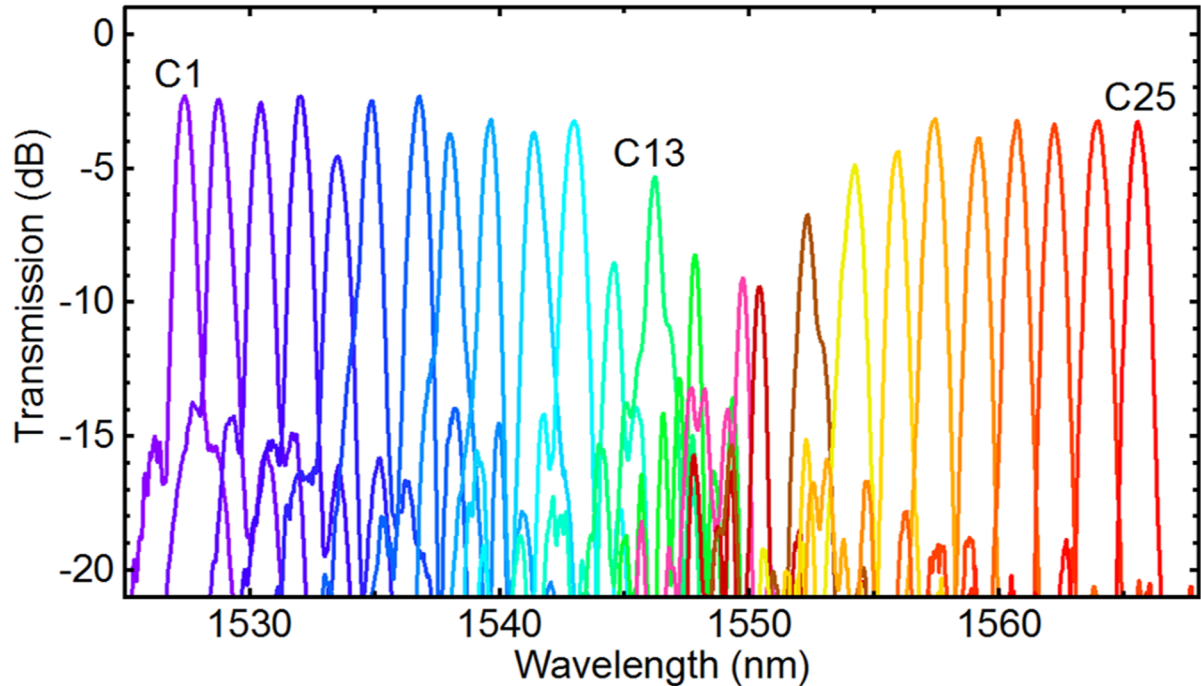


Figure 5.38: Measured transmission spectrum of the 1×25 200 GHz channel spacing EG.

results of this device is shown in Figure 5.38. Although the actual operating wavelength deviates around 2.4 nm with respect to the design, this can not be verified by a simulation result with a calibrated effective refractive index as before. Additionally, it is easy to observe that ‘broken’ channels are present in this large device as well and the number of the ‘broken’ channels achieves six. While, if ignoring these ‘broken’ channels, the remaining channels (which are called functioning channels in the following) still work in a reasonable performance. The insertion loss of these functioning channels is 3.53 dB in average, the average crosstalk is -15.7 dB. The performance of these channels is not as homogeneous as for the devices with wider channels spacing presented in the former sections. All these comparisons show that the TSP method can make excellent designs for channel spacings larger than 200 GHz. For 200-GHz devices, the design method still requires some optimization. The optimization should aim at the elimination of the ‘broken’ channels, lower crosstalk and improved insertion loss. Nevertheless, the devices designed based on the TSP method still show better performance than the devices designed with the RC method.

Since the ‘broken’ channels exist in the devices designed with both methods, this is possibly a fabrication fault. This guess can be validated by the simulation to some extent. Up to now, all the devices show an excellent match between theoretical and actual performance, indicating that the simulation method is accurate enough to estimate the performance of a designed device. An example device, already presented in [133], is shown in Figure 5.39 with simulation and measurement results. As can be seen, there is no ‘broken’ channel existing in the simulation while the fifth channel of this device shows significant performance deterioration in the measurement. Considering the accuracy of the simulation validated by the other devices, we have the reason to suspect that the fabrication is not so mature that some errors happen. The waveguides and the reflectors should be checked carefully with the original design. However, removing the cladding of the device to take SEM picture requires quite a lot of time, and could not be performed in the scope of this thesis.

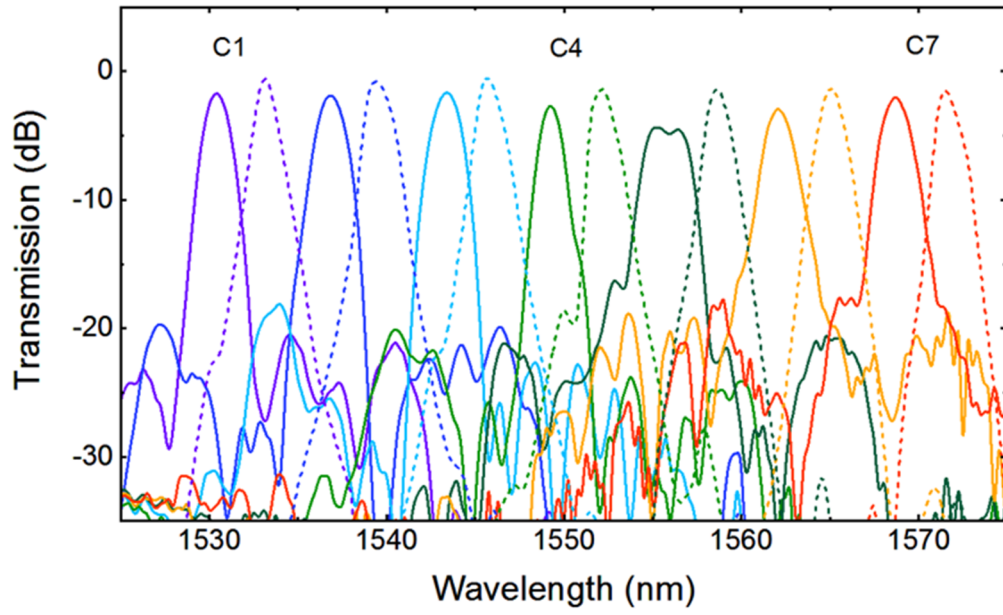


Figure 5.39: A 1×7 800-GHz device for illustration designed based on TSP method but with 'broken' channel.

6 Optical Link Demonstration

This chapter will introduce the components used in setting up the optical transmission link. The measured eye diagrams of the modulators will be made and illustrated.

6.1 Fiber to chip coupling

There are several methods to couple the light between a photonic chip and a fiber [143][144][145], which can be classified into in-plane and out-of-plane coupling.

For wafer-scale design and measurement, the out-of-plane coupling method makes more sense and representative designs can be found in [144][145]. On one hand, there might be multiple individual components on one common chip (for instance these individual modulators in the fourth chapter) which requires individual laser signals. In this case, out-of-plane grating couplers can provide more flexibilities, since the fiber port position is not limited to a polished chip edge. On the other hand, one can also manually adjust the oblique angle and the height between fiber and chip to optimize the coupling efficiency. In this thesis, out-of-plane coupling is uniformly used to make the characterization. The angle-polished fibers will be used in the final integrated demonstrator. A layout of the used grating couplers is shown in Figure 6.1. As can be seen, the grating coupler is designed to be wedge-like

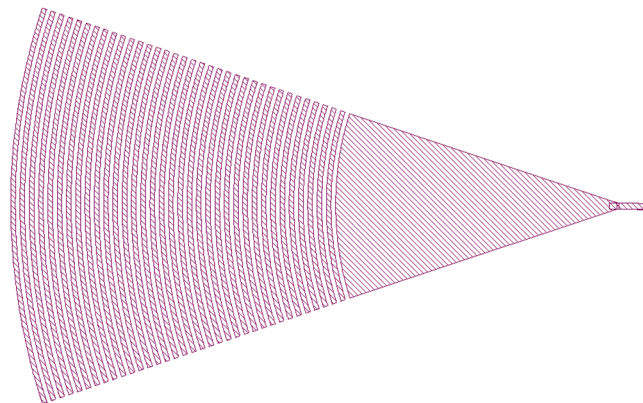


Figure 6.1: GDSII layout of the designed grating couplers.

structure. The reason for that is, the mode profile between the fiber mode and the waveguide mode is quite different. The fiber mode is circular with a radius of several micrometers while the waveguide mode in the used 250 nm SOI platform is rectangular with a dimension of 250 nm \times 500 nm. Therefore the wedge-like grating couplers are used to convert the mode shape. The grating region is generally designed based on Equation 2.6 and the optimized design should be made according to the numerical simulations. The grating period Λ is 595 nm with a filling factor of 50%. The etch depth of the grating part is 70 nm and the optimum angle θ is approximately 11° to the surface normal at a wavelength of 1550 nm. Changing the coupling position of the grating couplers can significantly affect the coupling efficiency. As shown in Figure 6.2, the blue transmission curve is measured for two grating couplers and 1 mm on-chip optical waveguide. The input optical power is 6 dBm and the highest output power for the blue curve (the best one within three measurements) appears at 1550 nm with a transmission of -5.8 dBm. If ignoring the loss from the 1 mm on-chip optical waveguide, the coupling loss from one grating coupler is approximately -5.9 dB. A better coupling efficiency can be obtained with finer

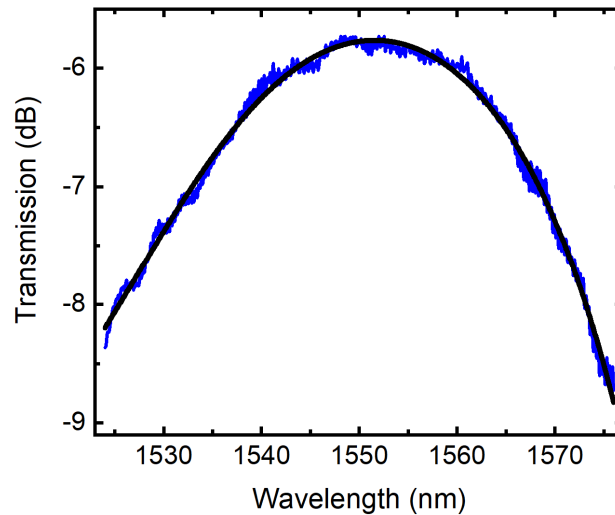


Figure 6.2: Transmission spectrum of two grating couplers and 1 mm on-chip optical waveguide.

adjustment, but the insertion loss resulting from the grating couplers can be compensated for characterizing the other components (like MMIs, MZMs).

Due to the significant instability of the error-prone out-of-plane coupling method, the final design of the integrated transmitter in this thesis will adopt a more efficient and stable coupling scheme between the chip and fiber, namely the surface coupling with angle polished fibers. As introduced before, if choosing a coupling angle of 10° , the fiber has to be cleaved by an angle of approximately 40° . The fiber polishing is made by a customized tool shown in Figure 6.3, produced by utilizing a 3D printer,



Figure 6.3: The customized fiber polishing tool.

Makerbot Replicator. Before the grinding, the fibers will be glued into grooves of a ceramic plate. The plate will be fixed in the middle of the cantilever with a clamp and the cantilever can move forward with a proper pressure on it. In addition, the plate is installed to extrude the cantilever slightly so that only the plate will touch the grinding machine to perform fiber polishing. The used grinding machine is a 'Struers LaboPol-5'. The polishing is divided into four steps, where the first step is completed by abrasive paper with a grit size of 320. Afterwards, three types of diamond polishing solutions are used with particle sizes of $9\ \mu\text{m}$, $3\ \mu\text{m}$, and $1\ \mu\text{m}$. Optimum results are obtained for a polishing duration of eight minutes for each step, where the rotation speed is 175 to 200 rounds per minute. A test of coupling efficiencies of two polished fibers is shown in Figure 6.4. Two angle-polished glass fibers are fixed with

to fiber holders. Between two holders, there is a photonic chip in the middle. Two fibers are placed above the chip, at optimized positions for the light coupling. The contacting of the electro-optic

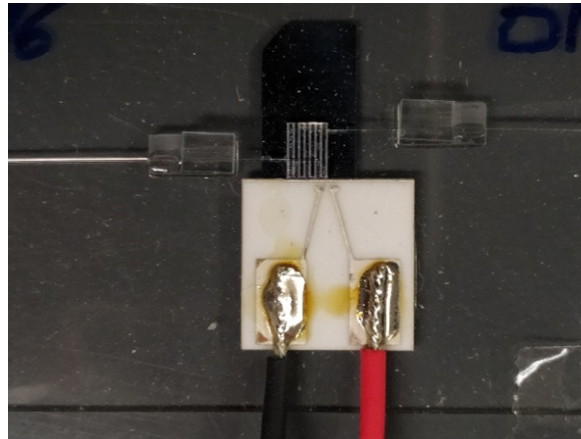


Figure 6.4: Test of the permanent fiber-to-chip coupling with angle polished fiber and the electrical contacting of an electro-optic modulator.

modulator is realized by the white plate next to the chip, to provide the required electrical signals. The result is very stable and the ratio between the highest and the lowest coupling efficiency is merely 1.1 dB during 2.7 years. A more detailed result can be found in [142].

6.2 Demonstrator setup

An optical link is mainly made of five parts: the laser source, the modulator driver, the photonic integrated transmitter, the transmission medium and the receiver. In the data transmission setup of this thesis as shown schematically in Figure 6.5, the driving signals for the MZMs are provided by a FPGA board together with an additional DWDM demultiplexer and a driver control board.

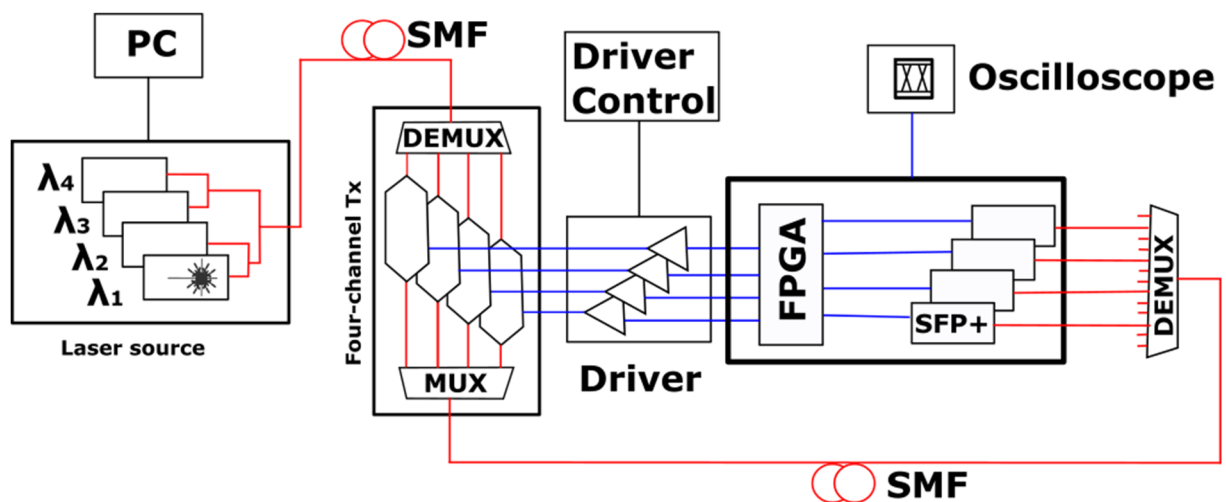


Figure 6.5: The schematic of the system demonstrator with four parallel working channels. The generation of PRBS and the analysis of BER are both realized by the FPGA development board.

The general mechanism of the data transmission system is almost similar to the measurement setup in the small signal characterization. The laser signals generated by the laser source are fed into a single mode fiber, transmitted to the photonic chip. On the chip, the combined optical carriers are separated by the on-chip DEMUX and fed to their corresponding modulators. The driver signals are generated by the

Optical Link Demonstration

FPGA and amplified by the drivers (HMC870), which are controlled by a driver control board. After the electro-optical modulation, the modulated optical carriers are combined by the on-chip MUX and conveyed to the receiver side by a SMF again. Using an off-chip DMUX, the combined optical signals are demultiplexed and transmitted to commercial SPF+ modules. These are electrically connected to the FPGA again. In addition to the bit error rate (BER) measurement, the eye pattern of the received signals can be monitored by a Tektronix CSA8200 Communication Signal Analyzer (CSA) with a Tektronix 80E04 sampling module.

The combination of four individual laser signals is done in a customized laser source. A photo of the assembled array without housing is shown in Figure 6.6 comprising four sub laser sources. Each

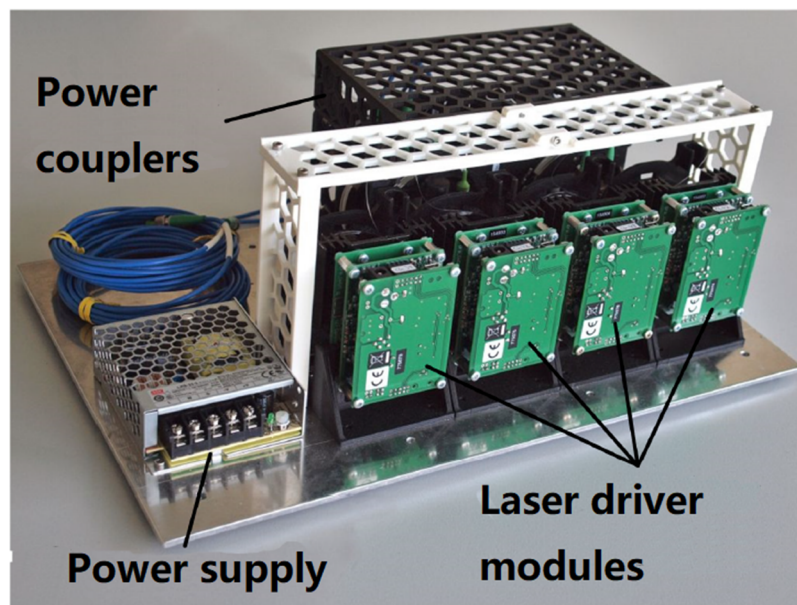


Figure 6.6: Assembly of the four-channel laser source, four laser diodes are merged to the two fiber connectors on the front plate, which is not present in the picture..

individual laser source is composed of a laser module and a laser driver. Four individual laser modules are mounted to a base plate with polarization maintaining power couplers and a common power supply. The base plate is mounted into a 'Bopla Intergo' housing. The output of this customized laser source are two 'FC/APC' SMF connectors for the optical output. It is worth mentioning that two of the four laser sources are combined by a 2×1 coupler to one signal. Another two signals are combined in the same way with another 2×1 coupler. Finally, the two multiplexed signals are combined with a 2×2 coupler in the same way, providing two similar optical outputs.

An individual sub laser source is illustrated in Figure 6.7. The laser diode is soldered to the mount board, which sits on top of the driver boards. A heat sink covers the entire surface of the butterfly package of the laser diode. For each sub laser source, a laser module 'EMCORE 1782' with a defined wavelength is used, which is characterized for the use as a CW optical source in DWDM networks. The required lasing current and the thermo-electric control is realized by 'OptoSci LDRS-OEM' laser drivers and configured by a dedicated software tool. Using the specified operating current (normally several hundred mAs) and temperature, the laser module emits signal at the desired wavelength fitting into the ITU-T G.694.1 grid.

The output power of the laser module ranges from 40 mW to 100 mW, the output power in this laser source is designed to be 40 mW. Each laser module has a built-in photodiode to monitor the output

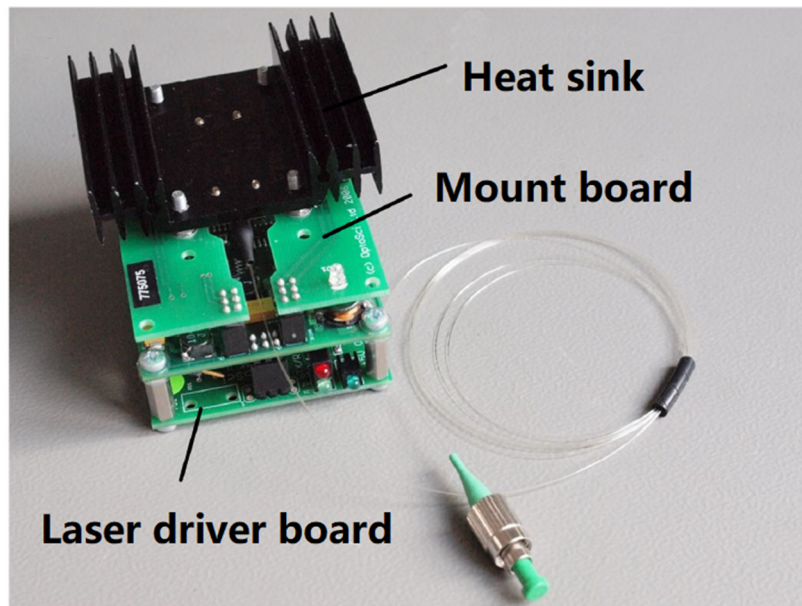


Figure 6.7: Photograph of a sub laser source, the laser diode is soldered to the mount board.

power. The emitting wavelength of the laser source can be slightly tuned by manipulating the laser's operating temperature with a limited magnitude of approximately 1 nm.

The driver circuitry for an MZM is shown in Figure 6.8, which is designed for supporting a 10Gb/s nonreturn-to-zero on/off shift keying signal with an 8B/10B coding scheme. As shown, a complete RF driver unit is made up of the driver board, the link board and the termination board. The driver board functions as signal amplifiers, the termination board is used to provide the required bias voltages for the MZMs and the termination of the transmission line while the link board is mainly designed for adapting the transmission line of the driver board to the dimensions suitable for wire bonding. The entire driver is powered by a common power supply, its successive stage 'driver control board' can generate all the required voltage levels of the entire driver namely the two bias voltages V_{B1} , V_{B2} and the DC operating voltage for the two consecutive amplifier stages.

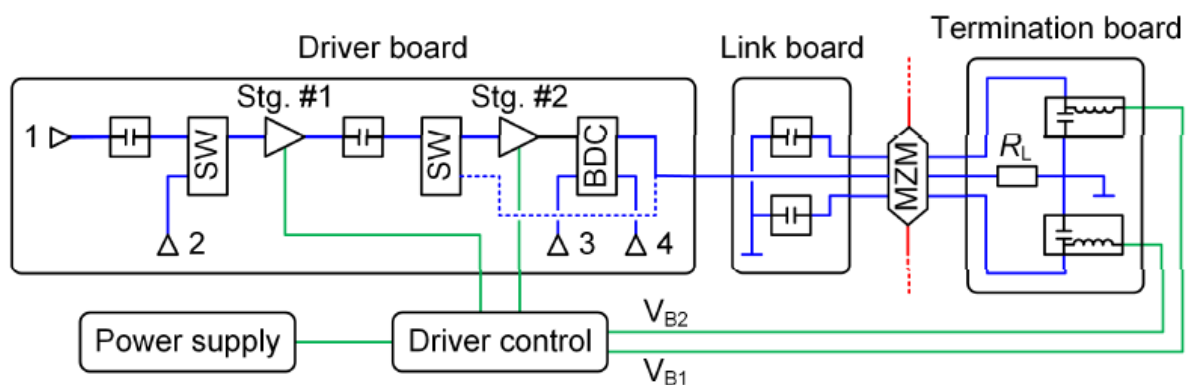


Figure 6.8: Schematic of the high frequency driver unit, showing the amplifier chain of one transmission channel.

The driver board is basically an amplifier chain assembled with discrete components. It is initially made up of two cascaded distributed amplifiers ‘Analog Devices HMC870’ by featuring 16-dB gain within a 20-GHz bandwidth. Each amplifier is operated on an evaluation board. However, in the practical design, the first HMC870 amplifier is replaced by an ‘Analog Devices HMC7144’ broadband driver amplifier, as it is more suitable as a pre-amplifier. The input sources can be either an AC signal (at Port 1) from the FPGA or a DC signal (at Port 2) from a calibration source controlled by a switch. The connection is realized by an additional bias-tee used in the chain. The AC signal should have a peak-to-peak voltage $V_{pp} = 0.5$ V. After the amplification, the amplitude is amplified to 1.2 V. The output signal from the first-stage amplifier is AC coupled to the next amplifier stage. With using another switch, the first-stage output can be connected to the output of the board directly, providing a relatively small driving signal. If the first-stage signal is further amplified by the second stage amplifier, the V_{pp} will achieve up to 8V. The last element of the driver board is the bi-directional coupler which has two ports (port 3 and port 4). The two ports of the coupler are used to monitor the output from amplifier chain and the reflected power from the load. As HMC7144 is capable of monitoring the output internally, no bi-directional coupler is equipped to the first-stage amplifier.

The link board, as another key part, is mainly used to adapt the waveguides in the driver boards to the dimensions of the contact pads of the MZMs. The RF ground is separated from the DC bias voltage of the MZMs by capacitors on the link board. The link board is attached to the driver board by semi-rigid cables with SMA connectors and the connection to the modulator contact pads is established by wire bonds.

The termination board has a termination resistance of $R_L = 50 \Omega$ to terminate the RF signal. In addition, the termination board is responsible for feeding the bias voltages V_{B1} and V_{B2} to the MZM. Since the bias potential has to be applied to the outer conductors of the modulator’s coplanar transmission line. An isolation between RF ground and the DC bias is required which are the capacitors in the link board.

A photo of the final transmitter unit comprising the driver and the photonic chip is illustrated in Figure 6.10 (two HMC870 are used). The photonic chip is fixed on a submount between the link board

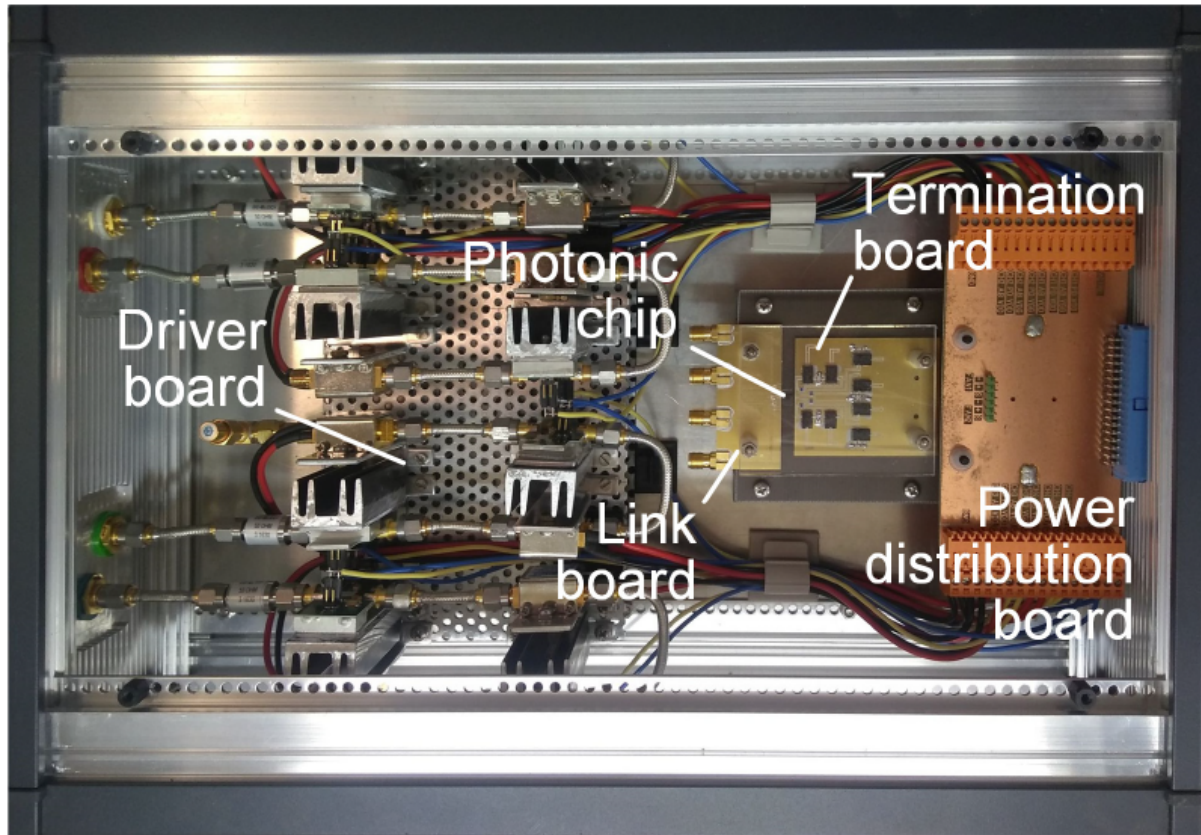


Figure 6.9: Top-view photograph of the 4-channel transmitter including the driver unit and the photonic chip.

and the termination board. The electrical contacts are established by wire bonding. Due to the large dimension of the driver unit, the next version of the driver will be integrated on a small chip as well so that the entire transmitter is compact enough for the application in a limited space. The input and output fibers are coupled to the chip by the surface fiber-to-chip coupling method with angle polished fiber introduced in the last section.

For the bit error rate (BER) measurements of the transmission link, an Altera Stratix V GX FPGA on a Transceiver Signal Integrity Development Board is used. This is a multi-functional development board that the user can select different features via a control program. In the BER testing, the GXB SMA transceivers of the board are used. On one side, PRBS signals can be fed to the SMA connectors of the RF driver as input signal. On the other hand, the received signal is also transmitted back to FPGA via this module. The opto-electrical conversion of the receiver is implemented by SFP+ transceivers, SFP-10GER-55, with a transmission bit rate from 3.1 Gb/s to 11.3 Gb/s. The interface between the SFP+ transceiver and the GXB transceiver of the FPGA board is realized by Hitech Global SMA to SFP/SFP+ conversion module, which supports dual direction transmission. After establishing the link, the FPGA will generate a PRBS test signal with a length of $2^N - 1$ where N can be set to 7, 15, 23 and 31. The transmission data rate could be set between 0.6 Gb/s to 12.5 Gb/s. Several key parameters can be adjusted for the front-end of the GXB transceiver. These are mainly the differential output voltage, the pre-emphasis of the transmitter signal, and the gain and equalization of the received signal.

Unfortunately, the complete transmission system covering all four wavelength channels could not be accomplished in time. Nevertheless, BER measurements of one single MZM could be made for analysis. According to the analysis of the previous chapter, the 2-mm MZM and 1-mm MZM have a larger cut-off frequency than the 10 Gb/s transmission speed. On the other hand, a shorter MZM will have a lower modulation effect at a specific bias voltage. The 2-mm asymmetric MZM will have a better performance and therefore was selected as the test modulator. It is worth mentioning that the 4-channel laser source

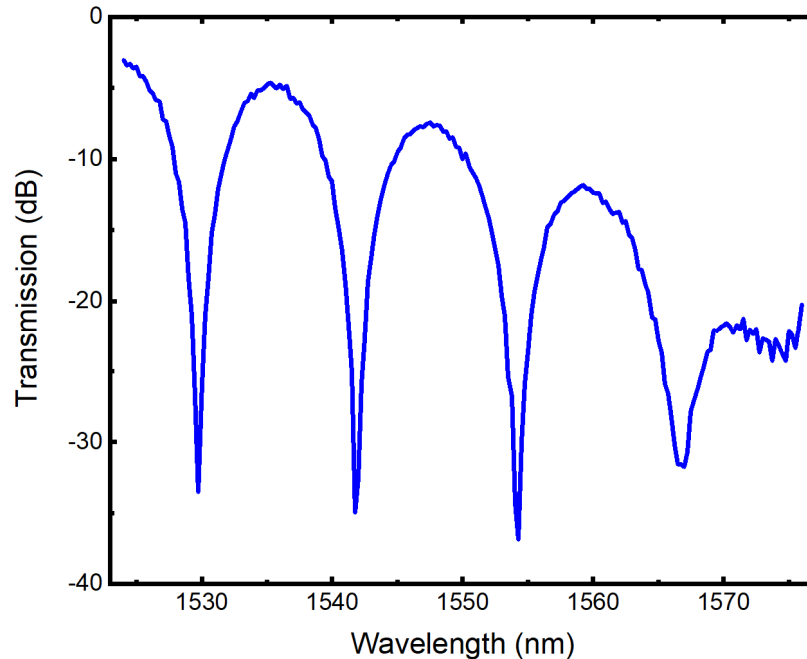


Figure 6.10: The transmission spectrum of the 2-mm asymmetric MZM with 5V reverse bias voltage.

was replaced by the tuneable laser source for convenience. To select an operating point, the DC characterization was made first of all where the input optical power from the laser source is 6 dBm. The measured transmission spectrum under a reverse bias voltage of 5V is shown in Figure 6.10. The first transmission peak appears at 1535 nm with an insertion loss of 4.7 dB. The operation point was selected to the point where the transmission is -3 dB at 1538.75 nm, the corresponding insertion loss from two grating couplers is 14.9 dB. The insertion loss introduced by the MZM is 7.9 dB. To obtain optimum transmission, the optical power was amplified by an EDFA to 0 dBm before being fed into the SFP+ module.

The measurement was carried out at a temperature of 24.9°C and a humidity of 55.1%. The RF signal was generated by the FPGA with a driving voltage of $V_{pp} = 500$ mV. The RF signal was amplified to 4.3 V_{pp} , 6.1 V_{pp} , 8.3 V_{pp} , 10.2 V_{pp} , 14.2 V_{pp} and 16.9 V_{pp} by adjusting the operating current of the driver. The corresponding eye diagrams are shown in Figure 6.11. It can be observed that with higher driving amplitude, a wider eye opening can be obtained. Since the measured characteristic impedance of the MZM is approximately 30 Ω , only a fraction of the electric signal was loaded onto the modulator.

With these RF signals, BER measurements were made. For all measurements, the transmitted number of bits were 4.0×10^{12} for the convenience of comparison. The resulting BER are 2.0×10^{-3} , 1.8×10^{-3} , 4.1×10^{-6} , 2.8×10^{-6} , 1.1×10^{-7} , 7.9×10^{-8} and 2.6×10^{-10} . According to the measurement results, although the 2-mm MZM has a sufficient cutoff frequency, the modulation efficiency is relatively low. The modulation effect can be improved in several aspects, including increasing the modulator length,

ensuring accurate doping concentrations and optimizing transmission line to ensure matched characteristic impedance. Nevertheless, once the driving voltage reached a reasonable amplitude, the BER can be very low to the order of 10^{-10} . With accurate doping concentrations, the designed modulator could meet the transmission bandwidth well.

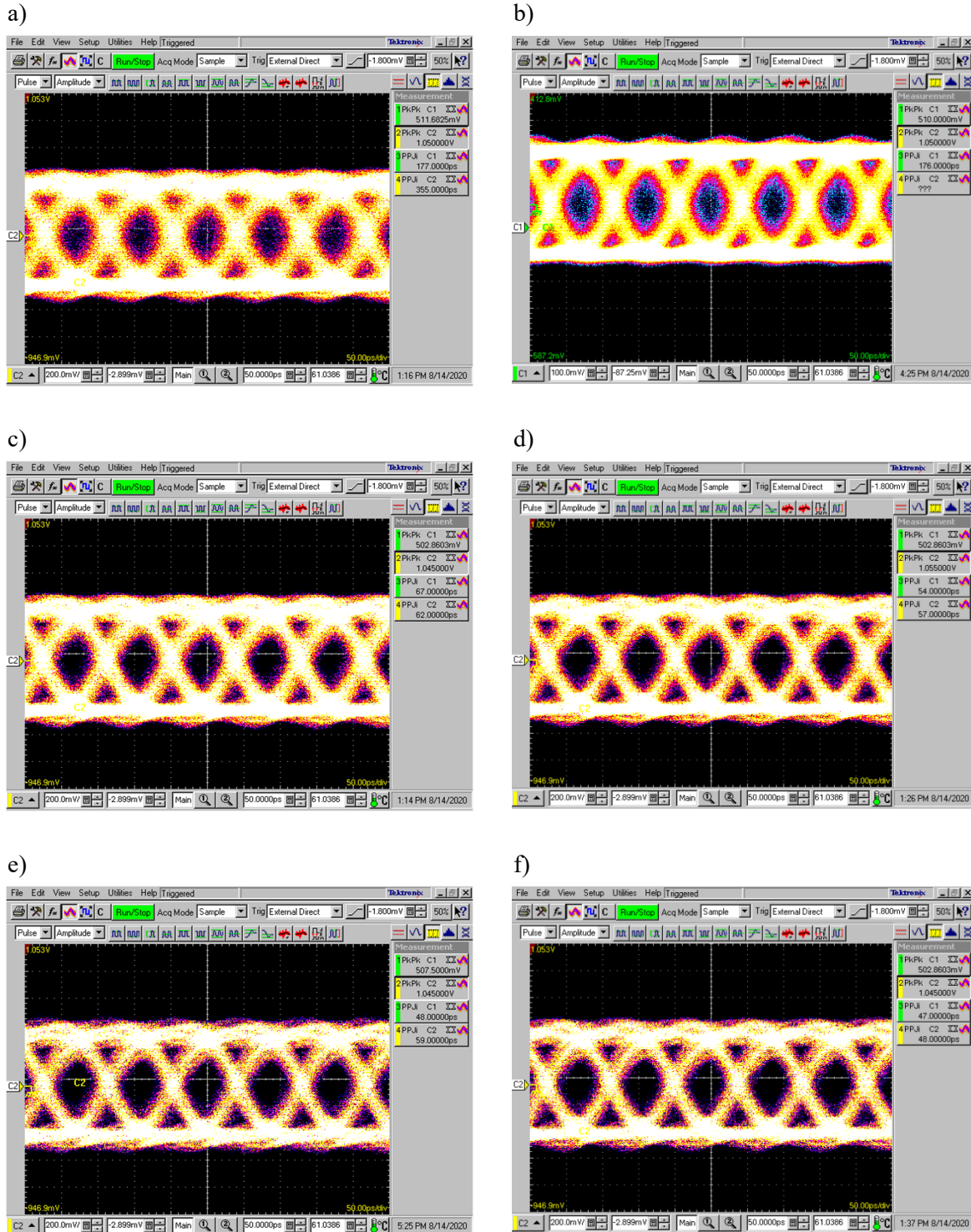


Figure 6.11: Measured eye patterns of the 2-mm MZM with complete optical link at different driving amplitudes, a) $4.3 V_{pp}$, b) $6.1 V_{pp}$, c) $8.3 V_{pp}$, d) $10.2 V_{pp}$, e) $14.2 V_{pp}$, and f) $16.9 V_{pp}$.

7 Conclusion

In this thesis, the challenges existing in the optical data transmission in detector instrumentation are investigated. Due to the considerable transmission bandwidth requirements and the harsh operating environment of particle detectors, a generic data readout concept is proposed based on the WDM technique and SOI platform with a potential transmission bandwidth up to several Tb/s to cope with the challenges in detector instrumentation. Based on the previous work within the institute, this thesis focuses on a critical part of the concept, namely the integrated $n\text{-}\lambda$ transmitter. To this end, a photonic chip was designed and fabricated to study the two key building blocks DMUX and MZM modulators together with a full integrated $4\text{-}\lambda$ transmitter.

For the study of MZMs, a complete simulation process to calculate the static performance of the designed modulators is established based on the software TCAD Sentaurus, MATLAB and COMSOL Multiphysics. Through the simulations, several parameters that can affect the modulation efficiency, including the doping concentration of the p- and n- regions of a pn phase shifter, the junction line offset, and also the cross-section design of the phase shifter were identified. These parameters present different degrees of impact on the modulation efficiency in the simulations, while the doping concentration is the dominant one.

For the purpose of verification, a set of modulators with identical design parameters but different lengths were designed and fabricated on a 250 nm SOI platform, where the estimated $V_{\pi}\cdot L$ should be around $1.22 V_{\pi}\cdot\text{cm}$ in case of ideal doping profiles (7×10^{17} and 5×10^{17} for the p- and n- regions, respectively). However, the measurements show a much lower $V_{\pi}\cdot\text{cm}$ of $3.9 V_{\pi}\cdot\text{cm}$ at maximum. Associated with the simulation results, this is most likely due to a low doping concentration. Also, the doping technique is quite uneven since the two phase shifters of one modulator show rather different performances in general.

To cope with the degradation under particle irradiation, modulators with shallower etching depths were also designed and fabricated. According to the simulations, such a kind of modulators shows lower modulation efficiency than the normally etched modulators. However, the shallow etched modulators show a general higher modulation efficiency of up to $4.1 V_{\pi}\cdot\text{cm}$. Again, the comparison indicates that the doping technique of the foundry is not mature enough and significantly affects the performance of the modulators.

In the RF measurements, I firstly made the electrical scattering parameter measurements for all the electrodes. The cutoff frequencies of the 1-mm and 2-mm electrodes are beyond our measurement ability while the measured values are 10.2 GHz and 4.9 GHz for the 3-mm and 4-mm MZMs, respectively. However, in the small signal characterization, the cutoff frequencies of the MZMs decreased significantly. But an increase of the bias voltages can increase the cutoff frequencies. According to the results, on one hand, either the length of the modulator can be decreased or the bias voltage can be increased to improve the cutoff frequency. On the other hand, the cutoff frequency of modulators are higher than that of the electric electrodes. Not only the doping technique but also the modulator design (for example the velocity and the resistance matching) can be optimized to improve the entire modulator performance.

MMIs are used as optical power splitters and combiners in a MZM in this thesis. Both the 2×2 50:50 design and the 2×2 86:14 design show favorable performance and excellent agreement between simulation and measurement results. Two types of MMIs have a total insertion loss less than 0.5 dB while maintaining stable splitting ratios over the entire C band, which indicates that the 2D simulation model used in this thesis can provide accurate estimations.

For the design of WDM wavelength filters, two popular design methods to construct the Echelle grating demultiplexers are introduced, while this thesis is more focused on the two stigmatic point method over the Rowland circle method. A new design parameter ΔN is introduced to make the design more flexible. By modifying ΔN , the trajectory of the grating points is tunable. Simultaneously, the footprint and the performance of the designed devices can be altered. Usually, a reference device can be found when the input angle is close to 90° . The simulation results show that the reference device has the minimum grating span and the most compact footprint, resulting in slightly worse performance than the others. Consequently, both increasing and decreasing ΔN can improve the performance of the devices with respect to the reference device. All the devices designed with the method presented in this thesis show relatively low phase errors while a positive ΔN tends to provide a smaller phase error. Although the phase error can be optimized further, the influence on image reconstruction from the phase error is weaker than from the grating span, according to the comparison. To validate the generality of the developed method, a series of 400 GHz devices is designed and compared as well. The corresponding comparison shows similar results, which indicates that the design method is feasible in a more general case. Finally, the device with the largest grating span together with a very low phase error is selected for fabrication. The fabricated 1×7 EG DMUX is ultra-compact with an on-chip footprint of $301 \times 717 \mu\text{m}^2$. The measured transmission, channel-to-channel crosstalk and 1-dB bandwidth are -2.30 dB, -24.80 dB and 0.46 nm, respectively, very close to the simulation results. The excellent agreement between the simulation and the measurement results validates the design method in a practical way. This shows that the developed method in this thesis provides an effective way to design high-performance Echelle grating demultiplexers.

The fabricated $4\text{-}\lambda$ integrated transmitter unit which comprises two Echelle grating demultiplexers and four 3-mm MZM modulators, features a very compact dimension of $3.8 \times 1.67 \text{ mm}^2$, enabling the application inside the limited space of a particle detector. While the $4\text{-}\lambda$ data transmission could not be set up in time, the experiment of a $1\text{-}\lambda$ data transmission based on a 2-mm MZM was conducted. Clear opening eyes were obtained at a transmission speed of 11.3 Gb/s, a reverse bias voltage of 5 V and different driving amplitudes ($4.3 V_{\text{pp}}$ - $16.9 V_{\text{pp}}$). Increasing the driving amplitude can improve the transmission quality where the bit error rate will be lower for identical transmitted bits. For the current design, relatively large driving signals and reverse bias voltages are required due to the low doping concentration and resistance mismatch. However, we believe this can be improved significantly with proper optimization. The designed system is quite feasible for the aimed 40 Gb/s transmission.

To sum up, the essential building blocks of an integrated $n\text{-}\lambda$ SOI transmitter are presented in this thesis, the relevant simulation models can accurately predict the performance of the designed devices. With the help of IMS CHIPS, the $4\text{-}\lambda$ integrated transmitter was fabricated as well. The successful demonstration of the $1\text{-}\lambda$ data transmission presents the feasibility of the design. With further irradiation experiments and optimization, the critical building blocks will be available for the proposed data transmission concept that may revolutionize the detector readout.

8 Acknowledgements

Doing a PhD is a very hard job, especially in a foreign country. Fortunately, I have a very kind professor, supervisor and nice colleagues. Time flies, everything seems to have happened yesterday while I have to admit I had a lot of fun here.

Thank you, Prof. Dr. Marc Weber sincerely for giving me the chance to study here. I really gained a lot in the past 4 years' study, not only the knowledge on optical data transmission but also on the culture of Germany and even Europe. Also, thank you so much for taking a lot of time revising my papers and thesis even though you were very busy. More importantly, you really provide me a super research environment especially various academic activities. You always support me to take part in any kinds of conferences and trainings, I am very grateful for it.

The most time I spent is with my supervisor, Marc Schneider. I appreciate your patience a lot. I have to admit that I had little experience on our project and photonics design at the very beginning. But you explained the concept, the design and even how to make the measurements to me again and again until I really understood it. More importantly, you taught me how to be a researcher, I learned from you to be as accurate as possible with research. This is the most valuable treasure in my life. Of course, we are more of friends than colleagues. I like talking with you about cartoons, weather, foods etc.. Thank you very much for keeping bringing funs to me.

I also thank for the help from my colleague Julius. I usually asked you to help me to make phone calls or write emails concerning German. Without your help, I cannot imagine how I can survive. I also admire your beneficent opinions, protecting environment and advocating peace etc..

From Lars and Djorn, I learned a lot, you are so open that I bothered you again and again while you never complained. I can usually learn new terms from you, especially interesting things in life. I feel great to make friends with you. It's really a pity that I still cannot swim, still cannot open my eyes in the water and still cannot play the Linux game well. I really hope I can have the opportunity to do it with you in the future.

I got a lot of help from my other nice colleagues as well. Thank you Thomas for supporting me with all kinds of measurements. Thank you Sascha for explaining all that I cannot understand.

Last but not the least, I feel so sorry for my family, sorry that I cannot travel back to China frequently. Sorry I cannot accompany my parents more, sorry I cannot celebrate the past four Spring Festivals with you. But thank you very very much for supporting me with the PhD study abroad.

A List of abbreviations

WDM	Wavelength Division Multiplexing
CMS	Compact Muon Solenoid
AGIPD	Adaptive Gain Integrating Pixel Detector
CERN	European Organization for Nuclear Research
LHC	Large Hadron Collider
ATLAS	A Toroidal LHC ApparatuS
MZM	Mach Zehnder Modulator
DMUX	De-multiplexer
SMF	Single Mode Glass Fiber
RC	Rowland Circle
TSP	Two Stigmatic Point
BER	Bit Error Rate
BOX	Buried Oxide
CMOS	Complementary Metal–oxide–semiconductor
ALICE	A Large Ion Collider Experiment
RF	Radio Frequency
VCSEL	Vertical-cavity Surface-emitting Laser Diodes
DBR	Distributed Bragg Reflectors
MMI	Multimode Interferometers
EG	Echelle Grating
MZI	Mach-zehnder Interferometer
OOK	On off shift Keying
QAM	Quadrature Amplitude Modulation
TCAD	Technology Computer Aided Design
FSR	Free Spectral Range
CPW	Coplanar Waveguide
CPS	Coplanar Strips
SPP	Series Push-pull
VNA	Vector Network Analyzer
PRBS	Pseudo-random Bit Sequence
EDFA	Erbium-doped Fiber Amplifier

A: List of abbreviations

AWG	Arrayed Waveguide Gratings
CWDM	Coarse Wavelength Division Multiplexing
DWDM	Dense Wavelength Division Multiplexing
SOI	Silicon on Insulator
SEM	Scanning Electron Microscope
CSA	Communication Signal Analyzer
CW	Continuous Wavelength

B List of mathematical symbols

W_G	Bandgap energy
Δn	Change of refractive index
k_0	Wave vector in free space
n_{eff}	Effective refractive index
β	Propagation constant
$\mathbf{E}(r, t)$	The electric field of a plane wave
$J_\nu(u)$	Bessel functions, used to describe the radial field distribution in the core
$K_\nu(\omega)$	Bessel functions, used to describe the radial field distribution in the cladding
Λ	Grating period
n_{clad}	Refractive index of the cladding
$\Delta\alpha$	Change of attenuation constant
Δn_{eff}	Change of the effective refractive index
$\Phi(x, y, z)$	Electric potential
ϵ_s	Permittivity of the semiconductor
$\rho(x, y, z)$	Local charge density ($C \cdot cm^{-3}$)
N_d^+	Concentration of ionized donor atoms in the semiconductor
N_a^-	Concentration of ionized acceptor atoms in the semiconductor
l_{p0}	Length of the depletion region at the p-type side
l_{n0}	Length of the depletion region at the n-type side
$\Delta\varphi$	Phase shift
Φ_0	Built-in potential between the p- and n-side of the pn junction
V_a	Applied bias voltage
Δl	Path difference
$P(I, T)$	Output power of a laser, as a function of the current and temperature
$\eta(T)$	Differential quantum efficiency, as a function of the temperature
$I_{th}(T)$	Lasering threshold current, as a function of the temperature
$R(T)$	Resistance of VECSEL, as a function of the temperature
r_{33}	Coefficient in the Pockels effect
n_{33}	Refractive index in the direction of the applied electric field
\bar{n}	Complex refractive index
ω	Angular frequency
S_{Tr}	Transfer function

B: List of mathematical symbols

n_g	Group index
FSR	Free spectral range
σ	Conductivity
μ_e	Electron mobility
μ_p	Hole mobility
A	Surface area of the parallel plates
R	Resistance
C	Capacitance
ϵ_{re}	Relative permittivity
$V_\pi L$	Unit used to characterize the modulation efficiency of a modulator
β_m	Propagation constant of the m^{th} order mode
θ_{in}	Input angle of the Echelle grating demultiplexer
θ_{out}	Output angle of the Echelle grating demultiplexer
$d\theta$	Difference of the output angles between two adjacent output ports
$d\lambda$	Difference of the peak output wavelengths between two adjacent output ports
\bar{E}	Average phase error
L_l	Length of desired optical path of the l^{th} grating point

References

- [1] S. Abachi et al. "Observation of the top quark." *Physical Review Letters* 74.14 (1995): 2632.
- [2] K. Kodama et al. "Observation of tau neutrino interactions." *Physics Letters B* 504.3 (2001): 218-224.
- [3] CMS collaboration. "CMS-PAS-HIG-14-009." *arXiv preprint arXiv:1412.8662* (2014).
- [4] G. Aad et al. "Measurement of the Higgs boson mass from the $H \rightarrow \gamma\gamma$ and $H \rightarrow ZZ^* \rightarrow 4\ell$ channels with the ATLAS detector using 25 fb^{-1} of pp collision data." *Physical Review D (particles, Fields, Gravitation and Cosmology)* 90 (2014).
- [5] S. K. Selvaraja et al. "Fabrication of photonic wire and crystal circuits in silicon-on-insulator using 193-nm optical lithography." *Journal of Lightwave Technology* 27.18 (2009): 4076-4083.
- [6] <https://spie.org/news/spie-professional-magazine-archive/2015-october/silicon-data-links-at-cern-lhc?SSO=1>
- [7] J. P. Koutchouk et al. *A solution for phase-one upgrade of the LHC low-beta quadrupoles based on Nb-Ti*. No. LHC-PROJECT-Report-1000. 2007.
- [8] <https://blog.microfocus.com/how-much-data-is-created-on-the-internet-each-day/>
- [9] "Nortel launches first 10 Gbit/s transmission system in Asia," On-line: <https://www.hpcwire.com/1997/06/13/nortel-launches-first-10-gbits-transmission-system-in-asia/> (1997).
- [10] S. M. Sze and K. K. Ng. *Physics of semiconductor devices*. John Wiley & Sons, 2006.
- [11] G. T. Reed and A. P. Knights. *Silicon photonics: an introduction*. John Wiley & Sons, 2004.
- [12] W. P. Maszara et al. "Bonding of silicon wafers for silicon-on-insulator." *Journal of Applied Physics* 64.10 (1988): 4943-4950.
- [13] M. Bruel "Silicon on insulator material technology." *Electronics letters* 31.14 (1995): 1201-1202.
- [14] L. Vivien and L. Pavesi. *Handbook of silicon photonics*. Taylor & Francis, 2016.
- [15] C. W. Holzwarth et al. "Optimization of hydrogen silsesquioxane for photonic applications." *Journal of Vacuum Science & Technology B: Microelectronics and Nanometer Structures Processing, Measurement, and Phenomena* 25.6 (2007): 2658-2661.
- [16] J. W. Mayer and S. S. Lau. *Electronic materials science: for integrated circuits in Si and GaAs*. Prentice Hall, 1990.
- [17] G. Grau and W. Freude, *Optische Nachrichtentechnik: Eine Einführung*. Berlin: Springer, 1991.
- [18] K. S. Chiang. "Performance of the effective-index method for the analysis of dielectric waveguides." *Optics letters* 16.10 (1991): 714-716.
- [19] <https://www.lumerical.com>.
- [20] <https://www.synopsys.com>.
- [21] <https://www.comsol.com>.

References

- [22] J. M. Senior and M. Y. Jamro. *Optical fiber communications: principles and practice*. Pearson Education, 2009.
- [23] R. A. Soref and B. R. Bennett. "Electrooptical effects in silicon." *IEEE journal of quantum electronics* 23.1 (1987): 123-129.
- [24] M. Nedeljkovic et al. "Free-Carrier Electrorefraction and Electroabsorption Modulation Predictions for Silicon Over the 1–14- μm Infrared Wavelength Range." *IEEE Photonics Journal* 3.6 (2011): 1171-1180.
- [25] LHCb Collaboration. "LHCb technical design report: Reoptimized detector design and performance." *CERN/LHCC* 30 (2003).
- [26] ALICE, Collaboration. "ALICE: Technical Proposal for a Large Ion Collider Experiment at the CERN LHC." *CERN/LHCC/, LHCC P 3* (1995): 95-71.
- [27] L. Evans and P. Bryant. "LHC machine." *Journal of instrumentation* 3.08 (2008): S08001.
- [28] L. Rossi and O. Brüning. "Introduction to the HL-LHC Project." *The High Luminosity Large Hadron Collider: The New Machine for Illuminating the Mysteries of Universe*. 2015. 1-17.
- [29] K. Aamodt et al. "The ALICE experiment at the CERN LHC." *Journal of Instrumentation* 3.08 (2008): S08002.
- [30] A. A. Alves Jr et al. "The LHCb detector at the LHC." *Journal of instrumentation* 3.08 (2008): S08005.
- [31] CMS Collaboration, "The CMS electromagnetic calorimeter project," Technical Design Report CERN-LHCC-97-033; CMS-TDR-4, 1997.
- [32] CMS Collaboration, "The CMS hadron calorimeter project," Technical Design Report CERN-LHCC-97-031; CMS-TDR-2, 1997.
- [33] Collaboration, C. M. S. "CMS MUON Project Technical Design Report." *Preprint* (1997): 97-32.
- [34] Collaboration, C. M. S. "The CMS experiment at the CERN LHC." (2008).
- [35] R. Musenich et al. *CMS TriDAS project: Technical Design Report, Volume 1: The Trigger Systems*. No. CERN-LHCC-2000-038. CMS-TDR-006-1, 2000.
- [36] A. Rácz and P. Sphicas. *CMS The TriDAS Project: Technical Design Report, Volume 2: Data Acquisition and High-Level Trigger*. No. CERN-LHCC-2002-026. CMS-TDR-006, 2002.
- [37] S. Dasu et al. *CMS. The TriDAS project. Technical design report, vol. 1: The trigger systems*. No. CERN-LHCC-2000-038. 2000.
- [38] P. La Rocca and F. Riggi. "The upgrade programme of the major experiments at the Large Hadron Collider." *Journal of Physics: Conference Series*. Vol. 515. No. 1. IOP Publishing, 2014.
- [39] CMS Collaboration. *Technical proposal for the upgrade of the CMS detector through 2020*. No. CMS-UG-TP-1. 2011.
- [40] CMS Collaboration. "Technical proposal for the phase-II upgrade of the CMS detector." *CMS Technical proposal CERN-LHCC-2015-010, CMS-TDR-15-02, CERN* (2015).

- [41] M. Altarelli et al. "The European x-ray free-electron laser technical design report." *DESY 97.2006* (2006): 4.
- [42] M. Altarelli. "The European X-ray free-electron laser facility in Hamburg." *Nuclear Instruments and Methods in Physics Research Section B: Beam Interactions with Materials and Atoms* 269.24 (2011): 2845-2849.
- [43] A. Allahgholi et al. "AGIPD, a high dynamic range fast detector for the European XFEL." *Journal of Instrumentation* 10.01 (2015): C01023.
- [44] J. Troska et al. "Optical readout and control systems for the CMS tracker." *2002 IEEE Nuclear Science Symposium Conference Record*. Vol. 1. IEEE, 2002.
- [45] F. Vasey et al. "Development of radiation-hard optical links for the CMS tracker at CERN." *IEEE transactions on nuclear science* 45.3 (1998): 331-337.
- [46] G. Cervelli et al. "A radiation tolerant laser driver array for optical transmission in the LHC experiments." (2001).
- [47] J. Troska et al. "Radiation-hard optoelectronic data readout for the ATLAS SCT." *Photonics for Space Environments VII*. Vol. 4134. International Society for Optics and Photonics, 2000.
- [48] K. Gill et al. "High Statistics Testing of Radiation Hardness and Reliability of Lasers and Photodiodes." (2004).
- [49] J. Troska et al. "Radiation damage studies of lasers and photodiodes for use in multi-Gb/s optical data links." *IEEE Transactions on Nuclear Science* 58.6 (2011): 3103-3110.
- [50] F. Vasey et al. "The Versatile Link common project: feasibility report." *Journal of Instrumentation* 7.01 (2012): C01075.
- [51] P. Moreira et al., "The GBT Project". (2009), <https://cds.cern.ch/record/1235836>.
- [52] J. Troska et al. "Laser and photodiode environmental evaluation for the Versatile Link project." *Journal of Instrumentation* 8.02 (2013): C02053.
- [53] Laser components (UK) Ltd. Goldlay House, 114 Parkway, Chelmsford, Essex. CM2 7PR UK. <http://www.lasercomponents.co.uk>.
- [54] R. Michalzik. *VCSELs: fundamentals, technology and applications of vertical-cavity surface-emitting lasers*. Vol. 166. Springer, 2012.
- [55] Y. C. Chang et al. "High-efficiency, high-speed VCSELs with 35 Gbit/s error-free operation." *Electronics Letters* 43.19 (2007): 1022-1023.
- [56] <https://www.datasheetarchive.com/>.
- [57] V. Lakovlev et al. "High-performance single-mode VCSELs in the 1310-nm waveband." *IEEE Photonics Technology Letters* 17.5 (2005): 947-949.
- [58] A. Caliman et al. "25 Gbps direct modulation and 10 km data transmission with 1310 nm waveband wafer fused VCSELs." *Optics express* 24.15 (2016): 16329-16335.
- [59] A. Caliman et al. "> 25 Gbps direct modulation and data transmission with 1310 nm waveband wafer fused VCSELs." *Optical Fiber Communication Conference*. Optical Society of America, 2016.
- [60] A. Mutig. *High speed VCSELs for optical interconnects*. Springer Science & Business Media, 2011.

References

- [61] P. Stejskal. *Radiation Effects in Optical Link Components for Future Particle Physics Detectors*, Ph.D. thesis, CERN (2013-04-02), http://inspirehep.net/record/1296400/files/783314135_CERN-THESIS-2013-115.pdf.
- [62] Y. Liu et al. "Numerical investigation of self-heating effects of oxide-confined vertical-cavity surface-emitting lasers." *IEEE journal of quantum electronics* 41.1 (2005): 15-25.
- [63] J. Troska et al. "Radiation damage studies of lasers and photodiodes for use in multi-Gb/s optical data links." *IEEE Transactions on Nuclear Science* 58.6 (2011): 3103-3110.
- [64] X. Zheng et al. "Ultralow power 80 Gb/s arrayed CMOS silicon photonic transceivers for WDM optical links." *Journal of Lightwave Technology* 30.4 (2012): 641-650.
- [65] A. Alduino et al. "Demonstration of a high speed 4-channel integrated silicon photonics WDM link with hybrid silicon lasers." *Integrated Photonics Research, Silicon and Nanophotonics*. Optical Society of America, 2010.
- [66] O. Krebs and P. Voisin. "Giant optical anisotropy of semiconductor heterostructures with no common atom and the quantum-confined Pockels effect." *Physical review letters* 77.9 (1996): 1829.
- [67] B. Chmielak et al. "Pockels effect based fully integrated, strained silicon electro-optic modulator." *Optics express* 19.18 (2011): 17212-17219.
- [68] B. O. Seraphin and N. Bottka. "Franz-Keldysh effect of the refractive index in semiconductors." *Physical Review* 139.2A (1965): A560.
- [69] V. Lucarini et al. *Kramers-Kronig relations in optical materials research*. Vol. 110. Springer Science & Business Media, 2005.
- [70] H. Miura et al. "High thermal stability 40 GHz electro-optic polymer modulators." *Optics Express* 25.23 (2017): 28643-28649.
- [71] S. Sun et al. "Hybrid Silicon and Lithium Niobate Mach-Zehnder Modulators with Silicon Thermal-optic Phase Shifter." *Asia Communications and Photonics Conference*. Optical Society of America, 2019.
- [72] M. W. Geis et al. "Submicrosecond submilliwatt silicon-on-insulator thermo-optic switch." *IEEE photonics technology letters* 16.11 (2004): 2514-2516.
- [73] A. H. Gnauck and P. J. Winzer. "Optical phase-shift-keyed transmission." *Journal of lightwave technology* 23.1 (2005): 115.
- [74] E. Agrell et al. "Roadmap of optical communications." *Journal of Optics* 18.6 (2016): 063002.
- [75] J. X. Cai. "Advanced technologies for high capacity transoceanic distance transmission systems." *Optical Fiber Communication Conference*. Optical Society of America, 2017.
- [76] A. Ghazisaeidi et al. "65Tb/s transoceanic transmission using probabilistically-shaped PDM-64QAM." *ECOC 2016-Post Deadline Paper; 42nd European Conference on Optical Communication*. VDE, 2016.
- [77] S. Zhang et al. "Capacity-approaching transmission over 6375 km at spectral efficiency of 8.3 bit/s/Hz." *2016 Optical Fiber Communications Conference and Exhibition (OFC)*. IEEE, 2016.
- [78] L. Vivien et al. "Comparison between strip and rib SOI microwaveguides for intra-chip light distribution." *Optical materials* 27.5 (2005): 756-762.
- [79] L. Brillouin. *Wave propagation and group velocity*. Vol. 8. Academic Press, 2013.
- [80] G. T. Reed. *Silicon photonics: the state of the art*. John Wiley & Sons, 2008.
- [81] D. Thomson et al. "Using SiO₂ carrier confinement in total internal reflection optical switches to restrict carrier diffusion in the guiding layer." *Journal of lightwave technology* 26.10 (2008): 1288-1294.

- [82] D. Thomson et al. "Total internal reflection optical switch in SOI with defect engineered barrier region." *Journal of lightwave technology* 28.17 (2010): 2483-2491.
- [83] T. W. Ang et al. "Integrated optics in unibond for greater flexibility." *Silicon-on-insulator Technology and Devices: Proceedings of the Ninth International Symposium on Silicon-on-Insulator Technology and Devices*. Vol. 99. No. 3. The Electrochemical Society, 1999.
- [84] C. E. Png et al. "Optical phase modulators for MHz and GHz modulation in silicon-on-insulator (SOI)." *Journal of lightwave technology* 22.6 (2004): 1573.
- [85] W. M. J. Green et al. "Ultra-compact, low RF power, 10 Gb/s silicon Mach-Zehnder modulator." *Optics express* 15.25 (2007): 17106-17113.
- [86] Q. Xu et al. "12.5 Gbit/s carrier-injection-based silicon micro-ring silicon modulators." *Optics express* 15.2 (2007): 430-436.
- [87] A. Liu et al. "A high-speed silicon optical modulator based on a metal-oxide-semiconductor capacitor." *Nature* 427.6975 (2004): 615-618.
- [88] L. Liao et al. "High speed silicon Mach-Zehnder modulator." *Optics express* 13.8 (2005): 3129-3135.
- [89] H. Yu et al. "Performance tradeoff between lateral and interdigitated doping patterns for high speed carrier-depletion based silicon modulators." *Optics express* 20.12 (2012): 12926-12938.
- [90] W. D. Callister Jr and D.G. Rethwisch. *Materials science and engineering: an introduction*. New York: Wiley, 2018.
- [91] W. D. Callister Jr and D.G. Rethwisch. *Fundamentals of materials science and engineering: an integrated approach*. John Wiley & Sons, 2012.
- [92] G. Bruguier and J. M. Palau. "Single particle-induced latchup." *IEEE transactions on nuclear science* 43.2 (1996): 522-532.
- [93] E. Normand. "Single event upset at ground level." *IEEE transactions on Nuclear Science* 43.6 (1996): 2742-2750.
- [94] J. H. Hohl and K. F. Galloway. "Analytical model for single event burnout of power MOSFETs." *IEEE Transactions on Nuclear Science* 34.6 (1987): 1275-1280.
- [95] S. S. E. I. Nasr-Storey et al. "Silicon photonics for high energy physics data transmission applications." *11th International Conference on Group IV Photonics (GFP)*. IEEE, 2014.
- [96] S. S. E. I. Nasr-Storey et al. "Neutron and X-ray irradiation of silicon based Mach-Zehnder modulators." *Journal of Instrumentation* 10.03 (2015): C03040.
- [97] S. S. E. I. Nasr-Storey et al. "Effect of radiation on a Mach-Zehnder interferometer silicon modulator for HL-LHC data transmission applications." *IEEE Transactions on Nuclear Science* 62.1 (2015): 329-335.
- [98] M. Zeiler et al. "Radiation hardness evaluation and phase shift enhancement through ionizing radiation in silicon Mach-Zehnder modulators." *2016 16th European Conference on Radiation and Its Effects on Components and Systems (RADECS)*. IEEE, 2016.
- [99] L. Chen et al. "Chirp and dispersion tolerance of a single-drive push-pull silicon modulator at 28 Gb/s." *IEEE Photonics Technology Letters* 24.11 (2012): 936-938.
- [100] P. Dong et al. "High-speed low-voltage single-drive push-pull silicon Mach-Zehnder modulators." *Optics express* 20.6 (2012): 6163-6169.
- [101] H. Yu and W. Bogaerts. "An equivalent circuit model of the traveling wave electrode for carrier-depletion-based silicon optical modulators." *Journal of lightwave technology* 30.11 (2012): 1602-1609.
- [102] H. F. Talbot. "LXXVI. Facts relating to optical science. No. IV." *The London, Edinburgh, and Dublin Philosophical Magazine and Journal of Science* 9.56 (1836): 401-407.

References

- [103] Lord Rayleigh. "XXV. On copying diffraction-gratings, and on some phenomena connected therewith." *The London, Edinburgh, and Dublin Philosophical Magazine and Journal of Science* 11.67 (1881): 196-205.
- [104] J. M. Cowley, and A. F. Moodie. "Fourier images: I-the point source." *Proceedings of the Physical Society. Section B* 70.5 (1957): 486.
- [105] E. A. Hiedemann and M. A. Breazeale. "Secondary interference in the Fresnel zone of gratings." *JOSA* 49.4 (1959): 372-375.
- [106] J. T. Winthrop and C. R. Worthington. "Theory of Fresnel images. I. Plane periodic objects in monochromatic light." *JOSA* 55.4 (1965): 373-381.
- [107] L. A. Rivlin et al. "Multimode waveguides for coherent light." *Radiophysics and Quantum Electronics* 11.4 (1968): 318-321.
- [108] O. Bryngdahl et al. "Image formation using self-imaging techniques." *JOSA* 63.4 (1973): 416-419.
- [109] R. Ulrich and G. Ankele. "Self-imaging in homogeneous planar optical waveguides." *Applied Physics Letters* 27.6 (1975): 337-339.
- [110] Y. Zhang et al. "A compact and low loss Y-junction for submicron silicon waveguide." *Optics express* 21.1 (2013): 1310-1316.
- [111] J. C. Mikkelsen et al. "Dimensional variation tolerant silicon-on-insulator directional couplers." *Optics Express* 22.3 (2014): 3145-3150.
- [112] H. Yun et al. "2x2 adiabatic 3-dB coupler on silicon-on-insulator rib waveguides." *Photonics North 2013*. Vol. 8915. International Society for Optics and Photonics, 2013.
- [113] R. Halir et al. "A design procedure for high-performance, rib-waveguide-based multimode interference couplers in silicon-on-insulator." *Journal of lightwave technology* 26.16 (2008): 2928-2936.
- [114] M. Bachmann et al. "General self-imaging properties in $N \times N$ multimode interference couplers including phase relations." *Applied optics* 33.18 (1994): 3905-3911.
- [115] B. E. Little et al. "Microring resonator channel dropping filters." *Journal of lightwave technology* 15.6 (1997): 998-1005.
- [116] F. C. Blom et al. "Experimental study of integrated-optics microcavity resonators: Toward an all-optical switching device." *Applied physics letters* 71.6 (1997): 747-749.
- [117] D. J. W. Klunder et al. "Vertically and laterally waveguide-coupled cylindrical microresonators in Si₃N₄ on SiO₂ technology." *Applied Physics B* 73.5-6 (2001): 603-608.
- [118] D. H. Geuzebroek et al. "Thermally tuneable, wide FSR switch based on micro-ring resonators." *Proceedings Symposium IEEE/LEOS Benelux Chapter*. 2002.
- [119] Y. Hu et al. "High-speed silicon modulator based on cascaded microring resonators." *Optics express* 20.14 (2012): 15079-15085.
- [120] K. Yamada et al. "Silicon-wire-based ultrasmall lattice filters with wide free spectral ranges." *Optics letters* 28.18 (2003): 1663-1664.
- [121] S. K. Chu et al. "Cascaded microring resonators for crosstalk reduction and spectrum cleanup in add-drop filters." *IEEE Photonics Technology Letters* 11.11 (1999): 1423-1425.

- [122] Y. P. Li et al. "Monolithic optical waveguide 1.31/1.55/ μm WDM with-50 dB crosstalk over 100 nm bandwidth." *Electronics Letters* 31.24 (1995): 2100-2101.
- [123] F. Horst et al. "Cascaded Mach-Zehnder wavelength filters in silicon photonics for low loss and flat pass-band WDM (de-) multiplexing." *Optics express* 21.10 (2013): 11652-11658.
- [124] H. Xu and Y. Shi. "Flat-top CWDM (de) multiplexer based on MZI with bent directional couplers." *IEEE Photonics Technology Letters* 30.2 (2017): 169-172.
- [125] H. Takahashi et al. "Arrayed-waveguide grating for wavelength division multi/demultiplexer with nanometre resolution." *Electronics letters* 26.2 (1990): 87-88.
- [126] C. Castellan et al. "Low crosstalk silicon arrayed waveguide gratings for on-chip optical multiplexing." *Silicon Photonics: From Fundamental Research to Manufacturing*. Vol. 10686. International Society for Optics and Photonics, 2018.
- [127] S. Tondini et al. "Methods for low crosstalk and wavelength tunability in arrayed-waveguide grating for on-silicon optical network." *Journal of Lightwave Technology* 35.23 (2017): 5134-5141.
- [128] R. J. Lycett et al. "Perfect chirped echelle grating wavelength multiplexor: design and optimization." *IEEE Photonics Journal* 5.2 (2013): 2400123-2400123.
- [129] W. Heiss et al. "Epitaxial Bragg mirrors for the mid-infrared and their applications." *Progress in Quantum Electronics* 25.5-6 (2001): 193-228.
- [130] International Telecommunication Union, "Spectral grids for WDM applications: DWDM frequency grid," Recommendation G.694.1, Feb. 2012.
- [131] Y. Fu et al. "Efficient adiabatic silicon-on-insulator waveguide taper." *Photonics Research* 2.3 (2014): A41-A44.
- [132] L. Liu et al. "Design of nanostructured adiabatic waveguide tapers with ultra-short lengths." *Asia Communications and Photonics Conference*. Optical Society of America, 2017.
- [133] Y. Zhang et al. "Low-loss and robust DWDM Echelle grating (de-) multiplexers in SOI technology." *Optical Components and Materials XVI*. Vol. 10914. International Society for Optics and Photonics, 2019.
- [134] R. Güther and S. Polze. "The construction of stigmatic points for concave gratings." *Optica Acta: International Journal of Optics* 29.5 (1982): 659-665.
- [135] J. D. F. Bartoe et al. "New stigmatic, coma-free, concave-grating spectrograph." *JOSA* 65.1 (1975): 13-21.
- [136] H. Wen et al. "Design of a flat-field EDG wavelength demultiplexer using a two stigmatic points method." *Acta Photonica Sinica* 32.3 (2003): 307.
- [137] T. Harada et al. "Mechanically ruled stigmatic concave gratings." *Japanese Journal of Applied Physics* 14.S1 (1975): 175.
- [138] F. Horst et al. "Echelle grating WDM (de-) multiplexers in SOI technology, based on a design with two stigmatic points." *Silicon Photonics and Photonic Integrated Circuits*. Vol. 6996. International Society for Optics and Photonics, 2008.
- [139] F. Horst et al. "Silicon-on-insulator echelle grating WDM demultiplexers with two stigmatic points." *IEEE Photonics Technology Letters* 21.23 (2009): 1743-1745.

References

- [140] Y. Zhang et al. "A high-performance Echelle grating de-multiplexer based on two stigmatic points and its flat-top solution." *Optical Interconnects XX*. Vol. 11286. International Society for Optics and Photonics, 2020.
- [141] Y. Zhang et al. "Building blocks of a scalable and radiation-hardened integrated transmitter unit based on 250-nm SOI." *Optical Interconnects XX*. Vol. 11286. International Society for Optics and Photonics, 2020.
- [142] K. Djorn et al. "Efficient, easy-to-use, planar fiber-to-chip coupling process with angle-polished fibers." *2017 IEEE 67th Electronic Components and Technology Conference (ECTC)*. IEEE, 2017.
- [143] D. Taillaert et al. "An out-of-plane grating coupler for efficient butt-coupling between compact planar waveguides and single-mode fibers." *IEEE Journal of Quantum Electronics* 38.7 (2002): 949-955.
- [144] D. Taillaert et al. "Compact efficient broadband grating coupler for silicon-on-insulator waveguides." *Optics letters* 29.23 (2004): 2749-2751.
- [145] Y. Tang et al. "Highly efficient nonuniform grating coupler for silicon-on-insulator nanophotonic circuits." *Optics letters* 35.8 (2010): 1290-1292.